

STRUCTURAL DAMAGE DETECTION USING SIGNAL-BASED PATTERN
RECOGNITION

by

LONG QIAO

B.S., Xian University of Architecture and Technology, China, 1998
M.S., Texas Tech University, Lubbock, 2003

AN ABSTRACT OF A DISSERTATION

submitted in partial fulfillment of the requirements for the degree

DOCTOR OF PHILOSOPHY

Department of Civil Engineering
College of Engineering

KANSAS STATE UNIVERSITY
Manhattan, Kansas

2009

Abstract

Civil structures are susceptible to damages over their service lives due to aging, environmental loading, fatigue and excessive response. Such deterioration significantly affects the performance and safety of structure. Therefore, it is necessary to monitor the structural performance, detect and assess damages at the earliest possible stage in order to reduce the life-cycle cost of structure and improve its reliability. Over the last two decades, extensive research has been conducted on structural health monitoring and damage detection.

In this study, a signal-based pattern-recognition method was applied to detect structural damages with a single or limited number of input/output signals. This method is based on the extraction of sensitive features of the structural response under a known excitation that present a unique pattern for any particular damage scenario. Frequency-based features and time-frequency-based features of the acceleration response were extracted from the measured vibration signals by Fast Fourier Transform (FFT) and Continuous Wavelet Transform (CWT) to form one-dimensional or two-dimensional patterns, respectively. Three pattern recognition algorithms were investigated when performing pattern-matching: (1) correlation, (2) least square distance, and (3) Cosh spectral distance.

To demonstrate the validity and accuracy of the method, numerical and experimental studies were conducted on a simple small-scale three-story steel building. In addition, the efficiency of the features extracted by Wavelet Packet Transform (WPT) was examined in the experimental study. The results show that the features of the signal for different damage scenarios can be uniquely identified by these transformations. Suitable correlation algorithm can then be used to identify the most probable damage scenario. The proposed method is suitable for structural health monitoring, especially for the online monitoring applications. Meanwhile, the choice of wavelet function affects the resolution of the detection process and is discussed in the “experimental study part” of this report.

STRUCTURAL DAMAGE DETECTION USING SIGNAL-BASED PATTERN
RECOGNITION

by

LONG QIAO

B.S., Xian University of Architecture and Technology, China, 1998
M.S., Texas Tech University, Lubbock, 2003

A DISSERTATION

submitted in partial fulfillment of the requirements for the degree

DOCTOR OF PHILOSOPHY

Department of Civil Engineering
College of Engineering

KANSAS STATE UNIVERSITY
Manhattan, Kansas

2009

Approved by:

Major Professor
Asad Esmaeily

Copyright

LONG QIAO

2009

Abstract

Civil structures are susceptible to damages over their service lives due to aging, environmental loading, fatigue and excessive response. Such deterioration significantly affects the performance and safety of structure. Therefore, it is necessary to monitor the structural performance, detect and assess damages at the earliest possible stage in order to reduce the life-cycle cost of structure and improve its reliability. Over the last two decades, extensive research has been conducted on structural health monitoring and damage detection.

In this study, a signal-based pattern-recognition method was applied to detect structural damages with a single or limited number of input/output signals. This method is based on the extraction of sensitive features of the structural response under a known excitation that present a unique pattern for any particular damage scenario. Frequency-based features and time-frequency-based features of the acceleration response were extracted from the measured vibration signals by Fast Fourier Transform (FFT) and Continuous Wavelet Transform (CWT) to form one-dimensional or two-dimensional patterns, respectively. Three pattern recognition algorithms were investigated when performing pattern-matching: (1) correlation, (2) least square distance, and (3) Cosh spectral distance.

To demonstrate the validity and accuracy of the method, numerical and experimental studies were conducted on a simple small-scale three-story steel building. In addition, the efficiency of the features extracted by Wavelet Packet Transform (WPT) was examined in the experimental study. The results show that the features of the signal for different damage scenarios can be uniquely identified by these transformations. Suitable correlation algorithm can then be used to identify the most probable damage scenario. The proposed method is suitable for structural health monitoring, especially for the online monitoring applications. Meanwhile, the choice of wavelet function affects the resolution of the detection process and is discussed in the “experimental study part” of this report.

Table of Contents

List of Figures	ix
List of Tables	xv
Acknowledgements	xvi
Dedication	xvii
CHAPTER 1 - INTRODUCTION	1
1.1 Introduction	1
1.2 Objectives	4
CHAPTER 2 - LITERATURE REVIEW	6
2.1 Feature Extraction and Selection	6
2.1.1 Time-domain Methods	6
2.1.2 Frequency-domain Methods	11
2.1.3 Time-Frequency (or Scale)-domain Methods	13
2.2 Pattern Recognition	21
2.2.1 Fisher's Discriminant	21
2.2.2 X-bar Control Chart	21
2.2.3 Outlier Detection	22
2.2.4 Bayesian Probabilistic Approach	23
2.2.5 Neural Networks	25
2.3 Applications to Special Structures	27
2.3.1 Damage Detection on Bridge	27
2.3.2 Crack Detection on Beam and Plate	29
2.3.3 Damage Detection on Mechanical Structures	31
CHAPTER 3 - THEORETICAL BACKGROUND	33
3.1 Fourier Transforms	34
3.1.1 Continuous Fourier Transform	34
3.1.2 Discrete Fourier Transform	35
3.1.3 Fast Fourier Transform	35
3.1.4 Short Time Fourier Transform	40

3.2 Wavelet Transforms.....	40
3.2.1 Continuous Wavelet Transform (CWT)	42
3.2.2 Discrete Wavelet Transform (DWT)	48
3.2.3 Wavelet Packet Transform (WPT).....	55
3.3 Pattern Recognition Techniques	58
CHAPTER 4 - PRELIMINARY NUMERICAL STUDY.....	60
4.1 Descriptions of Test Structure and FE Model	60
4.2 Numerical Simulation of the Dynamic Response of the Structure.....	64
4.3 Signal Processing and Feature Extraction and Normalization.....	71
4.4 Damage Pattern Database Construction	74
4.5 Case Studies and Pattern Matching	76
4.6 Discussion on Preliminarily numerical Study	80
CHAPTER 5 - EXPERIMENTAL TEST AND VERIFICATION	81
5.1 Design and Construction of the Representative Test Structure	81
5.2 Impulse Applicator	85
5.3 Sensor and Data Acquisition System.....	90
5.3.1 Accelerometer	90
5.3.2 Base Station	91
5.3.3 Software	92
5.4 Test Procedure	94
5.5 Damage Pattern Database	96
5.5.1 3-D FE Model	96
5.5.2 Tuning the 3-D FE Model.....	98
5.5.3 Constructing Damage Pattern Database.....	98
5.6 Case Studies and Pattern Matching	98
5.7 Discussion on Experimental Study	100
5.8 WPT-Based Feature Extraction and Pattern Recognition.....	101
CHAPTER 6 - CONCLUSIONS	109
6.1 Research Summary	109
6.2 Conclusion	110
6.3 Recommended Future Work.....	112

References	113
------------------	-----

List of Figures

Figure 1.1 SHM and Damage Detection Categories.....	1
Figure 3.1 Butterfly.....	38
Figure 3.2 The Harmonic Signal and Its FFT Spectrum.....	39
Figure 3.3 The Morlet Wavelet.....	41
Figure 3.4 Fourier Transform, $H(\omega)$ of the Morlet Wavelet.....	42
Figure 3.5 Signal $f(t)$ along with the Morlet Wavelet (denoted by w) at Three Scales and Shifts.....	44
Figure 3.6 Wavelet Morlet (blue) and Center Frequency Based Approximation.....	45
Figure 3.7 CWT Scale-Space (time) Contours of Signal, $f(t)$	46
Figure 3.8 CWT Frequency-Time Contour of Signal, $f(t)$	47
Figure 3.9 3-D View of CWT Frequency-Time Contour of Signal, $f(t)$	48
Figure 3.10 Some Example of Pairs of Functions ϕ , ψ : (a) The Meyer Wavelets; (b) and (c) Battle-Lemarie Wavelets; (d) The Haar Wavelet (Daubechies, 1992)	51
Figure 3.11 Three-Level Wavelet Decomposition Tree	52
Figure 3.12 Splitting the Signal with an Iterated Filter Bank	52
Figure 3.13 Three-Level Wavelet Reconstruction Tree	53
Figure 3.14 Decompose Signal at Depth 3 with Discrete Wavelet.....	54
Figure 3.15 Tree Structure for Wavelet Packet Analysis	57
Figure 3.16 Components of the 3 rd Level WPT for the Harmonic signal, $f(t)$	57
Figure 4.1 Flowchart of Pattern Recognition.....	61
Figure 4.2 3-D Steel Structure and 2-D FE Model	62
Figure 4.3 2-D Model in ANSYS Graphical User Interface.....	63
Figure 4.4 Element Geometric Properties (Real Constants) Screen	64
Figure 4.5 Load Steps and Time Steps	67
Figure 4.6 Apply F/M on Nodes Window	67
Figure 4.7 Time and Time Steps Options Window	68
Figure 4.8 Write Load Step File Window.....	68
Figure 4.9 Add Time-History Variable Window	69

Figure 4.10 Define Nodal Data Window	69
Figure 4.11 Derivative of Time-History Variables Window	70
Figure 4.12 Time History Variables Window.....	70
Figure 4.13 Acceleration Signal for Baseline Condition (Damage Case 0-0-0).....	71
Figure 4.14 FFT Spectrums for Different Damage Case: (a) Damage Case 0-0-0 (Baseline Condition), (b) Damage Case 20-40-60, (c) Damage Case 60-20-40, (d) Damage Case 60-60-60	72
Figure 4.15 CWT Contours for Different Damage Cases: (a) Damage Case 0-0-0 (Baseline Condition), (b) Damage Case 40-60-60, (c) Damage Case 60-40-60, (d) Damage Case 60-60-60	74
Figure 4.16 FFT Pattern Database 3-D Graph	75
Figure 4.17 Acceleration Signals for Damage Case 0-38-38	78
Figure 5.1 Test Three-Story Steel Structure	82
Figure 5.2 Slab and Flat Bar Connection.....	83
Figure 5.3 Slab and Flat Bar Connection.....	84
Figure 5.4 Foundation Slab Fixing	84
Figure 5.5 Close View of Magnetic Base, Ball, Chain and Frame.....	86
Figure 5.6 [Left] Relative High level Impulse Force Applicator; [Right] Relative low level Impulse Force Applicator.....	87
Figure 5.7 Structure Acceleration Signals Caused by Two Different Level Excitations	88
Figure 5.8 Normalized FFT Spectrums of Structure Accelerations by Two Different Level Impulse Excitations.....	89
Figure 5.9 Normalized CWT Contours of Structure Response under Different Level Impulse Excitations.....	90
Figure 5.10 G-Link and Its Physical Axis Orientation	91
Figure 5.11 USB Base Station	92
Figure 5.12 Agile-Link™ software interface.....	93
Figure 5.13 G-Link Configuration Screen	93
Figure 5.14 Installation of the G-Link	95
Figure 5.15 Damage Simulation on experimental structure	95
Figure 5.16 3-D FE model	96

Figure 5.17 Experimental Acceleration Signals of Structure under Damage Case 20-20-40, Original and De-noised	100
Figure 5.18 Correlation Matching for Damage Case 0-0-20, FFT & CWT Pattern Matching...	103
Figure 5.19 Least Square Distance (LSD) Matching for Damage Case 0-0-20, FFT & CWT Pattern Matching	104
Figure 5.20 Cosh Spectral Distance (CSD) Matching for Damage Case 0-0-20, FFT & CWT Pattern Matching	105
Figure 5.21 Correlation Matching for Damage Case 0-0-20, WPT Pattern Matching	106
Figure 5.22 Correlation Matching for Damage Case 0-20-0, WPT Pattern Matching	106
Figure 5.23 Correlation Matching for Damage Case 0-0-40, WPT Pattern Matching	107
Figure 5.24 Correlation Matching for Damage Case 20-20-0, WPT Pattern Matching	107
Figure 5.25 Correlation Matching for Damage Case 0-20-20, WPT Pattern Matching	108
Figure 5.26 Correlation Matching for Damage Case 20-20-20, WPT Pattern Matching	108
Figure B.1 Correlation Matching for Damage Case 19-0-0 (FFT Pattern Database).....	127
Figure B.2 Correlation Matching for Damage Case 0-38-38 (FFT Pattern Database).....	130
Figure B.3 Correlation Matching for Damage Case 58-38-19 (FFT Pattern Database).....	132
Figure B.4 Correlation Matching for Damage Case 58-58-58 (FFT Pattern Database).....	134
Figure B.5 Least Square Distance (LSD) Matching for Damage Case 19-0-0 (FFT Pattern Database).....	136
Figure B.6 Least Square Distance (LSD) Matching for Damage Case 0-38-38 (FFT Pattern Database).....	138
Figure B.7 Least Square Distance (LSD) Matching for Damage Case 58-38-19 (FFT Pattern Database).....	140
Figure B.8 Least Square Distance (LSD) Matching for Damage Case 58-58-58 (FFT Pattern Database).....	142
Figure B.9 Cosh Spectral Distance (CSD) Matching for Damage Case 19-0-0 (FFT Pattern Database).....	144
Figure B.10 Cosh Spectral Distance (CSD) Matching for Damage Case 0-38-38 (FFT Pattern Database).....	146
Figure B.11 Cosh Spectral Distance (CSD) Matching for Damage Case 58-38-19 (FFT Pattern Database).....	148

Figure B.12 Cosh Spectral Distance (CSD) Matching for Damage Case 58-58-58 (FFT Pattern Database).....	150
Figure B.13 Correlation Matching for Damage Case 19-0-0 (CWT Pattern Database).....	152
Figure B.14 Correlation Matching for Damage Case 0-38-38 (CWT Pattern Database).....	154
Figure B.15 Correlation Matching for Damage Case 58-38-19 (CWT Pattern Database).....	156
Figure B.16 Correlation Matching for Damage Case 58-58-58 (CWT Pattern Database).....	158
Figure B.17 Least Square Distance (LSD) Matching for Damage Case 19-0-0 (CWT Pattern Database).....	160
Figure B.18 Least Square Distance (LSD) Matching for Damage Case 0-38-38 (CWT Pattern Database).....	162
Figure B.19 Least Square Distance (LSD) Matching for Damage Case 58-38-19 (CWT Pattern Database).....	164
Figure B.20 Least Square Distance Matching for Damage Case 58-58-58 (CWT Pattern Database).....	166
Figure B.21 Cosh Spectral Distance (CSD) Matching for Damage Case 19-0-0 (CWT Pattern Database).....	168
Figure B.22 Cosh Spectral Distance Matching for Damage Case 0-38-38 (CWT Pattern Database).....	170
Figure B.23 Cosh Spectral Distance (CSD) Matching for Damage Case 58-38-19 (CWT Pattern Database).....	172
Figure B.24 Cosh Spectral Distance (CSD) Matching for Damage Case 58-58-58 (CWT Pattern Database).....	174
Figure D.1 Correlation Matching for Damage Case 0-20-0, FFT & CWT Pattern Matching....	181
Figure D.2 Least Square Distance (LSD) Matching for Damage Case 0-20-0, FFT & CWT Pattern Matching.....	183
Figure D.3 Cosh Spectral Distance (CSD) Matching for Damage Case 0-20-0, FFT & CWT Pattern Matching.....	184
Figure D.4 Correlation Matching for Damage Case 20-0-0, FFT & CWT Pattern Matching....	185
Figure D.5 Least Square Distance (LSD) Matching for Damage Case 20-0-0, FFT & CWT Pattern Matching.....	186

Figure D.6 Cosh Spectral Distance (CSD) Matching for Damage Case 20-0-0, FFT & CWT	
Pattern Matching	187
Figure D.7 Correlation Matching for Damage Case 0-20-20, FFT & CWT Pattern Matching..	188
Figure D.8 Least Square Distance (LSD) Matching for Damage Case 0-20-20, FFT & CWT	
Matching	189
Figure D.9 Cosh Spectral Distance (CSD) Matching for Damage Case 0-20-20, FFT & CWT	
Pattern Matching	190
Figure D.10 Correlation Matching for Damage Case 20-0-20, FFT & CWT Pattern Matching	191
Figure D.11 Least Square Distance (LSD) Matching for Damage Case 20-0-20, FFT & CWT	
Pattern Matching	192
Figure D.12 Cosh Spectral Distance (CSD) Matching for Damage Case 20-0-20, FFT & CWT	
Pattern Matching	193
Figure D.13 Correlation Matching for Damage Case 20-20-0, FFT & CWT Pattern Matching	194
Figure D.14 Least Square Distance (LSD) Matching for Damage Case 20-20-0, FFT & CWT	
Pattern Matching	195
Figure D.15 Cosh Spectral Distance (CSD) Matching for Damage Case 20-20-0, FFT & CWT	
Pattern Matching	196
Figure D.16 Correlation Matching for Damage Case 0-20-40, FFT & CWT Pattern Matching	197
Figure D.17 Least Square Distance (LSD) Matching for Damage Case 0-20-40, FFT & CWT	
Pattern Matching	198
Figure D.18 Cosh Spectral Distance (CSD) Matching for Damage Case 0-20-40, FFT & CWT	
Pattern Matching	199
Figure D.19 Correlation Matching for Damage Case 20-20-20, FFT & CWT Pattern Matching	
.....	200
Figure D.20 Least Square Distance (LSD) Matching for Damage Case 20-20-20, FFT & CWT	
Pattern Matching	201
Figure D.21 Cosh Spectral Distance (CSD) Matching for Damage Case 20-20-20, FFT & CWT	
Pattern Matching	202
Figure D.22 Correlation Matching for Damage Case 20-20-40, FFT & CWT Pattern Matching	
.....	203

Figure D.23 Least Square Distance (LSD) Matching for Damage Case 20-20-40, FFT & CWT	
Pattern Matching	204
Figure D.24 Cosh Spectral Distance (CSD) Matching for Damage Case 20-20-40, FFT & CWT	
Pattern Matching	205
Figure D.25 Correlation Matching for Damage Case 40-60-20, FFT & CWT Pattern Matching	
.....	206
Figure D.26 Least Square Distance (LSD) Matching for Damage Case 40-60-20, FFT & CWT	
Pattern Matching	207
Figure D.27 Cosh Spectral Distance (CSD) Matching for Damage Case 40-60-20, FFT & CWT	
Pattern Matching	208

List of Tables

Table 4.1 Peak Values on the FFT Spectrums	73
Table 4.2 Numerical Test Cases	76
Table 4.3 Signal Properties	77
Table 4.4 FFT and CWT Pattern Recognition Results	80
Table 5.1 Dimensions, Weights and Amount of Structure Components	82
Table 5.2 G-Link Specifications	91
Table 5.3 3-D FE Model Baseline Properties	97
Table 5.4 Experimental Test Cases.....	99
Table E.1 CWT Pattern-Matching Resolution Based on Different Wavelet Function.....	209

Acknowledgements

I would like to express my deepest and sincerest gratitude to my major professor Dr. Asad Esmaeily. I also express my appreciation for the support received from Dr. Hani G. Melhem. Their knowledge, insight, patience and encouragement have been highly appreciated.

I would also like to thank Dr. Jacob Najjar and Dr. Jack Xin for serving on my committee and Dr. David Schmidt for being the outside committee chair. Their advice and support are highly appreciated. I would also like to thank Mr. Dave Suhling, a research technologist in Civil Engineering Lab, for providing assistance during construction and testing of the experimental structure.

This work was financially supported by Dr. Esmaeily's start up funds provided by Kansas State University, Engineering Experimental Station, through the pertinent contract. I would like to acknowledge and express my thanks for the opportunity that made this work possible.

Dedication

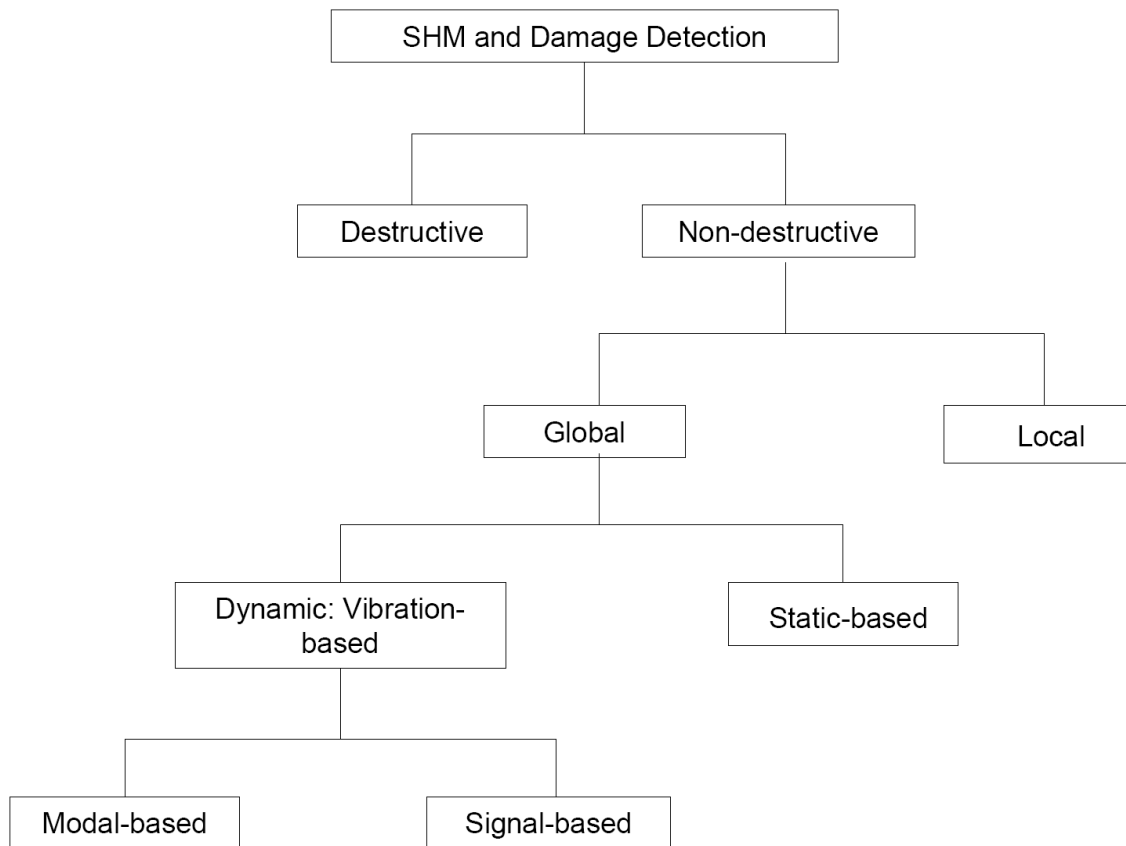
This work is dedicated to my parents and my wife for their encouragement, patience, support, and love.

CHAPTER 1 - INTRODUCTION

1.1 Introduction

Deterioration of structures due to aging, cumulative crack growth or excessive response decreases their stiffness and integrity, and therefore significantly affects the performance and safety of structures during their service life. Structural Health Monitoring (SHM) and damage detection denotes the ability to monitor the performance of structure, detect and assess any damage at the earliest stage in order to reduce the life-cycle cost of structure and improve its reliability and safety. Figure 1.1 shows a brief classification of different damage detection categories, methods and basic algorithms.

Figure 1.1 SHM and Damage Detection Categories



In this field, Destructive Damage Detection (DDD) and/or Non-destructive Damage Detection (NDD) techniques are employed to continuously monitor the structure, detect the possible damage, and evaluate the safety of the structure. Recent advances in computer, sensors and other electronic technologies make NDD techniques far more convenient and cost effective than destructive detection techniques which usually evaluate the safety of a structure by testing samples removed from the structure. NDD techniques can be classified into two categories: (1) local methods; and (2) global methods.

Current highly effective localized NDD methods include acoustic or ultrasonic methods, magnetic field methods, radiograph, microwave/ground penetrating radar, fiber optics, eddy-current methods and thermal field methods. These methods are visual or localized experimental methods that detect damage on or near the surface of the structure by measuring light, sound, electromagnetic field intensity, displacements, or temperature. Some of these methods are particularly effective for a specific application. For example, eddy current is very effective for crack detection at welded joint (Chang and Liu, 2003). But these methods have several limitations when testing large and complex structures. First, the depth of wave penetration is limited. Second, the vicinity of the damage should be known and the portion of the structure being inspected should readily be accessible. However, there is no easy way to determine the global health condition of a structure. Chang and Liu (2003) provided detailed information about “local” methods.

Static-based and vibration-based NDD methods provide the opportunity to detect and assess damage on a global basis. Static-based methods rely on the strain or displacement measurements from a structure under known static loads and the finite-element model updating to determine changes in deflection, stiffness, and load-carrying capacity of the structure. These methods are widely used for bridge health monitoring and evaluation. Examples of such work are Barr et al. (2006) and Cardinale and Orlando (2004). The drawbacks of static-based NDD methods are: (1) they require a large amount of measured data; (2) they require the finite-element model updating using accurate material properties; (3) they require static-load tests which will interrupt the structure service. These drawbacks will make static-based NDD methods more difficult for online damage detection of an in-service structure. Vibration-based NDD methods rely on the change of vibration characteristics and signals as indication of damage due to the reason that the damage changes the physical properties of a structure, which in turn will cause

changes to the vibration characteristics and signals of the structure. Over the last two decades, extensive research has been conducted on Vibration-based detection approach, leading to various experimental techniques, methodologies, and signal processing algorithms. Doebling et al. (1996) and Sohn et al. (2003) presented comprehensive literature reviews of vibration based damage detection and health monitoring methods for structural and mechanical systems. These methods can be classified into either modal-based or signal-based categories.

Modal-based methods use changes in measured modal parameters (resonant frequencies, modal damping, mode shapes, etc.) or their derivatives as a sign of change in physical-dynamic properties of the structure (stiffness, mass and damping). The basic premise behind the methods is that a change in stiffness leads to a change in natural frequencies and mode shapes. Modal-based methods have been applied successfully to identify the dynamic properties of linearized and time-invariant equivalent structural systems. The methods include mode shape curvature method, the change in flexibility method, the change in stiffness method, modal strain energy, etc. Examples of such work are Kosmatka and Ricles (1999), Ren and Roeck (2002), Shi et al. (2000) and Kim et al. (2003). Recently, wavelet-based and Hilbert-based approaches have been developed as enhanced techniques for parametric identification of non-linear and time-variant systems. Examples of such work are Staszewski (1998), Kijewski and Kareem (2003), Yang et al. (2004), Huang et al. (2005), Hou et al. (2006), Chen et al. (2006) and Yan and Miyamoto (2006). Although modal-based methods are generally applicable for the purpose of damage detection and structural health monitoring, they still have many problems and challenges: (1) damage is a local phenomenon and may not significantly influence modal parameters, particularly for large structures; (2) variation in the mass of the structure or environmental noise may also introduce uncertainties in the measured modal parameters; (3) the number of sensors, the types of sensors, and the coordinates of sensors may have a crucial effect on the accuracy of the damage detection procedure (Kim et al. 2003).

Signal-based methods examine changes in the features derived directly from the measured time histories or their corresponding spectra through proper signal processing methods and algorithms to detect damage. Based on different signal processing techniques for feature extraction, these methods are classified into time-domain methods, frequency-domain methods, and time-frequency (or time-scale)-domain methods. Time-domain methods use linear and nonlinear functions of time histories to extract the signal features. Examples of this category are

Auto-Regressive (AR) model, Auto-Regressive Moving Average (ARMA) model, Auto-Regressive with eXogenous input (ARX) model and Extended Kalman Filter (EKF). Frequency-domain methods use Fourier analysis and cepstrum (the inverse Fourier transform of the logarithm of the Fourier spectra magnitude squared) analysis to extract features in a given time window. Examples of this category are Frequency Response Functions (FRFs), frequency spectra, cross power spectra, power spectra, and power spectral density. Time-frequency domain methods employ Wigner-Ville distribution and wavelet analysis to extract the signal features. Examples of this category are spectrogram, continuous wavelet transform coefficients, wavelet packet energies and wavelet entropy. Detailed descriptions of these signal-based features, feature extraction and successful applications will be presented in Chapter Two. As an enhancement for feature extraction, selection and classification, pattern recognition techniques are deeply integrated into signal-based damage detection. Staszewski (2000) and Farrar et al. (2001) presented the detailed descriptions of feature extraction, selection and analysis in the context of statistical pattern recognition. Some cases of successful application of the procedure for damage detection can be found in Sohn et al. (2000, 2001), Trendafilova (2001), Posenato et al. (2008) and Fang et al. (2005). Detailed descriptions of these mostly used pattern recognition methods and successful applications for damage detection will also be presented in Chapter Two. Compared with modal-based methods, signal-based methods have received considerable attentions from the civil, aerospace, and mechanical communities because they are particularly more effective for structures with complicated nonlinear behavior and the incomplete, incoherent, and noise-contaminated measurements of structural response (Adeli and Jiang 2006). They are also more cost effective and suitable for online structural monitoring.

1.2 Objectives

The overall problem of structural damage detection involves five levels of damage identification which are categorized according to a logical sequence: level 1, existence of damage; level 2, location of damage; level 3, type of damage; level 4, quantity of the damage; and level 5, life to failure (Sohn et al. 2003, Doebling et al. 1996, Rytter 1993). The first four levels are mostly related to identification and modeling of structural systems, signal processing, feature extraction and statistical pattern recognition. The last level of identification generally

falls into the fields of fatigue life analysis, fracture mechanics, design assessment, reliability analysis and machine learning.

The main goal of any damage detection method is to detect the damage, assess the level and type, and spot the location. As detailed in the introduction, there are many methods and algorithms that can be used depending on the type of structure, source of possible damage and the desired accuracy of detection.

The method used in this study is a signal-based method in which the features of the acceleration response signal, under a known excitation serve as the structural signature. This signature will change when the dynamic properties of the structure changes due to an inflicted damage that will alter the dynamic properties of the structure.

The main goal of this study was to: (1) explore various signal processing methods in optimal extraction and preservation of the features of the response signal; (2) identify the best pattern recognition method; (3) develop a process of pattern extraction and recognition for damage detection and online structural monitoring.

In this study, a signal-based pattern extraction and recognition method, using a number of signal transformations and pattern matching algorithms, was investigated to detect structural damage. The vibration acceleration signals of a structure excited by a known dynamic excitation, such as an impulse force, were decomposed by Fast Fourier Transform (FFT), Continuous Wavelet Transform (CWT) or Wavelet Packet Transform (WPT) for feature extraction. Three statistical algorithms were also investigated to perform pattern matching separately: correlation, least square distance, and Cosh spectral distance. The method proposed in this study implements feature extraction and pattern recognition algorithms in damage detection procedure. To show the validity and accuracy of the method and related transformation and pattern recognition algorithms, numerical simulation and experimental case studies were conducted on a small-scale three-story steel structure. The structural dynamic response under different damage scenarios excited by an impulsive load was numerically simulated by a detailed finite element model using ANSYS, and the recorded vibration response was processed using MATLAB.

CHAPTER 2 - LITERATURE REVIEW

Recently, signal-based damage detection methods have received many attentions. These methods involve two main processes: (1) feature extraction and selection, and (2) pattern recognition. Feature extraction and selection is the process of identifying and selecting damage-sensitive features derived from the measured dynamic response, to quantify the damage state of the structure (Sohn et al. 2003). This process often involves fusing and condensing the large amount of available data from multiple sensors into a much smaller data set that can be better analyzed in a statistical manner. Also, various forms of data normalization are employed in the process in an effort to separate changes in the measured response caused by varying operational and environmental condition from changes caused by damage.

A pattern can be a set of features given by continuous, discrete or discrete-binary variables formed in vector or matrix notation. “Pattern recognition is concerned with the implementation of the algorithms that operate on the extracted features and unambiguously determine the damage state of the structure” (Farrar et al. 2001).

2.1 Feature Extraction and Selection

A variety of methods are employed to improve the feature extraction and selection procedure. Based on different signal processing techniques for feature extraction, these methods are classified into time-domain methods, frequency-domain methods, and time-frequency methods.

2.1.1 Time-domain Methods

Time-domain methods use linear and nonlinear functions of time histories to extract features. Sohn et al. (2000) used an auto-regressive (AR) model to fit the measured time history on a structure. Damage diagnoses using X-bar control chart were performed using AR coefficients as damage-sensitive features. In the $AR(n)$ model, the current point in a time series is modeled as a linear combination of the previous n points

$$x(t) = \sum_{j=1}^n \phi_j x(t-j) + e_x(t) \quad (2.1)$$

where $x(t)$ is the time history at time t ; ϕ_j is the unknown AR coefficient; and $e_x(t)$ is the random error with zero mean and constant variance. The value of ϕ_j is estimated by fitting the AR model to the time history data. The AR coefficients of the model fit to subsequent new data were monitored relative to the baseline AR coefficients. The X-bar control chart was used to provide a framework for monitoring the changes in the mean values of the AR coefficients and identifying samples that were inconsistent with the past data sets. A statistically significant number of AR coefficients outside the control limits indicated that the system was transited from a healthy state to a damaged state. Principal component analysis and linear and quadratic projections were applied to transform the time series from multiple measurement points into a single time series in an effort to reduce the dimensionality of the data and enhance the discrimination between features from undamaged and damaged structures. For demonstration, the authors applied the AR model combined with X-bar control chart to determine the existence of damage on a concrete bridge column as the column was progressively damaged. The AR coefficients on the X-bar control chart as detailed in the method indicated the damage existence.

Sohn and Farrar (2001) proposed a two-stage time history prediction model, combining auto-regressive (AR) model and an autoregressive with exogenous inputs (ARX) model. The residual error, which was the difference between the actual acceleration measurement for the new signal and the prediction obtained from the AR-ARX model from the reference signal, was defined as the damage-sensitive feature. The increase in residual errors was monitored to detect system anomalies. In this method, the ARX model is expressed as

$$x(t) = \sum_{i=1}^a \alpha_i x(t-i) + \sum_{j=1}^b \beta_j e_x(t-j) + \epsilon_x(t) \quad (2.2)$$

where a and b are the order of the ARX model; α_i and β_j are the coefficients of the AR and the exogenous input, respectively; $\epsilon_x(t)$ is the residual error after fitting the $ARX(a,b)$ model to the $e_x(t)$ and $x(t)$ pair in the one-stage ahead AR model. If the ARX model obtained from the reference signal block pair $x(t)$ and $e_x(t)$ were not be a good representation of the newly obtained block pair $y(t)$ and $e_y(t)$, there would be a significant change in the residual error,

$\varepsilon_y(t)$, compared to $\varepsilon_x(t)$. The standard deviation ratio of the residual errors, $\sigma(\varepsilon_y)/\sigma(\varepsilon_x)$, would reach its maximum value at the sensors instrumented near the actual damage locations. The applicability of this approach was demonstrated by the authors using acceleration time histories obtained from an eight degree-of-freedom mass-spring system.

Sohn et al. (2002) developed a unique combination of the AR-ARX model, auto-associative neural network, and statistical pattern recognition techniques for damage classification explicitly taking the environmental and operational variations of the system in the consideration. In this method, AR-ARX model is developed to extract damage sensitive features, which are the α_i and β_j coefficients of the ARX model. An auto-associative neural network is trained to characterize the dependency of the extracted features on the variations caused by environmental and operation conditions. A damage classifier is constructed using a sequential probability ratio test to automatically determine the damage condition of the system. The authors demonstrated the proposed approach using a numerical example of a computer hard disk and an experimental study of an eight degree-of-freedom spring-mass system.

Bodeux and Golival (2001) applied the autoregressive moving average vector (ARMAV) model and statistical tools such as confidence interval and the normal distribution of random variable for damage detection. In the state space, the ARMAV model is expressed as

$$x[n] = Ax[n-1] + W[n] \quad (2.3)$$

where $x[n]$ is the observed vibration vector at the n th discrete time point; A is the matrix containing the different coefficients of the autoregressive (AR) part; $W[n]$ is a matrix containing the moving average (MA) terms. The natural eigenfrequencies f_r and damping ratios ζ_r can be extracted from the eigenvalues τ_r of the AR matrix A as

$$f_r = \frac{|\ln(\tau_r)|}{2\pi \Delta t} \quad (2.4)$$

$$\zeta_r = \frac{\text{Real}(\ln(\tau_r))}{|\ln(\tau_r)|} \quad (2.5)$$

where Δt is the discrete time interval. The authors used the changes in the frequencies estimated by the ARMAV model to detect the damage on the Steel-Quake structure at the Joint Research Center in Ispra, Italy. The frequencies were assumed to be independently distributed variables

and a negative change in frequencies indicated damage caused by structure change. As damage indicator, the probability of negative change $P_{\delta f_i}$ in frequency f_i is given by

$$P_{\delta f_i} = 1 - \Phi \left(\frac{f_i - f_{i0}}{\sigma_i^2 + \sigma_{i0}^2} \right) \quad (2.6)$$

where σ_i^2 and σ_{i0}^2 are the variances of the frequencies f_i and f_{i0} corresponding to the damaged and undamaged states. Φ is the unit normal distribution function. The structure was assumed damaged if the probability was close to one. The proposed method was limited to only detecting the damage existence.

Nair et al. (2006) applied an Auto-Regressive Moving Average (ARMA) model for damage identification and localization. A damage-sensitive feature, DSF, was defined as a function of the first three auto regressive (AR) components. The mean values of the DSF obtained from the damaged and undamaged signals were significantly different. In this method, the vibration signals obtained from sensors are modeled as ARMA time series as

$$x_{ij} = \sum_{k=1}^p \phi_k x_{ij}(t-k) + \sum_{k=1}^q \theta_k \varepsilon_{ij}(t-k) + \varepsilon_{ij}(t) \quad (2.7)$$

where $x_{ij}(t)$ is the normalized acceleration signal; ϕ_k and θ_k are the k -th AR (Auto-Regressive) and MA (Moving Average) coefficients, respectively; p and q are the model orders of the AR and MA processes, respectively; and $\varepsilon_{ij}(t)$ is the residual term. DSF is defined as

$$DSF = \frac{\alpha_1}{\sqrt{\alpha_1^2 + \alpha_2^2 + \alpha_3^2}} \quad (2.8)$$

where α_1 , α_2 and α_3 are the first three AR coefficients. A hypothesis test involving the t-test was used to determine the existence of damages on the structure. Two indices, LI_1 and LI_2 , were introduced based on the AR coefficient space to localize damages. At the sensor locations where damage was introduced, LI_1 and LI_2 had comparatively large values. The authors tested the proposed methodologies on the analytical and experimental results of the ASCE benchmark structure. The results of the damage detection indicated that DSF was able to detect the existence of all damage patterns in the ASCE Benchmark simulation experiment. The results of the damage localization indicated that LI_1 and LI_2 were all able to localize minor damages but LI_1 was more robust than LI_2 .

Nair and Kiremidjian (2007) utilized the Gaussian Mixture Model (GMM) to detect the existence and extent of damage. The vibration signals obtained from the structure were modeled as ARMA processes. The first three autoregressive coefficients obtained from the modeling of the vibration signals formed the feature vector. The feature vectors were clustered by Gaussian mixture model. The existence of damage was detected using the gap statistic to ascertain the optimal number of mixtures in a particular database. A migration of the number of mixtures indicated the existence of damage. The Mahalanobis distance between the centroids of the mixture in question and the undamaged mixture was chosen as a good indicator of damage extent. The authors used the simulation data from the ASCE benchmark structure to test the efficacy of the method. It was demonstrated that GMM-based algorithm was able to detect minor, moderate, and major damage patterns; the Mahalanobis distance was highly correlated to the damage extent even under the presence of noise. The limitations of the algorithm were that this algorithm was effective only for linear stationary signals; and changes are identified relative to the initial measurement which was assumed to be the undamaged state.

Liu et al. (2007) presented a damage sensitive feature index for damage detection based on Auto-Regressive Moving Average (ARMA) time series analysis. The acceleration signal was modeled as ARMA models, and a principal component matrix derived from the AR coefficients of these models was utilized to establish the Mahalanobis distance criterion function. The Mahalanobis-distances of m-dimensional vector x_i from the principal component matrix of damaged structure to the ones of undamaged structure were defined as the damage sensitive feature (DSF) index. It is expressed as

$$D_{DSF} = \left[(x - \mu)^T \Sigma^{-1} (x - \mu) \right]^{\frac{1}{2}} \quad (2.9)$$

where μ and Σ are mathematics expectation and covariance matrices of the m-dimensional vector from the principal component matrix of undamaged structure, respectively. A hypothesis test involving the t-test method was further applied to make a damage alarming decision by determining the statistical significance in the difference of mean values of D_{DSF} obtained from the damaged and undamaged cases. These methodologies were tested on a numerical three-span-girder beam model containing some subtle damages. The results show that the defined index is sensitive to these subtle structure damages, and the proposed algorithm can be applied to the on-line damage alarming in structural health monitoring.

Yan et al. (2004) applied the residual errors of the prediction model and statistical process control techniques for damage diagnosis. A Kalman model was constructed to fit the measured vibration response histories of the undamaged structure. The residual error of the prediction by the identified Kalman model with respect to the actual measurement of signals was defined as a damage-sensitive feature. The X-bar control chart was constructed to provide a quantitative indicator of damage. The damage locations were determined as the errors reached the maximum values at the sensors instrumented in the damaged sub-structures. The authors successfully applied this method to indicate the system anomaly on an aircraft model in a laboratory and on a real bridge.

Omenzetter and Brownjohn (2006) applied the time series analysis to process data from a continuously operating SHM system installed in a major bridge structure. The strain data recorded during the construction and service life of the bridge were modeled using a vector seasonal autoregressive integrated moving average (ARIMA) model. The model is expressed as

$$D(B)D^{(s)}(B)\Phi_t(B)\Phi_t^{(s)}(B)x_t = \Theta_t(B)\Theta_t^{(s)}(B)e_t \quad (2.10)$$

where $\{x_t\}$ ($t = 1, 2, \dots, N$) is the p -dimensional vector of the time series of analyzed signal; $\{e_t\}$ is zero mean multivariate Gaussian white noise; B denotes the backshift operator; $\Phi_t(B)$, $\Phi_t^{(s)}(B)$, $\Theta_t(B)$, and $\Theta_t^{(s)}(B)$ are all matrix polynomials in the backshift operator. The coefficients of the ARIMA model were identified on-line by an extended Kalman filter and chosen as damage sensitive features. The various changes in the features were statistically examined using an outlier detection technique to reveal unusual events as well as structural change or damage sustained by the structure.

2.1.2 Frequency-domain Methods

Frequency-domain methods analyze any stationary event localized in time domain. They use Fourier analysis, cepstrum (the inverse Fourier transform of the logarithm of the Fourier spectra magnitude squared) analysis, spectral analysis, frequency response technique, etc to extract features in a given time window. Tang et al. (1991) quantitatively diagnosed gear-wear through cepstrum analysis of gear noise signals. The amplitude value of the peak in cepstrum represented gear mesh-harmonics in spectrum. The trend of the change of gear-wear degree was about the same as that of the change of the value of a peak in cepstrum. The value was

independent of intensity of gear noise signal and was used as an indicator for quantitatively diagnosing gear-wear. Based on analyzing the results of experiments with gearboxes, the thresholds of the gear wear by cepstrum diagnosis was determined to distinguish normal, moderate and serious wears. The theoretical analysis agreed with the experimental results very well.

Kamarthi and Pittner (1997) presented sensor data representation schemes for flank wear estimation in turning processes. The sensor data representation algorithm based on fast Fourier transform (FFT) transformed a time series vector X of the sensor signal from turning experiments into the spectral vector \hat{x} , and then formed the vector \hat{x}_f with the set $\{i_1, i_2, \dots, i_d\}$. The features x_r , the d -dimensional sensor data representation of X , was computed through the relation

$$x_r = S_w^{-1/2} \hat{x}_f \quad (2.11)$$

The features were used by recurrent neural network architecture to continually compute the flank wear estimates.

Lee and Kim (2007) used the frequency analysis to detect and localize damage. A signal anomaly index (SAI) which quantified the change of frequency response was developed as damage feature. The SAI is defined as a Euclidean norm of the difference between two frequency response function (FRFs) of basis and compared state as

$$SAI = \left(\frac{\sum_{f_i=f_1}^{f_n} |H^B(f_i) - H^C(f_i)|^2}{\sum_{f_i=f_1}^{f_n} |H^B(f_i)|^2} \right)^{1/2} = \frac{\|FRF^B - FRF^C\|}{\|FRF^B\|} \quad (2.12)$$

where, $H(\)$ and FRF represent the frequency response function in continuous form and discrete form respectively, superscript B and C stand for the state of Basic and Compared. The symbols, f_1 and f_n are the lowest and highest frequency of the considering frequency range, respectively. Changes in the shape of the FRF due to the reason of structural damage caused the increase of SAI value. The presence of damage was identified from the SAI value. All SAI values calculated from different sensors and different frequency ranges formed a SAI matrix which showed variation patterns of the FRF in both the space and the frequency domain. The SAI matrix was used as input for the neural network to identify the location of damage. The authors conducted a series of experimental tests and numerical simulation on an experimental model bridge to demonstrate the feasibility of the proposed algorithm. The results of this

example application show that the SAI based pattern recognition approach has the great potential for structural health monitoring on a real bridge.

Fasel et al. (2005) used a frequency domain auto-regressive model with exogenous inputs (ARX) to detect joint damage in steel moment-resisting frame structures. Damage sensitive features were extracted from the ARX model in the consideration of non-linear system input/output relationships. A frequency domain ARX model was used to predict the response at a particular frequency based on the input at that frequency, as well as responses at surrounding frequencies. The responses at the surrounding frequencies were included as inputs to the model to account for sub-harmonics and super-harmonics introduced to the system through non-linear feedback. To accounts for non-linearity in the system, first-order ARX model in the frequency domain is built as

$$Y(k) = B(k)U(k) + A_1(k)Y(k-1) + A_{-1}(k)Y(k+1) \quad k = 2, 3, \dots, N_f - 1 \quad (2.13)$$

where N_f is the highest frequency value examined, $Y(k)$ is the response at the k -th frequency, $U(k)$ is the input at the k -th frequency, and $Y(k-1)$ and $Y(k+1)$ are the responses at the $(k-1)$ th and $(k+1)$ th frequencies, respectively. $A_1(k)$ and $A_{-1}(k)$ are the frequency domain auto-regressive coefficients, and $B(k)$ is the exogenous coefficient. The frequency response of one accelerometer was treated as an input and the other accelerometer response was treated as an output. The auto-regressive coefficients in this frequency domain model were used as features. These features were then analyzed using extreme value statistics (EVS) to differentiate between damage and undamaged conditions. The suitability of the ARX model, combined with EVS, to non-linear damage detection was demonstrated on a three-story building model.

2.1.3 Time-Frequency (or Scale)-domain Methods

In contrast to the frequency-domain methods, the time-frequency (or scale) methods can be used to analyze any non-stationary event localized in time domain. Staszewski et al. (1997) applied the Wigner-Ville distribution (WVD) to detect local tooth faults in spur gears. The authors showed that the visual observation of the WVD contour plots could be used for fault detection. Dark zones and curved bands in the contour plots were the main features of an impulse produced by the fault in the spur gear. The changes in features of the distribution were used to monitor the progression of a fault. For the sake of automatic fault detection, the authors

chose the two-dimensional contour plots of the WVD as patterns, and the amplitude values of the contour plots as features. Pattern recognition procedures based on the statistical and neural approaches were used for classification of different fault conditions.

Biemans et al. (2001) employed the orthogonal wavelet analysis of the strain data measured from piezoceramic sensors to detect crack growth in the middle of a rectangular aluminum plate. The strain data measured from the plate under the Gaussian white noise excitation was decomposed into orthogonal wavelet levels. The logarithm of the variance of the orthogonal wavelet coefficients was calculated for all wavelet levels. The mean vector $\bar{\mu}$, of the logarithms for the undamaged plate formed the template for the similarity analysis. A Euclidean distance between the template $\bar{\mu}$ and the logarithms \bar{x} , for the damaged plate was used as a damage index. The damage index is denoted as

$$d_{x,\mu}^2 = (\bar{x} - \bar{\mu})^T (\bar{x} - \bar{\mu}) \quad (2.14)$$

The mean and standard deviation of the damage index representing the undamaged condition of the plate were used to establish an alarm level. The damage could be considered existence in the plate if the damage index was above the alarm level. The experimental results on the aluminum plate show that such damage index can be used to successfully detect as small as 6-7mm crack and to monitor the crack growth.

Hou et al. (2000) presented the great potential of wavelet analysis for singularity extraction in the signals. Characteristics of four types of representative vibration signals were examined by continuous and discrete wavelet transforms. The singularity in these signals were extracted and best illustrated in the plot of wavelet coefficient in the time-scale plane. The fringe pattern in the continuous wavelet coefficient contour plot indicated the existence of a singularity in the local time and the spike in the discrete wavelet coefficient plot also indicated the existence of a singularity in the local time. The sensitivity of wavelet results to a singularity was effectively used to detect possible structural damage using measured acceleration response data. To demonstrate the feasibility of the proposed method, the authors used both numerical simulation data from a simple structural model with multiple paralleled breakable springs and actual acceleration data recorded on the roof of a building during an earthquake event. The detection results showed that occurrence of damage could be detected by spikes in the detailed of the wavelet decomposition of the response data, and the locations of these spikes could

accurately indicate the moments when the damage occurred. The similar work can also be found on Hera and Hou (2004), Ovanesova and Suarez (2004) and Melhem and Kim (2003, 2004).

Kim and Kim (2005) used the ratio of the incident wave toward and the reflected wave from the damage as index to assess the damage size. The ratio was estimated by the continuous wavelet transform of the measured signal and the ridge analysis. In the time-frequency plane of the continuous wavelet transform, the ridge was traced to compare the magnitude of the incident wave and the magnitude of the reflected wave from the damage. It was found that “the ratio of these magnitudes along the two ridges was the same as the ratio of the magnitude of the incident wave to the magnitude of the reflected wave. Due to the fact that the magnitude and frequency-dependent pattern of the ratio varied with damage size, it was able to correlate the ratio and the damage size except when the damage size was very small” (Kim and Kim 2005). The authors conducted the wave experiments in a cylindrical ferromagnetic beam. Magnetostrictive sensors were used to measure the bending waves in the beam cross section. The continuous Gabor wavelet transform was employed to estimate the crack size in the beam.

Robertson et al. (2002) used the Holder exponent as damage-sensitive to detect the presence of damage and determine the moment of damage occurrence because of its time-varying nature. The authors provided a procedure to capture the time-varying nature of the Holder exponent based on wavelet transforms and demonstrated this procedure through applications to non-stationary random signals associated with earthquake ground motion and to a harmonically excited mechanical system that had a loose part inside. Statistical process control was established to identify the changes of the Holder exponent in time. The results show that Holder exponent is an effective feature for such damage detection that introduces discontinuities into the measured system acceleration signal.

Yen and Lin (2000) investigated the feasibility of applying the Wavelet Packet Transform (WPT) to detect and classify the mechanical vibration signals. They introduced a wavelet packet component energy index and demonstrated that the wavelet packet component energy had more potential for use in signal classification as compared to the wavelet packet component coefficients alone. The component energy is defined as

$$E_j^i = \int_{-\infty}^{\infty} f_j^i(t)^2 dt \quad (2.15)$$

where $f_j^i(t)$ is the i th component after j levels of decomposition. Sun and Chang (2002) applied the wavelet packet component energy index to assess structural damage. The vibration signals of a structure were decomposed into wavelet packet components. The component energies were calculated and the ones which were both significant in value and sensitive to the change in rigidity were selected as damage indices and then used as inputs into neural network models for damage assessment. The authors performed numerical simulations on a three-span continuous bridge under impact excitation. Various levels of damage assessment including identifying the occurrence, location, and severity of the damage were studied. The results show that the WPT-based component energies are sensitive to structural damage and can be used for various levels of damage assessment.

Sun and Chang (2004) also derived two damage indicators from the WPT component energies. The acceleration signals of a structure excited by a pulse load were decomposed into wavelet packet components. The energies of these wavelet packet components were calculated and sorted by their magnitudes. The dominant component energies which were highly sensitive to structural damage were defined as the wave packet signature (WPS). Two damage indicators, SAD (sum of absolute difference) and SSD (square sum of difference), were then formulated to quantify the changes of these WPSs. SAD and SSD are defined as

$$SAD = \sum_{i=1}^m \left| E_j^i - \hat{E}_j^i \right| \quad (2.16)$$

$$SSD = \sum_{i=1}^m \left(E_j^i - \hat{E}_j^i \right)^2 \quad (2.17)$$

where \hat{E}_j^i ($i=1,2,\dots,m$) are termed as the baseline WPS that are used as a reference; and

E_j^i ($i=1,2,\dots,m$) are WPS obtained from any subsequent measurement. These two indicators basically quantified the deviations of the WPS from the baseline reference. To monitor the change of these damage indicators, the X-bar control charts were constructed and one-sided confidence limits were set as thresholds for damage alarming. For demonstration, the authors conducted an experimental study on the health monitoring of a steel cantilever I beam. Four damage cases, involving line cuts of different severities in the flanges at one cross section, were introduced. Results show that the health condition of the beam can be accurately monitored by

the proposed method; the two damage indicators are sensitive to structural damage and yet insensitive to measured noise.

Yam et al. (2003) constructed a non-dimensional damage feature proxy vector for damage detection of composite structures. The damage feature proxy vector was calculated based on energy variation of the wavelet packet components of the structural vibration response before and after the occurrence of structural damage. The damage feature proxy vector, V_d is defined as

$$V_d = \left\{ 1 - \frac{U_{L,1}^d}{U_{L,1}^0}, 1 - \frac{U_{L,2}^d}{U_{L,2}^0}, \dots, 1 - \frac{U_{L,2^{L-1}}^d}{U_{L,2^{L-1}}^0} \right\}^T \quad (2.18)$$

where $U_{L,j}^0$ and $U_{L,j}^d$ are the energy of the j th order sub-signal of the intact and damaged structures, respectively; L is the layer number of the tree structure of wavelet decomposition. Artificial neural network (ANN) was used to establish the mapping relationship between the damage feature proxy and damage location and severity. The method was applied to crack damage detection of a PVC sandwich plate. The results show that the damage feature proxy exhibits high sensitivity to small damage.

Han et al. (2005) proposed a damage detection index called wavelet packet energy rate index (WPERI) for the damage detection. The rate of signal wavelet packet energy $\Delta(E_{f_j})$ at j level is defined as

$$\Delta(E_{f_j}) = \sum_{i=1}^{2^j} \frac{\left| \left(E_{f_j^i} \right)_b - \left(E_{f_j^i} \right)_a \right|}{\left(E_{f_j^i} \right)_a} \quad (2.19)$$

where $E_{f_j^i}$ is the energy stored in the component signal $f_j^i(t)$ after j levels of decomposition;

$\left(E_{f_j^i} \right)_a$ is the component signal energy $E_{f_j^i}$ at j level without damage; and $\left(E_{f_j^i} \right)_b$ is the component signal energy $E_{f_j^i}$ with some damage. It was assumed that structural damage would affect the energies of wavelet packet components and therefore altered this damage indicator. To establish threshold values for damage indexes, WPERIs, X-bar control charts were constructed and one-sided confidence limits were set as thresholds for damage alarming. The proposed method was applied to a simulated simply supported beam and to the steel beams with three damage

scenarios in the laboratory. Both simulated and experimental studies demonstrated that the WPT-based energy rate index is a good candidate index that is sensitive to structural local damage.

Shinde and Hou (2005) incorporated a wavelet packet based sifting process with the classical Hilbert transform for structural health monitoring. The original signal was decomposed into its components by a wavelet packet analysis with a symmetrical mother wavelet. The energy entropy and the Shannon entropy were used as the sifting criterion. The dominant components with nearly distinct frequency contents were sifted out based on their percentage contribution of entropy of an individual component to the total one of the original signal. The dominant component of the original signal from the wavelet packet based sifting process had quite simple frequency characteristic and was suitable for the classical Hilbert transform. The transient frequency content or the so-called instantaneous frequency of the component was found from the phase curve of Hilbert transform of the component. Since for a healthy structure, the associated instantaneous frequency is time-invariant, any reduction in the instantaneous frequency can be used as an indicator to reflect structural damage. The proposed sifting process used for structural health monitoring, including both detecting abrupt loss of structural stiffness and monitoring development of progressive stiffness degradation, was demonstrated by two case studies.

Diao et al. (2006) proposed a two-step structural damage detection approach based on wavelet packet analysis and neural network. The wavelet packet component energy change γ_{si} was selected as an input into probabilistic neural network to determine the location of the damage. The γ_{si} is defined as

$$\gamma_{si} = \frac{E_{si}^d - E_{si}^u}{E_{si}^u} \quad (2.20)$$

where E_{si}^u is the i th component energy at s level without damage, E_{si}^d is the i th component energy at s level with damage. The component energy was selected as input into back-propagation network to determine the damage extent. The method was demonstrated by numerical simulation of a tree-dimensional four-layer steel frame.

Chen et al. (2006) introduced an improved Hilbert-Huang Transform (HHT) to extract the structural damage information from the response signals of a simulated composite wingbox.

The signals was firstly decomposed into sub-signals using Wavelet Packet Transform (WPT). These sub-signals were then decomposed into multiple Intrinsic Mode Function (IMF) components by Empirical Mode Decomposition (EMD). The IMF selection criterion was then applied to eliminate the unrelated IMF components. The retained IMF components were transformed using HHT to obtain instantaneous energy of all sub-signals. By comparing the instantaneous energy corresponding to IMFs of intact wingbox with those of damaged wingbox, it was found that some instantaneous energy was changed obviously. Based on this fact, the authors constructed the variation quantity of instantaneous energy ΔE_t as feature index vector, which is defined as

$$\Delta E_t = \left(\frac{E_t}{E_t^0} - 1 \right) \times 100\% \quad (2.21)$$

where E_t^0 and E_t are instantaneous energy of intact and damaged structure respectively at time t . Reduction in Young's modulus was used to characterize damage in wingbox. The detection results show that the feature index vector distinctly reflects the wingbox damage status, and is more sensitive to small damage.

Ding et al. (2008) developed a procedure for damage alarming of frame structures based on energy variations of structural dynamic responses decomposed by wavelet packet transform. The damage alarming index ERVD, extracted from the wavelet packet energy spectrum is expressed as

$$ERVD = \sqrt{\sum_{p=1}^m \left(ERV_p - \overline{ERV} \right)^2} \quad (2.22)$$

$$ERV_p = |I_{up} - I_{dp}| \quad (p = 1, 2, \dots, m) \quad (2.23)$$

$$I_p = \frac{E_{i,p}}{\left(\sum_{j=1}^{2^l-1} E_{i,j} \right) / 2^i} \quad (p = 1, 2, \dots, m) \quad (2.24)$$

where I_{up} and I_{dp} are the damage indication vector in the p th dominant frequency band of the intact and damaged structures, respectively. $E_{i,j}$ is the j th component energy at l level. The authors demonstrated the practicability of the damage alarming method for the frame structures by using the ASCE structural benchmark data. The results reveal that the WPT-based damage alarming index ERVD is sensitive to structural local damage affected by the actual measurement

noise; the index ERVD constructed under the lower decomposition level and dominant frequency bands is efficient for the detection of the damage occurrence.

Ren and Sun (2008) combined wavelet transform with Shannon entropy to detect structural damage from measured vibration signals. Wavelet entropy, relative wavelet entropy and wavelet-time entropy were used as features to detect and locate damage. The wavelet entropy is defined as

$$S_{WT} = S_{WT}(p) = - \sum_{j < 0} p_j \cdot \ln[p_j] \quad (2.25)$$

where $\{p_j\}$ is the wavelet energy vector, which represents energy distribution in a time-scale. It gives a suitable tool for detecting and characterizing singular features of a signal in time-frequency domain. For the j th scale, the wavelet energy ratio vector $\{p_j\}$ is defined as

$$p_j = \frac{E_j}{E_{tol}} \quad (2.26)$$

The relative wavelet entropy (RWE) is defined as

$$S_{WT}(p/q) = \sum_{j < 0} p_j \cdot \ln\left[\frac{p_j}{q_j}\right] \quad (2.27)$$

which gives a measure of the degree of similarity between two probability distributions. The wavelet-time entropy is defined as

$$S_{WT}^{(i)}(p) = - \sum_{j < 0} p_j^{(i)} \cdot \ln[p_j^{(i)}] \quad (2.28)$$

where $p_j^{(i)}$ is the time evolution of relative wavelet energy at a resolution level j in the time interval i

$$p_j^{(i)} = \frac{E_j^{(i)}}{E_{tol}^{(i)}} \quad (2.29)$$

These features were investigated by numerically simulated harmonic signals and two laboratory test cases. “It is demonstrate that wavelet-time entropy is a sensitive damage feature in detecting the abnormality in measured successive vibration signals; relative wavelet entropy is a good damage feature to detect damage occurrence and damage location through the vibration signals measured from the intact and damaged structures; and the relative wavelet entropy method is

flexible in choosing the reference signal simultaneously measured from any undamaged location of the target structure” (Ren and Sun 2008).

2.2 Pattern Recognition

Feature patterns represent different conditions of an analyzed structure or machine. The objective of pattern recognition in damage detection is to distinguish between different classes of patterns presenting these conditions based either on a prior knowledge or on statistical information extracted from the patterns (Chang and Yang, 2004). Classical methods of pattern recognition use statistical and syntactic approaches. In recent years neural networks have been established as a powerful tool for pattern recognition. An overview of these methods can be found in Jain et al. (2000) and Duda et al. (2000). A brief description of some applications for damage detection is given below.

2.2.1 Fisher’s Discriminant

Fisher’s discriminant is a classification method that projects multi-dimensional feature vectors onto one-dimensional subspace to perform classification. The projection maximizes the distance between the mean of the two classes while minimizing the variance within each class. Farrar et al. (2001) defined Fisher’s discriminate using data from the vibration tests conducted on the columns under both undamaged condition and the damage condition of initial yielding of the steel reinforcement. “The time series were modeled using auto-regressive estimation referred to as linear predictive coding (LPC). Subsequent damage levels were then identified based on this same Fisher projection. When Fisher’s discriminant was applied to data from both sensors on undamaged and damaged columns, there was statistically separation between the LPC coefficients for the undamaged cases and damaged cases. While increasing damage was not necessarily related to increasing Fisher coordinate, all damaged cases had a profile significantly different from that of the undamaged case”. The authors showed a strong potential for using linear discriminant operators to identify the presence of damage.

2.2.2 X-bar Control Chart

Sohn et al. (2000) applied a statistical process control (SPC) technique, known as an “X-bar control chart”, to monitoring a reinforced concrete bridge column. “Acceleration time series were recorded from the vibration tests of the bridge column and auto-regressive (AR) prediction

models were used to fit the time series. Then, control charts were constructed using the AR coefficients of the AR model as the observation quantities. The upper and lower control limits were set to correspond to the 99% confidence intervals of a normal distribution. The mean and the standard deviation of the normal distribution were derived from the AR coefficients of the normal operational condition. After the yielding of the concrete rebar was gradually introduced in the column, new sets of AR coefficients were computed from various levels of damage. These new AR coefficients were plotted on the control charts whose limits were set from the initial undamaged state of the system. If a significant number of the coefficients (at least more than 1% of the coefficients) fell out of the limits, either a state of damage or a significant change in environmental conditions was reached. Since the authors used a third order AR model, there were three control charts for each damage level of the column. The authors determined that the third AR coefficient was the most sensitive to damages in this particular experiment” (Sohn et al. 2003). The core of this technique is to establish the lower and upper control limits (LCL and UCL) which enclose the variation of the extracted damage indicators due to measurement noise with a large probability. Once any damage indicator falls outside of the enclosure, it will signify the change of the structural condition with high probability (Sun and Chang, 2004). Similar studies can also be found in Sun and Chang (2004) and Han et al. (2005)

2.2.3 Outlier Detection

Sohn et al. (2001) employed an outlier analysis based on the Mahalanobis distance to monitoring a surface-effect fast patrol boat. Three strain time signals were obtained from two different structural conditions. Signal 1 and signal 2 were measured when the ship was in structural condition 1 while signal 3 was measured when ship was in structural condition 2. Two-stage time series analysis combining auto-regressive (AR) and auto-regressive with exogenous inputs (ARX) prediction models were used to fit the time signals. The 30-dimensional AR parameters were used for the outlier analysis. The training data were composed of half of signal 1 and 2. In order to compensate for the nonstationarity of the AR parameter sequence, the training data and testing data were taken alternately from the relevant feature sets. The Mahalanobis squared distance of the potential outlier was checked against a confidence threshold of 99.99%. Any values above this threshold had a less than 0.01% probability of arising as a random fluctuation on the normal condition set. The results show that there is an

extremely clear separation between structural condition 1 and structural condition 2. All points in the testing set from signal 1 and 2 are well below the threshold implying no false-positive indication of changes in structural conditions.

2.2.4 Bayesian Probabilistic Approach

Sohn and Law (1997) used Bayesian probabilistic approach to detect the locations and amount of damage in a structure. “The system stiffness matrix was represented as an assembly of the substructure stiffness matrices and a non-dimensional parameter θ_i was introduced to model the stiffness contribution of the i th substructure. The mass matrix was assumed to known and invariant. A uniform probability density function (PDF) was assumed for the non-dimensional parameter θ_i . The authors formulated the relative posterior probability of an assumed damage event and applied a branch-and-bound search scheme to identify the most likely damage event. The measurement noise and modeling error between the structure and the analytical model were taken account into the Bayesian probabilistic framework. Several examples using a shear frame structure, a two-story and a five-story three dimensional frame structure was simulated to demonstrate the proposed method. It was found that as long as sufficient modal data sets were available, the proposed method was able to identify the actual damage locations and amount in most cases. The computational cost of the method was significantly reduced by using a branch-and-bound search scheme” (Sohn and Law 1997).

Vanik et al. (2000) presented a continual on-line structural health monitoring (SHM) method, which utilized Bayesian probabilistic approach to identify damage indicators from sets of modal parameter data in the presence of uncertainties. “The method required a linear structural model whose stiffness matrix was parameterized to develop a class of possible models by grouping the elements of the structural model into substructures. Modal data (i.e. frequencies and mode-shapes) measured from a structure was used to identify the model substructure stiffness parameters. The differences in the stiffness parameters estimated from different modal data sets were used as indicators of damage. Bayes’ theorem was used to develop a probability density function (PDF) for the model stiffness parameters conditional on measured modal data and the class of possible models” (Beck et al. 1999). The authors illustrated their method with a 10 DOF shear building model that included story masses and inter-story stiffness. Using modal data simulated from a numerical model, they tested their algorithms with a 20% stiffness loss in

the fifth story. Results were favorable only when the damage indicators were based on the current monitoring cycle. Any addition of the prior training seemed to create an unreal bias towards undamaged states.

Sohn and Law (2000) used Bayesian probabilistic approach to predict the location of plastic hinge deformation using the experimental data obtained from the vibration tests of a reinforced concrete bridge column. The column was statically pushed incrementally with lateral displacements until a plastic hinge was fully formed at the bottom portion of the column. Vibration tests were performed at different damage stage. “The proposed damage detection method was able to locate the damaged region using a simplified analytical model and the modal parameters estimated from the vibration tests. Also the Bayesian framework was able to systematically update the damage probabilities when new test data became available. Better diagnosis was obtained by employing multiple data sets than just by using each test data set separately” (Sohn and Law 2000).

Ching and Beck (2004a, b) proposed a two-step probabilistic structural health monitoring approach, which involved modal identification followed by damage assessment using the pre- and post-damage modal parameters based on the Bayesian model updating algorithm. “The approach aimed to attack the structural health monitoring problems with incomplete mode shape information by including the underlying full mode shapes of the system as extra random variables, and by employing the Expectation-Maximization algorithm to determine the most probable value of the parameters. The non-concave non-linear optimization problem associated with incomplete mode shape cases was converted into two coupled quadratic optimization problems, so that the computation becomes simpler and more robust” (Ching and Beck 2004b). The authors illustrated the approach by analyzing the IASC-ASCE Phase II simulated and experimental benchmark problems. The results of the analysis show that the brace damage can be successfully detected and assessed from either the hammer or ambient vibration data. The connection damage is much more difficult to reliably detect and assess because the identified modal parameters are less sensitive to connection damage, allowing the modeling errors to have more influence on the results.

2.2.5 Neural Networks

Many damage detection schemes utilize neural networks to detect, localize, and quantify damage in structure and machinery. They are powerful pattern recognizers and classifiers. Chang et al. (2000) proposed an iterative neural network technique for damage detection. “The network was first trained off-line using initial training data that contained a set of assumed structural parameters, which represented various damage cases, as output and their corresponding dynamic characteristics as inputs. A modified back-propagation learning algorithm was proposed to overcome possible saturation of the sigmoid function and speed up the training process. The trained NN model was used to predict the structural parameters by feeding in measured dynamic characteristics. The predicted structural parameters were then used in the FE model to calculate the dynamic characteristics. The network model could go through the second training phase if the simulated dynamic characteristics significantly deviated from the measured ones. The identified structural parameters were then used to infer the location and the extent of structural damages. This iterative neural network method was verified on a clamped-clamped RC T beam using both simulated and experimental data” (Chang et al).

Chen and Wang (2002) used a multi-layer perceptron (MLP) with back-error propagation for fault detection on a gearbox. The MLP consisted of one input, output and hidden layers. The input layer had 19 nodes, and the output layer consisted of 4 neurons, each of which delivered one classification vote. The wavelet instantaneous scale distribution (ISD) pattern along the scale domain was used as input, and the hyperbolic tangent was used as the linear active function of the hidden neurons. The back-error propagation algorithm was employed in the MLP training, and the momentum and adaptive training techniques were implemented in the training algorithm.

Sun and Chang (2002) proposed a damage assessment procedure based on the WPT and the neural network (NN) models. Numerical simulations were performed on a three-span continuous bridge under impact excitation. A set of wavelet packet component energies were used as inputs to the NN model. Two NN models, NN1 and NN2 were used. The NN1 model consisted of a 10-node input layer, a 6-node hidden layer, and a 1-node output layer and was used to identify damage occurrence. The NN2 model consisted of a 10-node input layer, a 7-node hidden layer, and a 5-node output layer and was used to identify the location and severity of damage. As for training of these two models, a total of 16 training cases were used. The training

process of NN1 was stopped when the average mean square error was smaller than 2×10^{-5} or when the number of iterations reached 8,000. For NN2, the training was stopped when the average mean square error was smaller than 2×10^{-7} or when the number of iterations reached 10,000. The results show that the NN1 model is capable of identifying the presence of structural damage that corresponded to as small as 4% of the rigidity reduction in any element. And the NN2 model can locate and quantify moderate (10-20% EI reduction) and severe (20-30% EI reduction) damage with reasonable accuracy. The assessment accuracy of both models is not affected by the presence of measurement noise.

Fang et al. (2005) explored the structural damage detection using frequency response functions (FRFs) as input data to the back-propagation neural network (BPNN). Various training algorithms, such as the dynamic steepest descent (DSD) algorithm, the fuzzy steepest descent (FSD) algorithm and the tunable steepest descent (TSD) were studied. Numerical examples demonstrated that “using the heuristic procedure, the TSD training algorithm outperformed significantly the DSD and FSD algorithms in training effectiveness, efficiency and robustness without increasing the algorithm complexity” (Fang et al. 2005). The TSD based neural network was then used as the basis for structural stiffness loss detection on a cantilever beam. The neural network was a three-layer feed-forward network with 78 input nodes, 40 hidden nodes, and 5 output nodes. 30 numerical stiffness loss cases were used to train the network. The analysis results show that the neural network can assess damage conditions with very good accuracy in all considered damage cases.

Adeli and Jiang (2006) presented a dynamic time-delay fuzzy wavelet neural network model for nonparametric identification of structures using the nonlinear autoregressive moving average with exogenous inputs approach. The model integrates four different computing concepts: dynamic time delay neural network, wavelet, fuzzy logic, and the reconstructed state space concept from the chaos theory. Noise in the signals was removed using the discrete wavelet packet transform method to speed up the training convergence and improve the system identification accuracy. In order to preserve the dynamics of time series, the reconstructed state space concept from the chaos theory was employed to construct the input vector. In addition to de-noising, wavelets were employed in combination with two soft computing techniques, neural networks and fuzzy logic, to create a new pattern recognition model to capture the characteristics of the time series sensor data accurately and efficiently. The number of fuzzy wavelet neural

network nodes in the hidden layer was selected by the Akaike's final prediction error criterion. Experimental results on a 1/2-scaled five-story steel frame were used to validate the computational model and demonstrate its accuracy and efficiency.

Jeyasehar and Sumangala (2006) employed feed-forward artificial neural network (ANN) learning by back–approach algorithm, to assess the damage in pre-stressed concrete (PSC) beams. The post-crack stiffness obtained from the load-deflection characteristics of the beam and the natural frequency of the beam, were used as the test inputs to the ANN. The training and test data are generated from the experimental results obtained through the static and dynamic tests conducted on the damaged and perfect beams. The damage was introduced in the beam by electrochemical pitting corrosion to resemble natural damage in PSC beams. The efficiency of this damage assessment method was studied by testing this ANN with the test data of a damaged beam to different levels. It is demonstrated that ANN trained with post-crack stiffness and natural frequencies is sufficient to predict the damage with reasonable accuracy.

Li and Yang (2008) used back-propagation neural network (BPNN) to detect damage on a three-span continuous beam. The changes of variances (covariance) of structural displacements were adopted as input of neural network, and the damage status (location and extent) as output of neural network. Both single damage case and multi-damage case were numerically simulated on the beam, and several steps of damage location identification and damage extent detection were carried out in each case. The results show that BPNN with statistical property of structural response as input can correctly detect the damage location and identify the damage extent with high precision.

2.3 Applications to Special Structures

Some researchers have selected special structures to apply signal-based damage detection methods. A brief description of some cases is given below

2.3.1 Damage Detection on Bridge

Omenzetter et al. (2004) identified the unusual events in multi-channel bridge monitoring strain data using wavelet transform and outlier analysis. The strain data was recorded during continuous, long-term operation of a multi-sensor Structural Health Monitoring (SHM) system installed on a full-scale bridge. Outlier detection in multivariate data was applied to find and localize abnormal, sudden events in the strain data and wavelet transform was used to separate

the abrupt strain changes from slowly varying ones. The method was successfully tested using known events recorded during construction of the bridge and later effectively used for detection of anomalous post-construction events.

Omenzetter and Brownjohn (2006) proposed and examined the application of concepts of time series analysis to the processing of data from a continuously operating SHM system installed in a major bridge structure. The recorded static strain data was modeled using ARIMA models. The coefficients of the ARIMA models were identified on-line using an extended Kalman filter. The method was first applied to strains recorded during bridge construction, when structural changes corresponded to known significant events such as cable tensioning. Then the method was used to analyze signals recorded during the post-construction period when the bridge was in service. The results show that the method can provide information on structural performance under normal environmental and operational conditions.

Ding and Li (2007) proposed an online structural health monitoring method for long-term suspension bridge using wavelet packet transform (WPT). The method was based on the wavelet packet energy spectrum (WPES) variation of structural ambient vibration responses. As an example application, the WPES-based health monitoring system was used on the Runyang Suspension Bridge to monitor the responses of the bridge in real-time under various types of environmental conditions and mobile loads. As for the vibration monitoring of the bridge, a total of 27 uni-axial servo type accelerometers were installed at the nine sections of the bridge deck. In each deck section, one lateral accelerometer directly recorded the lateral response, and the vertical acceleration of the deck section was obtained by averaging the accelerations measured by the two vertical accelerometers located in the upriver and downriver cross section, respectively. The analysis showed that changes in environmental temperature had a long-term trend influence on the WPES, and the effect of traffic loadings on the WPES presented instantaneous changes.

Zhang (2007) presented a statistical damage identification procedure for bridge health monitoring. The damage features were extracted based on time series analysis combining autoregressive and autoregressive with exogenous input prediction models. The structural condition was evaluated in a statistical way based on the damage possibilities that were derived from a quite large number of data samples to minimize the effect of the variability in data acquisition process and in structural properties on the damage assessment. The proposed damage

identification procedure was applied to a numerical 3-span continuous girder bridge model under random ground excitations. Reasonable damage severities for beam structures as well as realistic noise levels were simulated. The results show that the damage identification procedure has great potential to detect structural damage at early stage, in which the structural modal frequency changes are almost imperceptible.

2.3.2 Crack Detection on Beam and Plate

Wang and Deng (1999) detected the crack on beam and plate structures based on wavelet analysis of spatially distributed structural response measurements. Simulated deflection signals of a beam containing a transverse crack and the displacement response of a plate with a through-thickness crack were used. Wavelet transforms were performed on these signals to obtain the wavelet coefficients along the span of the structures. The crack location was detected by observing a sudden change, such as a spike, in the distribution of the wavelet coefficients. The magnitude of the spike in the wavelet analysis was the maximum when the measurement point was next to the damage location.

Biemans et al. (2001) applied the piezoceramic sensors to monitoring crack propagation. The specimens used were two rectangular ($400 \times 150 \times 2$ mm) aluminum plate with cracks initiated by spark erosion in the middle of the plates. Each plate was instrumented with 6 piezoceramics bonded in a symmetrical configuration 20 mm below and above the initiated crack. One of the piezoceramics was used as an actuator excited by a sine sweep and Gaussian white noise signals to exploit broadband excitation. The plates were subjected to static and dynamic tensile loading. The growing crack was monitored by two of the remaining piezoceramic sensors. The response strain data was analyzed using a number of time, frequency, and wavelet domain statistical parameters. The results show that low frequency broadband excitation offers a possible means of on-line detection of cracks in metallic structures.

Yan et al. (2004) detected the crack damage in a honeycomb sandwich plate by using two structural vibration damage feature indexes: natural frequency and WPT energy index. The finite element dynamic model of a honeycomb sandwich plate was presented using different mesh division for the surface plate and the sandwich plate to accurately express the crack damage status (locations, length and direction) of the plate. In order to acquire the experimental dynamic response of the plate, two piezo-patches with a size of $25 \times 15 \times 0.28$ mm were bonded on

the surface of the plate. One of them acted as an actuator and the other acted as a sensor. The natural frequencies of the undamaged plate were experimentally measured to verify the numerical model. Based on the dynamic model verified by the experiment, the damage feature indexes for various crack damage status were numerically computed. Then the crack damage status was determined by comparing the damage feature indexes obtained from the numerical and experimental results. The authors found that natural frequency of structure might not be used to detect crack damage less than 10%, even up to 20% of the total size of a plate-like structure; energy spectrum of wavelet transform signals of structural dynamic response was so sensitive to crack damage that it could exhibit a crack length close to 2% of the dimension of a plate-like structure. They also found that high order modes of a structure contain more structural damage information; in order to detect a small damage, more vibration modes should be included in a structural dynamic model.

Chang and Chen (2005) detected the locations and sizes of multi-cracks in a beam by spatial wavelet analysis. The crack type was open crack and was represented as a rotational spring. The mode shapes of the multi-cracked beam under free vibration were analyzed by wavelet transformation. The positions of the cracks were observed as a sudden change in the plot of wavelet coefficients. The natural frequencies of the beam were used to predict the depth of the cracks through the characteristic equation. The limitation of this method is that there are two peaks near the boundaries in the wavelet plot and the crack can not be detected when the crack was near the boundaries.

Poudel et al. (2005, 2007) employed high-resolution images for damage detection on a simply supported prismatic steel beam. A high-speed digital video camera was used to recode the free vibration displacement of the beam which was excited by imposing an initial displacement near the mid-span from the left support. The camera had a Complimentary Metal Oxide Semiconductor (CMOS) sensor with 1280×1024 resolution and a 10-bit A/D converter. Its frame rate ranges was from 100 to 2000 frames/s. The displacement data with high spatial resolution were then used to obtain the mode shapes and the mode shape difference function between the reference and damage states of the structure. The spatial signal in terms of mode shape difference function was decomposed by wavelet transformation to display the changes due to cracking damage. The appropriate range of wavelet scale was determined by the spatial

frequency bandwidths of the mode shape difference functions. The maximum modulus and sign change of phase angle in the wavelet coefficients indicated the changes at the damage locations.

2.3.3 Damage Detection on Mechanical Structures

Staszewski and Tomlinson (1994) applied the wavelet transform to the problem of the detection of a broken tooth in a spur gear. The fault detection algorithm was based on pattern recognition analysis. Features of the pattern were the modulus of the wavelet transform. Spectral analysis and an orthogonal transform were used to compress feature elements. The Mahalanobis distance of two patterns obtained from the normal (no fault) condition and not normal (fault) condition was used as a fault detection symptom. Visual inspection of the modulus and phase of the wavelet transform were used to localize the fault.

Wang and McFadden (1995, 1996) used the wavelet transform to detect abnormal transients generated by gear damage. The early damage to a gear tooth usually caused a variation in the associated vibration signal over a short time, initially less than one tooth meshing period, taking the form of modulated or unmodulated oscillation. In later stages, the duration of the abnormal variation became longer, lasting more than one tooth meshing period. Other distributed faults, such as eccentricity and wear, might cover the most part of the whole revolution of the gear. Changes in the vibration signals therefore could be analyzed to provide an indicator of gear condition. When the size and shape of a wavelet were exactly the same as a section of the signal, the transform gave a maximum absolute value of wavelet coefficients. Therefore, the abnormal signal caused by a gear fault could be displayed by the wavelet transform, which could be regarded as a procedure for comparing the similarity of the signal and the chosen wavelet.

Li et al. (1998) applied neural networks to the detection of motor bearing conditions based on the frequency features of bearing vibration. Five basic frequencies related to rolling bearing dynamic movement were extracted by fast Fourier transform (FFT) technique. The basic frequency amplitude vectors were constructed to represent different bearing vibrations. These vectors were created from the power spectrum of the vibration signal and consisted of the five basic frequencies with varying amplitudes based on the defect present. The network consisted of five input measurements corresponding to the amplitudes of the five basic frequencies of interest, ten hidden nodes, and three output fault detectors (bearing looseness, defects on the inner

raceway, and defects on the rolling elements). The network was tested using the data generated by MOTORSIM. The results show that neural network can be an effective agent in the detection of various motor bearing faults through the measurement and interpretation of motor bearing vibration signals.

Liao et al. (2004) developed a novel technique for monitoring the gearbox condition based on the Self-Organizing Feature Maps (SOFM) network. Seven time-domain features parameters, i.e. standard deviation, Kurtosis, root mean square value, absolute mean value, crest factor, clearance factor and impulse factor were extracted from industrial gearbox vibration signals measured under different operating conditions. Trained with the SOFM network and visualized using the U-matrix method, the feature data were mapped into a two-dimensional space and formed clustering regions, each indicative of a specific gearbox work condition. Therefore the gearbox operating condition with fatigue crack or a broken tooth compared with the normal condition was identified clearly.

Kar and Mohanty (2006) applied the multi-resolution Fourier transform (MFT) of vibration and current signals to gearbox health monitoring. One and two teeth were artificially removed in one gear of the gearbox to simulate actual fault condition. When the gearbox was operated under several loads, the vibration signals were acquired from the tail-end bearing of the gearbox, and simultaneously the current drawn by the induction motor is acquired. The vibration and current signals were decomposed into four levels using discrete wavelet transform (DWT) with an orthogonal wavelet of 'db8'. Then a hanning window with 256 data points and 50% overlap was applied to the scaled signals to find the MFT coefficients. The MFT coefficients of signals were used to classify the types of defects by tracking the energy level possessed by the defect characteristic frequency.

CHAPTER 3 - THEORETICAL BACKGROUND

Signal-based damage detection methods examine changes in the non-parametric features derived directly from the measured vibration signal through signal processing to detect damage. The premise behind is that perturbations in a structure system will cause changes in measured vibration signals. These signals measured in vibration testing typically include acceleration, velocity, strain, and displacement. These real-life signals are analog signals which operate in the continuous-time domain. Before they can be processed with a computer, analog signals must be converted to digital signals which operate in discrete-time domain. An analog-to-digital (A/D) converter is used to convert a signal from analog to digital. After processing the signal digitally, it also can be converted to an analog signal using digital-to-analog (D/A) converter. The process of converting an analog signal to a digital signal involves sampling the signal, holding it for conversion, and converting it to the corresponding digital value. The sampling frequency must be high enough so as to avoid aliasing.

Aliasing is a phenomenon due to which a high-frequency signal when sampled using a low sampling rate becomes a low frequency signal that may interfere with the signal of interest. To avoid aliasing, the sampling theorem (or called Nyquist sampling theorem) states that the sampling frequency, f_s should be at least twice the highest frequency contents of the analog signal, f_{max} . For instance, if the highest frequency content in an analog signal is 10 kHz, it should be sampled at 20 kHz or more to avoid aliasing. Before encountering the A/D converter, the input signal is processed with a low-pass analog input filter to remove all frequencies above the Nyquist frequency (one-half the sampling rate). This is done to prevent aliasing during sampling. The result of sampling and converting an analog signal is a digital sequence presenting the signal samples. The processing is called digitizing. The sequence of these discrete data is referred as the digital signal.

Such a digital signal can be viewed from two different standpoints: (1) the frequency domain; (2) the time domain. The transformation of discrete data between the time and frequency domains is described in this chapter. The two domains provide complementary

information about the same signal. It may sometimes be more meaningful in an application to inspect the magnitude versus frequency plot for changes in the voltage amplitude at a particular frequency than to observe the voltage waveform in order, for example, to obtain an early indication of wear in a machine by fast Fourier transforming the output signal. The discrete transforms are used in the data compression of speech and video signals to allow transmission with reduced bandwidth. They are also used in image processing to obtain a reduced set of features for pattern recognition purposes. Of the available transforms, the discrete Fourier transform (DFT) and the fast Fourier transform (FFT) are the best known. Recently considerable efforts have been devoted to the wavelet transform due to its ability to describe stochastic signals of time varying frequency content in terms of wave amplitudes (Ifeachor and Jervis, 2001).

3.1 Fourier Transforms

The Fourier transform (named after its discoverer, the French mathematician Jean-Baptiste Joseph Fourier) is a frequency-based transform widely used in analysis of linear systems. It decomposes a signal into sine waves of different frequencies which sum to the original waveform, and also distinguishes such different frequency sine waves and their respective amplitudes.

3.1.1 Continuous Fourier Transform

Now, let $f(t)$ be a given continuous signal in time domain. The continuous Fourier transform of $f(t)$ is defined by the equation:

$$F(s) = \int_{-\infty}^{\infty} f(t) e^{-2\pi i s t} dt \quad (3.1)$$

where $i = \sqrt{-1}$ and s is often called frequency variable. Given $F(s)$, we can go backwards and get $f(t)$ by using inverse continuous Fourier transform:

$$f(t) = \int_{-\infty}^{\infty} F(s) e^{2\pi i s t} ds \quad (3.2)$$

Equations 3.1 and 3.2 are called Fourier transform pairs. $F(s)$ is the Fourier transform of $f(t)$ and that $f(t)$ is the inverse Fourier transform of $F(s)$. The only difference between the

forward and inverse Fourier transform is the sign above e , which makes it easy to go back and forth between time and frequency domain.

3.1.2 Discrete Fourier Transform

The continuous Fourier transform is a continuous function of frequency and is not suitable for computation with a digital signal processing (DSP). Discrete Fourier transform (DFT) representation of the continuous time signal permits the computer analysis and is used extensively in signal processing applications. The analog signal which consists of an infinite number of contiguous points is sampled at regular intervals. The input to the DFT is a sequence of sampled values rather than a continuous function of time $f(t)$, so that

$$F(k) = \sum_{n=0}^{N-1} f(n) e^{-2\pi i n k / N}, \quad k=0,1,2,\dots,(N-1) \quad (3.3)$$

and

$$f(n) = \frac{1}{N} \sum_{k=0}^{N-1} F(k) e^{2\pi i n k / N}, \quad n=0,1,2,\dots,(N-1) \quad (3.4)$$

The equation 3.3 is called the DFT and the equation 3.4 is called the inverse discrete Fourier transform (IDFT). $f(n)$ and $F(k)$ are the discrete sample values corresponding to $f(t)$ and $F(s)$. The N in the DFT pair denotes the number of elements in the $f(n)$ or $F(k)$ sequence.

The discrete Fourier transform allows calculating the Fourier transform on a computer, but it is not so efficient. The number of complex multiplications and additions required to implement Equations.3.3 and 3.4 is proportional to N^2 . For every $F(k)$, it needs to use all $f(0), \dots, f(N-1)$ and there are $N F(k)$ to calculate. For a large N , the computations can be prohibitively time-consuming, even for a high-speed computer.

3.1.3 Fast Fourier Transform

In 1965, Tuckey, J.W. and Cooley, J.W developed an algorithm to dramatically reduce the number of computations required in performing the DFT. This algorithm is known as the Fast Fourier transform (FFT). It reduces the number of computations from an order of N^2 to an order of $N \log_2 N$. The time saved compared with a direct calculation is roughly:

$$\text{gain} = \frac{N}{\log_2(N)} \quad (3.5)$$

If $N = 1024$, the FFT is about 100 times faster than the direct calculation based on the definition of the DFT.

Although there are many variations of the original Turkey-Cooley algorithm, these can be grouped into two basic types: **decimation-in-time** and **decimation-in-frequency** (Lathi, 1998).

The algorithm is simplified when N is a power of 2. Using the notation

$$W_N = e^{-(2\pi i / N)} \quad (3.6)$$

Equation 3.3 and Equation 3.4 become

$$F(k) = \sum_{n=0}^{N-1} f(n) W_N^{kn} \quad , \quad k=0,1,2,\dots,(N-1) \quad (3.7)$$

and

$$f(n) = \frac{1}{N} \sum_{k=0}^{N-1} F(k) W_N^{-kn} \quad , \quad k=0,1,2,\dots,(N-1) \quad (3.8)$$

The Decimation-in-Time Algorithm

The N -point data sequence $f(n)$ is divided into two sequences, each of length $N/2$.

One of the two is formed from the even-numbered points of the original samples, the other from the odd-numbered points, as follows:

$$\underbrace{f(0), f(2), f(4), \dots, f(N-2)}_{\text{sequence } g(k)} \quad \underbrace{f(1), f(3), f(5), \dots, f(N-1)}_{\text{sequence } h(k)}$$

Then Equation 3.7 becomes,

$$F(k) = \sum_{n=0}^{\frac{N}{2}-1} f(2n) W_N^{2kn} + \sum_{n=0}^{\frac{N}{2}-1} f(2n+1) W_N^{(2n+1)k} \quad (3.9)$$

Also, since

$$W_{\frac{N}{2}} = W_N^2 \quad (3.10)$$

it has

$$\begin{aligned} F(k) &= \sum_{n=0}^{\frac{N}{2}-1} f(2n) W_{\frac{N}{2}}^{kn} + W_N^k \sum_{n=0}^{\frac{N}{2}-1} f(2n+1) W_{\frac{N}{2}}^{kn} \\ &= G(k) + W_N^k H(k) \quad 0 \leq k \leq N-1 \end{aligned} \quad (3.11)$$

where $G(k)$ and $H(k)$ are the $\left(\frac{N}{2}\right)$ -point DFTs of the even- and odd-numbered sequences,

$g(k)$ and $h(k)$, respectively. Also, $G(k)$ and $H(k)$, being the $\left(\frac{N}{2}\right)$ -point DFTs, are $\left(\frac{N}{2}\right)$ -

periodic. Hence

$$\begin{aligned} G\left(k + \frac{N}{2}\right) &= G(k) \\ H\left(k + \frac{N}{2}\right) &= H(k) \end{aligned} \quad (3.12)$$

Moreover,

$$W_N^{k + \left(\frac{N}{2}\right)} = W_N^{\frac{N}{2}} W_N^k = e^{-i\pi} W_N^k = -W_N^k \quad (3.13)$$

From Equations (3.11), (3.12) and (3.13), it turns out

$$F\left(k + \frac{N}{2}\right) = G(k) - W_N^k H(k) \quad 0 \leq k \leq \frac{N}{2} - 1 \quad (3.14)$$

This property can be used to reduce the number of computations. The first $\left(\frac{N}{2}\right)$ points

$(0 \leq n \leq \frac{N}{2} - 1)$ of $F(k)$ can be computed using Equation 3.11 and the last $\left(\frac{N}{2}\right)$ points can be

computed using Equation 3.14 as

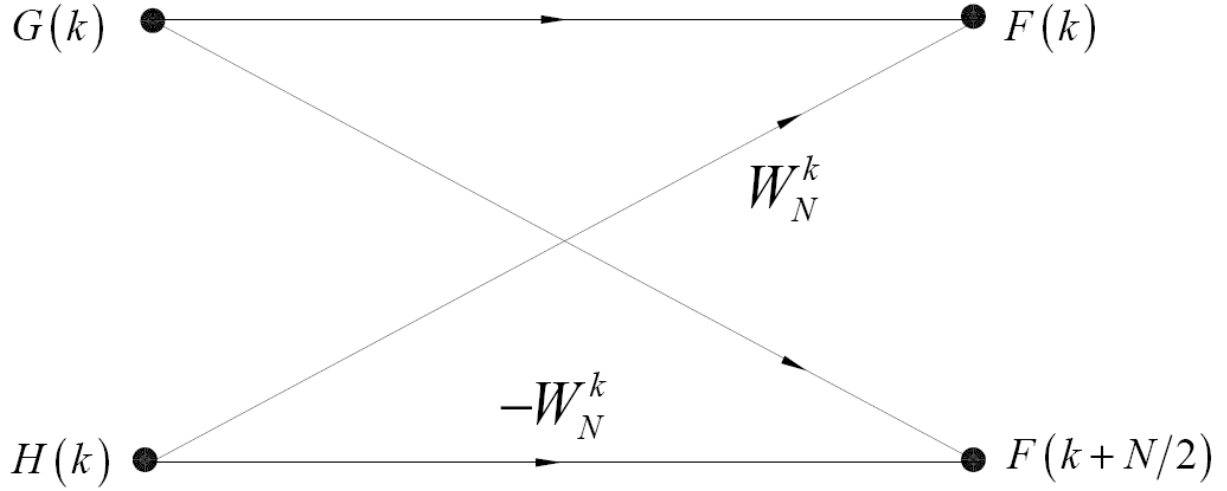
$$F(k) = G(k) + W_N^k H(k) \quad 0 \leq k \leq \frac{N}{2} - 1 \quad (3.15a)$$

$$F\left(k + \frac{N}{2}\right) = G(k) - W_N^k H(k) \quad 0 \leq k \leq \frac{N}{2} - 1 \quad (3.15b)$$

Thus, an N -point DFT can be computed by combining the two $\left(\frac{N}{2}\right)$ -point DFTs, as in

Equations 3.15. These equations can be represented conveniently by the signal flow graph depicted in Figure 3.1. This structure is known as a **butterfly**.

Figure 3.1 Butterfly



The next step is to compute the $\left(\frac{N}{2}\right)$ -point DFTs $G(k)$ and $H(k)$. The same procedure is repeated by dividing $g(k)$ and $h(k)$ into two $\left(\frac{N}{4}\right)$ -point sequences corresponding to the even- and odd-numbered samples. Then this process is continued until the one-point DFT is reached.

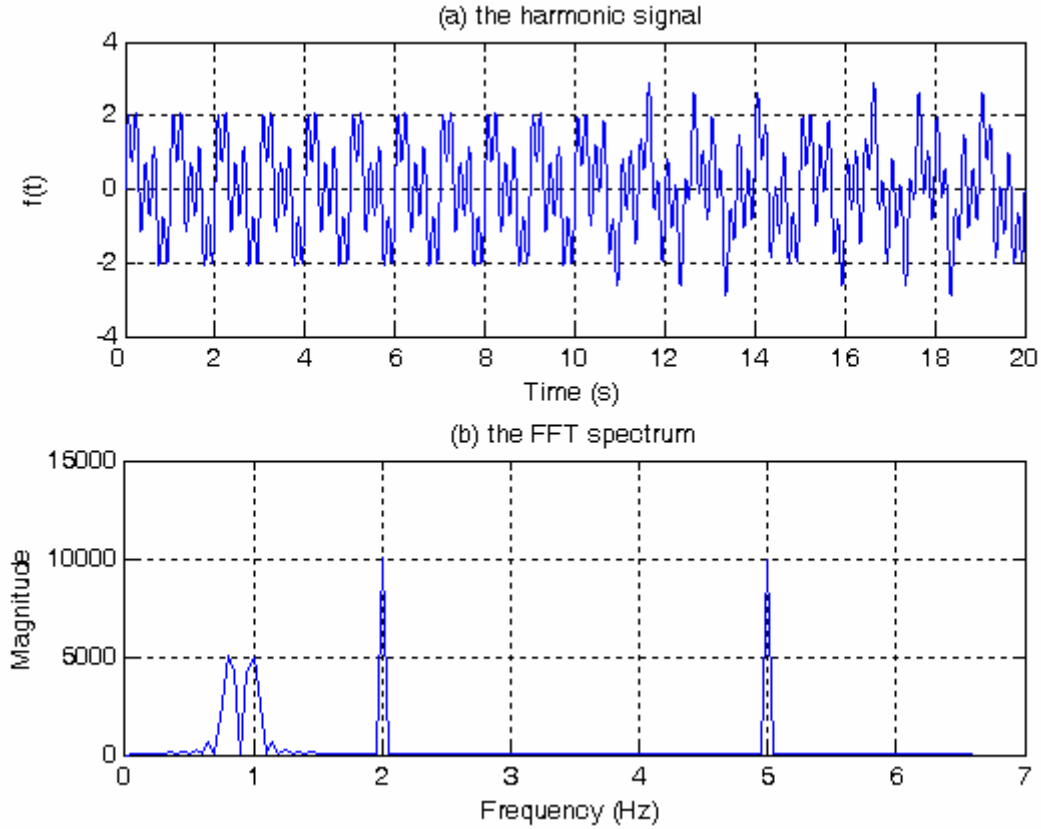
The procedure for obtaining IDFT is identical to that used to obtain the DFT except that $W_N = e^{i(2\pi/N)}$ instead of $e^{-i(2\pi/N)}$ (in addition to the multiplier $1/N$). Another FFT algorithm, the **decimation-in-frequency algorithm**, is similar to the decimation-in-time algorithm. The only difference is that $f(n)$ is divided into two sequences formed by the first $\frac{N}{2}$ and the last

$\frac{N}{2}$ digits, proceeding in the same way until a single-point DFT is reached. The total number of computations in this algorithm is the same as that in the decimation-in-time algorithm.

FFT is of great importance to digital signal processing. It has been widely used to extract the structure frequency response and has been successfully applied for fault detection on beam and rotating machinery. However, it should be noted that Fourier transform is not capable of preserving the information on time domain. If there is a local oscillation representing a particular frequency in the signal, its location on the time domain will be lost. Such disadvantage is illustrated by the harmonic signal $f(t)$ defined by:

$$f(t) = \begin{cases} \sin(2\pi t) + \sin(4\pi t) + \sin(10\pi t) & (0 \leq t \leq 10s) \\ \sin(1.6\pi t) + \sin(4\pi t) + \sin(10\pi t) & (10s < t \leq 20s) \end{cases} \quad (3.16)$$

Figure 3.2 The Harmonic Signal and Its FFT Spectrum



The signal $f(t)$ as plotted in Figure 3.2(a) contains three components with each frequency of 1, 2, and 5 Hz within the first 10 seconds. At exactly 10 second, only the 1 Hz component is suddenly reduced to 0.8 Hz, and others keep the same. This signal is sampled by 1000 Hz. The Fourier spectrum in Figure 3.2(b) shows the FT results of the signal within the first and the last 10 seconds. Although the frequency component of 0.8 Hz in the signal caused by the small perturbation is visible as peak in the spectrum, it is difficult to tell the exact time for the small perturbation. The time information is lost in the Fourier transform. The signal $f(t)$ is called a “non-stationary signal” whose frequencies change over the duration.

3.1.4 Short Time Fourier Transform

In order to overcome the problem with localizing the frequency components on time, the Short Time Fourier Transform (STFT) was designed to analyze the signal in a time-frequency domain. The STFT of a signal $f(t)$ is defined as:

$$STFT(\tau, \omega) = \int f(t) g(t - \tau) e^{-i\omega t} dt \quad (3.17)$$

where $g(t)$ is a window function. The drawback of STFT is its poor frequency resolution. Once you choose a particular size for the time window, this window is also the same for all frequency components. The STFT preserves information on time as well, but it is not as efficient as wavelet.

3.2 Wavelet Transforms

The wavelet transform was developed by Grossman and Morlet in the early 1980s to provide a time-frequency representation of the signal. It is probably the most recent solution to overcome the aforesaid deficiency mentioned for Fourier transform. Although Short Time Fourier Transform (STFT) can also be used to analyze non-stationary signals, it gives a constant resolution at all frequencies. The wavelet transform uses multi-resolution technique by which different frequencies are analyzed with different resolutions.

All wavelets are derived from a basis (mother) function, $\psi(t)$. There are a number of possible basis functions, chosen to have the following properties (Ifeachor and Jervis 2001, Rao and Boparadikar 1998):

(1) it is oscillatory or it has a wave appearance, which is expressed as;

$$\int_{-\infty}^{\infty} \psi(t) dt = 0 \quad (3.18)$$

(2) it decays rapidly towards zero with time or it has finite energy, which is expressed as;

$$\int_{-\infty}^{\infty} |\psi(t)|^2 dt < \infty \quad (3.19)$$

(3) it has no DC component (constant or zero frequency);

(4) it is bandpass (a function $f(t)$ is a band-pass function if its Fourier transform $F(\omega)$ is confined to a frequency interval $\omega_1 < |\omega| < \omega_2$, where $\omega_1 > 0$ and ω_2 is finite);

(5) it satisfies the admissibility condition that

$$C \equiv \int_{-\infty}^{\infty} \frac{|\psi(\omega)|^2}{|\omega|} d\omega < +\infty \quad (3.20)$$

The last property ensures the wavelet transform of a signal is unique and invertible. For example, the Morlet mother wavelet is

$$\psi(t) = e^{-t^2} \cos\left(\pi\sqrt{\frac{2}{\ln 2}}t\right) \quad (3.21)$$

Its plot is shown in Figure 3.3. More than 99% of the total energy of the function is contained in the interval $|t| \leq 2.5$ sec. Let $H(\omega)$ denotes the Fourier transform of $\psi(t)$:

$$H(\omega) = \int_{-\infty}^{\infty} \psi(t) e^{-i\omega t} dt \quad (3.22)$$

From the plot of $H(\omega)$ shown in Figure 3.4, it is seen that the wavelet is essentially a band-pass function.

Figure 3.3 The Morlet Wavelet

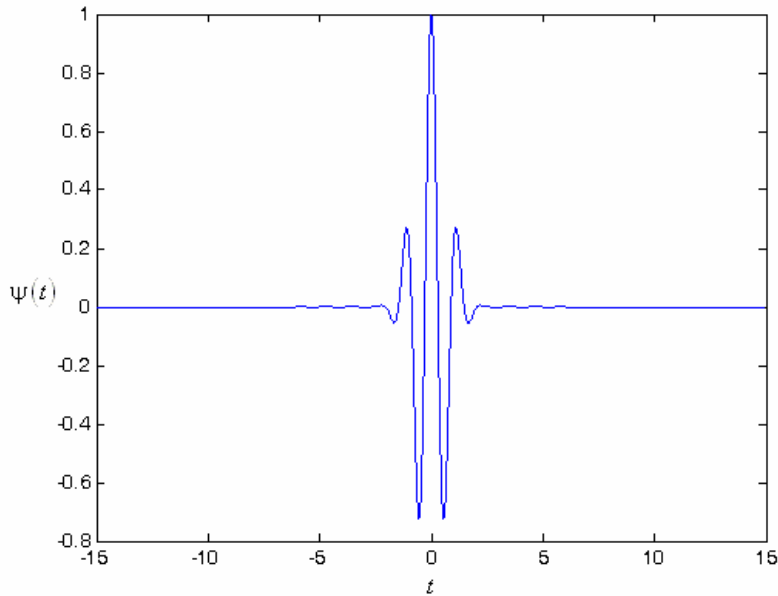
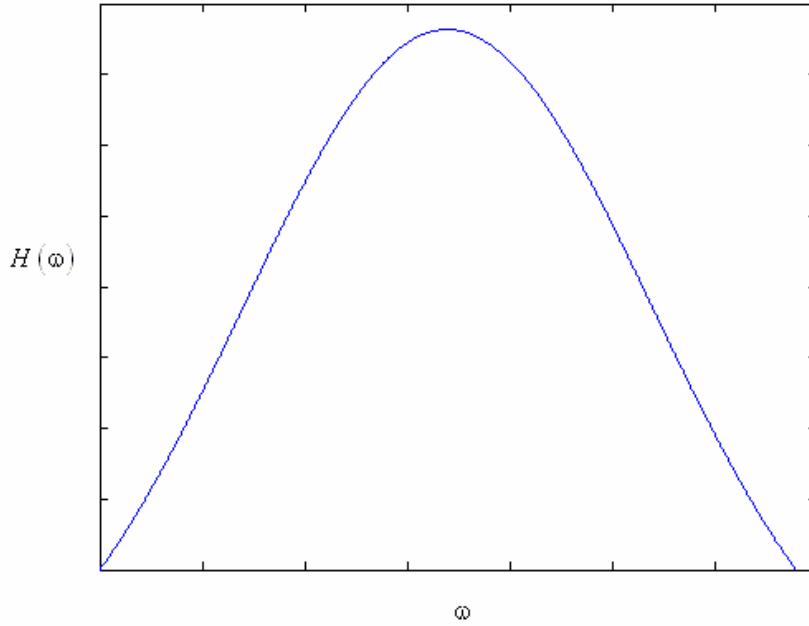


Figure 3.4 Fourier Transform, $H(\omega)$ of the Morlet Wavelet



3.2.1 Continuous Wavelet Transform (CWT)

The continuous wavelet transform (CWT) of the signal $f(t)$ with respect to a wavelet $\psi(t)$ is defined as (Rao and Boparadikar 1998)

$$W(a,b) = \frac{1}{\sqrt{a}} \int f(t) \psi^* \left(\frac{t-b}{a} \right) dt \quad (3.23)$$

where a and b are real and $*$ denotes complex conjugation. Thus, the wavelet transform is a function of two variables. Equation 3.23 can be written in a more compact form by defining

$$\psi_{a,b}(t) \equiv \frac{1}{\sqrt{|a|}} \psi \left(\frac{t-b}{a} \right) \quad (3.24)$$

Then, combining Equations 3.23 and 3.24,

$$W(a,b) = \int_{-\infty}^{\infty} f(t) \psi_{a,b}^*(t) dt \quad (3.25)$$

The signal $f(t)$ may be recovered or reconstructed by an inverse wavelet transform of $W(a,b)$ as defined by

$$f(t) = \frac{1}{C} \int_{a=-\infty}^{\infty} \int_{b=-\infty}^{\infty} \frac{1}{|a|^2} W(a,b) \psi_{a,b}(t) da db$$

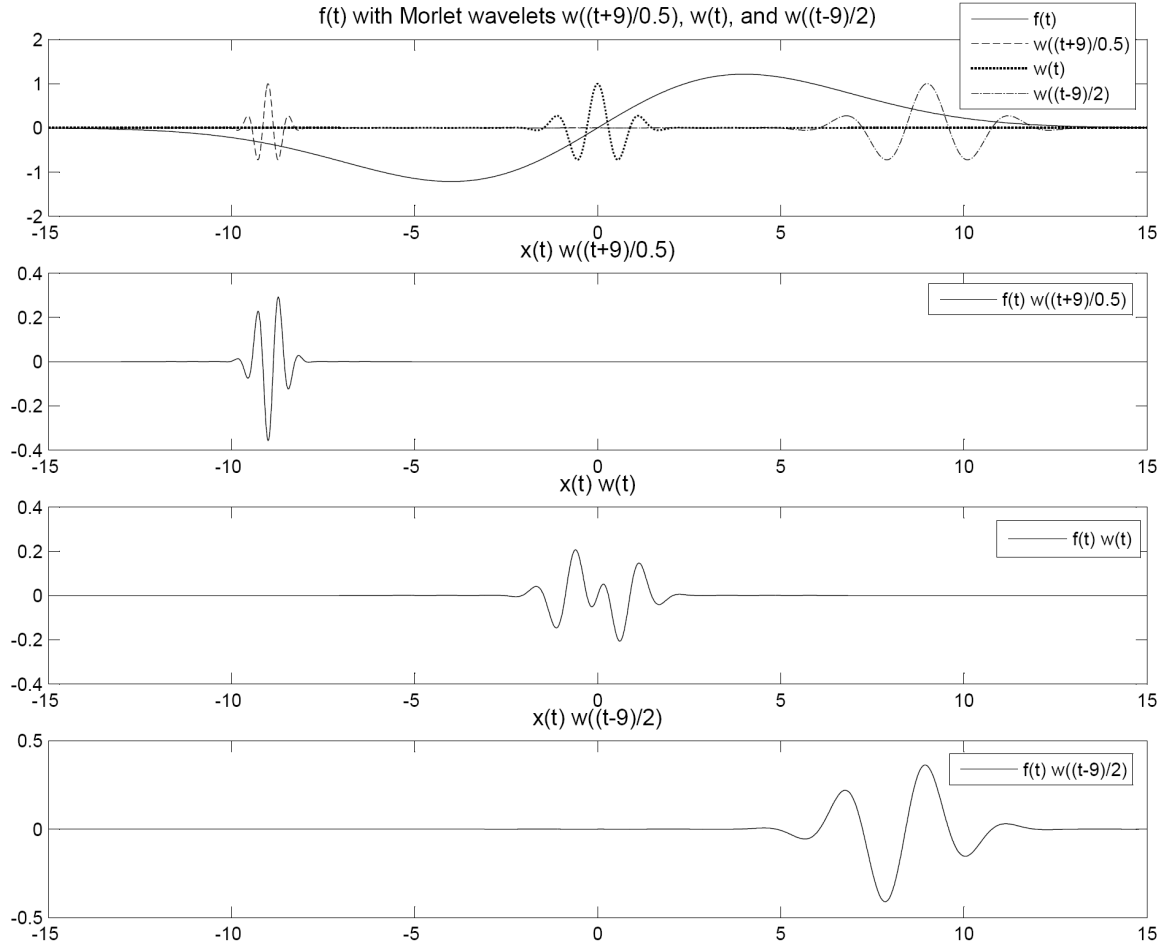
The normalizing factor of $1/\sqrt{|a|}$ ensures that the energy stays the same for all a and b ; that is,

$$\int_{-\infty}^{\infty} |\psi_{a,b}(t)|^2 dt = \int_{-\infty}^{\infty} |\psi(t)|^2 dt \quad (3.26)$$

For any given value of a , the function $\psi_{a,b}(t)$ is a shift of $\psi_{a,0}(t)$ by an amount b along the time axis. Thus, the variable b represents time shift or translation. Variable a determines the amount of time scaling or dilation, it is referred to as the scale or dilation variable. Figure 3.5 shows Morlet wavelet at three scales and shifts. If $a > 1$, there is a stretching of $\psi(t)$ along the time axis, whereas if $0 < a < 1$, there is a contraction of $\psi(t)$. The value of the scale a is proportional to the reciprocal of the frequency. The smaller the value of a , the more the band-pass shifts to a higher frequency, implying that the CWT at small scales contains information about $f(t)$ at the higher end of its frequency spectrum.

The CWT is the inner product or cross correlation of the signal $f(t)$ with the scaled and time shifted wavelet $\psi_{a,b}(t)$. This cross correlation is a measure of the similarity between the signal and the scaled and shifted wavelet. This point of view is illustrated in the Figure 3.5.

Figure 3.5 Signal $f(t)$ along with the Morlet Wavelet (denoted by w) at Three Scales and Shifts

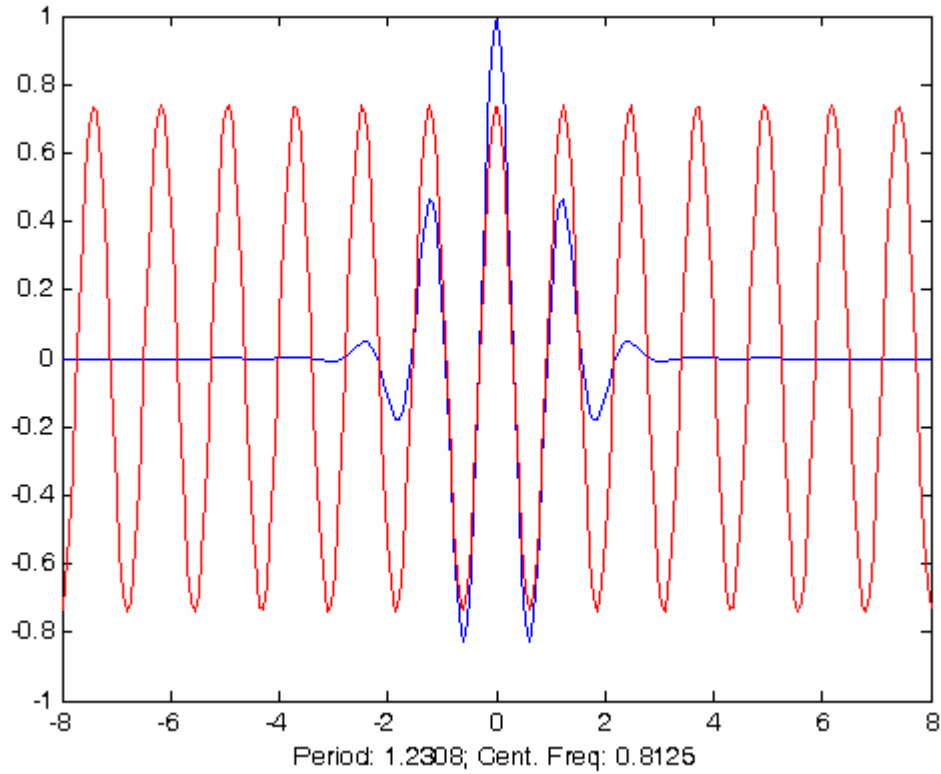


Scale parameter a in wavelet analysis is related to frequency as follows (Kim 2004, Yoon et al. 2000):

$$F_a = \frac{F_c}{a\Delta} \quad (3.27)$$

where a is a scale, Δ is the sampling period, F_c is the center frequency of a wavelet in Hz. F_a is the pseudo-frequency corresponding to the scale a , in Hz. Each wavelet has different center frequency, F_c . As shown in Figure 3.6, the approximation of center frequency for Morlet wavelet is 0.8125 Hz.

Figure 3.6 Wavelet Morlet (blue) and Center Frequency Based Approximation



The $W(a,b)$ coefficient is called the scalogram of signal $f(t)$. The scalogram can be plotted in 2-dimensional contours with time on the horizontal axis, scale on the vertical axis, and coefficient given by a gray-scale color. Alternately, it can be plotted in 3-dimensional contours. For illustration, the non-stationary signal, $f(t)$ in Figure 3.2(a) is transformed by CWT. As mentioned earlier, $f(t)$ contains three frequency components of 1, 2, and 5 Hz within the first 10 seconds. At exactly 10 second, only the 1 Hz component is suddenly reduced to 0.8 Hz, and others keep the same. The signal is sampled by 1000 Hz. By using the Morlet wavelet, the CWT scalogram of signal $f(t)$ is shown in Figure 3.7 as scale-space (time) contours. At scales of 163, 406, 813 and 1016, it shows the highest magnitude which indicates that these scales correspond to signal frequencies. At exact 10 seconds ($b = 10,000$), scale of 813 switches to scale of 1016 to show that one frequency component is changed. Using Equation 3.27, the scales of 1016, 813, 406 and 163 can be converted to pseudo-frequencies of 0.8, 1, 2 and 5, respectively

which are the exact the same as the frequency components of $f(t)$. The CWT scalogram using frequency instead of scale is plotted in Figure 3.8 and a 3-D plot of CWT scalogram is shown in Figure 3.9.

Figure 3.7 CWT Scale-Space (time) Contours of Signal, $f(t)$

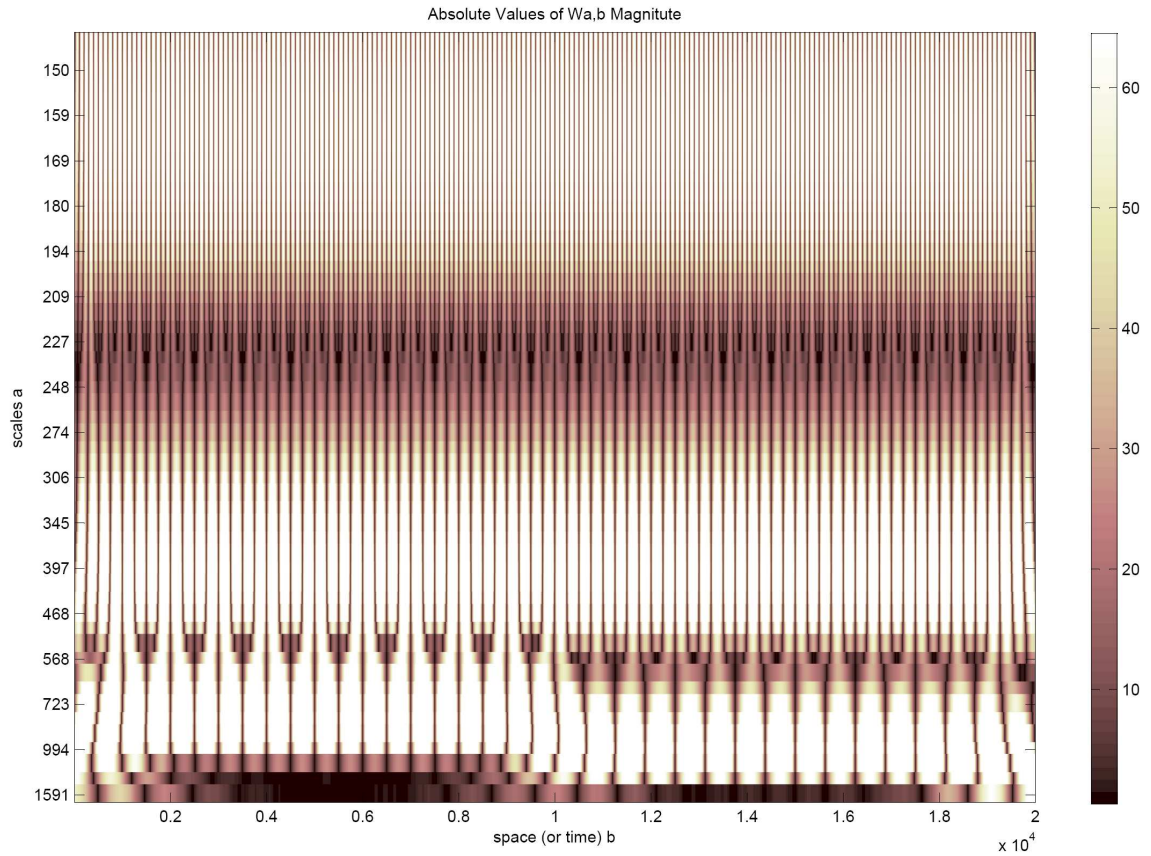


Figure 3.8 CWT Frequency-Time Contour of Signal, $f(t)$

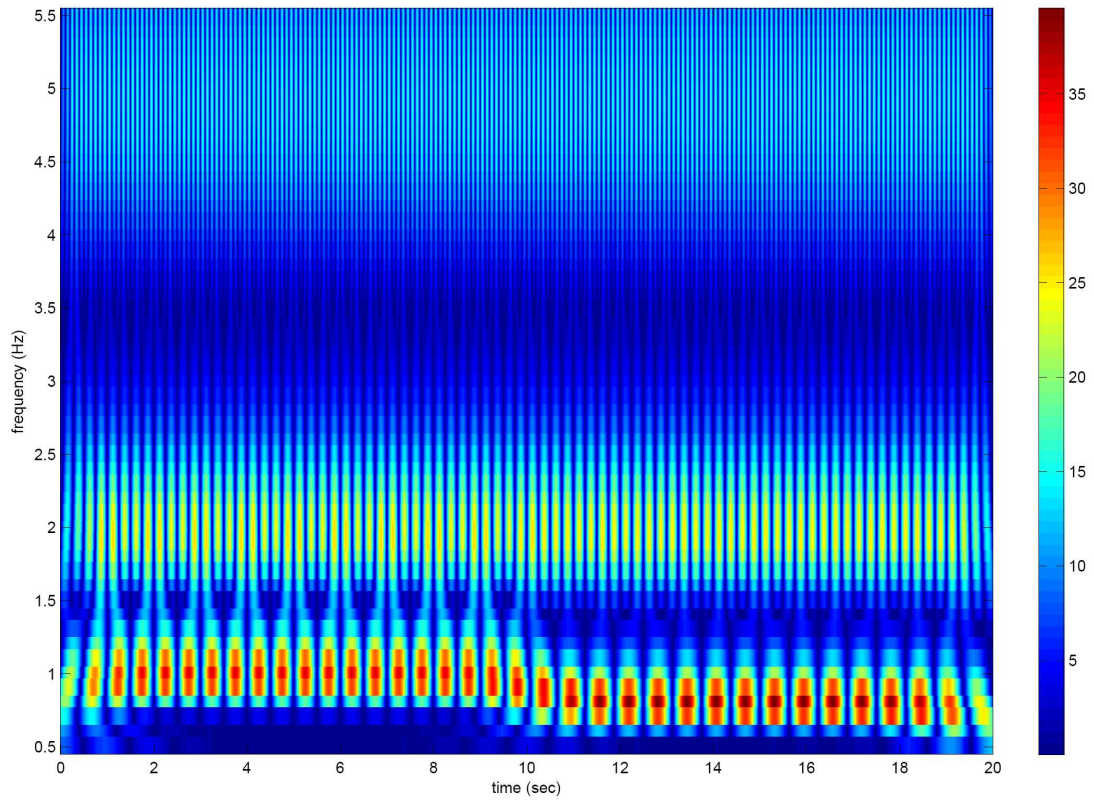
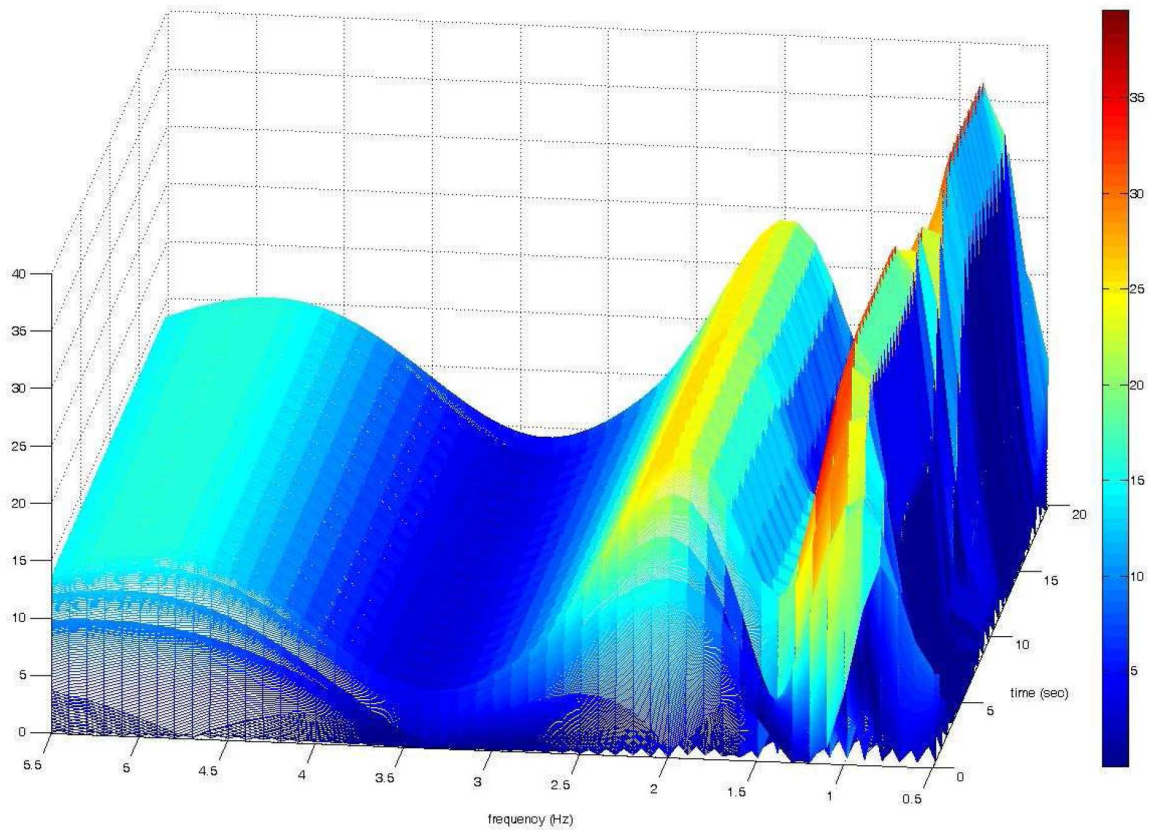


Figure 3.9 3-D View of CWT Frequency-Time Contour of Signal, $f(t)$



3.2.2 Discrete Wavelet Transform (DWT)

CWT calculates the wavelet coefficients by continuously shifting a scalable basis function over a signal and calculating the correlation between the two at every possible scale. Its computation may consume significant amount of time and resources, depending on the resolution required. DWT adopts scales and translations based on power of two, so called dyadic scales and translations to yield a fast computation of wavelet transform and to reduce the resources required.

Filters are one of the most used signal processing functions. In DWT, a time-scale representation of the digital signal is obtained by passing the signal through filters with different cutoff frequencies at different scales. The signal is passed through a series of high pass filters to analyze the high frequency, and through a series of low pass filters to analyze the low frequency. Low pass filters and high pass filters are related to the scaling function and the corresponding wavelet function, respectively. The corresponding wavelet function is

constructed from the scaling function. The scaling function $\phi(t)$ must satisfy the following three conditions (Rao and Boparadikar 1998):

(1) It integrates to one;

$$\int_{-\infty}^{\infty} \phi(t) dt = 1 \quad (3.28)$$

(2) It has unit energy;

$$\|\phi(t)\|^2 = \int_{-\infty}^{\infty} |\phi(t)|^2 dt = 1 \quad (3.29)$$

(3) The set consisting of $\phi(t)$ and its integer translation are orthogonal.

$$\langle \phi(t), \phi(t-n) \rangle = \delta(n) \quad (3.30)$$

The scaling function $\phi(t)$ with N coefficients is defined by

$$\phi(t) = \sum_{n=0}^{N-1} c(n) \phi(2t-n) \quad (3.31)$$

Coefficients $c(n)$ must satisfy following conditions (Newman 1993):

$$(i) \quad \sum_{n=0}^{N-1} c(n) = 2 \quad (3.32)$$

so that the scaling function is unique and retains unit area during iteration;

$$(ii) \quad \sum_{n=0}^{N-1} (-1)^n n^m c(n) = 0 \quad (3.33)$$

for integer $m = 0, 1, 2, \dots, N/2 - 1$ (as high as the available number of coefficients will allow), in order to achieve accuracy;

$$(iii) \quad \sum_{n=0}^{N-1} c(n) c(n+2m) = 0 \quad m \neq 0 \quad (3.34)$$

for $m = 1, 2, \dots, N/2 - 1$, in order to generate an orthogonal wavelet system, with the additional condition that

$$\sum_{n=0}^{N-1} c(n)^2 = 2 \quad (3.35)$$

The corresponding wavelet function $\psi(t)$ is defined by

$$\psi(t) = \sum_{n=0}^{N-1} (-1)^n c(n) \phi(2t+n-N+1) \quad (3.36)$$

Such function is called orthogonal wavelet function which is satisfying the following:

$$\int_{-\infty}^{\infty} \psi(t) dt = 0 \quad (3.37)$$

$$\int_{-\infty}^{\infty} |\psi(t)|^2 dt = 1 \quad (3.38)$$

$$\langle \psi(t), \psi(t-n) \rangle = \delta(n) \quad (3.39)$$

$$\langle \psi(t), \phi(t-n) \rangle = 0 \quad (3.40)$$

In order to obtain a smoother function, it is necessary to include more terms in the scaling function. If $N = 4$, the four-coefficient scaling function has a form

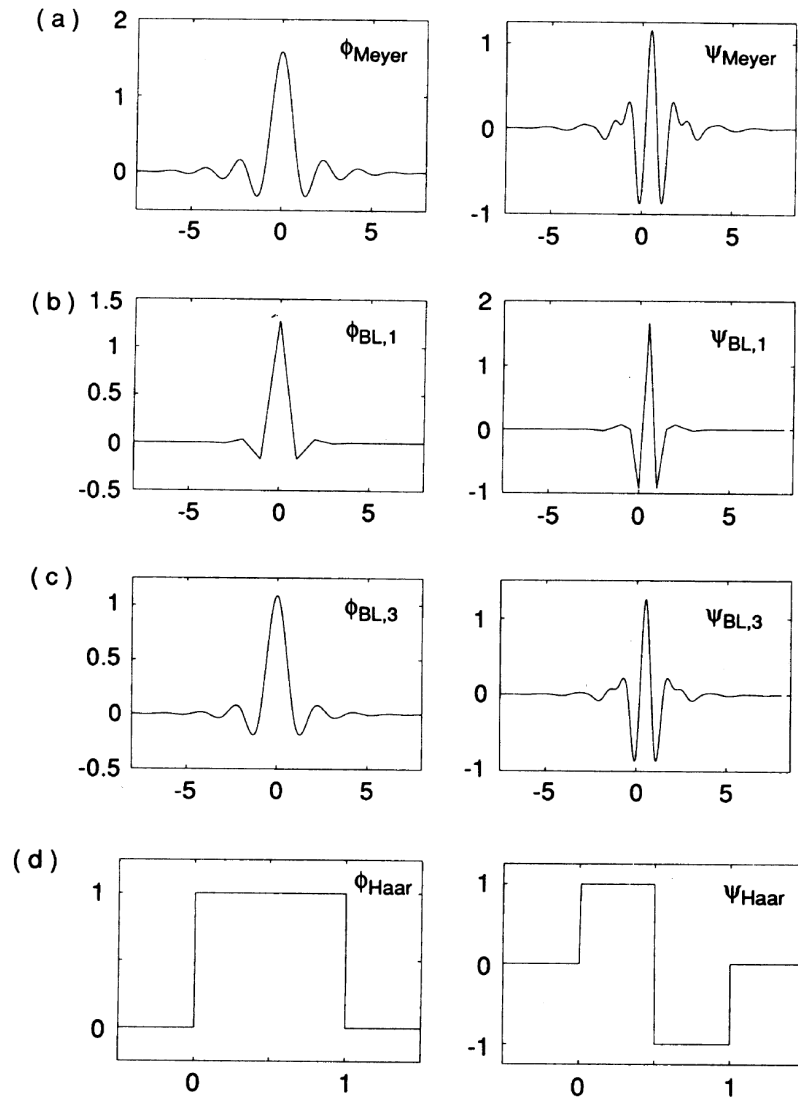
$$\phi(t) = c(0)\phi(2t) + c(1)\phi(2t-1) + c(2)\phi(2t-2) + c(3)\phi(2t-3) \quad (3.41)$$

and the corresponding wavelet function $\psi(t)$ is

$$\psi(t) = -c(3)\phi(2t) + c(2)\phi(2t-1) - c(1)\phi(2t-2) + c(0)\phi(2t-3) \quad (3.42)$$

Figure 3.10 shows some examples of pairs of function ϕ, ψ . The Meyer wavelets have compactly supported Fourier transform. ϕ, ψ themselves are infinitely supported. They are shown in Figure 3.10a; The Battle-Lemarie wavelets are spline functions (linear in Figure 3.10b, cubic in Figure 3.10c). Both ϕ, ψ have exponential decay. Their numerical decay is faster than for the Meyer wavelets; The Haar wavelet, in Figure 3.10d, can be viewed as the smallest degree Battle-Lemarie wavelet ($\psi_{\text{Haar}} = \psi_{\text{BL}, 0}$).

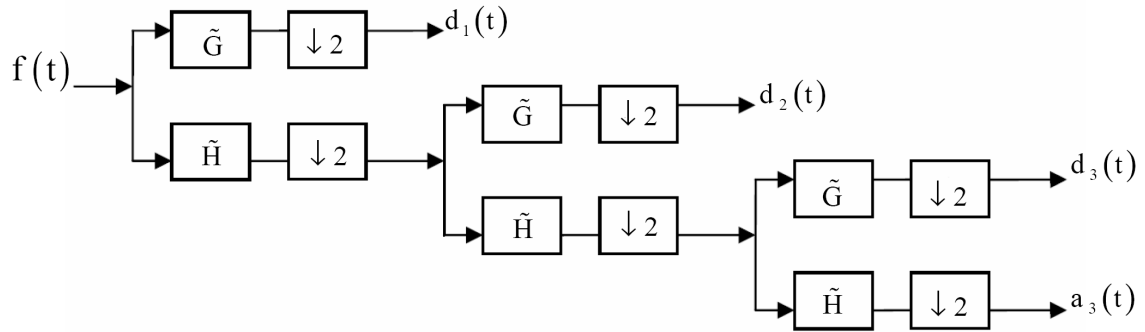
Figure 3.10 Some Example of Pairs of Functions ϕ , ψ : (a) The Meyer Wavelets; (b) and (c) Battle-Lemarie Wavelets; (d) The Haar Wavelet (Daubechies, 1992)



Each filter is generated from the coefficients of the scaling and wavelet function. The filter length is equal to the number of the coefficients. The DWT is computed by successive low pass and high pass filtering of the discrete time-domain signal as shown in Figure 3.11. This is called the Mallat algorithm or Mallat-tree decomposition. In this figure, the signal is denoted by $f(t)$. The low pass decomposition (or called analysis) filter is denoted by \tilde{H} with an impulse response of $\tilde{h}(n)$, while the high pass decomposition filter is denoted by \tilde{G} with an impulse

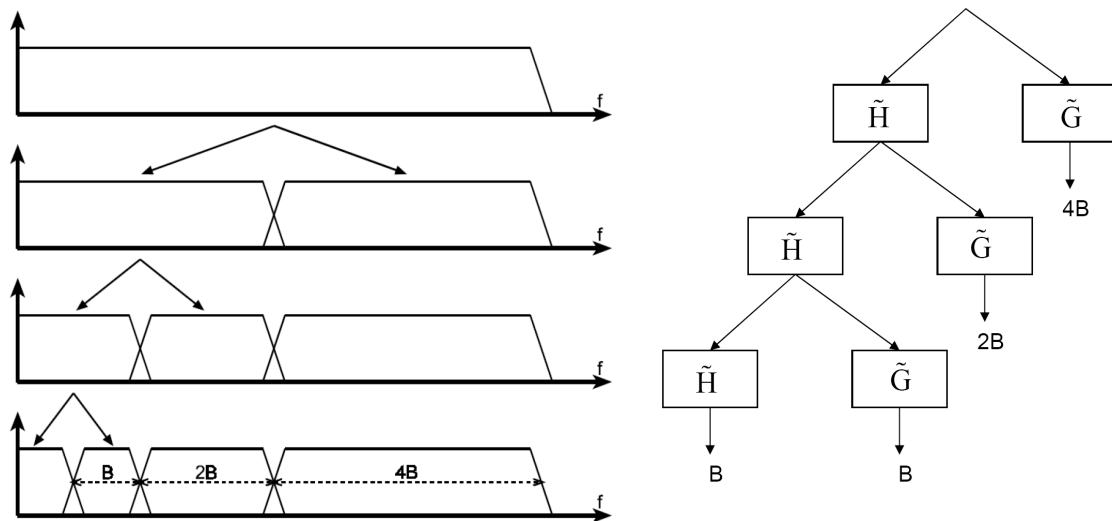
response of $\tilde{g}(n)$. At each level, the high filter produces detail information, $d[t]$, while the low pass filter associated with scaling function produces approximate information, $a[t]$.

Figure 3.11 Three-Level Wavelet Decomposition Tree



At each decomposition level, the half band filters produce signals spanning only half the frequency band. This doubles the frequency resolution as the uncertainty in frequency is reduced by half. Down-sampling discards half the samples and halves the time resolution as the entire signal is now represented by only half the number of samples. Thus, while the half band low pass filtering removes half of the frequencies and thus halves the resolution, the down-sampling double the scale (Rao and Boparadikar 1998). The process of splitting the spectrum is graphically displaced in Figure 3.12.

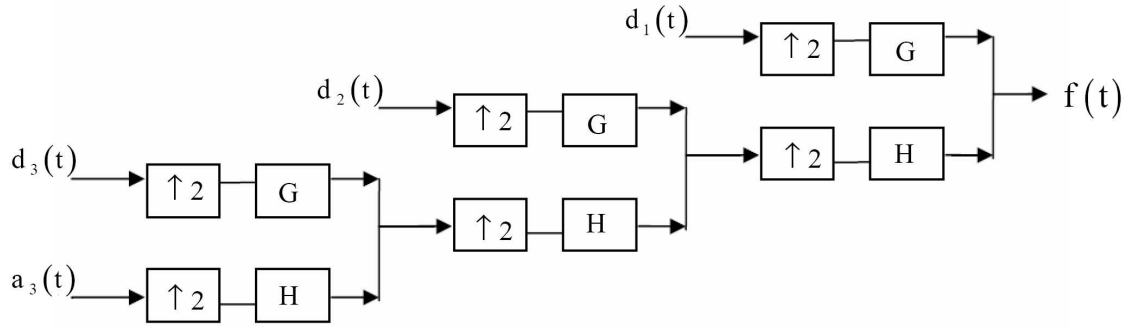
Figure 3.12 Splitting the Signal with an Iterated Filter Bank



The filtering and down-sampling process is continued until the desired level is reached. The maximum number of levels is determined by $\log_2 N$, where N is the length of the signal. By this approach, DWT yields good time resolution at high frequency components of signal, while good frequency resolution at low frequency components of signal.

The reconstruction of the original signal is the reverse process of decomposition. As shown in Figure 3.13, the approximation and detail coefficients at every level are up-sampled by two, passed through the low pass and high pass synthesis filters, H and G , and then added. This process is continued through the same number of levels as in the decomposition process to obtain the original signal.

Figure 3.13 Three-Level Wavelet Reconstruction Tree



The impulse response of low pass synthesis filter, $h(n)$, is found by

$$h(n) = \frac{c(n)}{2} \quad (3.43)$$

where $c(n)$ is the coefficient of the scaling function. The impulse response of the high pass synthesis filter, $g(n)$, is a quadrature mirror of $h(n)$ and defined as

$$g(n) = (-1)^n h(N+1-n) \quad \text{for } k = 1, 2, \dots, N \quad (3.44)$$

The impulse responses of decomposition filters, $\tilde{h}(n)$ and $\tilde{g}(n)$, are the reverse of $h(n)$ and $g(n)$

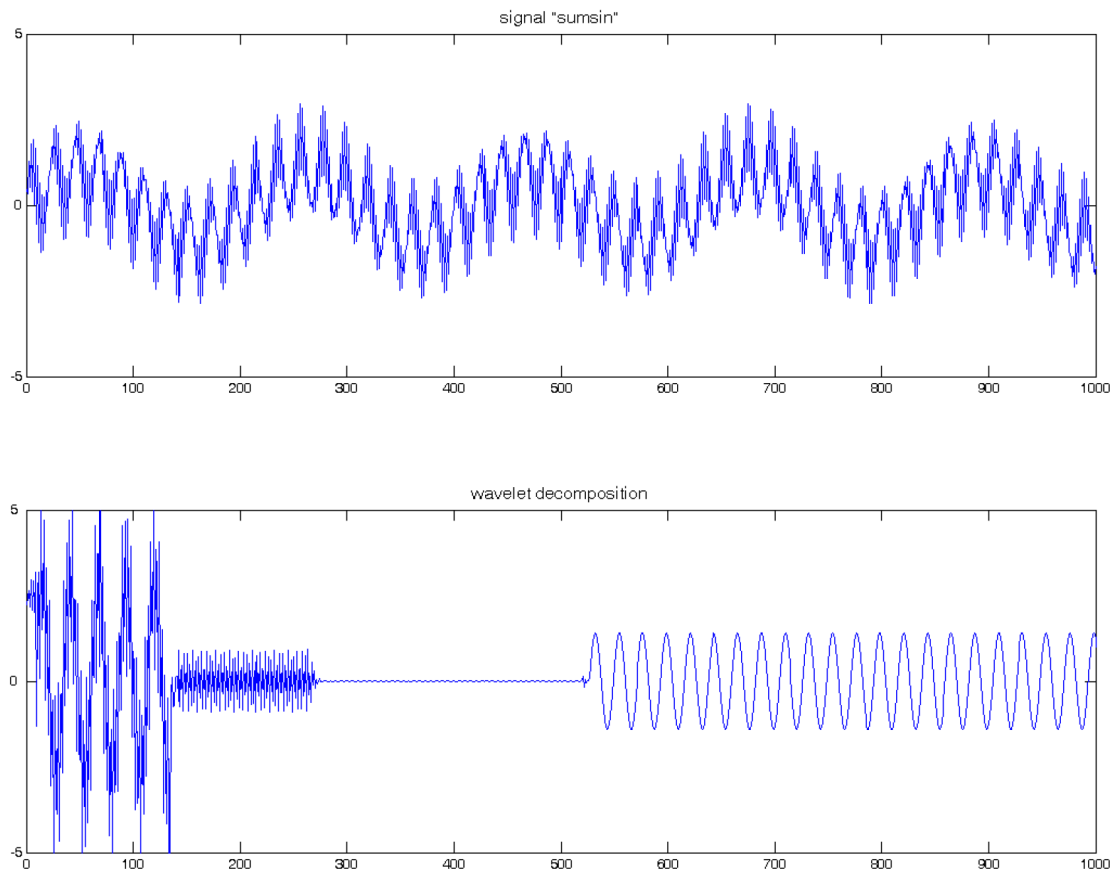
$$\tilde{h}(n) = h(-n) \quad (3.45)$$

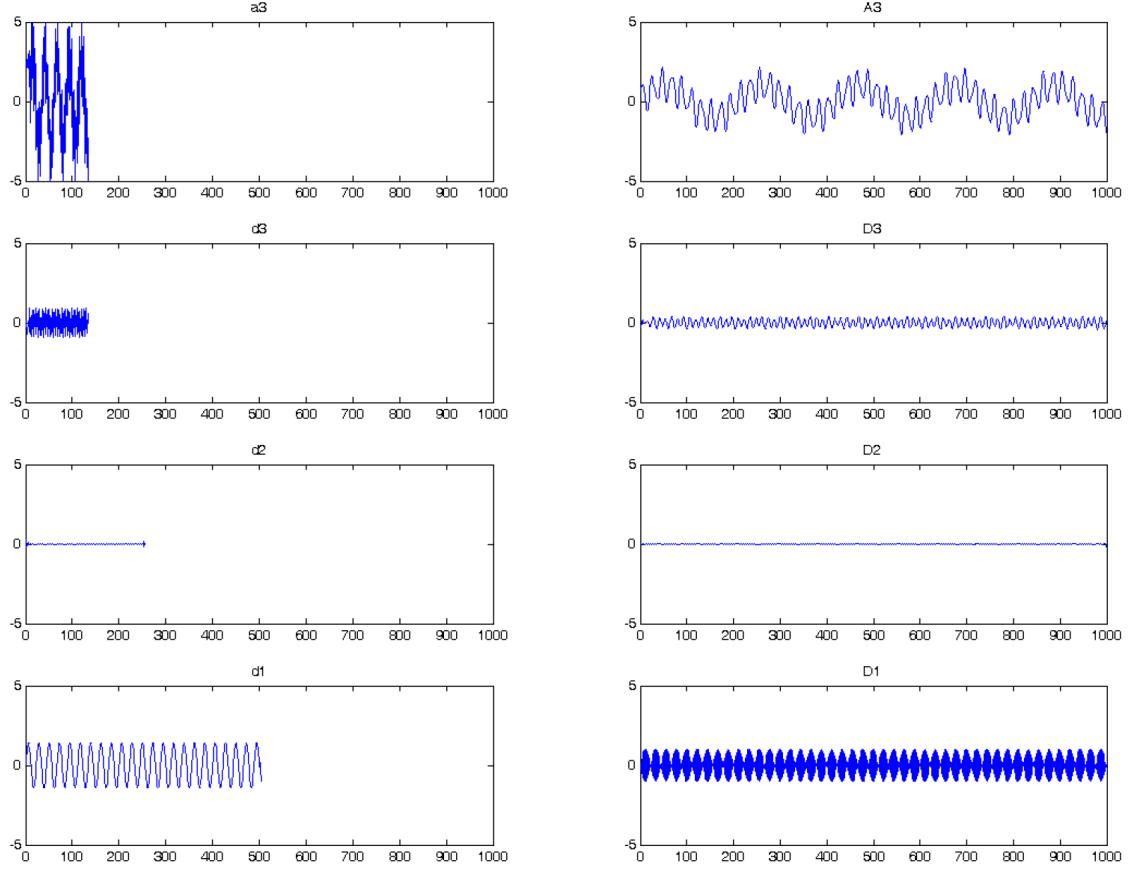
$$\tilde{g}(n) = g(-n) \quad (3.46)$$

As an example of decomposition and reconstruction, Figure 3.14 shows the three-level db6 discrete wavelet decomposition of the signal, named “sumsin”. The length of the signal

“sumsin” is 1000. After down-sampled by two, the length of detail coefficients at 1st and 2nd level, $d1$ and $d2$, are 500 and 250 respectively; the length of approximation coefficients and detail coefficients at 3rd level, $a3$ and $d3$, are 125. After up-sampled by two, the length of each of the reconstructed coefficients, $A3$, $D3$, $D2$, and $D1$ is 1000. By adding $A3$, $D3$, $D2$, and $D1$ together, the signal “simsin” can be reconstructed.

Figure 3.14 Decompose Signal at Depth 3 with Discrete Wavelet





3.2.3 Wavelet Packet Transform (WPT)

Wavelet packets consist of a set of linearly combined wavelet functions. The wavelet packets inherit properties such as orthonormality and time-frequency localization from their corresponding wavelet functions (Coifman and Wickerhauser, 1992). A wave packet is a function with three indices, $\psi_{j,k}^i(t)$, where integers i , j , and k are the modulation, the scale, and the translation parameters, respectively,

$$\psi_{j,k}^i(t) = 2^{j/2} \psi^i(2^j t - k) \quad i = 1, 2, \dots, \quad (3.47)$$

The wavelets ψ^i are obtained from the following recursive relationships:

$$\psi^{2i}(t) = \sqrt{2} \sum_{n=-\infty}^{\infty} h(n) \psi^i(2t - k) \quad (3.48)$$

$$\psi^{2i+1}(t) = \sqrt{2} \sum_{n=-\infty}^{\infty} g(n) \psi^i(2t - n) \quad (3.49)$$

where $h(n)$ and $g(n)$ are quadrature mirror filter responses mentioned formerly. The decomposition process is a recursive filter-decimation operation. Figure 3.15 shows a full wavelet packet transform tree of a time-domain signal $f(t)$ up to the 3rd level of decomposition. It is seen that the wavelet packet transform contains complete decomposition at every level and hence can achieve a higher resolution in the high frequency region. The recursive relations between the j th and the $j+1$ th level components are

$$f_j^i(t) = f_{j+1}^{2i-1}(t) + f_{j+1}^{2i}(t) \quad (3.50)$$

$$f_{j+1}^{2i-1}(t) = Hf_j^i(t) \quad (3.51)$$

$$f_{j+1}^{2i}(t) = Gf_j^i(t) \quad (3.52)$$

where H and G are filtering-decimation operations and are related to $h(n)$ and $g(n)$ through

$$H\{\bullet\} = \sum_{n=-\infty}^{\infty} h(n-2t) \quad (3.53)$$

$$G\{\bullet\} = \sum_{n=-\infty}^{\infty} g(k-2t) \quad (3.54)$$

After j level of decomposition, the original signal $f(t)$ can be expressed as

$$f(t) = \sum_{i=1}^{2^j} f_j^i(t) \quad (3.55)$$

The wavelet packet component signal $f_j^i(t)$ can be expressed by a linear combination of wavelet packet functions $\psi_{j,k}^i(t)$ as follows:

$$f_j^i(t) = \sum_{k=-\infty}^{\infty} c_{j,k}^i \psi_{j,k}^i(t) \quad (3.56)$$

The wavelet packet coefficients $c_{j,k}^i$ can be obtained from

$$c_{j,k}^i = \int_{-\infty}^{\infty} f(t) \psi_{j,k}^i(t) dt \quad (3.57)$$

providing that the wavelet packet functions are orthogonal.

$$\psi_{j,k}^m(t) \psi_{j,k}^n(t) = 0 \quad \text{if } m \neq n \quad (3.58)$$

Figure 3.15 Tree Structure for Wavelet Packet Analysis

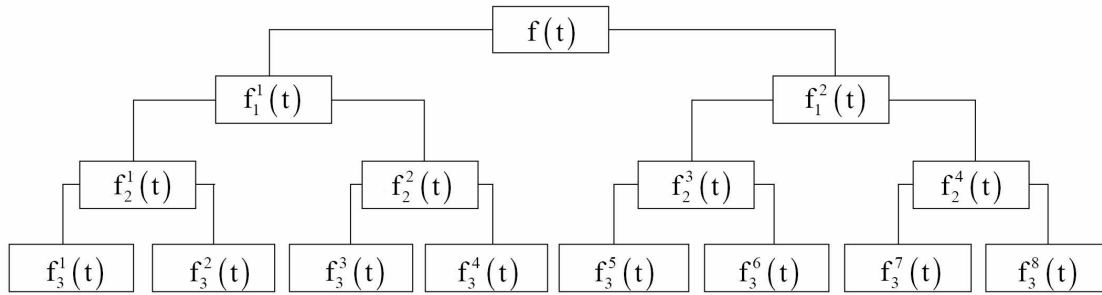
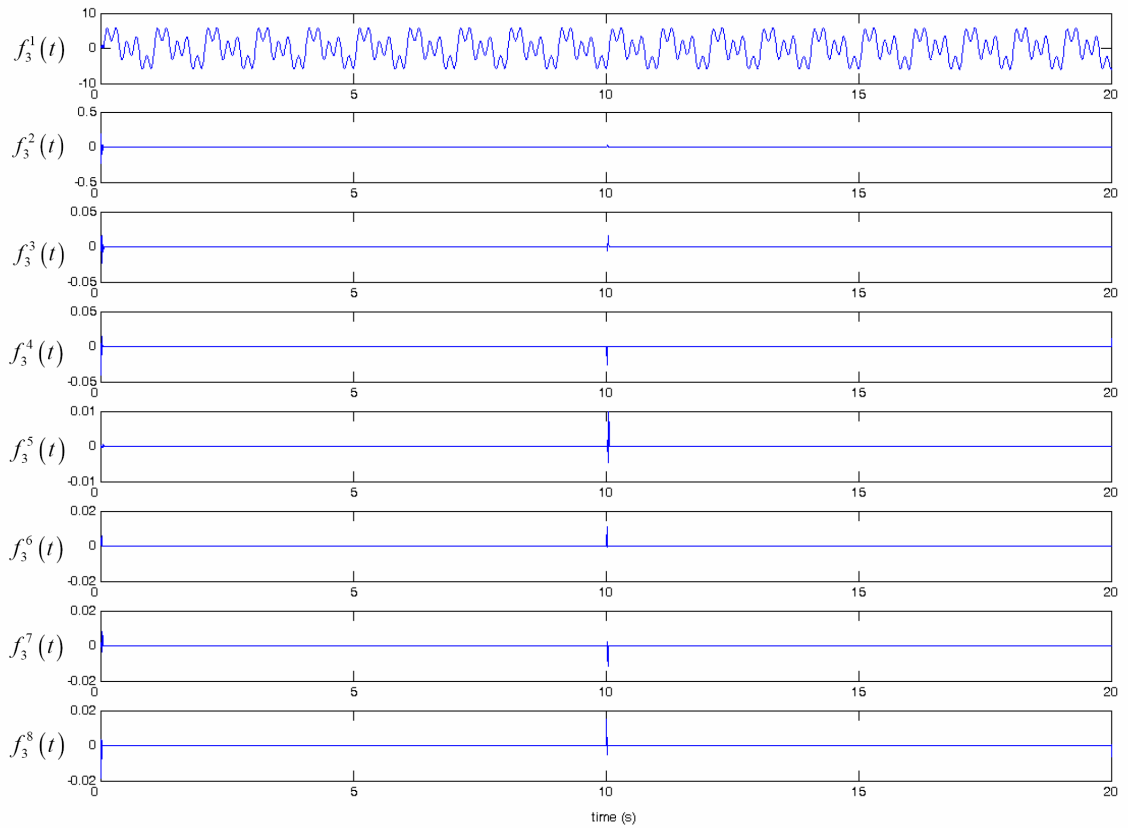


Figure 3.16 Components of the 3rd Level WPT for the Harmonic signal, $f(t)$



For illustration, harmonic signal $f(t)$, defined by Equation 3.16 is decomposed by WPT. Figure 3.16 shows the eight wavelet packet component signals after three levels of wavelet packet decomposition of $f(t)$ using db6 mother wavelet. It can be seen that the sudden shift of the 1 Hz frequency at 10 second is quite visible in the most of the wavelet component signals.

3.3 Pattern Recognition Techniques

A pattern can be a set of features formed in vector or matrix notation. A pattern class is a family of patterns that share a set of common properties. Pattern recognition involves techniques for assigning pattern to their respective class. Given a pattern, its recognition/classification may consist of one of the following two tasks: (1) supervised classification (e.g., discriminant analysis) in which the input pattern is identified as a member of a predefined class; (2) unsupervised classification (e.g., clustering) in which the pattern is assigned to a hitherto unknown class. The unsupervised classification can be applied to patterns not containing examples from the damage structure, but this approach is inherently limited to level one or level two damage classification, which identifies the presence of damage only. When patterns are available from both the undamaged and damaged structure, the supervised classification approach can be taken to move forward to higher level damage identification to classify and quantify damage (Jain et al. 2000).

One of the best known and most efficient approaches to pattern recognition is matching. As a generic operation in pattern recognition, matching is used to determine the similarity between two entities (points, curves, or shapes) of the same type. Pattern matching approach has been widely applied to speech recognition and fingerprint identification in which the pattern to be recognized is matched against the stored template. In this study, the pattern recognition is used to identify the damage location and level simultaneously by best matching the extracted features of the response signal of the structure against feature database while taking into account all possible damage scenarios. Three matching algorithms are used separately to perform “best-matching”. They are: (1) correlation, (2) least square of distance (LSD), and (3) Cosh spectral distance (CSD).

Correlation analysis calculates the correlation coefficient C_{ij} of two patterns (Posenato, et al. 2008). A correlation value of +1 indicates that the two patterns are identical, a correlation value of -1 means that they are diametrically opposite, and a correlation value of 0 means that they are completely different. A closer value to 1 shows a closer match between the two patterns.

$$C_{ij} = \frac{\sum_{k=1}^n (S_i(k) - \bar{S}_i)(S_j(k) - \bar{S}_j)}{\sqrt{\sum_{k=1}^n (S_i(k) - \bar{S}_i)^2} \sqrt{\sum_{k=1}^n (S_j(k) - \bar{S}_j)^2}} \quad (3.59)$$

Least Square Distance (LSD) has been widely applied for system modeling and identification, speech recognition and fingerprint identification. It is defined as

$$d_{ij} = \left(\sum_{k=1}^n \left(S_i(k) - S_j(k) \right)^2 \right)^{\frac{1}{2}} \quad (3.60)$$

The least value shows a closer match and vice-versa.

Cosh Spectral Distance (CSD) gives an indication about the global difference between two patterns (Haritos and Owen, 2004; Owen, 2003; Trendafilov, 2001). It is defined as

$$Co_{ij} = \frac{1}{2n} \sum_{k=1}^n \left(\frac{S_i(k)}{\bar{S}_i} - \log \frac{S_i(k)}{\bar{S}_j} + \frac{S_j(k)}{\bar{S}_j} - \log \frac{S_j(k)}{\bar{S}_i} - 2 \right) \quad (3.61)$$

where n is number of vector points in the pattern; $S_i(k)$ and $S_j(k)$ are the vector values of the patterns i and j at point k ; and \bar{S}_i and \bar{S}_j are the average values of the patterns i and j , respectively.

If i is the unknown-damage feature pattern, and j is a known feature pattern in the database, then the highest correlation coefficient, the lowest LSD coefficient, and the lowest CSD coefficient indicate the most similar pattern in the database which shows the most probable damage level and location for the unknown case.

CHAPTER 4 - PRELIMINARY NUMERICAL STUDY

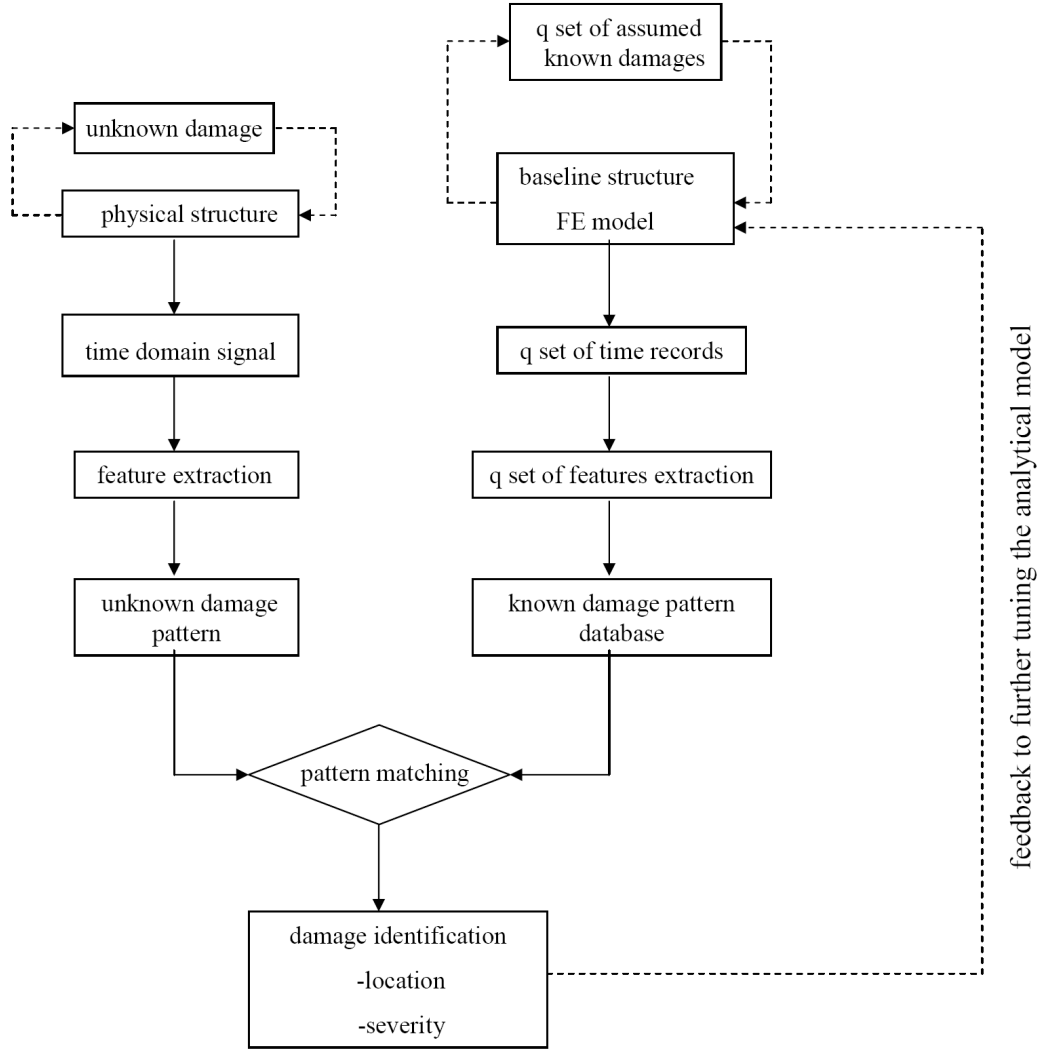
In order to realize structural damage detection using signal-based pattern recognition, it is necessary to obtain in advance the vibration response of structure with different damage scenarios. Because it is nearly impossible to let a practical structure experience all kinds of damage, the structural vibration response data with various possible damages is obtained through numerical simulation (Yam et al. 2003). Figure 4.1 shows the proposed process of pattern recognition method for structural damage detection in this study. It mainly includes five operation stages: (1) numerical simulation of the dynamic response of the structure under different known damage scenarios, (2) signal processing and feature extraction and normalization, (3) damage pattern database construction, (4) signal acquisition on a structure with an unknown damage, and (5) pattern matching to find the most probable damage case from the database which indicates the damage location and severity. For continuous structural monitoring, it is necessary to update the numerical model once damage has been found to accurately represent the physical condition of the structure.

As a preliminary numerical study, a three-story steel structure was initially constructed by a 2-D finite element model. This model was developed by ANSYS to numerically simulate the structural dynamic response without damage, as well as with various possible damages. For demonstration purpose, this model was also used to simulate “unknown” test damage cases on the structure and the associated dynamic response.

4.1 Descriptions of Test Structure and FE Model

A three-story steel structure shown in Figure 4.2(a) was used for this purpose. The structure was 60 in. tall and consisted of 3 floors and 30 columns. The floors were steel plates with dimensions of 26"×20"×2" and the columns were steel flat bars with dimensions of 20"×1"×0.25" .

Figure 4.1 Flowchart of Pattern Recognition



This structure was numerically constructed by ANSYS using a 2-D FE model, as shown in Figure 4.2(b). The ANSYS element type for floors and columns were 2-D elastic beam (beam3). The baseline geometric properties of the structure elements were: floor cross sectional area $A = 40 \text{ in}^2$, moment of inertia $I = 13.333 \text{ in}^4$; column cross sectional area $A = 1.25 \text{ in}^2$, and moment of inertia $I = 6.51 \times 10^{-3} \text{ in}^4$. The material properties of the model were mass density $\rho = 7.345 \times 10^{-4} \frac{\text{lb.s}^2}{\text{in}^4}$, Poisson ratio $\nu = 0.3$, modulus of elasticity $E = 2.9 \times 10^7 \text{ psi}$. The floor was assumed as rigid. The ratio of unit nodal rotation moment of the floor to that of column was more than 1×10^3 (see Appendix A -). All the connections were assumed to be fixed, therefore there were a total of 3 horizontal DOFs in the numerical structure. Figure 4.3 shows

the geometry of the 2-D model in the ANSYS Graphical User Interface (GUI). Figure 4.4 shows the input window of structure element geometry properties (also called real constants).

Figure 4.2 3-D Steel Structure and 2-D FE Model

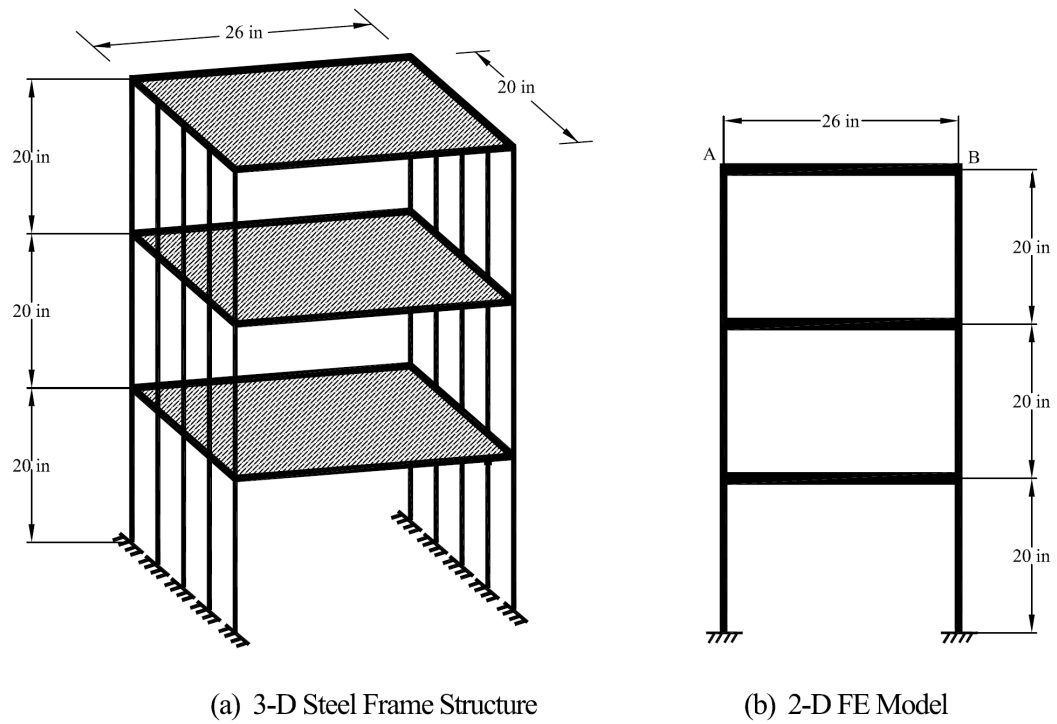


Figure 4.3 2-D Model in ANSYS Graphical User Interface

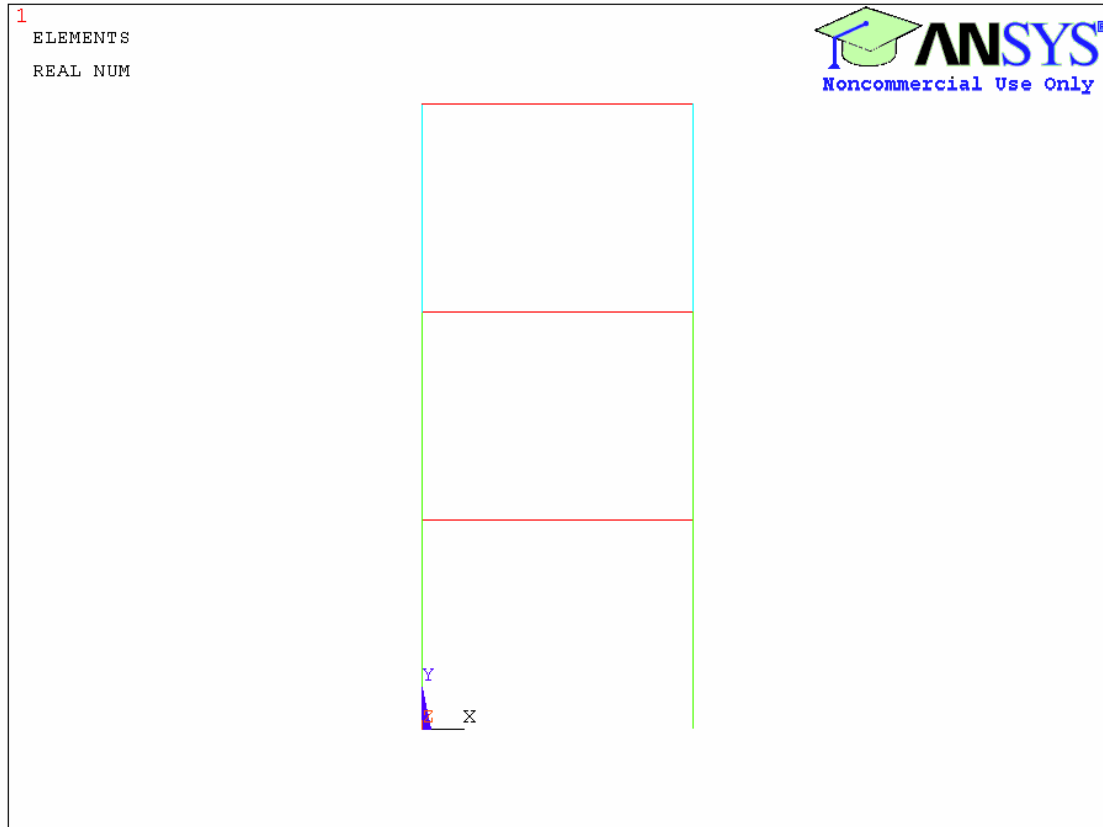


Figure 4.4 Element Geometric Properties (Real Constants) Screen

Property	Value
Element Type Reference No.	1
Real Constant Set No.	2
Cross-sectional area (AREA)	0.525
Area moment of inertia (IZZ)	0.002734
Total beam height (HEIGHT)	0.25
Shear deflection constant (SHEARZ)	0
Initial strain (ISTRN)	0
Added mass/unit length (ADDMA5)	0

The damage was simulated using the baseline FE model with various dynamic properties, i.e. EI, of the damaged components. In order to simplify the problem, various damage cases were introduced by symmetrically reducing the stiffness of columns at different stories to preserve the symmetry of the structure. For instance, the stiffness of the columns at the second story and at the third story was reduced by 40% and 20%, respectively. This damage case was denoted as 0-40-20 in this study.

4.2 Numerical Simulation of the Dynamic Response of the Structure

Transient dynamic analysis (sometimes called time-history analysis) is a technique used by ANSYS to determine the dynamic response of a structure under the action of any general time-dependent load. This type of analysis can be used to determine the time-varying displacements, strains, stresses, and forces in a structure as it responds to any combination of static, transient, and harmonic loads. The basis equation of motion solved by a transient dynamic analysis is

$$[M]\{\ddot{u}\} + [C]\{\dot{u}\} + [K]\{u\} = \{F(t)\} \quad (4.1)$$

where:

$[M]$ = mass matrix

$[C]$ = damping matrix

$[K]$ = stiffness matrix

$\{\ddot{u}\}$ = nodal acceleration vector

$\{\dot{u}\}$ = nodal velocity vector

$\{u\}$ = nodal displacement vector

$\{F(t)\}$ = load vector

The ANSYS program uses the Newmark time integration method to solve the equation at discrete time points. The time increment between successive time points is called the integration time step which determines the accuracy of the transient dynamic solution. The smaller the time step, the higher the accuracy. A time step that is too large will introduce error that affects the response of the higher modes and hence the overall response of the structure. For the Newmark time integration scheme, it has been found that using approximately twenty points per cycle of the highest frequency of interest results in a reasonable accurate solution. That is, if f is the frequency (in cycles/time), the integration time step (ITS) is equal to $\frac{1}{20f}$ (ANSYS).

Alpha damping and *Beta damping* are used to define Rayleigh damping constants α and β . The damping matrix $[C]$ is calculated by using these constants to multiply the mass matrix $[M]$ and stiffness matrix $[K]$:

$$[C] = \alpha[M] + \beta[K] \quad (4.2)$$

The value of α and β are calculated from modal damping ratios, ζ_i . If ω_i is the natural circular frequency of mode i , α and β satisfy the relation

$$\zeta_i = \frac{\alpha}{2} \frac{1}{\omega_i} + \frac{\beta}{2} \omega_i \quad (4.3)$$

In many practical structural problems, alpha damping (or mass damping) may be ignored ($\alpha = 0$). In such cases, β can be evaluated from known values of ζ_i and ω_i , as

$$\beta = \frac{2\zeta_i}{\omega_i} \quad (4.4)$$

only one value of β can be input in a load step, so the most dominant frequency active in that load step was chosen to calculate β .

In this preliminary numerical study, the excitation force on the structure was an impulse force of 50 lb with 0.02 seconds duration acting at node *A* (see Figure 4.2(b)). Transient dynamic analysis was performed by ANSYS to determine the dynamic response at node *B* (see Figure 4.2(b)) under such a step impulse load. The impulse load was defined using load steps (L.S). The time history curve in Figure 4.5 shows the load steps and time steps of the applied impulse force. Load and time at the end of load segment in each load step were defined in the *ANSYS windows of apply F/M on nodes* (see Figure 4.6) and *time and time step options* (see Figure 4.7), respectively. To determine the time step size, a preliminary modal analysis was conducted on this structure to calculate the modal frequencies. Since the highest frequency was 7.809Hz for baseline structure (see Appendix), the time step size should be smaller than 0.006 seconds ($\frac{1}{20f} = \frac{1}{20 \times 7.809} = 0.006$). The value of 0.004 was chosen as the time step size (equal to 250 Hz sampling frequency) and entered at the time step size box in Figure 4.7. Each defined load step was written and saved in a file (see Figure 4.8) and then solved by ANSYS. When specifying the damping in the transient analysis of the structure, the damping value β in all load step files will be changed to a certain value to meet specified damping ratio, ζ , according to the Equation 4.4. These new load step files will need to be re-executed by ANSYS.

The dynamic response of a certain node was viewed in *TimeHist Postprocessing* from the ANSYS main menu. Node *B* and its translation nodal DOF result were selected in the *Add Time-History Variable* window (see Figure 4.9) and defined in the *Define Nodal Data* dialog box (see Figure 4.10). The translation velocity and acceleration results of node *B* were the first and second derivative of the corresponding translation displacement result at node *B*, respectively which were defined in the *Derivative of Time-History Variables* window (see Figure 4.11). All of the time-history results of node *B* can be inquired and graphed in the *Time History Variables* window (see Figure 4.12). For illustration, Figure 4.13 shows the numerical acceleration result for structure under baseline condition.

Figure 4.5 Load Steps and Time Steps

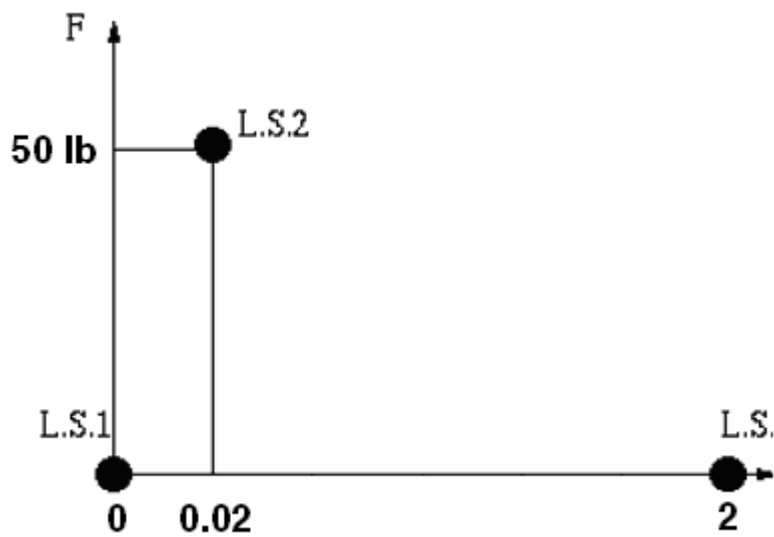


Figure 4.6 Apply F/M on Nodes Window

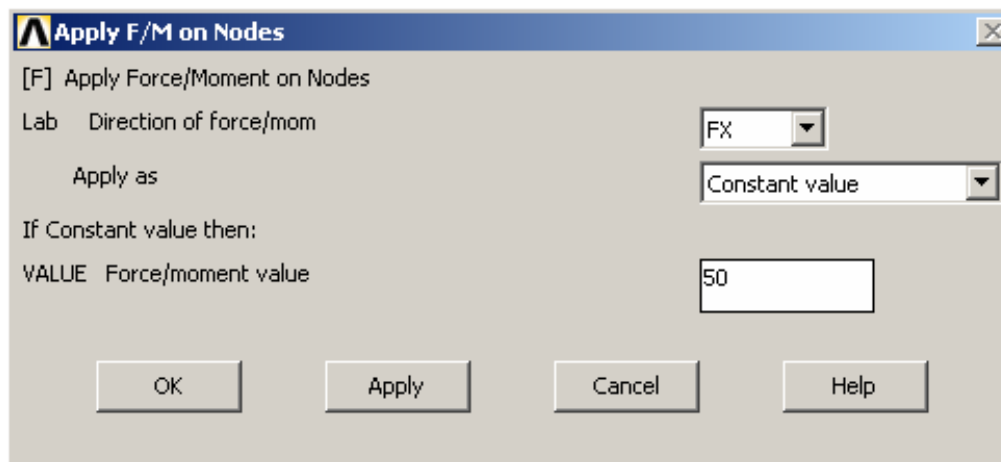
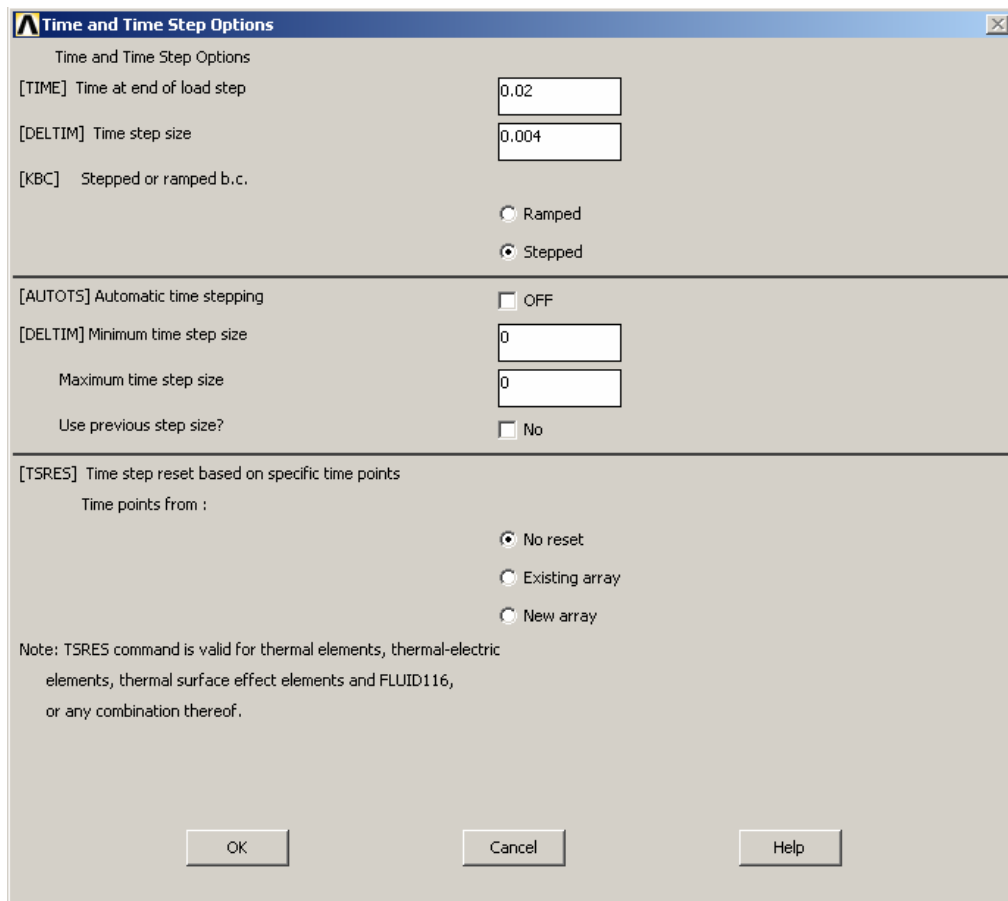


Figure 4.7 Time and Time Steps Options Window



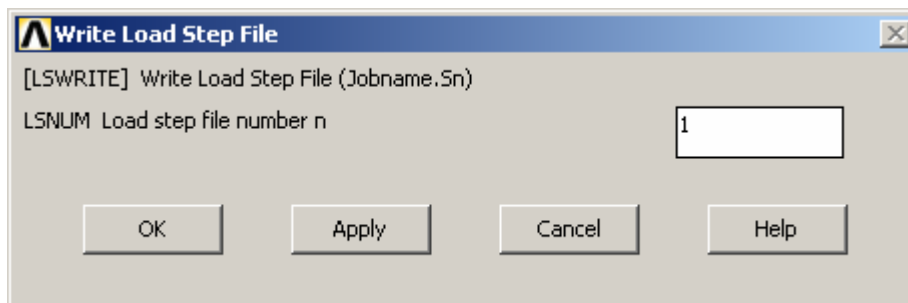
The dialog box is titled "Time and Time Step Options" and contains the following settings:

- Time and Time Step Options**
 - [TIME] Time at end of load step: 0.02
 - [DELTIM] Time step size: 0.004
 - [KBC] Stepped or ramped b.c.:
 - ☐ Ramped
 - ☒ Stepped
- Automatic time stepping**
 - [AUTOTS] Automatic time stepping: ☐ OFF
 - [DELTIM] Minimum time step size: 0
 - Maximum time step size: 0
 - Use previous step size?: ☐ No
- Time step reset based on specific time points**
 - Time points from :
 - ☒ No reset
 - ☐ Existing array
 - ☐ New array

Note: TSRES command is valid for thermal elements, thermal-electric elements, thermal surface effect elements and FLUID116, or any combination thereof.

Buttons: OK, Cancel, Help

Figure 4.8 Write Load Step File Window



The dialog box is titled "Write Load Step File" and contains the following settings:

- [LSWRITE] Write Load Step File (Jobname.Sn)
- LSNUM Load step file number n: 1

Buttons: OK, Apply, Cancel, Help

Figure 4.9 Add Time-History Variable Window

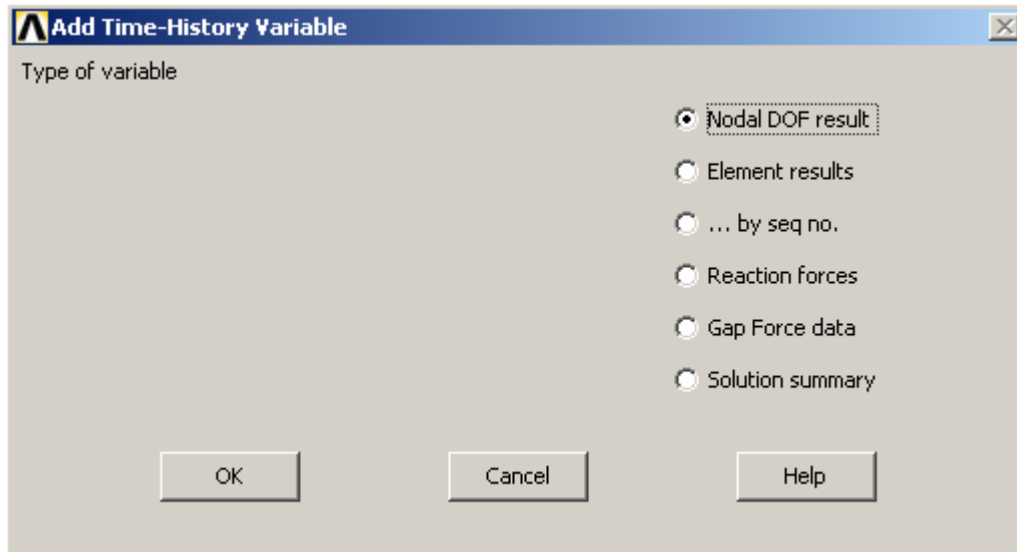


Figure 4.10 Define Nodal Data Window

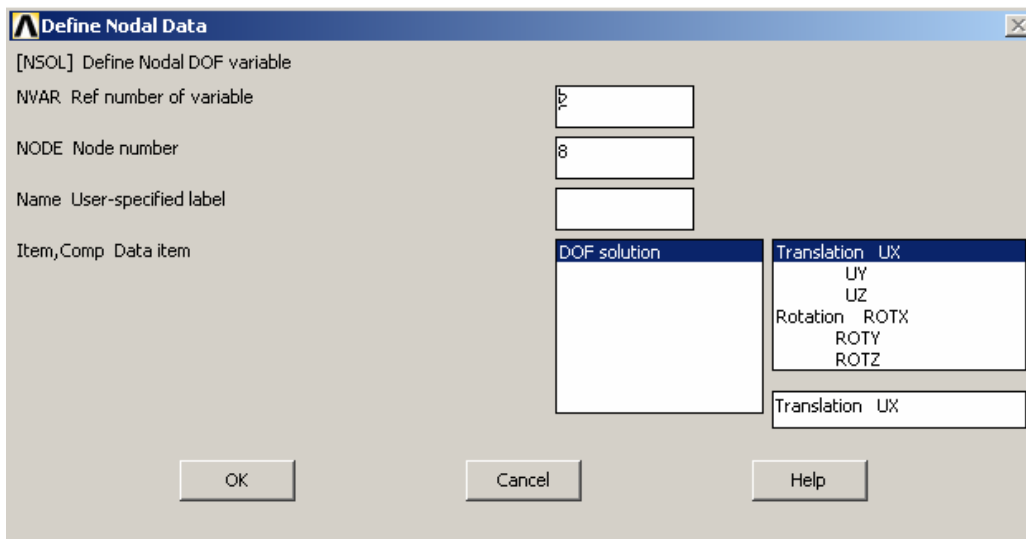



Figure 4.11 Derivative of Time-History Variables Window

 Derivative of Time-History Variables

[DERIV] $IR = FACTA * d(IY)/(d(IX))$

IR Reference number for result

3

FACTA Factor

1

IY 1st Variable

2

IX 2nd Variable

1

Name User-specified label

OK

Apply








Cancel

Help

Figure 4.12 Time History Variables Window

Time History Variables - .\file.rdsp

File Help



Real

Variable List

Name	Element	Node	Result Item	Minimum	Maximum	X-Axis
TIME			Time	0	2	<input checked="" type="radio"/>
UX		8	X-Component of displacement	-0.0748553	0.0741148	<input type="radio"/>
3			Calculated	-1.15594	1.25265	<input type="radio"/>
4			Calculated	-25.3821	62.2478	<input type="radio"/>

Calculator

=

(

)

MIN

CONJ

e^x

MAX

a+ib

LN

7

8

9

/

CLEAR

RCL

STO

RESP

LOG

4

5

6

*

←

INS MEM

SQRT

ABS

ATAN

x^2

1

2

3

-

ENTER

INT1

IMAG

INV

DERIV

REAL

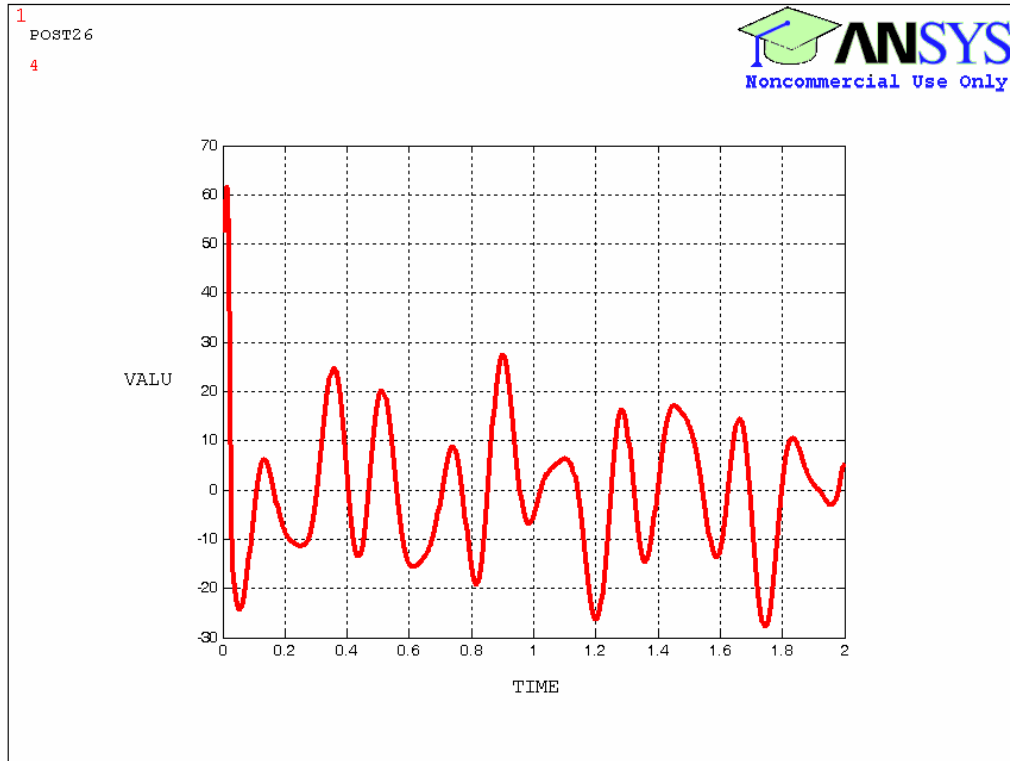
0

.

+

70

Figure 4.13 Acceleration Signal for Baseline Condition (Damage Case 0-0-0)



4.3 Signal Processing and Feature Extraction and Normalization

The purpose of signal processing and feature extraction is to reduce the raw data and extract features of the signal that can be used for identification of the structural condition, hence, damage detection. Feature normalization is a procedure to “normalize” feature sets so that feature changes caused by operational and environmental variations of the system can be separated from structural changes of interest. In a preliminary effort, frequency-based features were extracted by FFT. Figure 4.14(a), (b), (c) and (d) show the FFT spectrums of acceleration signals of the structure under damage cases 0-0-0, 20-40-60, 60-20-40 and 60-60-60, respectively. The frequencies and magnitudes corresponding to the three peaks in each of the FFT spectrums are listed in Table 4.1. It shows that due to different damage cases, the peak magnitude changes are more sensitive than the peak frequency shifts. The FFT magnitude vectors in frequency domain were selected as the sensitive features which also preserved the information of frequency shifting. Such a set of vectors formed a one-dimension pattern to

present a unique damage condition. Each magnitude vector in a pattern was normalized with respect to the square root of the sum of squares of each one in the pattern.

Figure 4.14 FFT Spectrums for Different Damage Case: (a) Damage Case 0-0-0 (Baseline Condition), (b) Damage Case 20-40-60, (c) Damage Case 60-20-40, (d) Damage Case 60-60-60

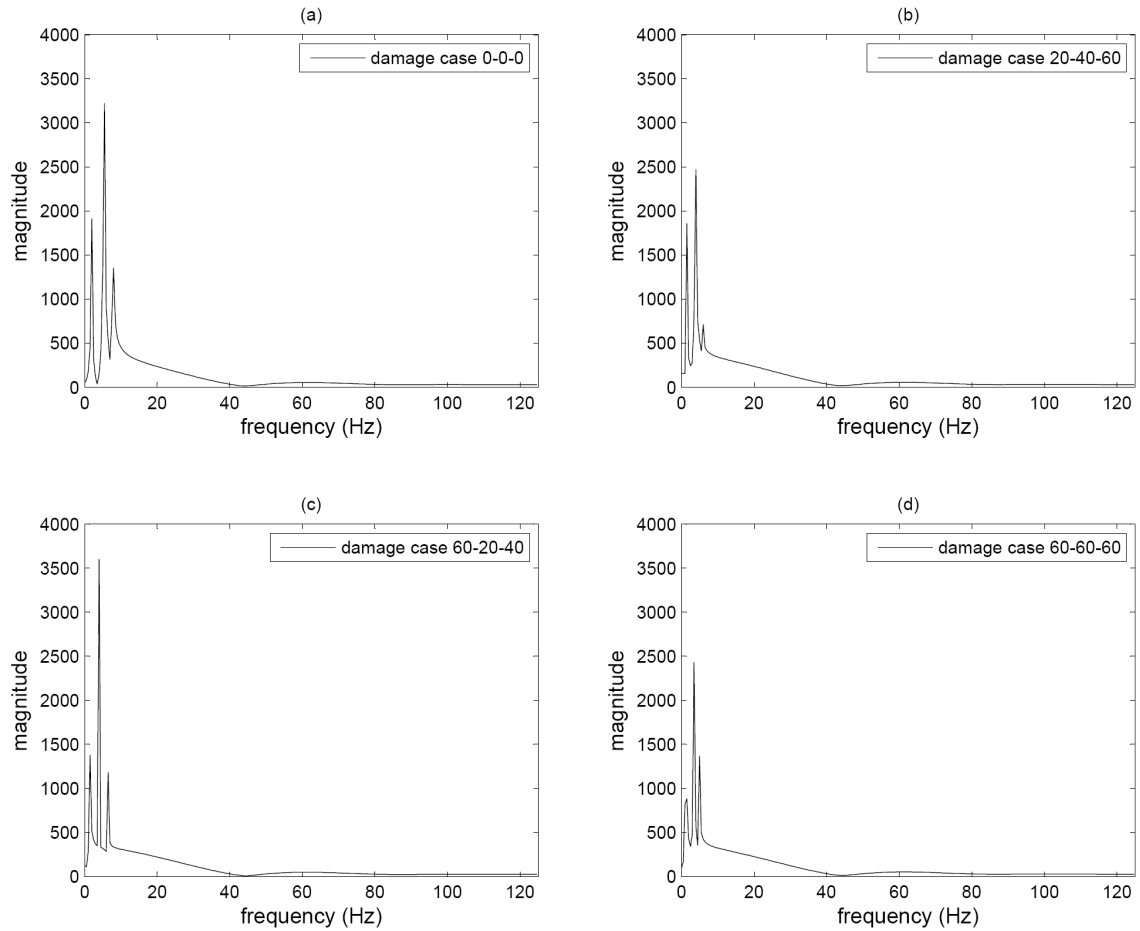
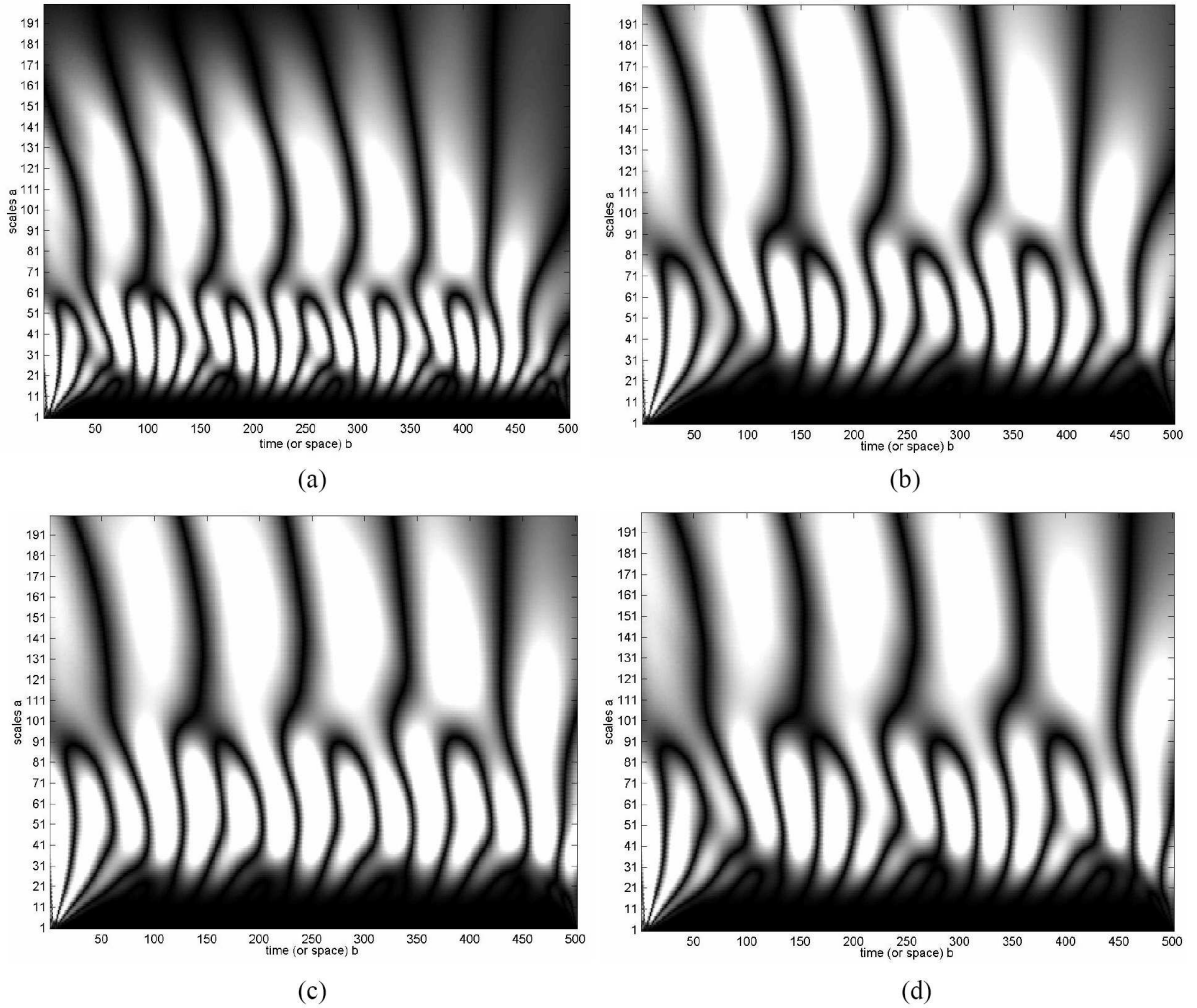


Table 4.1 Peak Values on the FFT Spectrums

Damage Case	Peak 1		Peak 2		Peak 3	
	frequency (Hz)	magnitude	frequency (Hz)	magnitude	frequency (Hz)	magnitude
0-0-0	1.996	1911.9	5.489	3220.8	7.984	1351.7
20-40-60	1.497	1858	3.992	2468.5	5.988	709.95
60-20-40	1.497	1376.3	3.992	3601.2	6.487	1181.9
60-60-60	1.497	882.4	3.493	2429.4	4.990	1366.1

At the second phase of the preliminary numerical study, time-frequency-based features were extracted by CWT. The db6 wavelet was used as the mother wavelet. The acceleration signal was decomposed by CWT and the extracted features were time-scale-based CWT coefficients. For example, Figure 4.15(a), (b), (c) and (d) show the CWT coefficients contours of acceleration signals of the structure under the selected damage cases. The value of the “*scale a*” was proportional to the reciprocal of the frequency, and “*time b*” was the moment of the wavelet along the time axis. Lighter shading in the contour indicates a higher wavelet coefficient value. Comparison of the four figures shows that the time-frequency-based CWT coefficients are sensitive to different damage cases. Such a set of coefficient vectors formed a two-dimensional pattern which presented a unique condition for a damage case. Each coefficient vector in a pattern was also normalized with respect to the square root of the sum of squares of the corresponding pattern.

Figure 4.15 CWT Contours for Different Damage Cases: (a) Damage Case 0-0-0 (Baseline Condition), (b) Damage Case 40-60-60, (c) Damage Case 60-40-60, (d) Damage Case 60-60-60

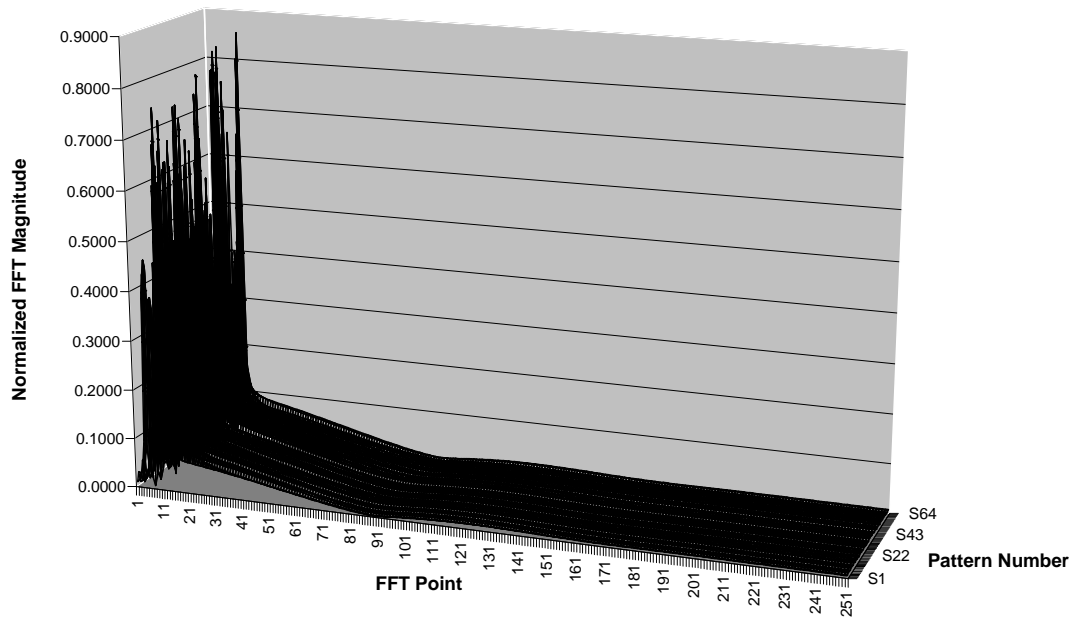


4.4 Damage Pattern Database Construction

As mentioned earlier, different damage levels and locations were numerically simulated by changing the properties of the baseline 2-D FE model of the structure, i.e. EI, of the damaged components. For demonstration purpose, the damage level was set on a scale of 0 to 60% with increments of 20% at different locations. A total of 64 sets of known damage cases, including the baseline condition, were selected to represent the possible structural damage conditions (level and location) for the sample structure. All the 64 sets of simulated acceleration response were transformed by FFT and CWT into FFT magnitude vectors and CWT coefficient matrices,

respectively. The resulting 64 sets of normalized FFT magnitude vectors and 64 sets of CWT coefficient matrices form the representative known damage feature patterns in the database individually. The three-dimensional graph of the FFT pattern database is shown in Figure 4.16

Figure 4.16 FFT Pattern Database 3-D Graph



4.5 Case Studies and Pattern Matching

In order to demonstrate the applicability of the proposed method, twenty damage cases slightly different from identical cases in the database were numerically simulated by changing the baseline 2-D FE model, and the corresponding dynamic response under the impulse excitation was also numerically generated by ANSYS. These test cases listed in Table 4.2 were grouped into four kinds of damage categories: single damage location (G1), multiple damage locations (G2), multiple damage locations and severities (G3), and high damage severity (G4). Gaussian white noise was added to the generated acceleration signals of the test cases to simulate the condition of signal contaminated with noise. The noise intensity is defined by the signal-to-noise ratio (SNR):

$$SNR(\text{db}) = 20 \log_{10} \frac{A_s}{A_N} \quad (4.5)$$

where A_s and A_N are the root-mean-square (RMS) value of the acceleration signal and the noise respectively. The signal-to-noise ratio (SNR) was chosen as 5 dB. The damping ratio (ζ) was chosen as 2% when generating the structure dynamic response with damping.

Table 4.3 shows the signal properties of some test cases. As an example, Figure 4.17 shows the generated acceleration signals for damage case 0-38-38 under the damping and noise environmental conditions.

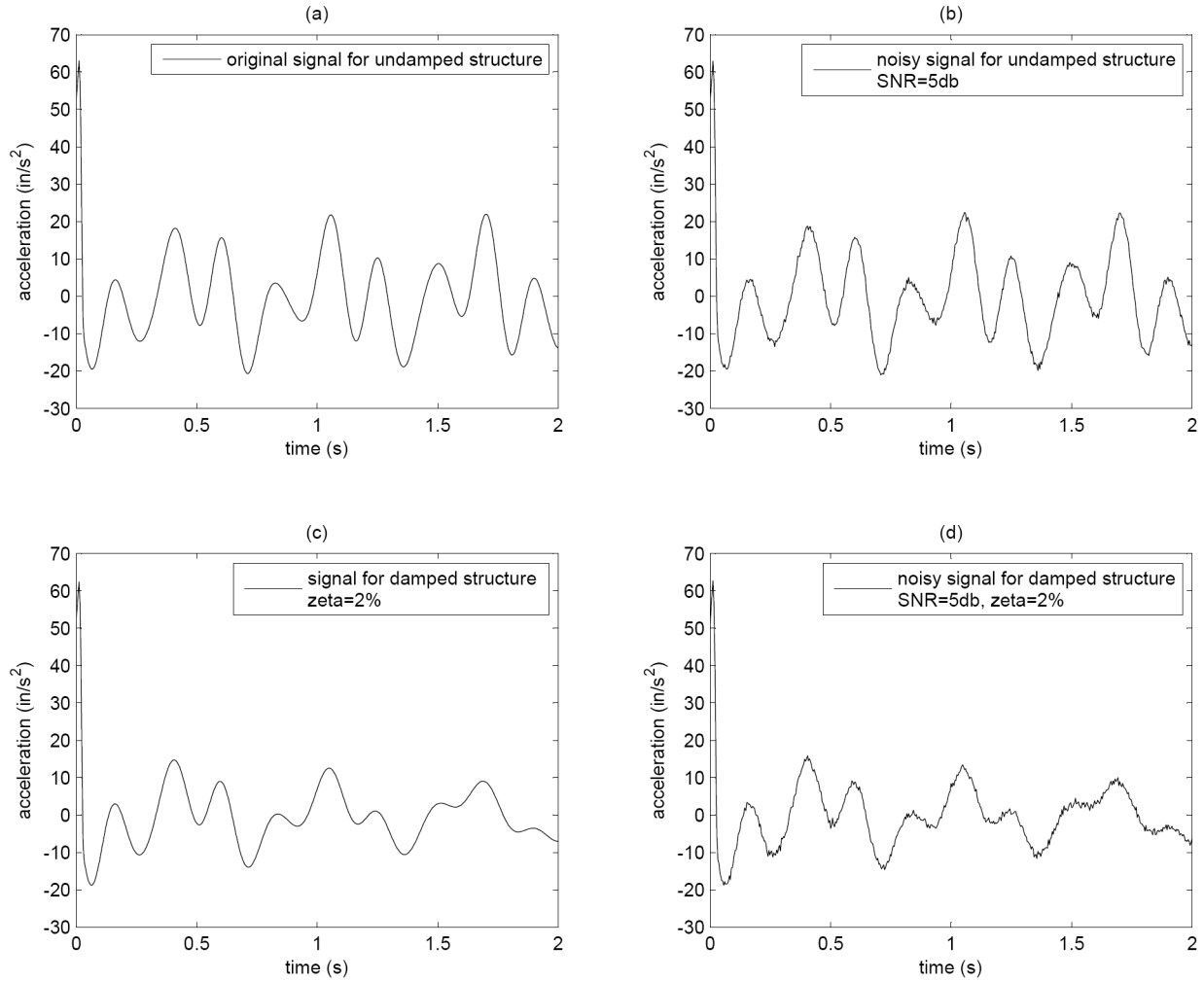
Table 4.2 Numerical Test Cases

single damage location (G1)	multiple damage locations (G2)	multiple damage locations & severities (G3)	highest damage severity (G4)
0-0-19	0-38-38	19-38-58	0-58-58
0-19-0	38-0-38	19-58-38	58-0-58
19-0-0	0-38-38	38-19-58	58-58-0
0-0-58	38-0-38	38-58-19	58-58-58
0-58-0		58-19-38	
58-0-0		58-38-19	

Table 4.3 Signal Properties

Damage Case		Displacement		Velocity		Acceleration	
		min	max	min	max	min	max
no damping	0-19-0	-0.0720	0.0699	-1.1211	1.2030	-24.3836	63.3905
	19-0-0	-0.0716	0.0694	-1.1856	1.1837	-28.3270	63.3905
	0-0-19	-0.0749	0.0743	-1.1530	1.2674	-25.7285	63.6380
	58-38-19	-0.0848	0.0823	-1.1788	1.2061	-22.7577	63.6381
	38-19-58	-0.1003	0.0960	-1.1553	1.2535	-18.5389	64.1505
	58-0-58	-0.0978	0.1045	-1.2639	1.2535	-19.9688	64.1506
	58-58-58	-0.1086	0.1123	-1.1608	1.2535	-17.8047	64.1506
Damping $\zeta=2\%$	0-19-0	-0.0556	0.0530	-0.8550	1.1622	-23.1592	63.0510
	19-0-0	-0.0537	0.0532	-0.9587	1.1622	-23.3039	63.0510
	0-0-19	-0.0636	0.0627	-0.9878	1.1879	-21.4090	63.3615
	58-38-19	-0.0678	0.0680	-0.9831	1.1880	-21.1116	63.3618
	38-19-58	-0.0910	0.0830	-1.0194	1.2433	-16.1213	64.0047
	58-0-58	-0.0898	0.0893	-1.0665	1.2433	-16.2771	64.0047
	58-58-58	-0.0908	0.0892	-0.9928	1.2433	-15.7636	64.0048

Figure 4.17 Acceleration Signals for Damage Case 0-38-38



As examples to show the test results, Figure B.1 to Figure B.4 show the FFT pattern correlation matching results for the test damage case 19-0-0, 0-38-38, 58-38-19 and 58-58-58 under four environmental conditions, respectively. The highest correlation value corresponds to the most similar pattern in the database. In Figure B.1, the highest correlation value for each environmental condition was achieved for pattern 20-0-0 (damage condition: 20-0-0) in the FFT pattern database, correctly detected the closest damage case in the database. The similar correlation matching results can also be found in Figure B.2, Figure B.3, and Figure B.4

Figure B.5 to Figure B.10 show the FFT pattern least square distance (LSD) matching results for the test damage case 19-0-0, 0-38-38, 58-38-19 and 58-58-58 under four different environmental conditions, respectively. The lowest LSD value corresponds to the most similar pattern in the database. In Figure B.5 and Figure B.6, the lowest LSD values for each

environmental condition were achieved for pattern 20-0-0 (damage condition: 20-0-0) and pattern 0-40-40 (damage condition: 0-40-40) in the FFT pattern database, respectively. These matching results correctly detected the closest damage cases in the database which indicated the damage locations and levels. In Figure B.7 and Figure B.8, the lowest LSD values for environmental conditions of damping and damping & noise were achieved for pattern 40-20-40 (damage condition: 40-20-40) and pattern 40-60-60 (damage condition: 40-60-60) in the FFT pattern database, respectively. These matching results failed to indicate the closet damage locations and level in the database.

Figure B.9 to Figure B.12 show the FFT pattern Cosh spectral distance (CSD) matching results for the test damage case 19-0-0, 0-38-38, 58-38-19 and 58-58-58 under four different environmental conditions, respectively. The lowest CSD value corresponds to the most similar pattern in the database. In Figure B.9 and Figure B.10 the lowest CSD values for each environmental condition were achieved for pattern 20-0-0 (damage condition: 20-0-0) and pattern 0-40-40 (damage condition: 0-40-40) in the FFT pattern database, respectively. These matching results correctly indicated the closest damage cases in the database which indicated the damage locations and levels. In Figure B.11 and Figure B.12, the lowest CSD values: for environmental conditions of none and noise were achieved for pattern 60-20-40 (damage condition: 60-20-40) and pattern 60-40-60 (damage condition: 60-40-60) in the FFT pattern database, respectively; and for environmental conditions of damping and damping & noise were achieved for pattern 40-0-40 (damage condition: 40-0-40) and pattern 20-0-60 (damage condition: 20-0-60) in the FFT pattern database, respectively. These matching results failed to indicate the closet damage locations and level in the database.

Similar as FFT pattern matching, Figure B.13 to Figure B.24 show the CWT pattern matching results for the test damage case 19-0-0, 0-38-38, 58-38-19 and 58-58-58 under four environmental conditions by using correlation, LSD and CSD matching algorithms.

Table 4.4 shows the FFT and CWT pattern matching results for all the test cases by using the three different matching algorithms. The results show that correlation algorithm can best perform pattern matching to identify the damage case even when the signal is highly contaminated with noise and structure has a damping slightly different from the damping used in the database.

Table 4.4 FFT and CWT Pattern Recognition Results

Environmental condition	Damage condition	FFT Matching Correctness			CWT Matching Correctness		
		Correlation	LSD	CSD	Correlation	LSD	CSD
None	G1	6/6	6/6	3/6	6/6	6/6	3/6
	G2	4/4	4/4	4/4	4/4	4/4	0/4
	G3	6/6	6/6	0/6	6/6	6/6	0/6
	G4	4/4	4/4	0/4	4/4	4/4	0/4
Noise Only	G1	6/6	6/6	3/6	6/6	6/6	3/6
	G2	4/4	4/4	4/4	4/4	4/4	0/4
	G3	6/6	6/6	0/6	6/6	6/6	0/6
	G4	4/4	4/4	0/4	4/4	4/4	0/4
Damping Only	G1	6/6	6/6	3/6	6/6	6/6	0/6
	G2	4/4	4/4	4/4	4/4	4/4	0/4
	G3	6/6	1/6	0/6	6/6	6/6	0/6
	G4	4/4	0/4	0/4	4/4	4/4	0/4
Damping & Noise	G1	6/6	6/6	3/6	6/6	6/6	0/6
	G2	4/4	4/4	4/4	4/4	4/4	0/4
	G3	6/6	1/6	0/6	6/6	6/6	0/6
	G4	4/4	0/4	0/4	4/4	4/4	0/4

4.6 Discussion on Preliminarily numerical Study

The structure under different damage scenarios shows unique patterns that are formed by frequency magnitudes in frequency domain. It also preserves the information of frequency shifting. These patterns were successfully used as sensitive features for damage detection. Continuous wavelet coefficients show the changes in both frequency and time domain. The patterns formed by these coefficients were also successfully used as sensitive features. Pattern-matching method with the two types of sensitive features has been proved to be an efficient tool to detect damage level and location with more accuracy.

CHAPTER 5 - EXPERIMENTAL TEST AND VERIFICATION

Following the successful initial numerical study, which was conducted on a 2-D simulation of a three-story structure, the work progressed into the experimental verification phase. At this phase, a three-story steel structure was experimentally constructed. An impulse applicator was developed to simulate a consistent impulse load on the experimental structure. A wireless data acquisition system was used to sample and record the vibration response of the structure under impulse load excitation. An experimentally-tuned 3-D finite element model of the structure was developed using ANSYS to numerically simulate the structural dynamic response without damage, as well as with various possible damages excited by an impulse load. Structural vibration signals from numerical simulations and experimental measurements were then decomposed by fast Fourier transform or continuous Wavelet transform for feature extraction. The normalized signal features from numerical simulations generated for the baseline (healthy) structure, as well as with various possible damages were collected into a damage pattern database. The normalized signal features of the experimental measurement for an unknown damage case, was then compared against this database to detect the most probable damage case, using three different pattern matching algorithms separately: (1) correlation, (2) least square distance, and (3) Cosh spectral distance. Twenty-eight damage cases were experimentally simulated on the structure as “unknown” damage to demonstrate the validity and accuracy of the proposed damage detection method.

In addition, Wavelet Packet Transform (WPT) was also investigated for feature extraction and pattern recognition. The db6 wavelet was used as the mother wavelet for CWT feature extraction. Meanwhile, the choice of wavelet functions was also discussed.

5.1 Design and Construction of the Representative Test Structure

To simplify the experimental demonstration, a small simple structure was designed and constructed. The structure took two theoretical assumptions: 1) the rigid floor; 2) the rigid connections. As shown in Figure 5.1, the structure was 36 inches tall and consisted of 3 floors (steel slabs) and 30 columns (steel flat bars). Each floor was supported on ten columns. The

steel was cold rolled steel. The clear height for each story was 12 inches. The dimensions, weights and amount of the steel slabs and the flat bars are listed in Table 5.1. The dimensions of the slabs and flat bars on the structure satisfied stability requirements and rigid floor theoretical assumption (see Appendix C -).

Figure 5.1 Test Three-Story Steel Structure

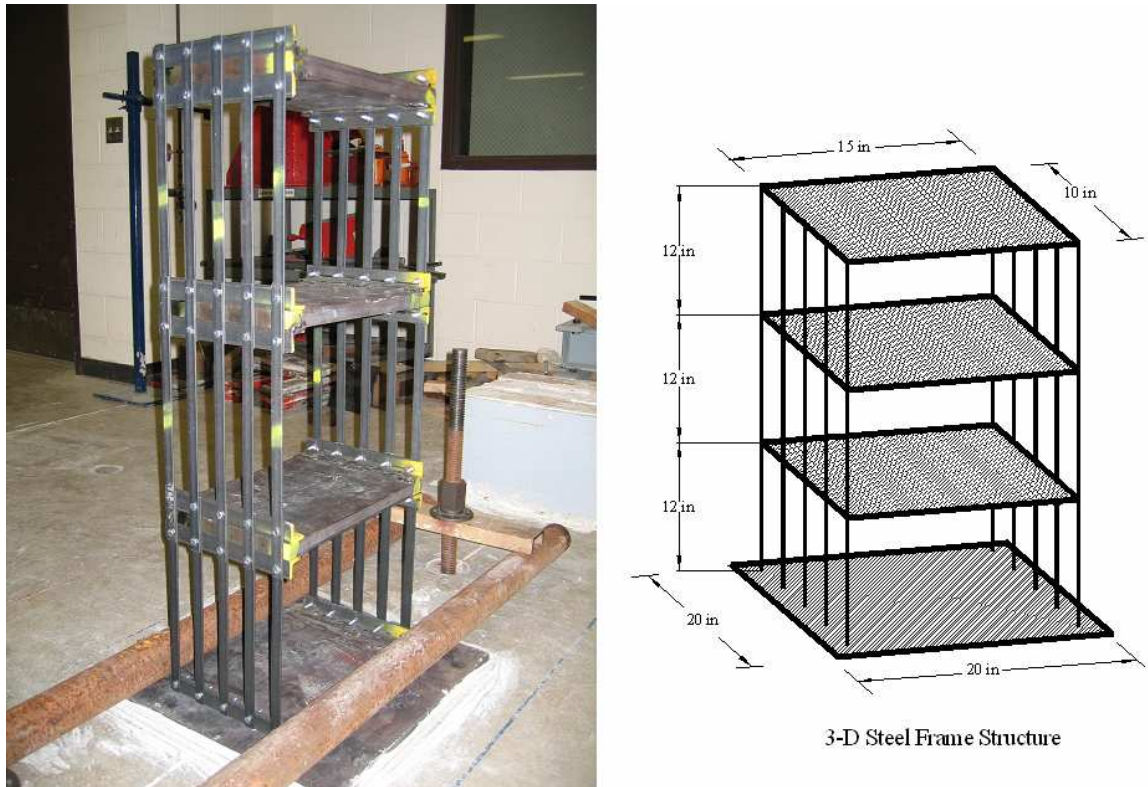


Table 5.1 Dimensions, Weights and Amount of Structure Components

Component	Dimensions Height \times Width (in \times in)	Thickness (in)	Weight (lb/piece)	Amount	Location
Steel Slab (Floor)	10 \times 15	1	42.6	3	1-3 floor
	20 \times 20	1	114	1	foundation
Steel Flat Bar (Column)	16.5 \times 0.75	0.125	0.319	20	2 nd & 3 rd floor
	14.25 \times 0.75	0.125	0.319	10	1 st floor

For easy removal of the columns from the structure and easy replacement of the columns for different damage scenario simulation, bolts were used to connect the steel slab and the steel flat bar. To make the rigid connection between the steel slab and the steel flat column, four pieces of steel angles ($\frac{1}{4} \times 1 \frac{1}{4} \times 1 \frac{1}{4}$; length: 10 inches) were welded on the two faces of the short edges of the floor plates (see Figure 5.2 and Figure 5.3); and two pieces of steel angles ($\frac{1}{4} \times 1 \frac{1}{4} \times 1 \frac{1}{4}$; length: 10 inches) were welded on the top face and on the short edges of the foundation slab. A total of fourteen pieces of steel angles were used. The columns were connected to the angles vertical legs using four bolts ($\frac{1}{4}$; Grade: 5). To prevent rotation and drift, the foundation slab was fixed to the ground by using hydrocal plaster and also two steel pipes (see Figure 5.4).

Figure 5.2 Slab and Flat Bar Connection



Figure 5.3 Slab and Flat Bar Connection



Figure 5.4 Foundation Slab Fixing



5.2 Impulse Applicator

To apply a consistent impulse force on the structure, a steel ball with a diameter of 1.75 inches and a mass of $1.546 \times 10^{-3} \text{ lb.s}^2/\text{in}$ was used. As shown in Figure 5.5, the steel ball was magnetically adhered to the top of a frame. It was tied by a 20.5 inches chain to this frame so that when the magnet was turned off, the ball dropped 20.5 inches traveling on a circular path to its lowest position, where it hit the third floor slab and then bounced off the structure to create an impulse force on the structure.

The impact was mostly elastic; however, since the response was normalized, the impulse magnitude did not affect the recognition process as long as it did not push the structure into non-linear response range. This fact was demonstrated by investigating the FFT feature patterns of the structural acceleration response signals caused by two different impulse forces (see Figure 5.6) applied on the structure separately. The acceleration signals caused by the two different levels of excitation are shown in Figure 5.7. By transforming the two signals into FFT spectrums, it was found that the relative low level impulse force only caused relative low magnitude in the FFT pattern but it did not affect the pattern's shape. After normalizing the two patterns, it resulted in the exactly same two patterns (see Figure 5.8). The correlation coefficient for such two patterns was 0.97. The impulse force magnitude did not affect the FFT pattern's shape as long as the force did not push the structure into non-linear range. The same result can also be found in Figure 5.9. The normalized CWT contours of structure response under low and high impulse force excitation were exactly the same. The correlation coefficient for such two contours was 0.96. The data normalization procedure eliminated the changes in the pattern caused by impulse magnitude variability. Thus there was no need to measure the impulse magnitude. The swing ball system in Figure 5.6(Left) was used to apply the impulse force during this experimental study.

Figure 5.5 Close View of Magnetic Base, Ball, Chain and Frame



Figure 5.6 [Left] Relative High level Impulse Force Applicator; [Right] Relative low level Impulse Force Applicator



Figure 5.7 Structure Acceleration Signals Caused by Two Different Level Excitations

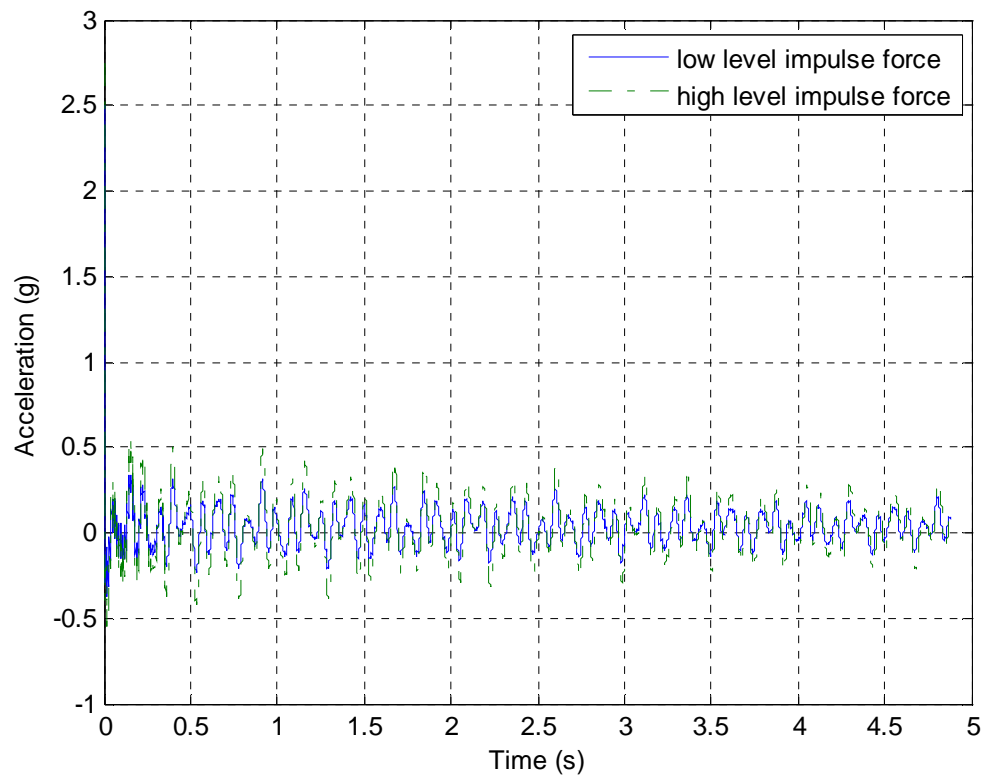


Figure 5.8 Normalized FFT Spectrums of Structure Accelerations by Two Different Level Impulse Excitations

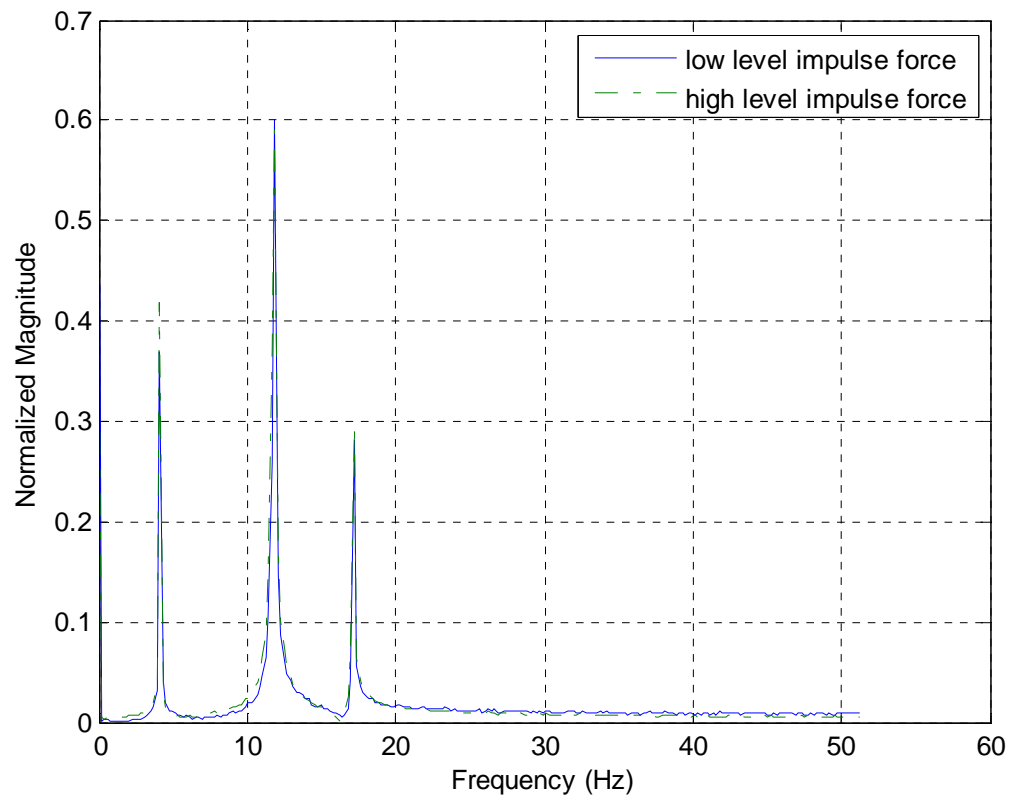
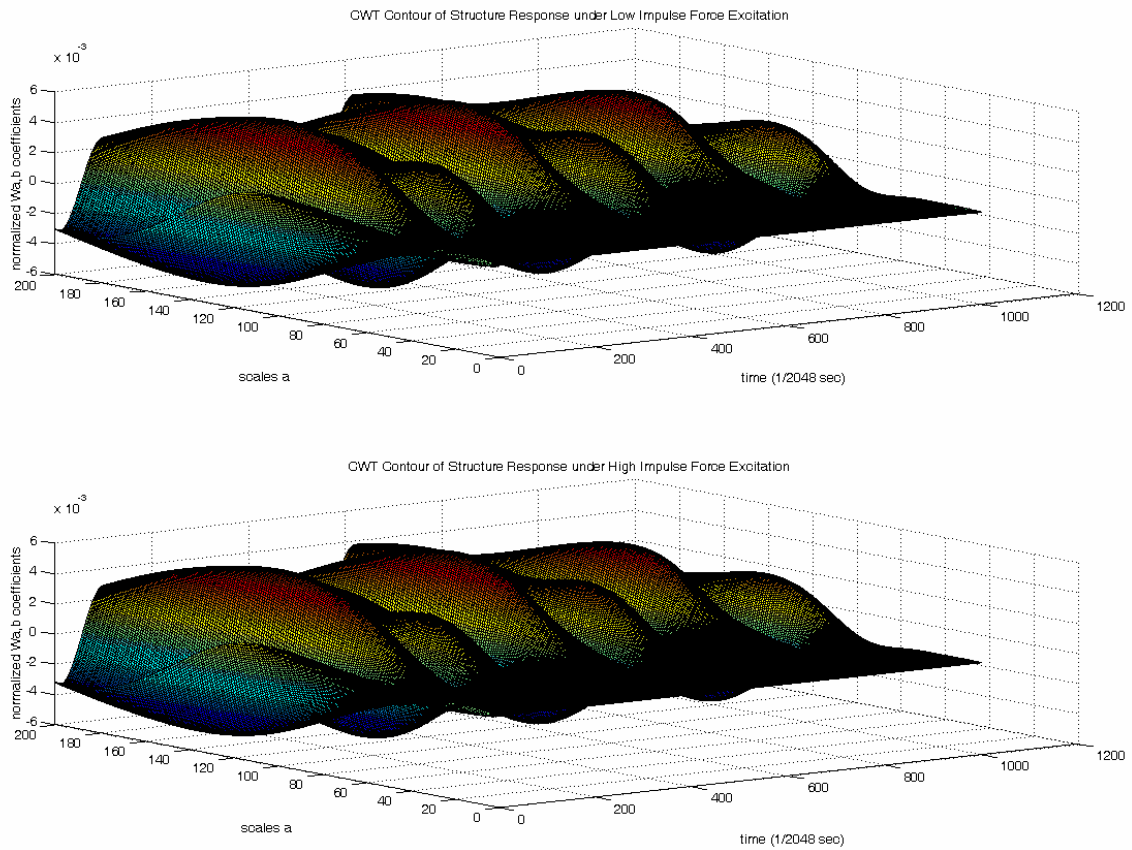


Figure 5.9 Normalized CWT Contours of Structure Response under Different Level Impulse Excitations



5.3 Sensor and Data Acquisition System

5.3.1 Accelerometer

The accelerometer used in the experimental test was MicroStrain, Inc.'s $\pm 2g$ G-Link. It has an integral tri-axial accelerometer built onto the board. The full scale range is approximately $\pm 2g$. The physical axis orientation for each accelerometer channel is indicated in the Figure 5.10. G-Link is a complete wireless measurement system that transmits data on a continuous basis for a fixed period of time. In addition, G-Link has the capability to datalog sensor or voltage data to onboard nonvolatile memory. Part of the G-Link's specification is listed in Table 5.2.

Figure 5.10 G-Link and Its Physical Axis Orientation



Table 5.2 G-Link Specifications

On-board acceleration	Triaxial MEMs accelerometers, Analog Devices ADXL202
Accelerometer range	± 2 g
Measurement Accuracy	10mg
resolution	200 μ g (data sample resolution 12bit)
Analog to digital (A/D) converter	Successive approximation type, 12 bit resolution
Data storage capacity	2 megabytes (approximately 1,000,000 data points)
Data logging mode	Log up to 1,000,000 data points (from 100 to 65,500 samples or continuous) at 32 Hz to 2048 Hz
Sensor event driven trigger	Commence data logging when threshold exceeded
Dimensions	58mm \times 43mm \times 26mm without antenna
Weight	46 grams
Software	Agile-Link TM Windows XP compatible

5.3.2 Base Station

G-Link can be configured and triggered to sample data from the wireless USB base station (see Figure 5.11), and also the sample data stored on G-Link can then be wirelessly downloaded to computer at a later time from the wireless base station.

Figure 5.11 USB Base Station



5.3.3 Software

Agile-Link™ software (see Figure 5.12) provides the functionality to communicate with G-Link and also to configure streaming and datalogging on the G-Link. The configuration window shown in Figure 5.13, allows the user to activate desired channels. The channel configuration settings apply for all modes of data collection, including streaming and data logging. A number of other tabs exist on the configuration menu. These tabs allow the user to configure different parameters of the device. These include real-time streaming parameters (how long you want to stream, etc.), datalogging parameters (i.e. the duration to datalog for, sample rate, etc.) and power management functions.

Figure 5.12 Agile-Link™ software interface

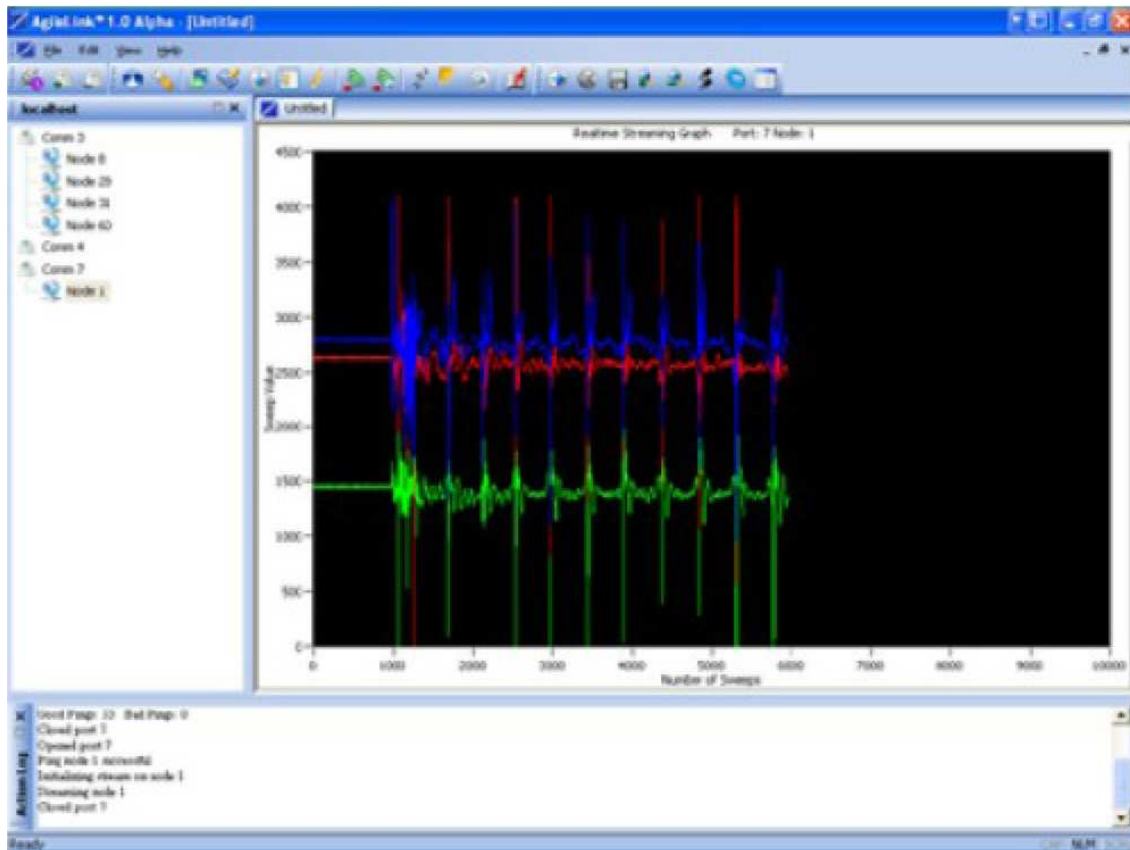
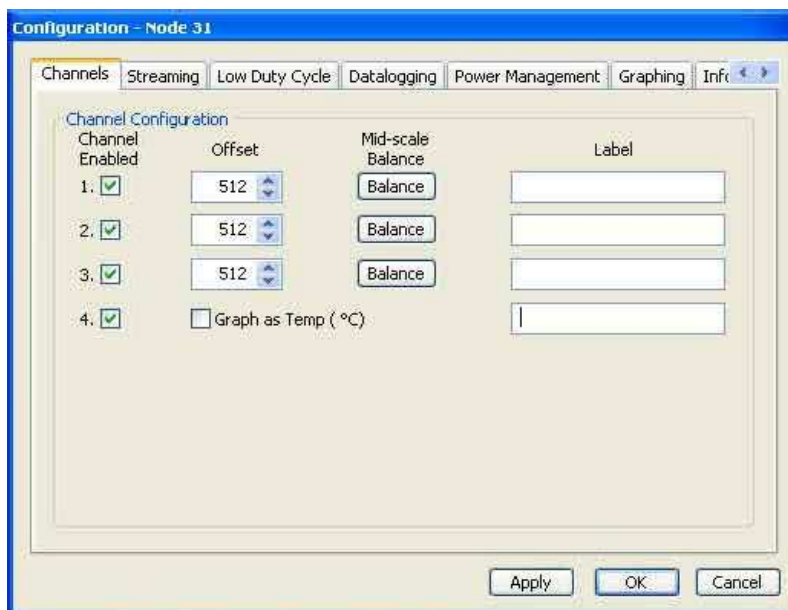


Figure 5.13 G-Link Configuration Screen



In this experimental test, the G-Link was triggered to sample and log from the base station. The sampling rate for datalogging was configured as 2048 Hz and the measured time duration was configured as 4.88 seconds.

5.4 Test Procedure

The following procedure was followed to conduct the experimental test.

- 1. Install the G-Link on the top of the third floor as shown in the Figure 5.14; connect the base station to the PC.
- 2. Select a damage case and simulate this damage case on the structure by removing corresponding columns from the structure. As an example, Figure 5.15 shows the simulated damage case 20-0-20. In order to simplify the problem, the columns are removed symmetrically to preserve the symmetry of the structure.
- 3. Set parameters on the Agile-LinkTM software (for example, the channel action, sampling rate, sampling duration, etc.).
- 4. Apply the impulse force on the still structure for each selected damage case and record the acceleration response.
- 5. Analyze the acceleration data.

Figure 5.14 Installation of the G-Link



Figure 5.15 Damage Simulation on experimental structure



5.5 Damage Pattern Database

5.5.1 3-D FE Model

A 3-D FE model of the structure was constructed by ANSYS, as shown in Figure 5.16. The element type for floors and columns was shell63 and beam4, respectively. In total, there were 126 elements and 142 nodes in the model. The fully constrained boundary condition and rigid connection between floor and column were also applied to the model. Transient dynamic analysis as detailed described in section 4.2, was carried out to determine the dynamic response of the structure under a step impulse force. The time-step was 0.000488 (1/2048).

Figure 5.16 3-D FE model

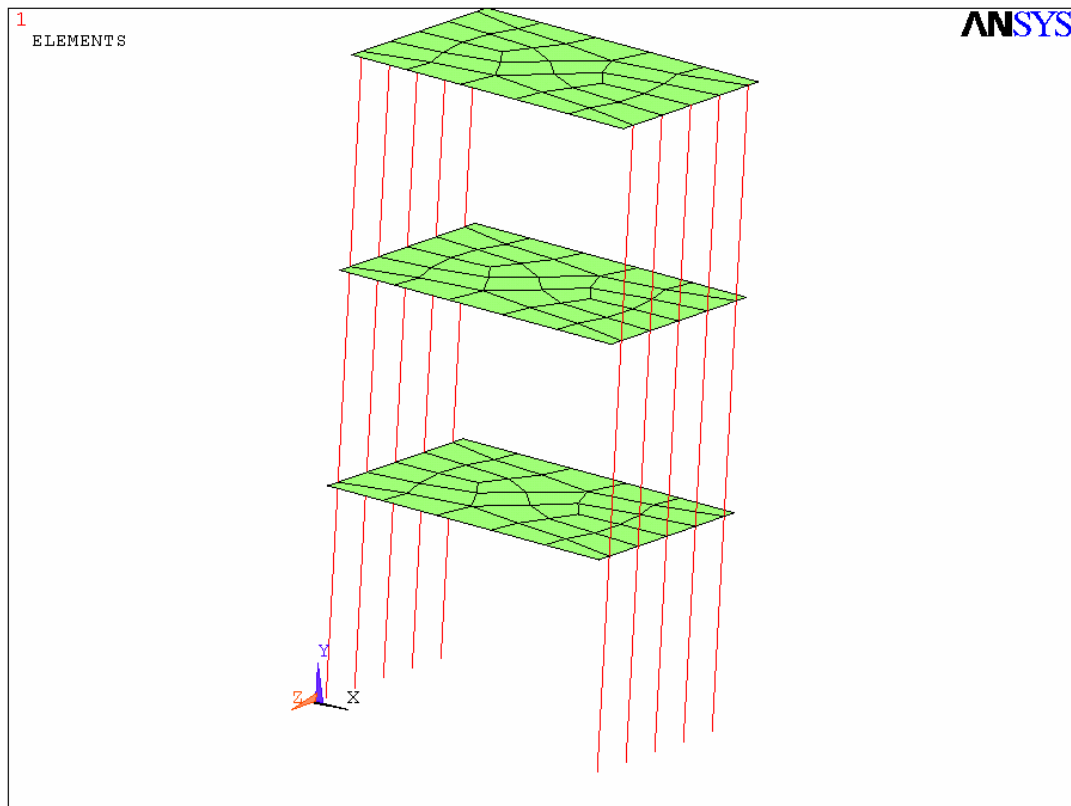


Table 5.3 3-D FE Model Baseline Properties

	Floor	Column	
Dimension	10'' × 15''	10'' (length)	
Element Type	shell63 (elastic 4node 63)	beam4 (3D elastic 4)	
Real Constant	shell thickness at node I TK(I): 1	No.1 (for second and third floor columns)	cross-section area =0.093
	at node J TK(J): 1		area moment of inertia Izz =0.000119
	at node K TK(K): 1		area moment of inertia Iyy =0.004359
	at node L TK(L): 1		thickness along Z axis =0.75
			thickness along Y axis =0.124
		No.2 (for first floor columns)	cross-section area =0.0915
			area moment of inertia Izz =0.000113
			area moment of inertia Iyy =0.004289
			thickness along Z axis =0.75
			thickness along Y axis =0.122
Material Properties	linear isotropic		
	modulus of elasticity of steel: 29,000ksi		
	poisson ratio: 0.3		
	density: 0.0007345		

5.5.2 Tuning the 3-D FE Model

To make 3-D FE model close to the physical baseline structure, the properties of the model were tuned against the physical structure. The FFT pattern of the acceleration signal obtained by FE model simulation was correlated to the one obtained by experimental test on the baseline (healthy) structure. The geometry dimensions and element types of the model were adjusted to achieve the highest FFT pattern correlation value. The FE model with the parameters in Table 5.3 was the final tuned model which corresponded to the relatively highest correlation value (correlation value =0.9). The tuned FE model represented the structure's baseline condition and was used in setting damage pattern database.

5.5.3 Constructing Damage Pattern Database

Various damage cases were introduced by symmetrically removing columns at different locations, which simulated the failure of one or more columns in the structure. 64 damage cases including the baseline condition were designed to represent possible structural damage conditions. In this study, the numerical dynamic responses of the structure under the 64 damage cases were simulated by removing corresponding columns from the 3-D FE model of the structure. The resulting 64 sets of normalized FFT magnitude vectors and 64 sets of CWT coefficient matrices formed the damage feature patterns in the database.

5.6 Case Studies and Pattern Matching

Twenty-eight experimental damage cases, as listed in Table 5.4 were chosen to test the proposed damage detection procedure and the associated patterns and pattern-matching algorithms. The acceleration response of the structure with each damage case was measured after application of the impulse using the impulse applicator. These acceleration signals were then de-noised and transformed by FFT and CWT. As an example, Figure 5.17 shows the original and the de-noised signals of experimental acceleration of the structure under damage case 20-20-40. The three pattern-matching algorithms were used for pattern recognition.

As examples of the test results, Figure 5.18 to Figure 5.20 show the FFT and CWT pattern-matching results for damage case 0-0-20 by using correlation, least square distance and Cosh spectral distance, respectively. Other examples are shown in Appendix D - The highest correlation value, the lowest least square distance value, and the lowest Cosh spectral distance

value indicate the most similar pattern in the database which indicates the most probable damage level and location for the unknown case.

All of the experimental test results indicate that both FFT and CWT patterns can preserve the damage information in term of level and location. However CWT can be more efficient to detect the damage, especially in terms of location when the output signal is from more than one sensor. Among all the three pattern-matching algorithms explored in this study, correlation algorithm could successfully perform a better recognition of the FFT and CWT patterns to detect damages for the entire experimental test cases; least square distance could also successfully recognize CWT patterns to detect damages for the entire experimental test cases, and all of the FFT patterns except for three multiple extreme damage case, 20-60-20, 40-40-40, 40-60-20 (see Figure D.26); and finally, Cosh spectral distance algorithm failed to detect the damage for most of the FFT and CWT patterns of the experimental cases.

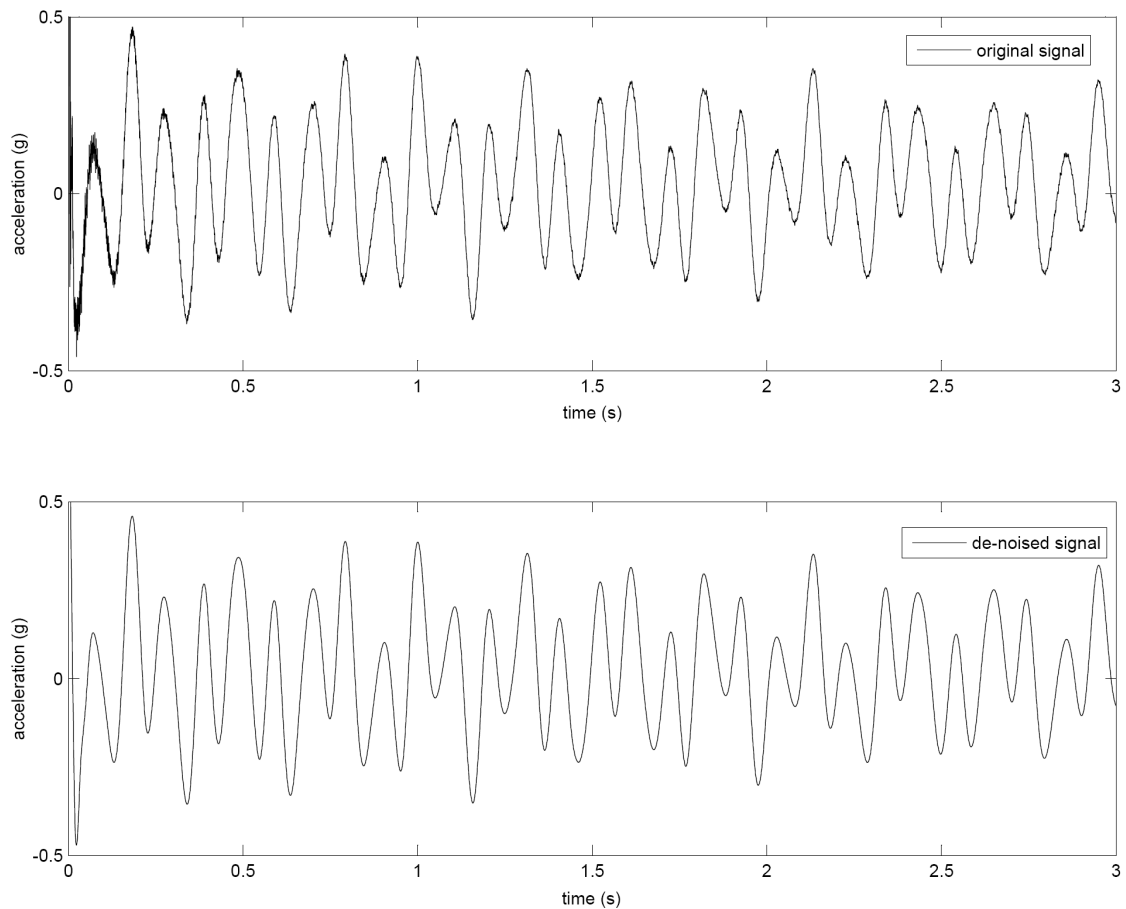
Table 5.4 Experimental Test Cases

Single Damage Location		Double Damage Locations		Triple Damage Locations	
0-0-20	0-0-60	0-20-20	20-40-0	20-20-20	40-40-40
20-0-0	0-60-0	20-0-20	40-20-0	20-20-40	40-60-20
0-20-0	60-0-0	20-20-0	40-0-20	20-40-20	
0-0-40		40-40-0	0-20-40	20-60-20	
0-40-0		0-40-40	0-40-20	40-20-20	
40-0-0		40-0-40		40-40-20	

There are a number of wavelet functions that can be used as the mother wavelet for CWT feature extraction. The choice of wavelet function will affect the computing time and pattern-matching resolution. For demonstration purpose, some widely used wavelet functions were chosen as mother wavelet for CWT- based pattern extraction (see Table E.1). Then correlation was used to perform pattern-matching to detect the selected three experimental damage cases: 0-0-20, 20-20-0, and 20-20-40. The successful detection results for all the three experimental damage cases by using different wavelet functions indicated that all of the selected wavelet functions could be used as mother wavelet for CWT-based sensitive feature extraction. The

matching resolution based on each wavelet function was calculated as the difference between the two highest correlation values divided by the highest correlation value, as listed on Table E.1 for each of the three experimental test cases. It shows that Haar, Daubechies, Symlets and Gaussian wavelets have the best performance. It is also found that Haar, Daubechies and Gaussian wavelets take less computing time. In contrast, Meyr and Dmey wavelets take much longer computing time.

Figure 5.17 Experimental Acceleration Signals of Structure under Damage Case 20-20-40, Original and De-noised



5.7 Discussion on Experimental Study

Experimental tests and case studies further validated the overall feasibility of the method for damage detection. Fourier and especially wavelet transform could well extract and preserve the features of the signal under damage conditions. Since the CWT pattern preserves the frequency and time sensitive features, it results in high pattern-matching resolution than FFT

pattern does. Wave function affects CWT-based pattern extraction and pattern-matching resolution. The wavelet function is chose based on its shape and its ability to analyze the signal

5.8 WPT-Based Feature Extraction and Pattern Recognition

Yen and Lin (2000) investigated the feasibility of applying the Wavelet Packet Transform (WPT) to the classification of vibration signals. They introduced the wavelet packet node energy and demonstrated that the node energy could be a robust signal feature for classification. Following this work, many researchers have derived a lot of feature indexes based on WPT node energy for damage detection. Detailed descriptions of these feature-indexes were included in chapter two. In this experimental study, energy variation vectors were selected as sensitive features. The energy of each WPT component signal $f_j^i(t)$ is defined as

$$E_j^i = \int_{-\infty}^{\infty} f_j^i(t)^2 dt \quad (5.1)$$

The energy variation of each component E_j^i due to damage is

$$V_j^i = E_j^i - \hat{E}_j^i \quad (5.2)$$

where \hat{E}_j^i is the baseline (health condition) component energy used as reference.

The acceleration signal was decomposed by WPT using db6 wavelet function. The wavelet packet decomposition level was set to 12 which resulted in a total of 4096 wavelet packet components after decomposition. The energy variation V_j^i for each component was calculated by Equation 5.2. Such a set of energy variation vectors formed a one-dimensional pattern which presented a unique condition under different damage case. Each energy vector in a pattern was also normalized with respect to the square root of sum of squares of each one in the pattern.

Same as FFT and CWT pattern database construction, the dynamic response of the structure under the 64 damage cases were numerically simulated by removing the corresponding columns from the 3-D FE model. All of the 64 sets of the simulated acceleration response by ANSYS were transformed by WPT into energy variation vectors. The resulting 64 sets of WPT energy variation vectors formed the damage feature patterns in the database.

Correlation algorithm was used to perform the pattern-matching. Six experimental damage cases: 0-0-20, 0-0-40, 0-20-0, 20-20-0, 0-20-20, and 20-20-20 were selected to

demonstrate the validity and accuracy of this method. The results shows that WPT-based energy variation vectors can best preserve the dynamic response features of a structure under damage with low level and few locations. And when increasing the level of damage and the number of damage location, the detection result will be overestimated (see Figure 5.21 to Figure 5.26). In order to overcome this drawback, increasing the number of sensors and employing an iterative detection process can be explored as a recommended future research work.

Figure 5.18 Correlation Matching for Damage Case 0-0-20, FFT & CWT Pattern Matching

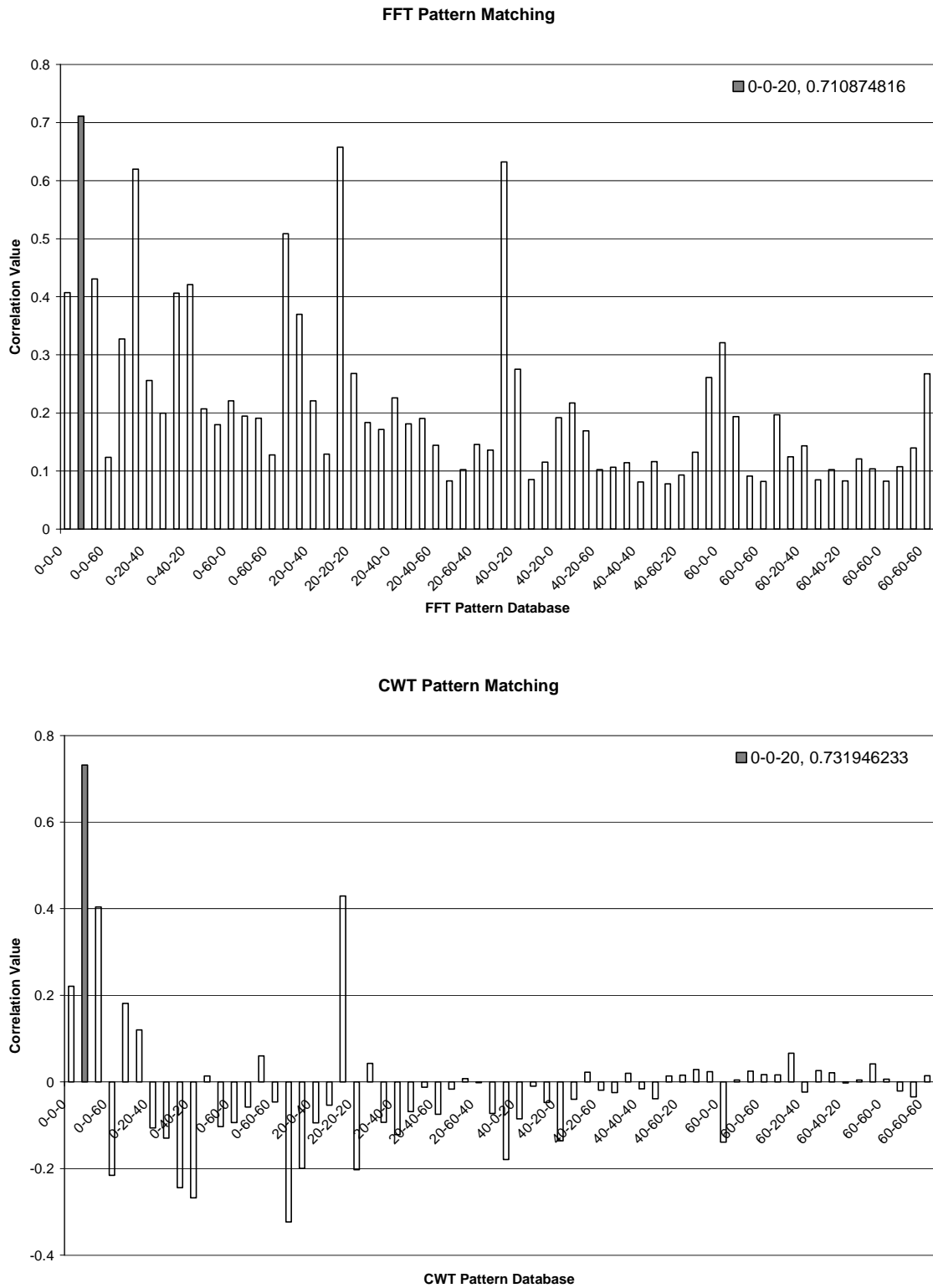


Figure 5.19 Least Square Distance (LSD) Matching for Damage Case 0-0-20, FFT & CWT Pattern Matching

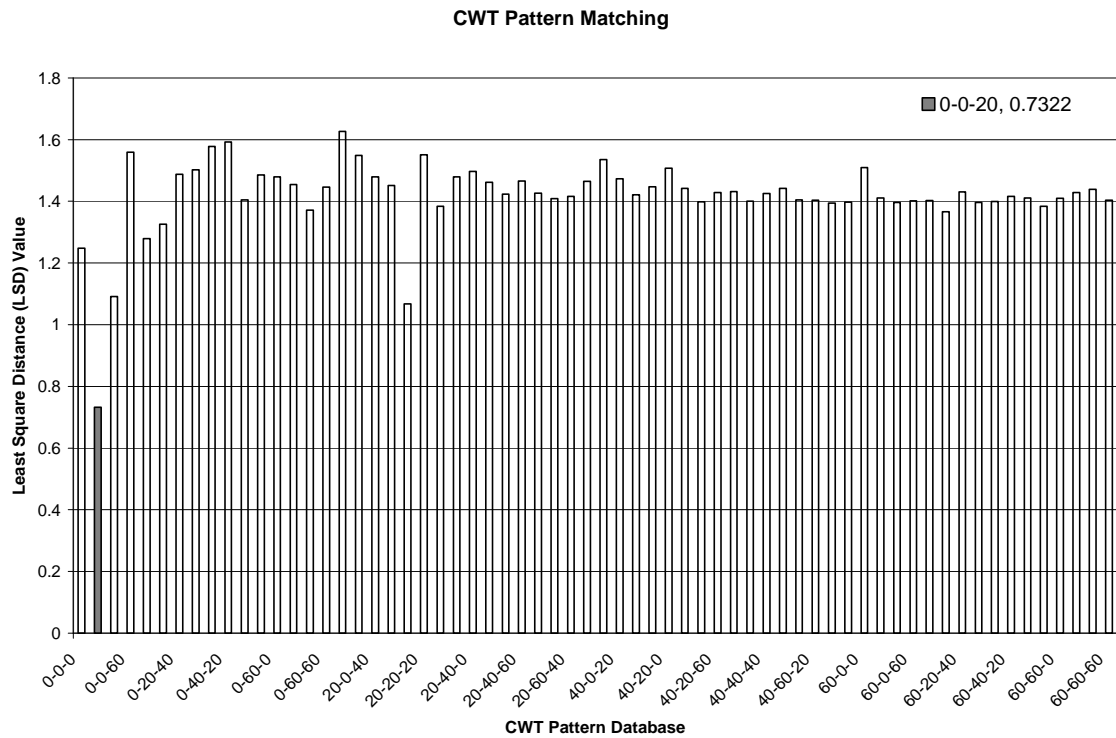
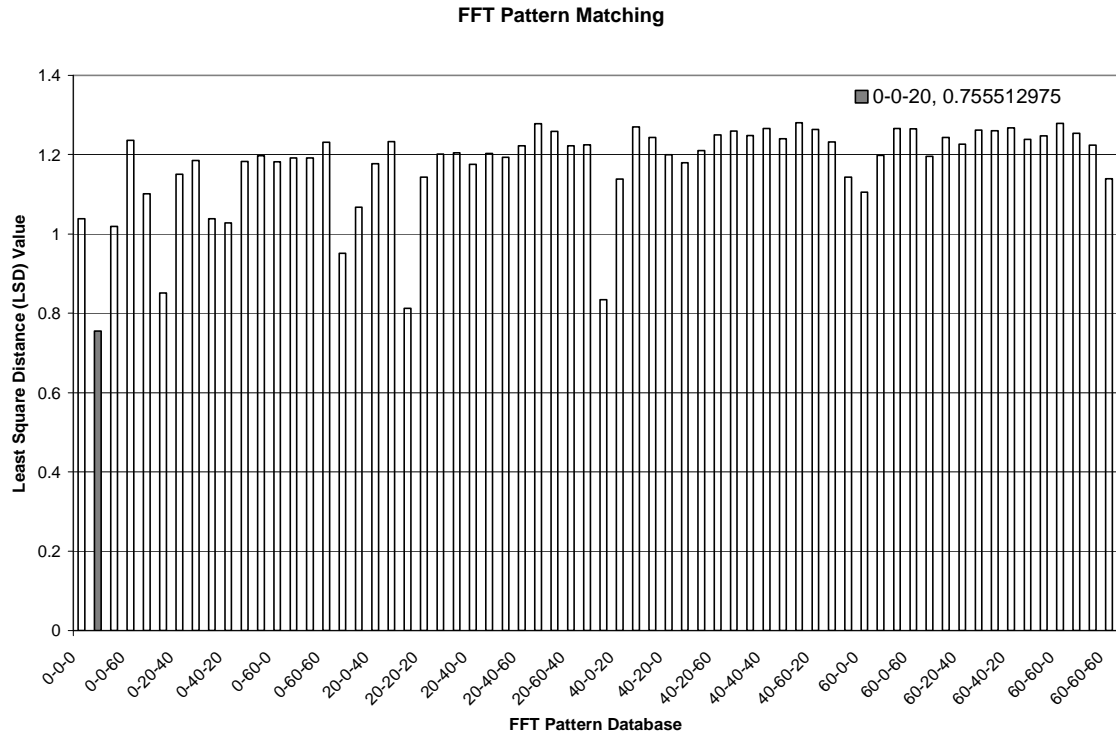


Figure 5.20 Cosh Spectral Distance (CSD) Matching for Damage Case 0-0-20, FFT & CWT Pattern Matching

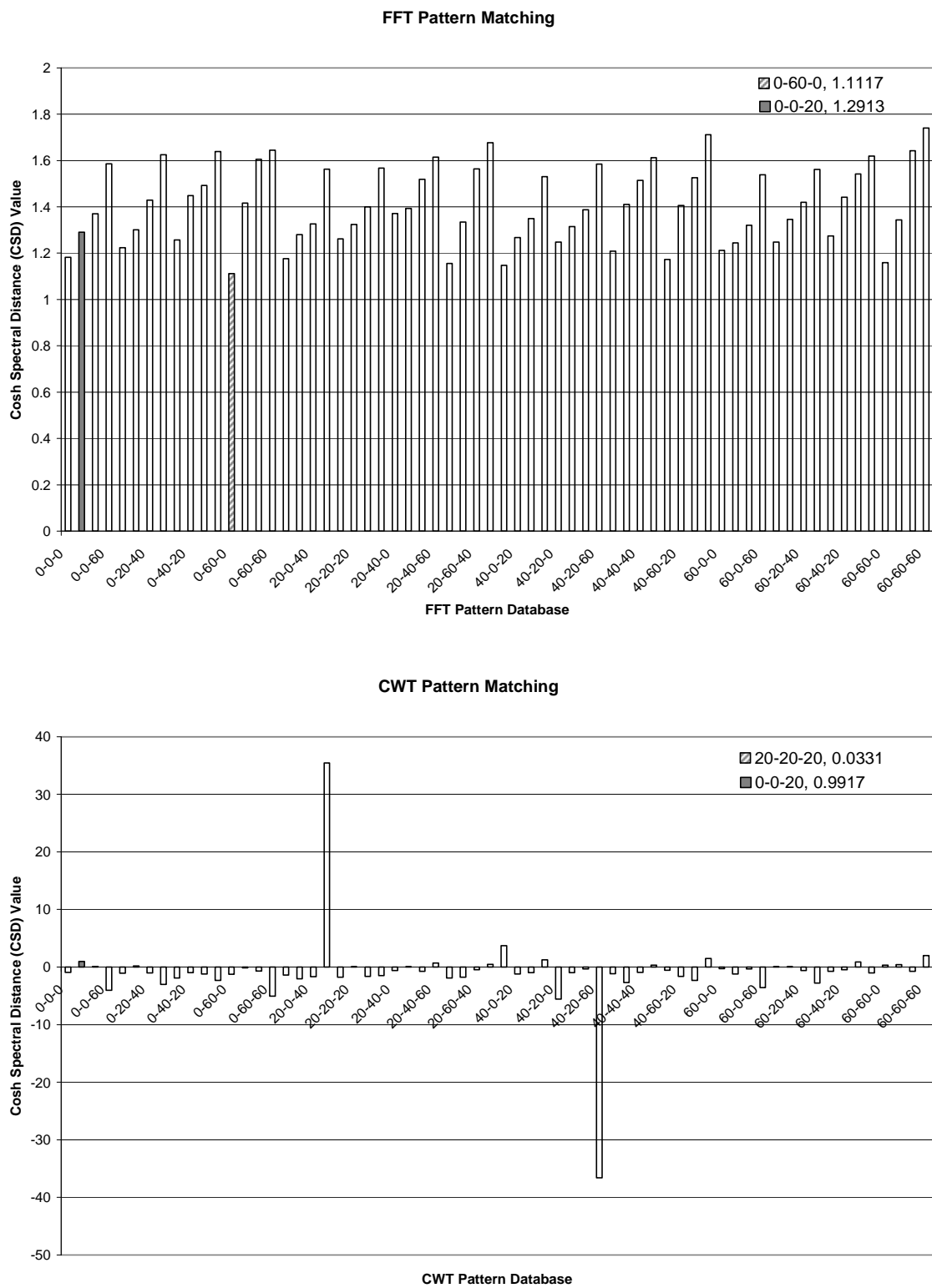


Figure 5.21 Correlation Matching for Damage Case 0-0-20, WPT Pattern Matching

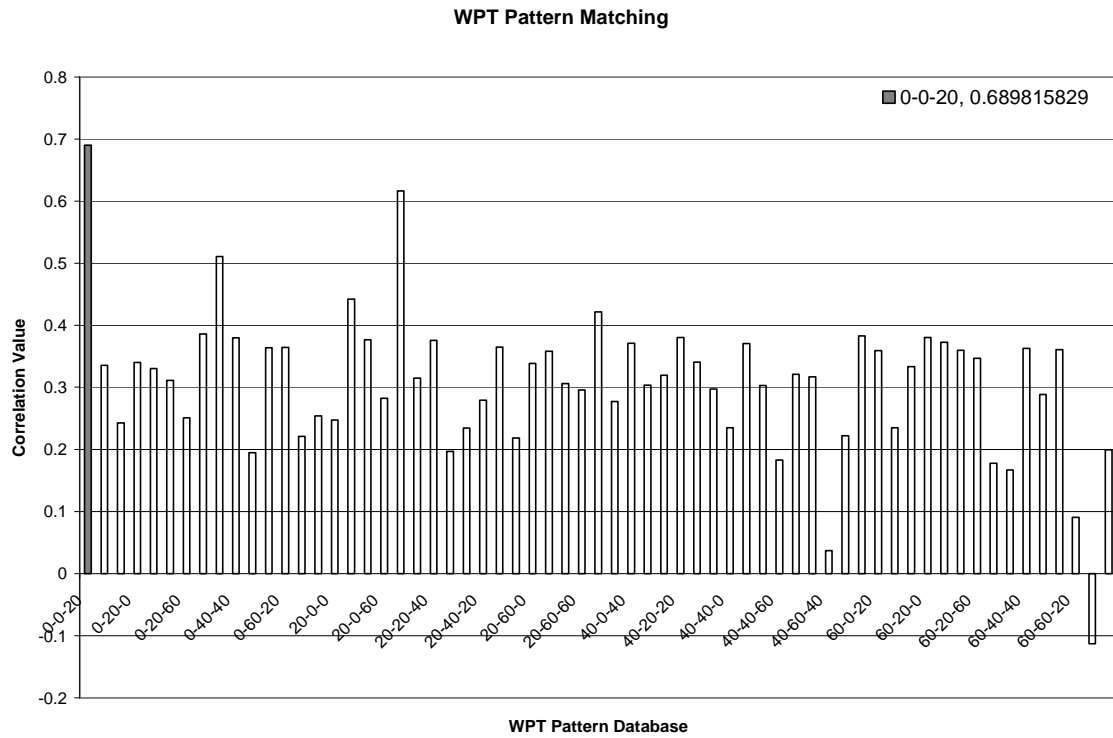


Figure 5.22 Correlation Matching for Damage Case 0-20-0, WPT Pattern Matching

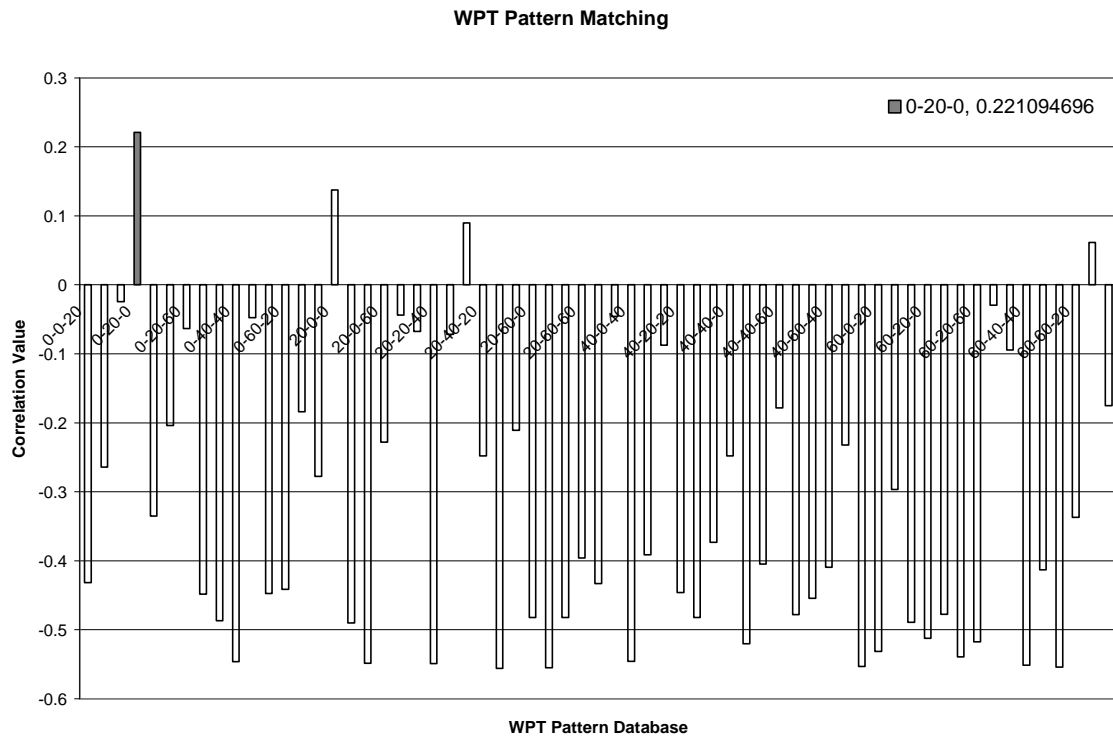


Figure 5.23 Correlation Matching for Damage Case 0-0-40, WPT Pattern Matching

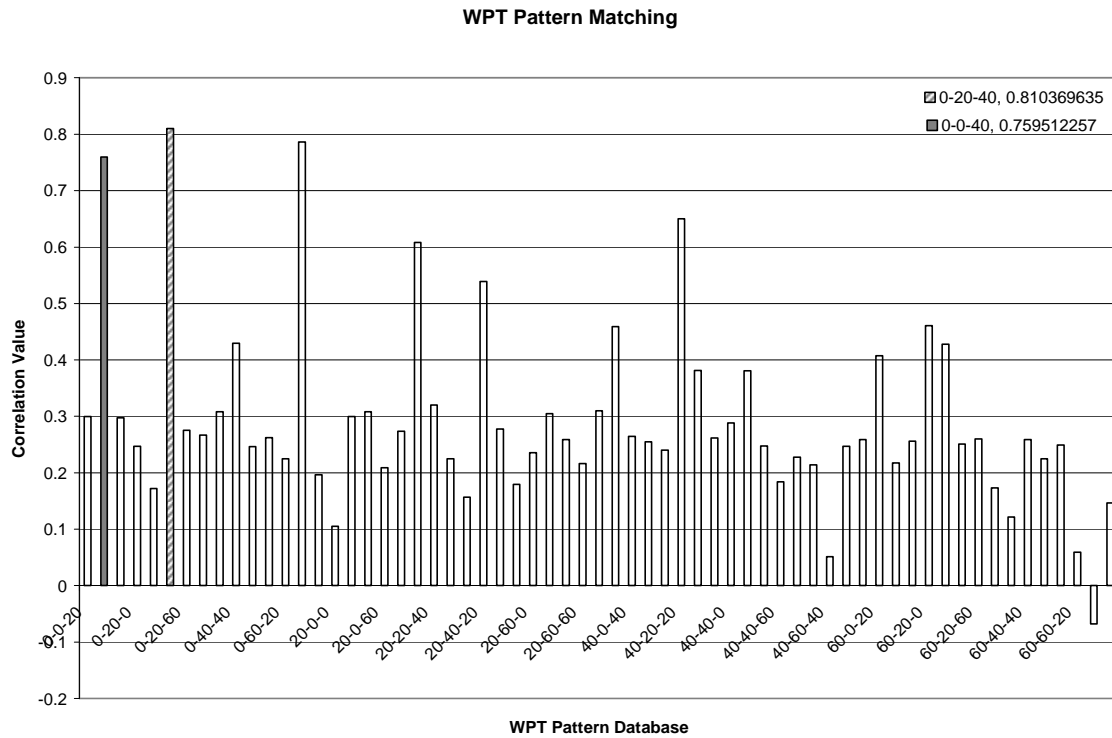


Figure 5.24 Correlation Matching for Damage Case 20-20-0, WPT Pattern Matching

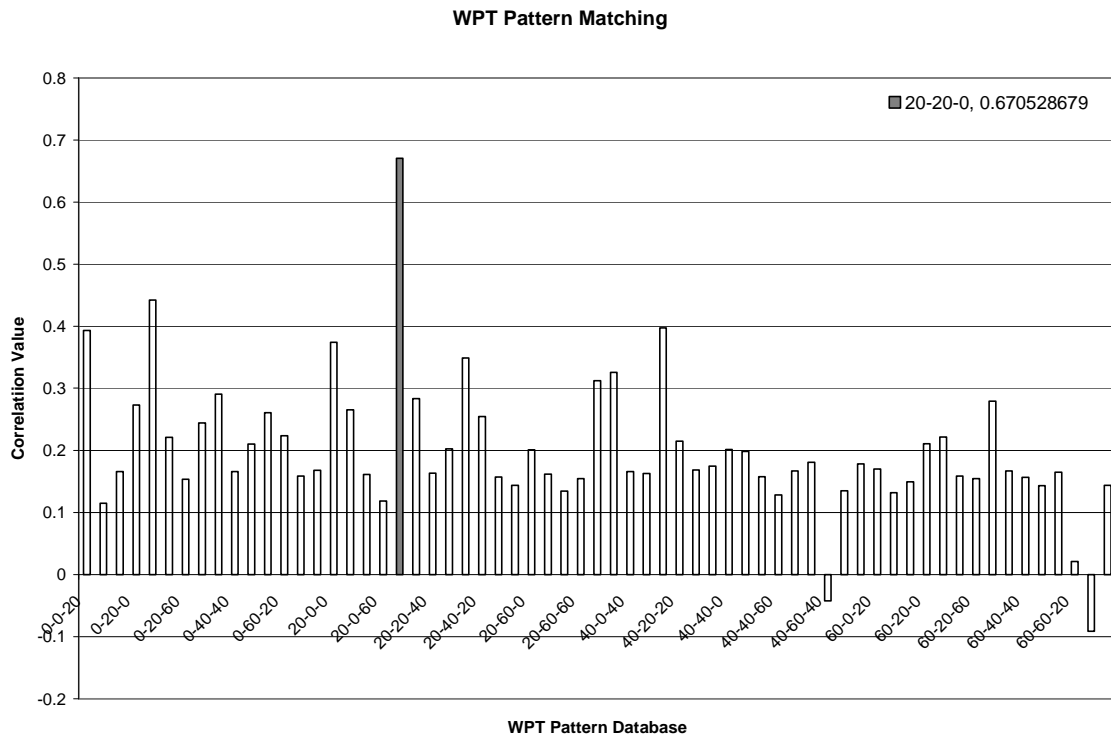


Figure 5.25 Correlation Matching for Damage Case 0-20-20, WPT Pattern Matching

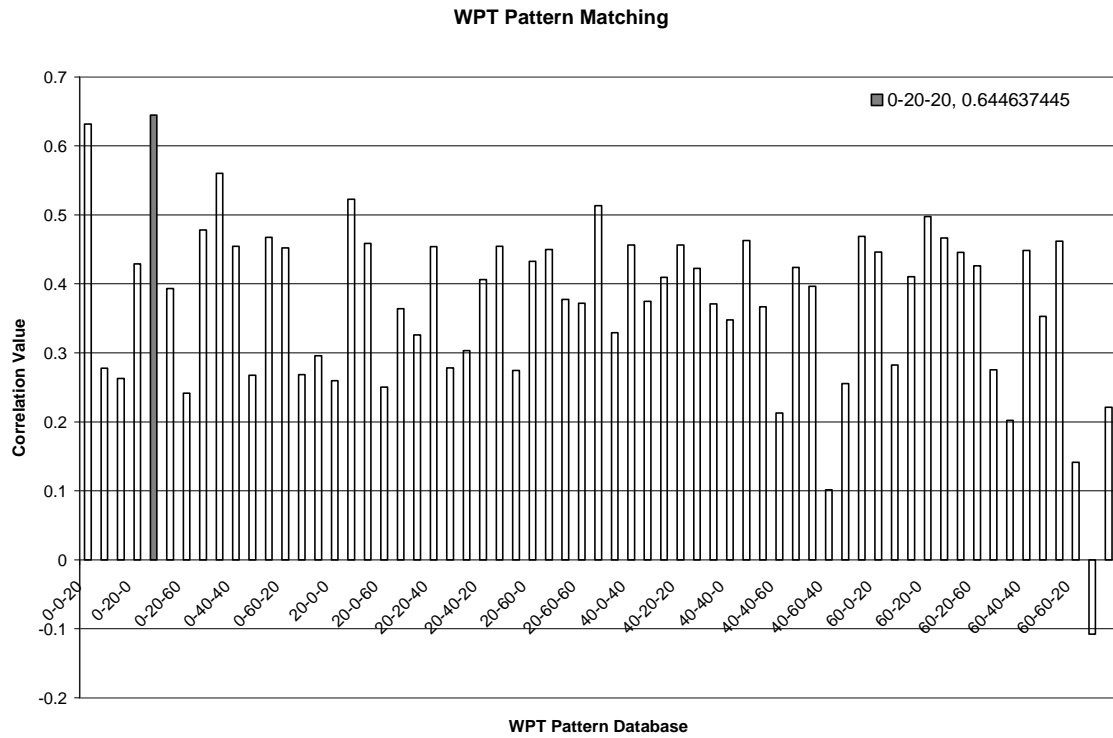
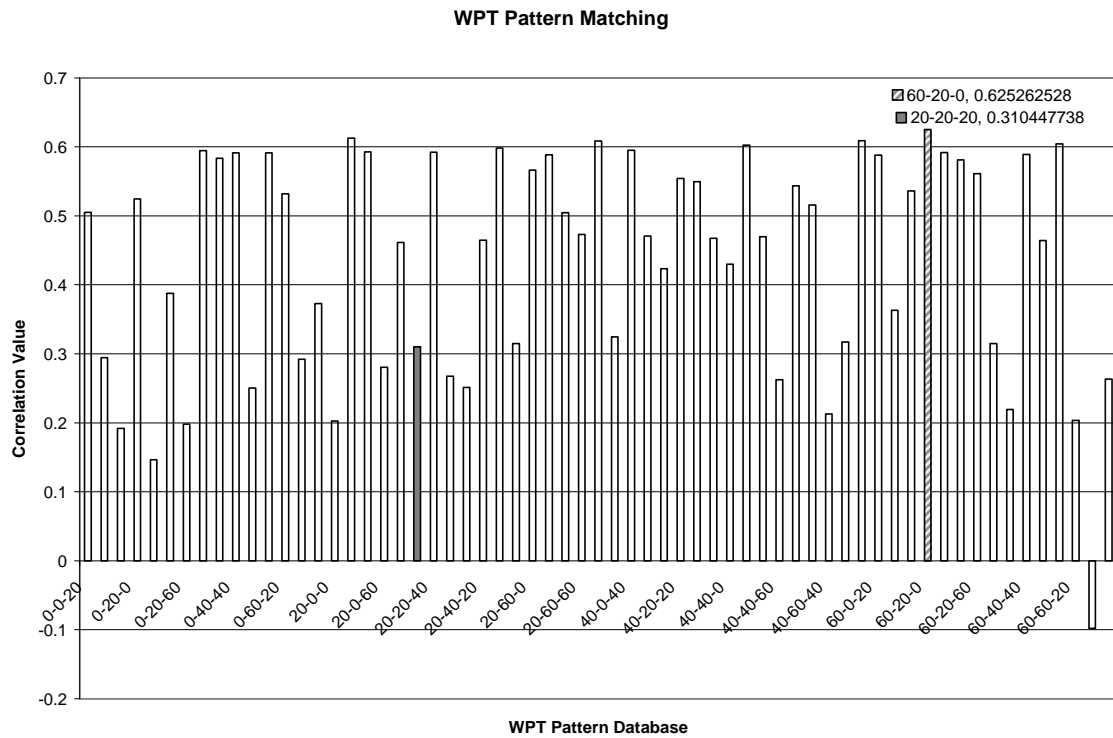


Figure 5.26 Correlation Matching for Damage Case 20-20-20, WPT Pattern Matching



CHAPTER 6 - CONCLUSIONS

6.1 Research Summary

In this study, a signal-based pattern extraction and recognition method, using a number of signal transformations and pattern matching algorithms, was investigated to detect structural damage. The method is based on the extraction of sensitive features of the structural response that present a unique pattern for a particular damage scenario. Frequency-based features and time-frequency-based features were extracted from the measured acceleration signal by Fast Fourier Transform (FFT) and Continuous Wavelet Transform (CWT) to construct one-dimensional or two-dimensional patterns, respectively. Three pattern recognition algorithms were also investigated to perform pattern recognition separately: (1) correlation, (2) least square distance, and (3) Cosh spectral distance. Damage-pattern database was developed analytically by simulating possible damage scenarios. Damage location and level were identified simultaneously by performing the matching of the unknown damage pattern with the known ones in the database.

To demonstrate the validity of the method, numerical and experimental studies were conducted on a small-scale three-story steel building. At the first phase of the numerical study, a 2-D three-story steel structure model numerically simulated the aforesaid steel structure and the method was applied to detect representative damage cases. Following the successful initial numerical study, conducted on the 2-D simulation of the three-story structure, the work progressed into the experimental verification phase. At this phase, the three-story small-scale steel structure was constructed in the Kansas State University (KSU) structural laboratory. An impulse applicator was developed to apply a consistent impulse load on the experimental structure. A wireless data acquisition system was used to sample and record the vibration response of the structure under the impulse load excitation. An experimentally-tuned 3-D finite element model of the structure was developed using ANSYS to numerically simulate the structural dynamic response without damage, as well as the response with various possible damages, excited by an impulse load. Structural vibration signals from numerical simulations and experimental measurements were then decomposed by fast Fourier transform or continuous

Wavelet transform for feature extraction. The normalized signal features from numerical simulations generated for the baseline (healthy) structure, and for the structure with various selected damages were collected into a damage pattern database. The normalized signal features of the experimental measurement for an unknown damage case, was then compared against this database to detect the closest damage case, using three different pattern matching algorithms separately: (1) correlation, (2) least square distance, and (3) Cosh spectral distance. Twenty-eight damage cases were experimentally simulated on the structure as “unknown” damage to demonstrate the applicability of the proposed damage detection method.

In addition, Wavelet Packet Transform (WPT) was also investigated for feature extraction and pattern recognition. Meanwhile, the choice of wavelet functions was also discussed.

6.2 Conclusion

The structure under a specific damage scenario, in terms of location, level and type, has a unique signature and shows a unique pattern in its dynamic response to an excitation. Fourier and Wavelet transforms provide means to extract and preserve the dynamic response features of a structure under various damage conditions. Different damage scenarios can be presented by the features extracted using these transformations. Since FFT preserves the frequency features of the signal, while CWT preserves its frequency as well as its time-sensitive features, CWT pattern results in a higher pattern-matching resolution than FFT pattern. Comparing dynamic response pattern of a damaged structure with a wide range of numerically-generated damage cases stored in a database can serve as a tool to detect the closest damage case in terms of its existence, severity and location. Among the three algorithms used, correlation was the best to perform pattern matching, even when the signal was contaminated with noise. The highest correlation, the lowest least square distance or Cosh spectral distance with a damage case in the database showed the closest damage case to the actual unknown damage. However, the numerical model must be carefully tuned to accurately represent the physical conditions of the structure. This experimental tune-up of the model should be done for the healthy structure in the beginning; and then updated if the dynamic properties of the structure changes. In this case, reconstruction of the damage pattern database is necessary. The potential advantages of this approach are:

1. It requires few measurements (single or limited number of input/output signals).
2. It can be used to detect multiple damage locations and the severity of damage at each damage location.
3. It gives a relatively good accuracy even in the presence of noise, for isolated damage cases.
4. The method can be implemented in various layers, starting from global (the whole structure) and ending to a structural member for a detailed detection.
5. Fine-tuning of the numerical model against the physical structure and expansion of the damage-pattern database enhances the detection process. However, statistical considerations are needed as will follow.
6. The process can be automated in terms of detection and continuous fine-tuning of the model and the database.

The method is particularly effective for large-scale structures due to their complicated nonlinear behavior and the incomplete, incoherent, and noise-contaminated measurements of structural response. Signal-based damage detection has shown great potential in the experimental studies. It should be noted that a structure may experience nonlinear deformations in a severe event; but during detection process, the input, here an impulse, excites the structure within its linear range. This is true for the numerical excitation used for reconstruction of the damage pattern database after a severe event.

The choice of wavelet function in CWT-based pattern extraction and recognition affects the computation time and pattern-matching resolution. Studies on signal-based damage detection, including the present work, have shown that Haar, Daubechies, Symlets and Gaussian wavelets have the best performance. It has also been found that Haar, Daubechies and Gaussian wavelets take less computation time. In contrast, Meyr and Dmey wavelets take much longer computation time. The wavelet function is selected based on its shape and its ability to analyze the signal and to preserve sensitive features.

This study has also shown that WPT-based energy variation vectors can best preserve the dynamic response features of a structure under damage with low level and few locations. Increasing the level of damage and the number of damage locations will result in a wrong detection. Increasing the number of sensors (accelerometers) and employing an iterative process may address this issue and is recommended as a future research work in this field.

6.3 Recommended Future Work

Further experimental work can be considered for other damage scenarios, e.g. “cracks” in a beam or buckling of a column. The adequacy of other feature extraction and feature recognition methods combined with correlation and other pattern-matching algorithms may be explored. The research may be applied to other types of structures such as bridges.

The probability of a correct detection depends on a realistic model and a detailed damage-pattern database. A statistical study, which is beyond the scope of this research program, is recommended to set the probability of a damage case detected by this method. While expansion of the damage-pattern database can enhance the detection; it increases the error margin for damage cases that may have close normalized patterns. Increasing the number of input/output signals can decrease the error, and a statistical study can give the optimal number of signals for a desired general detection accuracy.

WPT-based energy variation vectors can best preserve the dynamic response features of a structure under damage with low level and few locations. When increasing the level of damage and the number of damage locations, the detection will not be accurate. Increasing the number of sensors (accelerometers) and employing an iterative detection process may address this issue and is recommended as a future research work in this field.

References

- Adeli, H. and Jiang, X. (2006). "Dynamic fuzzy wavelet neural network model for structural system identification." *Journal of Structural Engineering*, Vol.132, No.1, pp. 102-111.
- ANSYS, Release 11. The ANSYS, Inc.
- Barr, P.J., Woodward, B., Najera, B. and Amin, M.N. (2006). "Long-term structural health monitoring of the San Ysidro bridge." *Journal of Performance of Constructed Facilities*, ASCE, Vol. 20, No.1, pp. 14-20.
- Beck, J.L., Au, S.K. and Vanik, M.W. (1999). "A Bayesian probabilistic approach to structural health monitoring." *Proceeding of the American Control Conferences*, June 1999, San Diego, California.
- Biemans, C., Staszewski, W.J., Boller, C. and Tomlinson, G.R. (2001). "Crack detection in metallic structures using broadband excitation of acousto-ultrasonics." *Journal of Intelligent Material Systems and Structures*, Vol. 12, pp. 589-597.
- Bodeux, J.B. and Golinval, J.C. (2001). "Application of ARMAV models to the identification and damage detection of mechanical and civil engineering structures." *Smart Materials and Structures*, Vol. 10, pp. 479-489.
- Cardinale, G. and Orlando, M. (2004). "Structural evaluation and strengthening of a reinforced concrete bridge." *Journal of Bridge Engineering*, ASCE, Vol. 9, No. 1, pp. 35-42.
- Chang, C.C., Chang, T.Y.P., Xu, Y.G. and Wang, M.L. (2000). "Structural damage detection using an iterative neural network." *Journal of Intelligent Material Systems and Structures*, Vol. 11, pp. 32-42.
- Chang, C.C. and Chen, L.W. (2005). "Detection of the location and size of cracks in the multiple cracked beam by spatial wavelet based approach." *Mechanical Systems and Signal Processing*, Vol. 19, pp. 139-155.
- Chang, C.C. and Yang, H.T.Y. (2004). "A correlation between pulse diagnosis of human body and health monitoring of structures." *Earthquake Engineering and Engineering Vibration*, Vol. 3, No.1, pp. 117-125.
- Chang, P.C. and Liu, S.C. (2003). "Recent research in nondestructive evaluation of civil infrastructures." *Journal of Materials in Civil Engineering*, ASCE, Vol. 15, No.3, pp. 298-304.

- Chen, D. and Wang, W.J. (2002). "Classification of wavelet map patterns using multi-layer neural networks for gear fault detection." *Mechanical systems and signal processing*, Vol. 16, No.4, pp. 695-704.
- Chen, H.G, Yan, Y.J and Jiang, J.S. (2006). "Vibration-based damage detection of composite wingbox structures using improved Hilbert-Huang transform." *Key Engineering Materials*, Vols. 324-325, pp. 539-542.
- Chen, S.L., Lai, H.C. and Ho, K.C. (2006). "Identification of linear time varying systems by Haar wavelet." *International Journal of Systems Science*, Vol. 37, No.9, pp. 619-628.
- Ching, J. and Beck, J.L. (2004a). "Bayesian analysis of the phase II IASC-ASCE structural health monitoring experimental benchmark data." *Journal of Engineering Mechanics*, ASCE, Vol. 130, No.10, pp. 1233-1244.
- Ching, J. and Beck, J.L. (2004b). "New Bayesian model updating algorithm applied to a structural health monitoring benchmark." *Structural Health Monitoring*, Vol. 3, No.4, pp. 313-332.
- Daubechies, I. (1992). "Ten Lectures on Wavelets." *Society for Industrial and Applied Mathematics*, Philadelphia, Pennsylvania.
- Diao, Y.S., Li, H.J. and Wang, Y. (2006). "A two-step structural damage detection approach based on wavelet packet analysis and neural network." *Proceeding of the 5th International Conference on Machine Learning and Cybernetics*, August 13-16, Dalian, China.
- Ding, Y.L. and Li, A.Q. (2007). "Structural health monitoring of long-span suspension bridges using wavelet packet analysis." *Earthquake Engineering and Engineering Vibration*, Vol. 6, No.3, pp. 289-294.
- Ding Y.L., Li A.Q. and Liu, T. (2008). "A study on the WPT-based structural damage alarming of the ASCE benchmark experiments." *Advances in Structural Engineering*, Vol. 11, No.1, pp. 121-127.
- Doebbling, S.W., Farrar, C.R., Prime, M.B. and Shevitz, D.W. (1996). "Damage identification and health monitoring of structural and mechanical systems from change in their vibration characteristics: A literature review. Report" LA-13070-MS, US-900: Los Alamos National Laboratory, NM.
- Duda, R.O., Hart, P.E. and Stork, D.G. (2000). "Pattern Classification." *John Wiley & Sons, Inc.*, New York, N.Y.
- Fang, X., Luo, H. and Tang, J. (2005). "Structural damage detection using neural network with learning rate improvement." *Computers and Structures*, Vol. 83, pp. 2150-2161.

- Farrar, C.R., Doebling, S.W. and Nix, D. (2001). "Vibration-based structural damage identification." *Philosophical Transactions of Royal Society of London Series A: Mathematical, Physical and Engineering Science*, London, Vol. 359, pp. 131-149.
- Fasel, T.R., Sohn, H., Park, G. and Farrar, C.R. (2005). "Active sensing using impedance-based ARX models and extreme value statistics for damage detection." *Earthquake Engineering and Structural Dynamics*, Vol. 34, pp. 763-785.
- Han, J.G., Ren, W.X. and Sun, Z.S. (2005). "Wavelet packet based damage identification of beam structures." *International Journal of Solids and Structures*, Vol. 42, pp. 6610-6627.
- Haritos, N. and Owen, J.S. (2004). "The use o vibration data for damage detection in bridge: a comparison of system identification and pattern recognition approach." *Structural Health Monotoring*, Vol. 3, No.2, pp. 141-163.
- Hera, A. and Hou, Z.K. (2004). "Application of wavelet approach for ASCE structural health monitoring benchmark studies." *Journal of Engineering Mechanics*, Vol. 130, No.1, pp. 96-104.
- Hou, Z., Noori,M., and Amand, R.St. (2000). "Wavelet-based approach for structural damage detection." *Journal of Engineering Mechanics*, Vol. 126, No.7, pp. 677-683.
- Hou, Z., Hera, A. and Shinde, A. (2006). "Wavelet-based structural health monitoring of earthquake excited structures." *Computer-Aided Civil and Infrastructure Engineering*, Vol. 21, pp. 268-279.
- Huang, C.S., Huang, S.L., Lin, C.I. and Su, W.C. (2005). "A wavelet-based approach to identifying structural modal parameters from seismic response and free vibration data." *Computer-Aided Civil and Infrastructure Engineering*, Vol. 20, pp. 408-423.
- Ifeachor, E.C. and Jervis, B.W. (2001). "Digital Signal Processing: A Practical Approach, Edition 2." *Addison-Wesley*.
- Jeyasehar, C.A. and Sumangala, K. (2006). "Nondestructive evaluation of prestressed concrete beams using an artificial neural network approach." *Structural Health Monitoring*, Vol. 5, No.4, pp. 313-323.
- Jain, A.K., Duin, R.P.W. and Mao, J. (2000). "Statistical Pattern Recognition: a review." *IEEE Transactions on Pattern Analysis and Machine Intelligence*, Vol. 22, No.1, pp. 4-37.
- Kamarthi, S. and Pittner, S. (1997). "Fourier and Wavelet transform for flank wear estimation – a comparison." *Mechanical Systems and Signal Processing*, Vol. 11, No.6, pp. 791-809.
- Kar, C. and Mohanty, A.R. (2006). "Technical note: gearbox health monitoring through multiresolution fourier transformation of vibration and current signals." *Structural Health Monitoring*, Vol. 5, pp. 195-200.

- Kijewski, T. and Kareem, A. (2003). "Wavelet transforms for system identification in civil engineering." *Computer-Aided Civil and Infrastructure Engineering*, Vol. 18, pp. 339-355.
- Kim, H. and Melhem, H. (2004). "Damage detection of structures by wavelet analysis." *Engineering Structures*, Vol. 26, pp. 347-362.
- Kim, I.K. and Kim, Y.Y. (2005). "Damage size estimation by the continuous wavelet ridge analysis of dispersive bending waves in a beam." *Journal of Sound and Vibration*, Vol. 287, pp. 707-722.
- Kim, J.T., Ryu, Y.S., Cho, H.M. and Stubbs, N. (2003). "Damage identification in beam-type structures: Frequency-based method vs mode-shape-based method." *Engineering Structures*, Vol. 25, pp. 57-67.
- Kosmatka, J.B. and Ricles, J.M. (1999). "Damage detection in structures by modal vibration characterization." *Journal of Structural Engineering*, Vol. 125, No.12, pp. 1384-1392.
- Lathi, B.P. (1998). "Signal Processing and Linear Systems." *Oxford University Press Inc.*, New York, New York.
- Lee, J. and Kim, S. (2007). "Structural damage detection in the frequency domain using neural networks." *Journal of Intelligent Materials Systems and Structures*, Vol. 18, pp. 785-792.
- Li, B., Goddu, G. and Chow, M.Y. (1998). "Detection of common motor bearing faults using frequency-domain vibration signals and a neural network based approach." *Proceedings of the 16th American Control Conference*, Philadelphia, PA, June, 1998.
- Li, Z.X. and Yang, X.M. (2008). "Damage identification for beams using ANN based on statistical property of structural responses." *Computers and Structures*, Vol. 86, pp. 64-71.
- Liao, G., Liu, S., Shi, T. and Zhang, G. (2004). "Gearbox condition monitoring using self-organizing feature maps." *Proceedings of the Institution of Mechanical Engineers. Part C, Journal of Mechanical Engineering Science*, Vol. 218, pp. 119-130.
- Liu, Y., Li, A., Fei, Q. and Ding, Y. (2007). "Feature extraction and damage alarming using time series analysis." *Journal of Southeast University*, Vol. 23, No.1, pp. 86-91.
- Masri, S.F., Nakamura, M., Chassiakos, A.G. and Caughey, T.K. (1996). "Neural network approach to detection of changes in structural parameters." *Journal of Engineering Mechanics*, Vol. 122, No.4, pp. 350-360.
- MATLAB, Release 2006. The MathWorks, Inc.
- Melhem, H. and Kim, H. (2003). "Damage detection in concrete by Fourier and Wavelet analyses." *Journal of Engineering Mechanics*, Vol. 129, pp. 571-577.

- Nair, K.K., Kiremidjian, A.S. and Law, K.H. (2006). "Time series-based damage detection and localization algorithm with application to the ASCE benchmark structure." *Journal of Sound and Vibration*, Vol. 291, pp. 349-368.
- Nair, K.K. and Kiremidjian, A.S. (2007). "Time series based structural damage detection algorithm using Gaussian mixtures modeling." *Journal of Dynamic Systems, Measurement, and Control*, Vol. 129, pp. 285-293.
- Newman, D.E. (1993). "An Introduction to Random Vibrations, Spectral & Wavelet Analysis, 3rd Edition." *Longman Science & Technical*, Essex, England.
- Omenzetter, P., Brownjohn, J.M.W. and Moyo, P. (2004). "Identification of unusual events in multi-channel bridge monitoring data." *Mechanical Systems and Signal Processing*, Vol.18, pp. 409-430.
- Omenzetter, P. and Brownjohn, J.M.W. (2006). "Application of time series analysis for bridge monitoring." *Smart Materials and Structures*, Vol. 15, pp. 129-138.
- Ovanesova, A.V. and Suarez, L.E. (2004). "Application of wavelet transforms to damage detection in frame structures." *Engineering Structures*, Vol. 26, pp. 39-49.
- Owen, J.S. (2003). "Monitoring the degradation of reinforced concrete beams under cyclic loading." *Key Engineering Materials*, Vols. 245-246, pp. 307-314.
- Posenato, D., Lanata, F., Inaudi, D. and Smith, I.F.C. (2008). "Model-free data interpretation for continuous monitoring of complex structures." *Advanced Engineering Informatics*, Vol. 22, No.1, pp. 135-144.
- Poudel, U.P., Fu, G. and Ye, J. (2005). "Structural damage detection using digital video imaging technique and Wavelet transformation." *Journal of Sound and Vibration*, Vol. 286, pp. 869-895.
- Poudel, U.P., Fu, G. and Ye, J. (2007). "Wavelet transformation of mode shape difference function for structural damage location identification." *Earthquake Engineering and Structural Dynamics*, Vol. 36, pp. 1089-1107.
- Rao, R.M. and Boparadikar, A.S. (1998). "Wavelet Transforms- Introduction to Theory and Applications." *Addison-Wesley*, Massachusetts.
- Ren, W.X. and Roeck, G.D. (2002). "Structural damage identification using modal data. I: Simulation verification." *Journal of Structural Engineering*, Vol. 128, No.1, pp. 87-95.
- Ren, W.X. and Sun, Z.S. (2008). "Structural damage identification by using wavelet entropy." *Engineering Structures*, Article in Press.

- Robertson, A.N., Farrar, C.R. and Sohn, H. (2002). "Singularity detection for structural health monitoring using Holder exponents." *Mechanical Systems and Signal Processing*, Vol. 17, No.6, pp. 1163-1184.
- Rytter, A. (1993). "Vibration based inspection of civil engineering structures." Ph.D. Dissertation, Aalborg University, Denmark.
- Shi, Z.Y., Law, S.S. and Zhang, L.M. (2000). "Structural damage detection from modal strain energy change." *Journal of Engineering Mechanics*, ASCE, Vol. 126, No.12, pp. 1216-1223.
- Shinde, A. and Hou, Z. (2005). "A wavelet packet based sifting process and its application for structural health monitoring." *Structural Health Monitoring*, Vol. 4, pp. 153-170.
- Sohn, H. and Law, K.H. (1997). "A Bayesian probabilistic approach for structure damage detection." *Earthquake Engineering and Structural Dynamics*, Vol. 26, pp. 1259-1281.
- Sohn, H. and Law, K.H. (2000). "Bayesian probabilistic damage detection of a reinforced-concrete bridge column." *Earthquake Engineering and Structural Dynamics*, Vol. 29, pp. 1131-1152.
- Sohn, H., Czarnecki, J.A. and Farrar, C.R. (2000). "Structural health monitoring using statistical process control." *Journal of Structural Engineering*, Vol. 126, No.11, pp. 1356-1363.
- Sohn, H. and Farrar, C.R. (2001). "Damage diagnosis using time-series analysis of vibration signals." *Smart Materials & Structures*, Vol. 10, No.3, pp. 446-451.
- Sohn, H., Worden, K. and Farrar, C.R. (2002). "Statistical damage classification under changing environmental and operational conditions." *Journal of Intelligent Material Systems and structures*, Vol. 13, No.9, pp. 561-574.
- Sohn, H., Farrar, C.R., Hemez, F.M., Shunk, D.D., Stinemates, D.W. and Nadler, B.R. (2003). "A review of structural health monitoring literature: 1996-2001. Report." LA-13976-MS: Los Alamos National Laboratory, NM.
- Staszewski, W.J. and Tomlinson, G.R. (1994). "Application of the wavelet transform to fault detection in a spur gear." *Mechanical Systems and Signal Processing*, Vol. 8, No.3, pp.289-307.
- Staszewski, W.J. (1998). "Identification of non-linear system using multi-scale ridges and skeletons of the wavelet transform." *Journal of Sound and Vibration*, Vol. 214, No.4, pp. 639-658.
- Staszewski, W.J., Worden, K. and Tomlinson, G.R. (1997). "Time-frequency analysis in gearbox fault detection using the Wigner-Ville distribution and pattern recognition." *Mechanical Systems and Signal Processing*, Vol. 11, No.5, pp. 673-692.

- Staszewski, W.J. (2000). "Advanced data pre-processing for damage identification based on pattern recognition." *International Journal of Systems Science*, Vol. 31, No.11, pp. 1381-1396.
- Sun, Z. and Chang, C.C. (2002). "Structural damage assessment based on wavelet packet transform." *Journal of Structural Engineering*, ASCE, Vol. 128, No.10, pp. 1354-1361.
- Sun, Z. and Chang, C.C. (2004). "Statistical wavelet-based method for structural health monitoring." *Journal of Structural Engineering*, Vol. 130, No.7, pp. 1055-1062.
- Tang, H., Cha, J.Z., Wang, Y. and Zhang, C. (1991). "The principal of cepstrum and its application in quantitative fault diagnostics of gears." *ASME Design Technical Conference*, Miami, FL, De-Vol. 38, pp. 141-144.
- Trendafilova, I. (2001). "Pattern recognition methods for damage diagnosis in structure from vibration measurements." Damage assessment of structures: proceedings of the 4th International Conference on Damage Assessment of Structures (DAMAS 2001), Cardiff, Wales, UK, June 25th-28th, 2001, *Key Engineering Materials*, Vol. 204-205, pp. 85-94.
- Vanik, M.W., Beck, J.L. and Au, S.K. (2000). "Bayesian probabilistic approach to structural health monitoring." *Journal of Engineering Mechanics*, ASCE, Vol. 126, No.7, pp. 738-745.
- Wang, Q. and Deng, X.M. (1999). "Damage detection with spatial wavelets." *International Journal of Solid and Structures*, Vol. 36, pp. 3443-3468.
- Wang, W.J. and McFadden. (1995). "Application of orthogonal wavelets to early gear damage detection." *Mechanical Systems and Signal Processing*, Vol. 9, No.5, pp. 497-507.
- Wang, W.J. and McFadden. (1996). "Application of wavelets to gearbox vibration signals for fault detection." *Journal of Sound and Vibration*, Vol. 192, No.5, pp. 927-939.
- Yam, L.H., Yan, Y.J. and Jiang, J.S. (2003). "Vibration-based damage detection for composite structures using wavelet transform and neural network identification." *Composite Structures*, Vol. 60, pp. 403-412.
- Yan, A.M., Boe, P.D. and Golinval, J.C. (2004). "Structural damage diagnosis by Kalman model based on stochastic subspace identification." *Structural Health Monitoring*, Vol. 3, No.2, pp. 103-119.
- Yan, Y.J. Hao, H.N. and Yam, L.H. (2004). "Vibration-based construction and extraction of structural damage feature index." *International Journal of Solid and Structures*, Vol. 41, pp. 6661-6676.

- Yan, B. and Miyamoto, A. (2006). "A comparative study of modal parameter identification based on wavelet and Hilbert-Huang transform." *Computer-Aided Civil and Infrastructure Engineering*, Vol. 21, pp. 9-23.
- Yang, J.N., Lei, Y., Lin, S. and Huang, N. (2004). "Hilbert-Huang based aproach for structural damage detection." *Journal of Engineering Mechanics*, Vol. 130, No.1, pp. 85-95.
- Yen, G.G. and Lin, K.C. (2000). "Wavelet packet feature extraction for vibration monitoring." *IEEE Transactions on Industrial Electronics*, Vol. 147, pp. 650-667.
- Yoon, D.J., Weiss, W.J. and Shah, S.P. (2000). "Assessing damage in corroded reinforced concrete using acoustic emission." *Journal of Engineering Mechanics*, ASCE, Vol. 126, No.3, pp. 273-283.
- Zhang, Q.W. (2007). "Statistical damage identification for bridge using ambient vibration data." *Computers and Structures*, Vol. 85, pp. 476-485.

Appendix A - Numerical Structure Properties

For the Column

$$b_c := 1 \quad h_c := \frac{2}{8} \quad E := 29000000 \quad L_c := 20$$

$$I_{c_single} := \frac{b_c \cdot h_c^3}{12}$$

$$I_{c_single} = 1.302 \times 10^{-3}$$

$$I_c := 5 \cdot I_{c_single}$$

$$I_c = 6.51 \times 10^{-3}$$

$$k := 2 \cdot \frac{12 \cdot E \cdot I_c}{L_c^3}$$

$$k = 566.406$$

$$K := \begin{pmatrix} k + k & -k & 0 \\ -k & k + k & -k \\ 0 & -k & k \end{pmatrix}$$

$$K = \begin{pmatrix} 1.133 \times 10^3 & -566.406 & 0 \\ -566.406 & 1.133 \times 10^3 & -566.406 \\ 0 & -566.406 & 566.406 \end{pmatrix}$$

$$w := 490 \frac{\text{lb}}{\text{ft}^3}$$

$$w = 0.284 \frac{\text{lb}}{\text{in}^3}$$

$$\text{density} := \frac{w}{g}$$

$$\text{density} = 7.345 \times 10^{-4} \frac{\text{lb} \cdot \text{s}^2}{\text{in}^4}$$

$$\rho := 7.345 \cdot 10^{-4}$$

$$b_{\text{floor}} := 20 \qquad h_{\text{floor}} := 2 \qquad L_{\text{floor}} := 26$$

$$m := \rho \cdot b_{\text{floor}} \cdot h_{\text{floor}} \cdot L_{\text{floor}}$$

$$m = 0.764$$

$$M := \begin{pmatrix} m & 0 & 0 \\ 0 & m & 0 \\ 0 & 0 & m \end{pmatrix} \qquad M = \begin{pmatrix} 0.764 & 0 & 0 \\ 0 & 0.764 & 0 \\ 0 & 0 & 0.764 \end{pmatrix}$$

$$\left| K - \omega^2 \cdot M \right| \rightarrow \frac{5954345703125}{32768} - 1470389.7399902343750 \cdot \omega^2 + 1652.5260720312500000 \cdot \omega^4 - .44573364644307200000 \cdot \omega^6$$

$$\frac{5954345703125}{32768} - 1470389.7399902343750 \cdot \omega + 1652.5260720312500000 \cdot \omega^2 - .44573364644307200000 \cdot \omega^3 \text{ solve, } \omega \rightarrow \begin{pmatrix} 146.86037640636072886 \\ 1152.9795314743318177 \\ 2407.5895967535431973 \end{pmatrix}$$

$$\omega_1 := \sqrt{146.86037640636072886}$$

$$\omega_1 = 12.119$$

$$f_1 := \frac{\omega_1}{2 \cdot \pi}$$

$$f_1 = 1.929$$

$$T_1 := \frac{1}{f_1}$$

$$T_1 = 0.518$$

$$\omega_2 := \sqrt{1152.9795314743318177}$$

$$\omega_2 = 33.956$$

$$f_2 := \frac{\omega_2}{2 \cdot \pi}$$

$$f_2 = 5.404$$

$$T_2 := \frac{1}{f_2}$$

$T_2 = 0.185$

$$\omega_3 := \sqrt{2407.5895967535431973}$$

$\omega_3 = 49.067$

$$f_3 := \frac{\omega_3}{2 \cdot \pi}$$

$f_3 = 7.809$

$$T_3 := \frac{1}{f_3}$$

$T_3 = 0.128$

Choose the acceleration record period

$$T_{\text{record}} := 3 \cdot \max(T_1, T_2, T_3)$$

$T_{\text{record}} = 1.555$

choose T=2 second

For the unit nodal rotation of the column

$$M_c := \frac{4 \cdot E \cdot I_c}{L_c}$$

$$M_c = 3.776 \times 10^4$$

For the floor

$$b_{\text{floor}} := 20$$

$$h_{\text{floor}} := 2$$

$$L_{\text{floor}} := 26$$

$$I_f := \frac{b_{\text{floor}} \cdot h_{\text{floor}}^3}{12}$$

$$I_f = 13.333$$

For the unit nodal rotation of the floor

$$M_f := \frac{4 \cdot E \cdot I_f}{L_{\text{floor}}}$$

$$M_f = 5.949 \times 10^7$$

$$n := \frac{M_f}{M_c}$$

$$n = 1.575 \times 10^3$$

Check the bucking

Both column ends fixed, lateral motion exists: $K=1$

$$E := 29000000$$

$$k := 1$$

Theoretical bucking load

$$P_{\text{cr}} := \frac{\pi^2 \cdot E \cdot I_{\text{c_single}}}{(k \cdot L_c)^2}$$

$$P_{\text{cr}} = 931.701$$

$$P := 4 \cdot P_{cr}$$

$$P = 3.727 \times 10^3$$

Design compression strength for flexural buckling

$$A_g := b_c \cdot h_c$$

$$A_g = 0.25$$

$$r := \sqrt{\frac{I_{c_single}}{A_g}}$$

$$r = 0.072$$

$$F_y := 36000$$

$$\lambda_c := \frac{k \cdot L_c}{r \cdot \pi} \cdot \sqrt{\frac{F_y}{E}}$$

$$\lambda_c = 3.108$$

$$\lambda > 1.5$$

$$F_{cr} := \frac{0.877}{\lambda_c^2} \cdot F_y$$

$$F_{cr} = 3.268 \times 10^3$$

$$P_n := A_g \cdot F_{cr}$$

$$P_n = 817.102$$

$$\phi := 0.85$$

$$P_{total} := 4 \cdot \phi \cdot P_n$$

$$P_{total} = 2.778 \times 10^3$$

$$w_{floor} := 490 \cdot \frac{b_{floor}}{12} \cdot \frac{h_{floor}}{12} \cdot \frac{L_{floor}}{12}$$

$$w_{floor} = 294.907$$

$$w_{\text{column}} := 490 \cdot \frac{b_c}{12} \cdot \frac{h_c}{12} \cdot \frac{L_c}{12}$$

$$W := 3 \cdot w_{\text{floor}} + 20 \cdot w_{\text{column}}$$

$$W = 913.079$$

$W < P$ that means under selfweight there is no buckling happened at each of the columns

$$P_{\text{column_compression}} := \frac{W}{4}$$

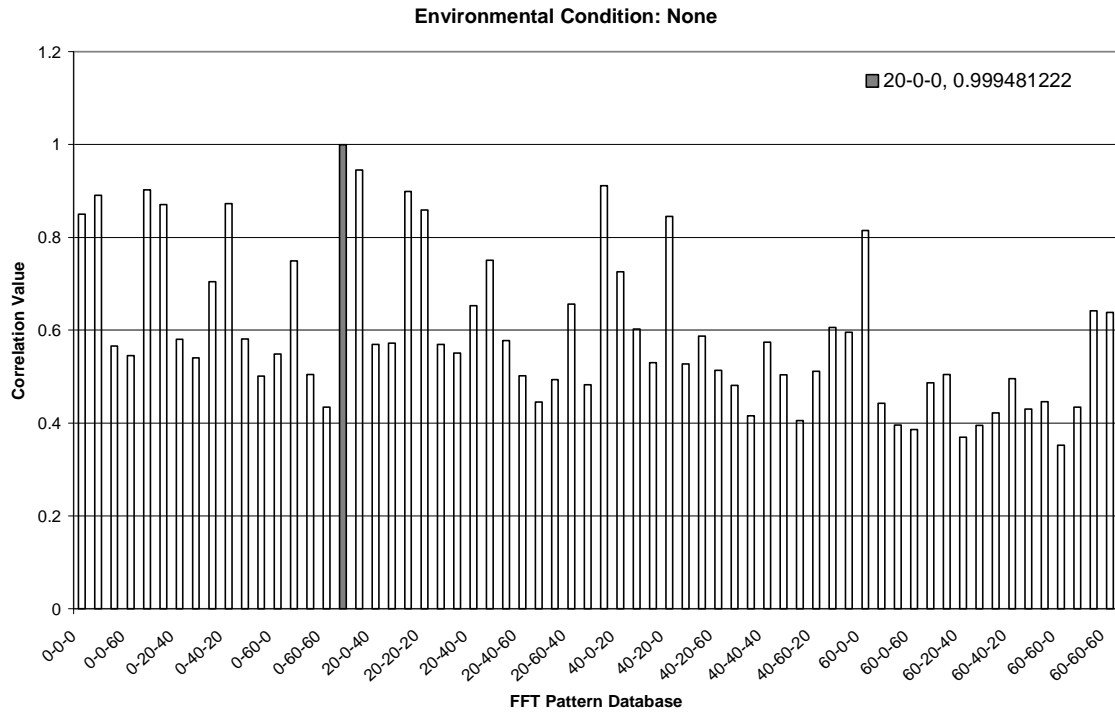
$$P_{\text{column_compression}} = 228.27$$

$$F := \frac{P_{\text{column_compression}}}{A_g}$$

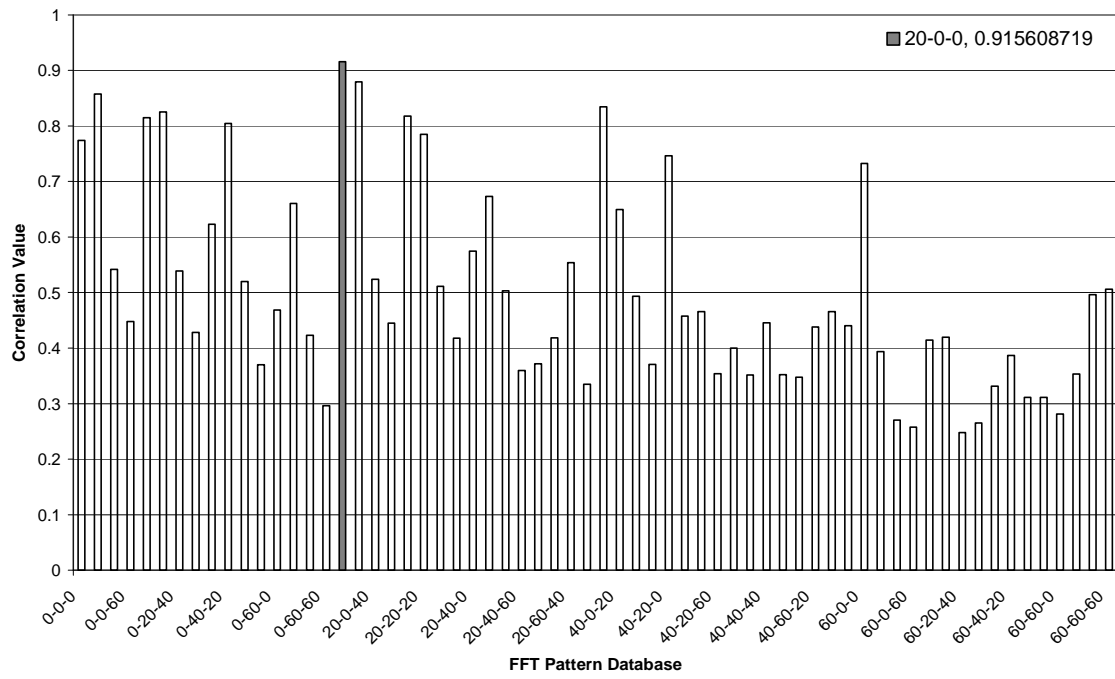
$$F = 913.079$$

Appendix B - Matching Results in Numerical Study

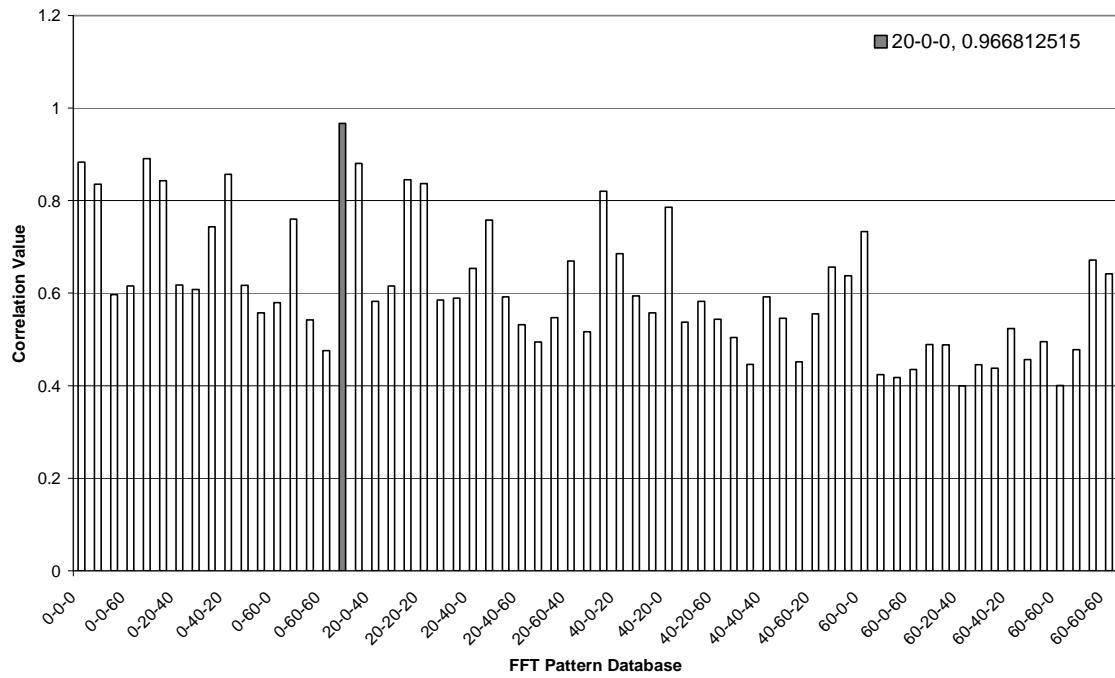
Figure B.1 Correlation Matching for Damage Case 19-0-0 (FFT Pattern Database)



Environmental Condition: Noise Only



Environmental Condition: Damping Only



Environmental Condition: Damping & Noise

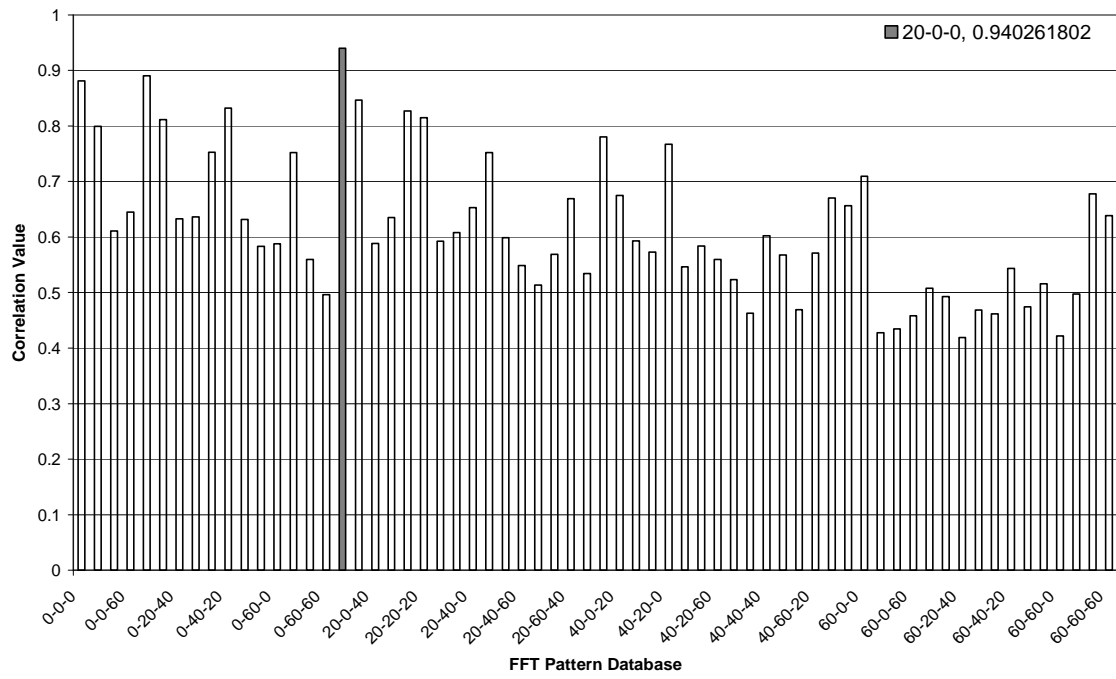
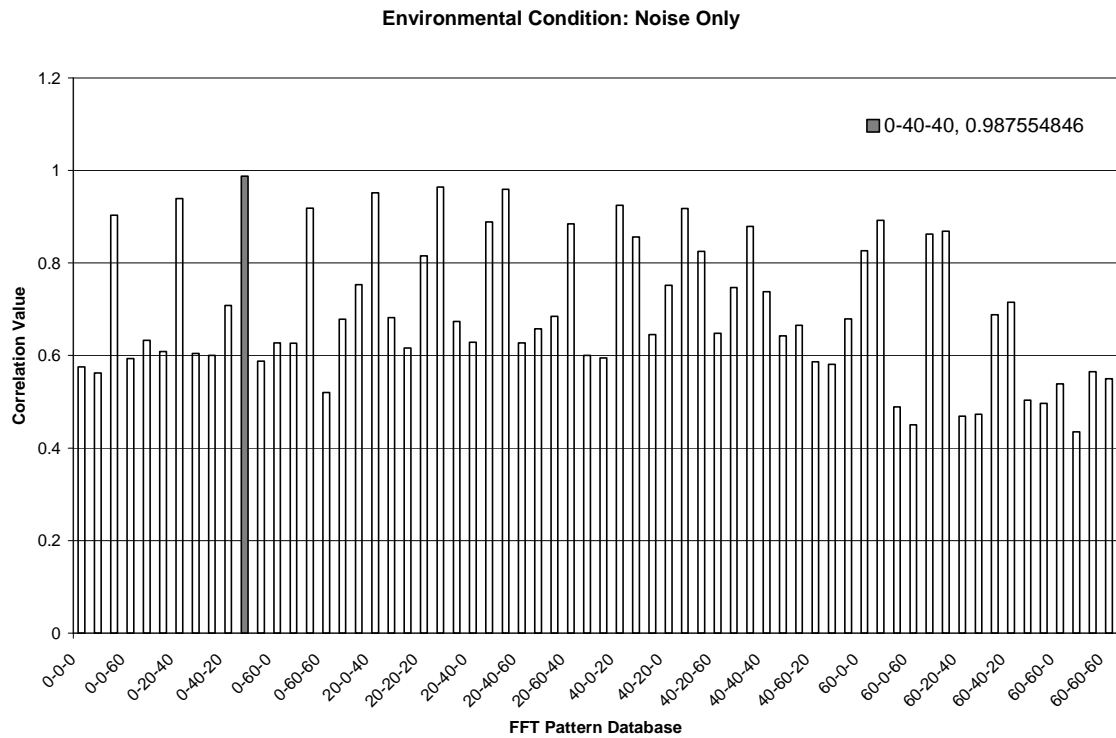
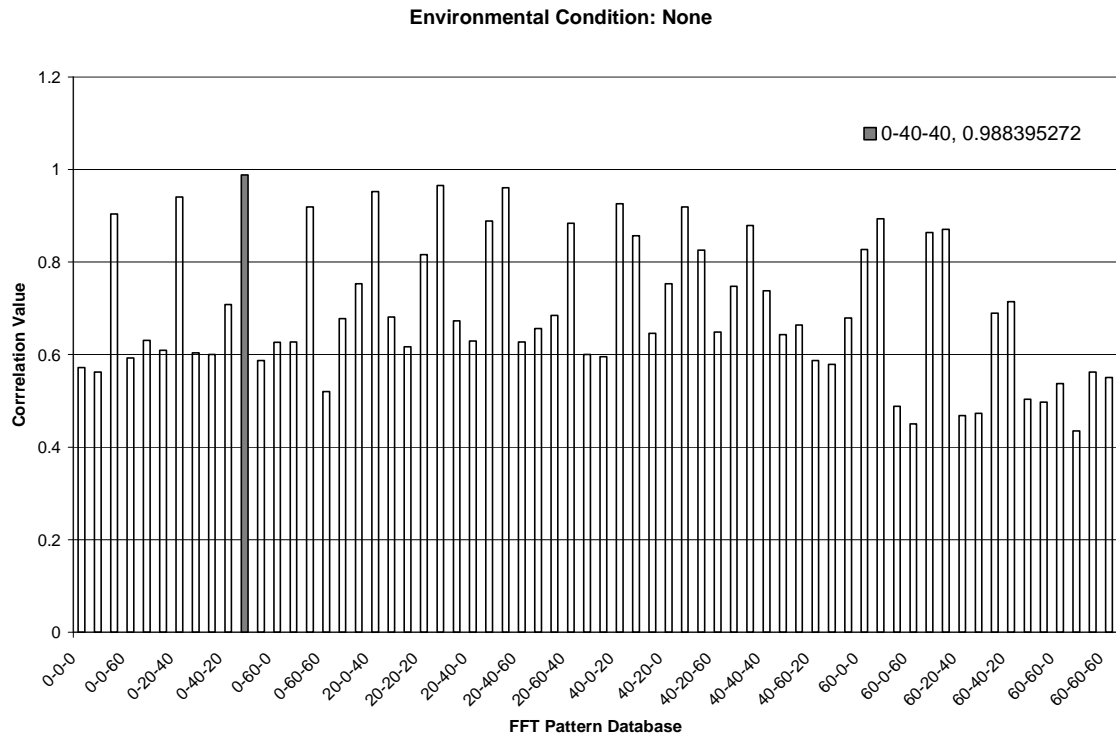
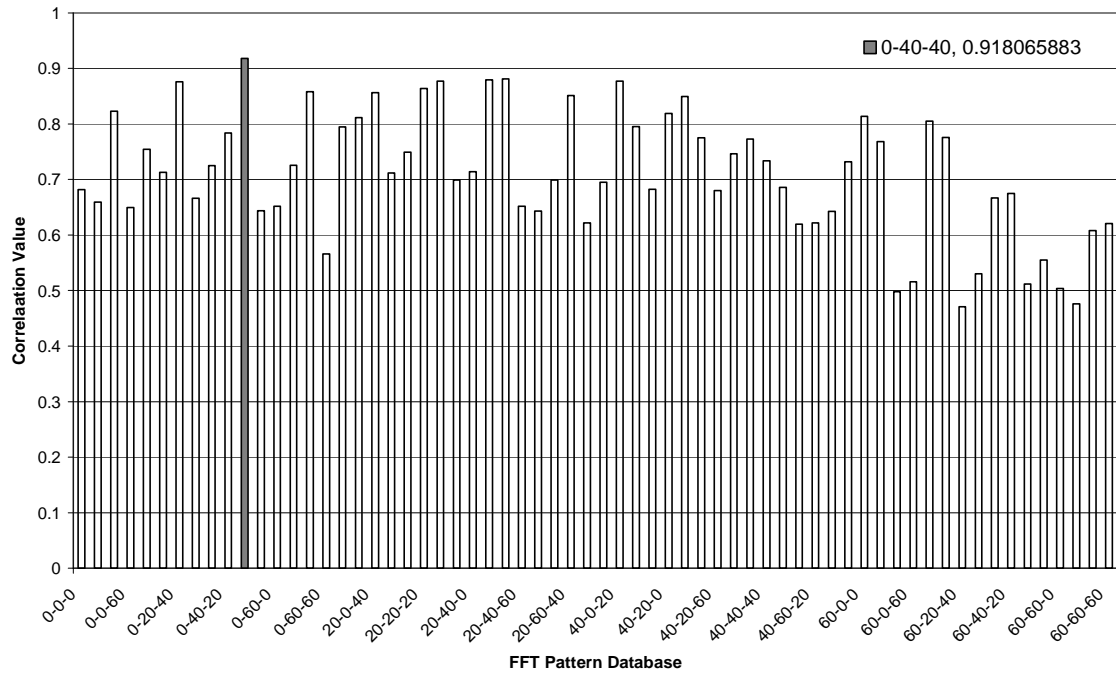


Figure B.2 Correlation Matching for Damage Case 0-38-38 (FFT Pattern Database)



Environmental Condition: Damping Only



Environmental Condition: Damping and Noise

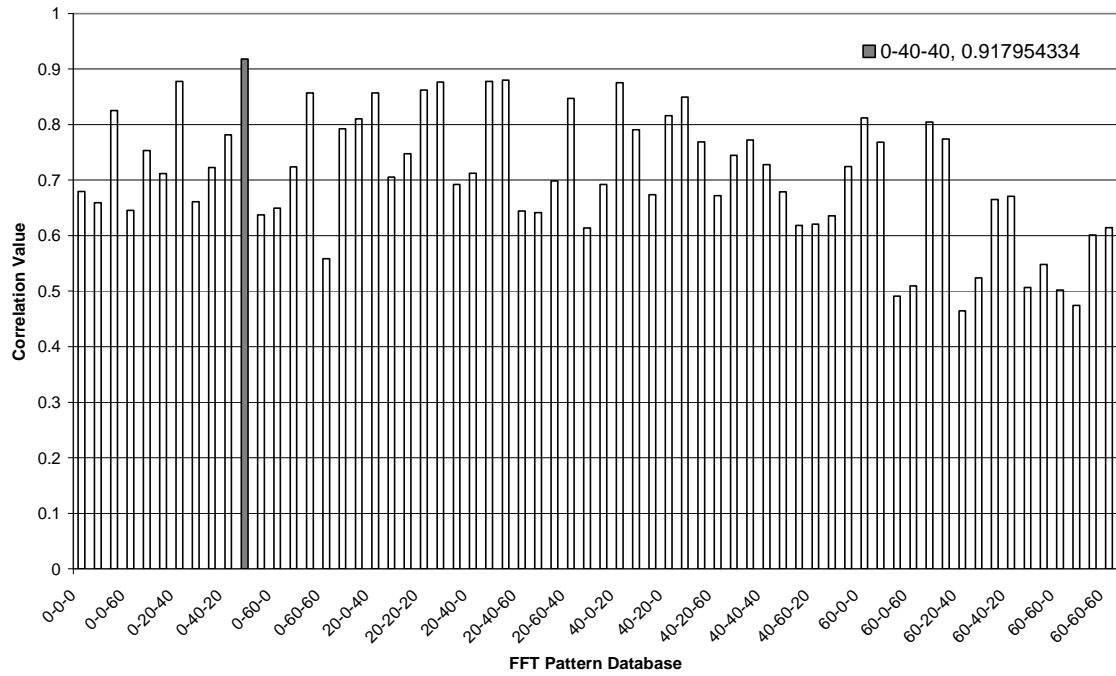
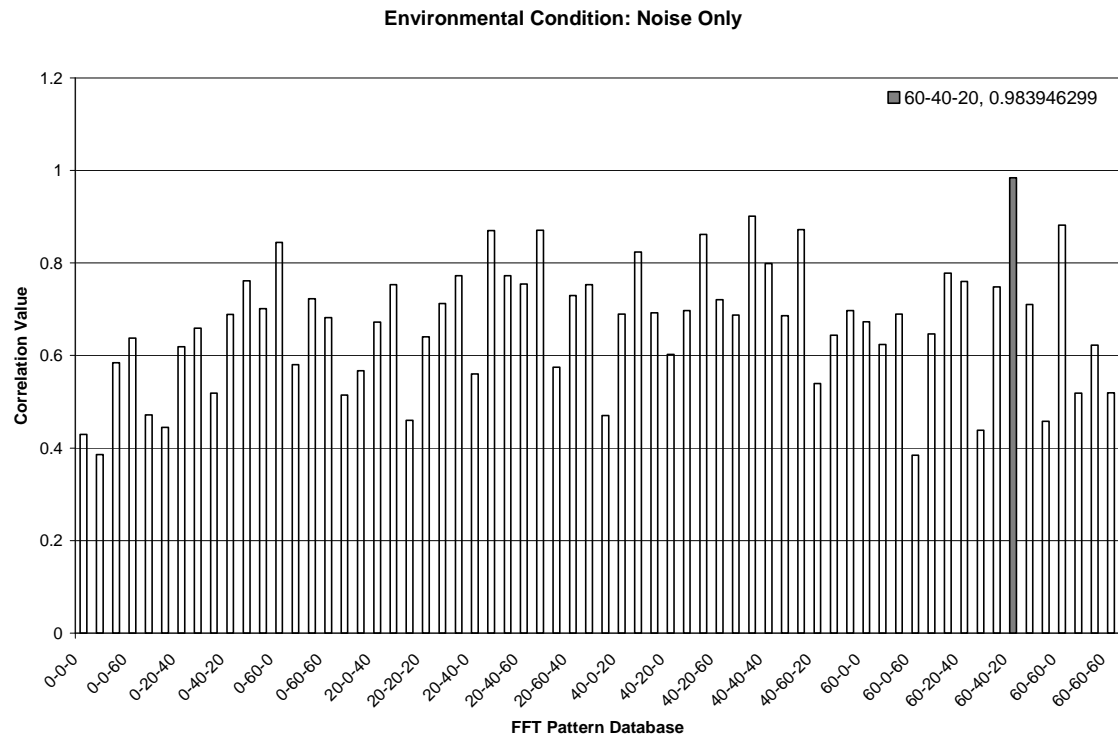
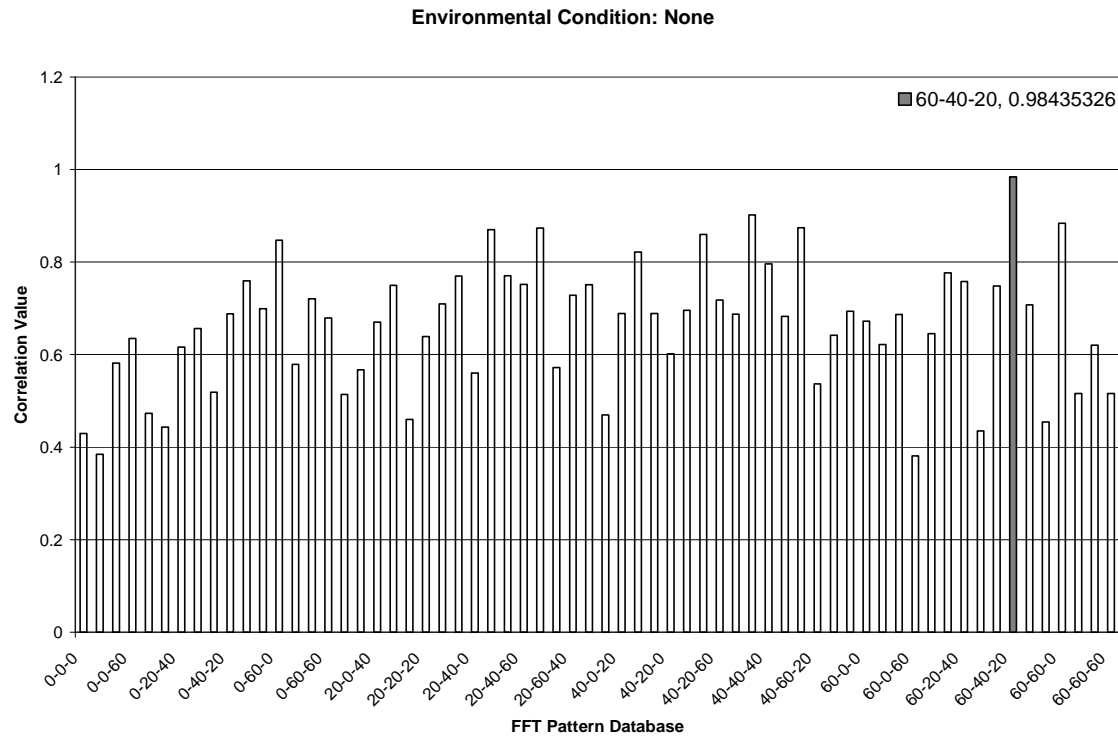
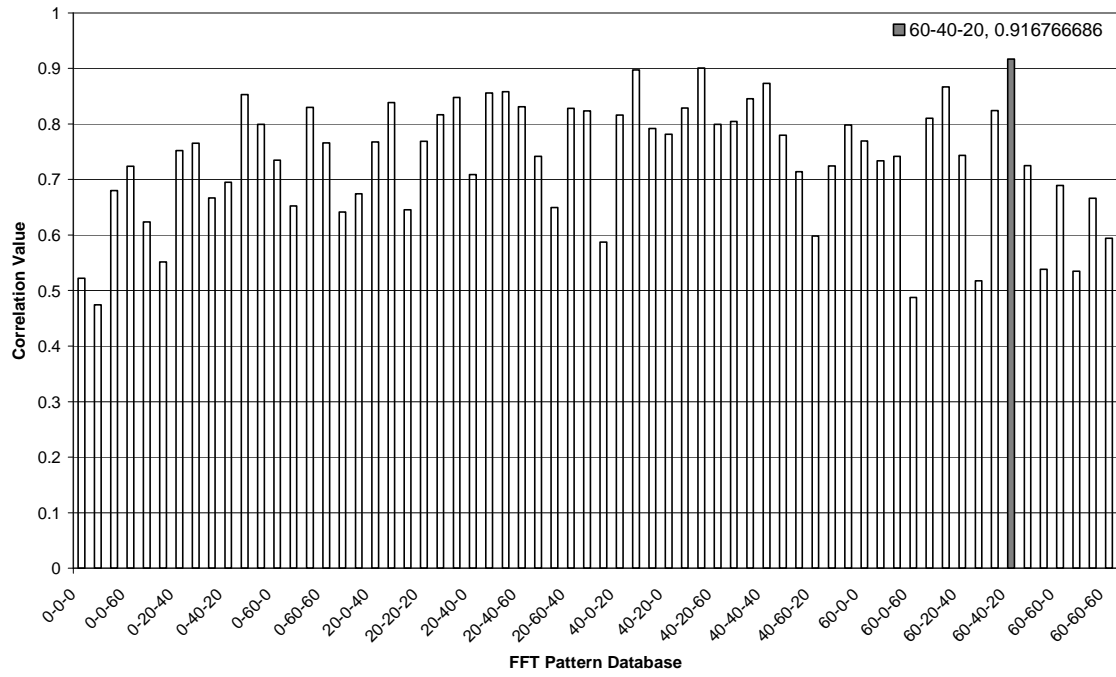


Figure B.3 Correlation Matching for Damage Case 58-38-19 (FFT Pattern Database)



Environmental Condition: Damping Only



Environmental Condition: Damping & Noise

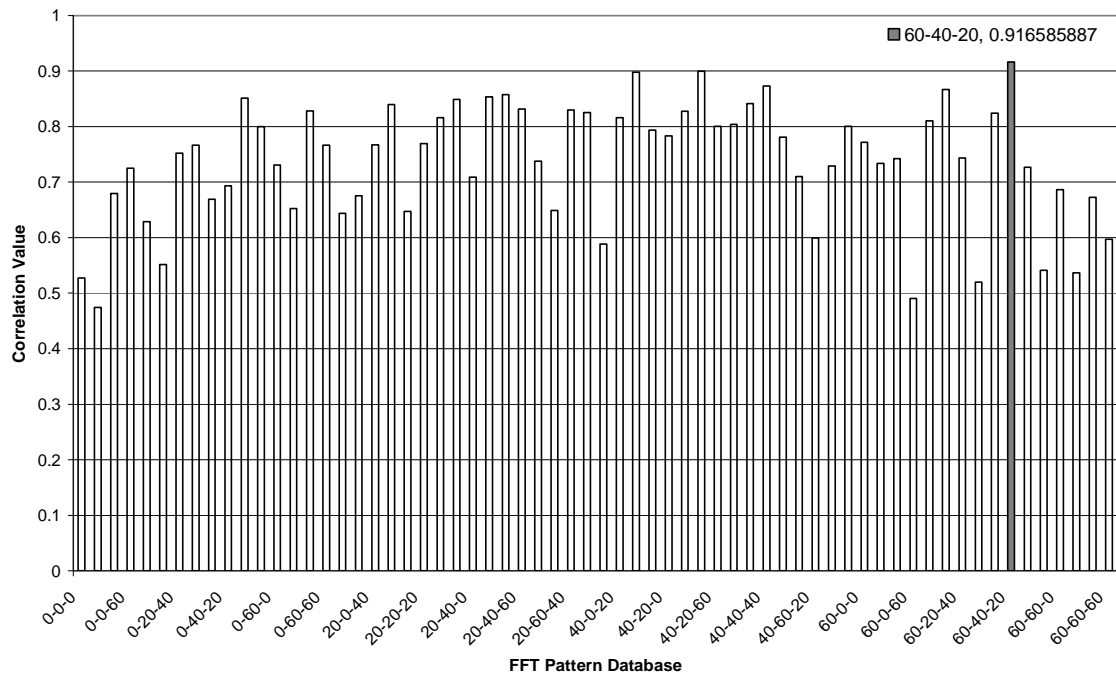
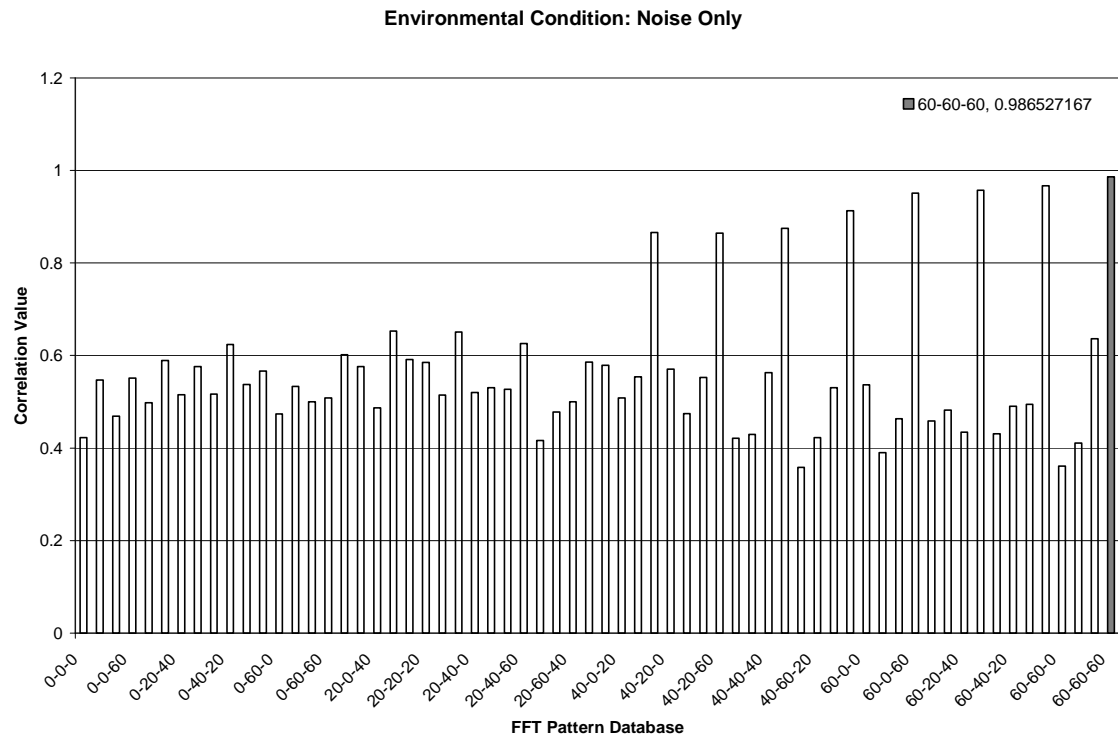
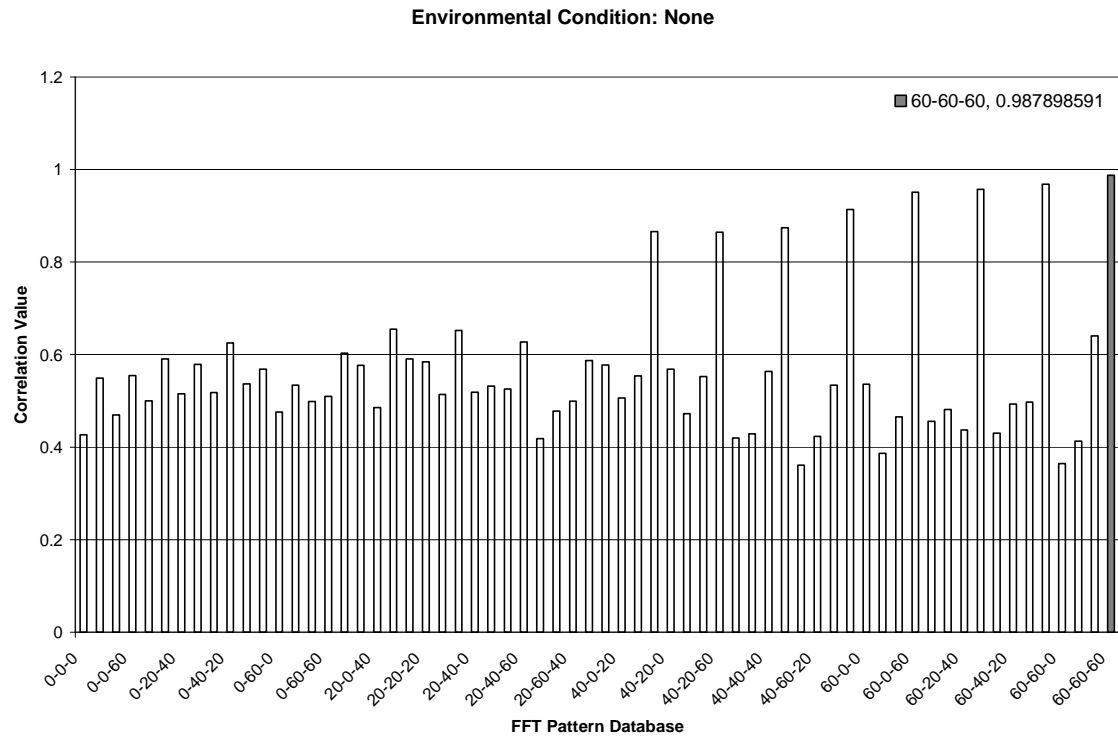
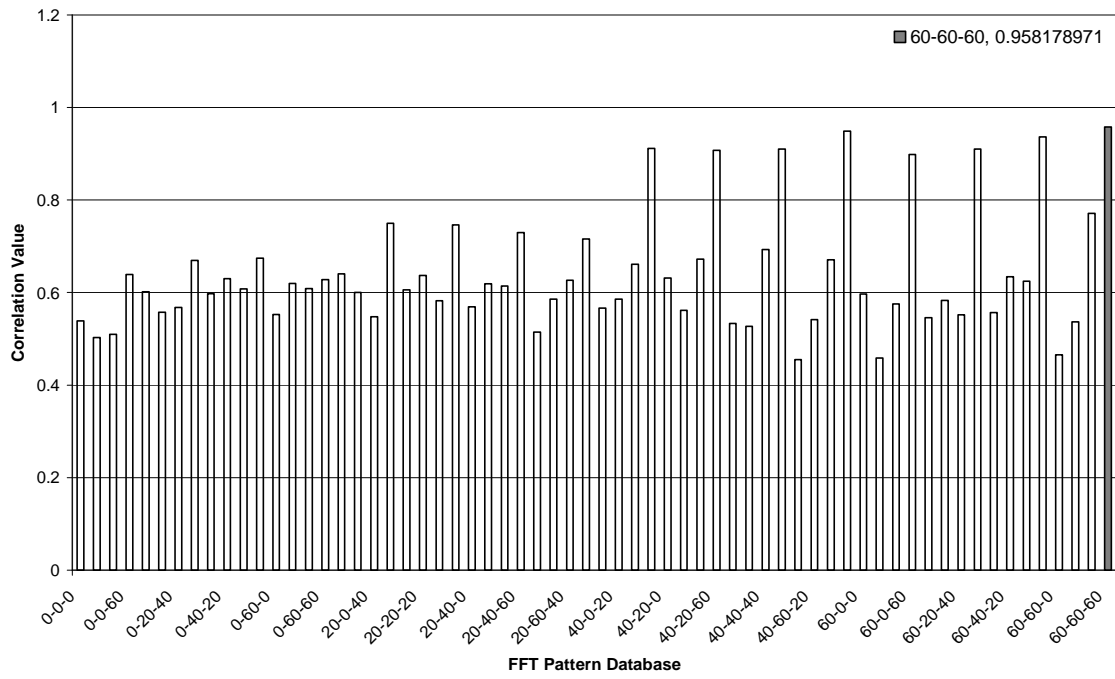


Figure B.4 Correlation Matching for Damage Case 58-58-58 (FFT Pattern Database)



Environmental Condition: Damping Only



Environmental Condition: Damping & Noise

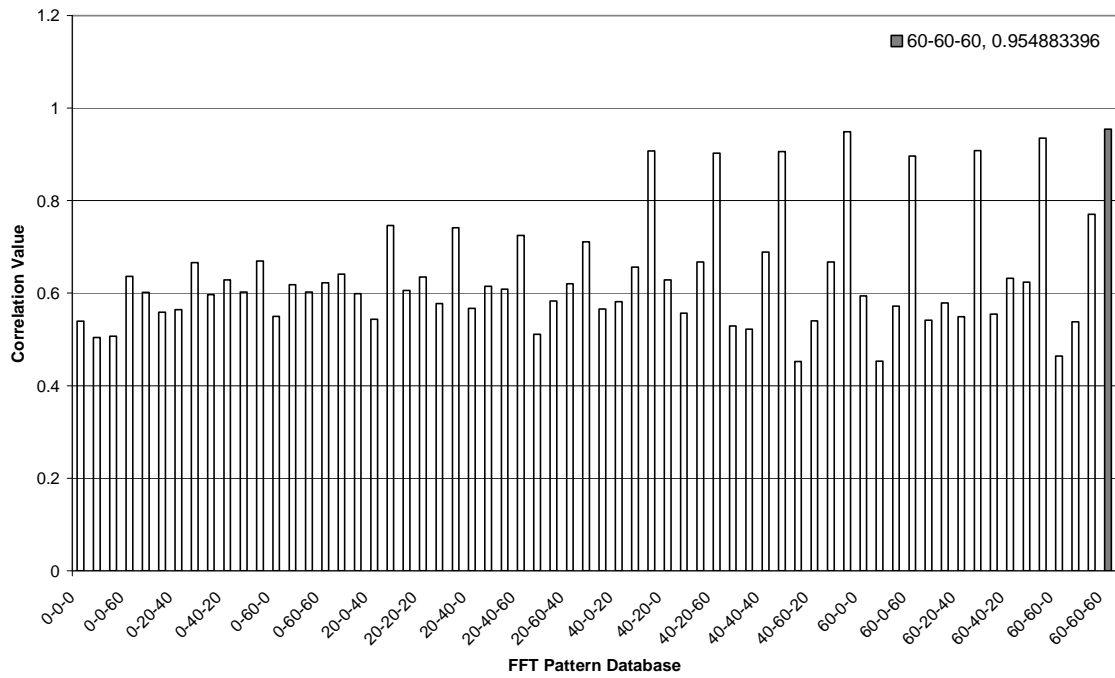
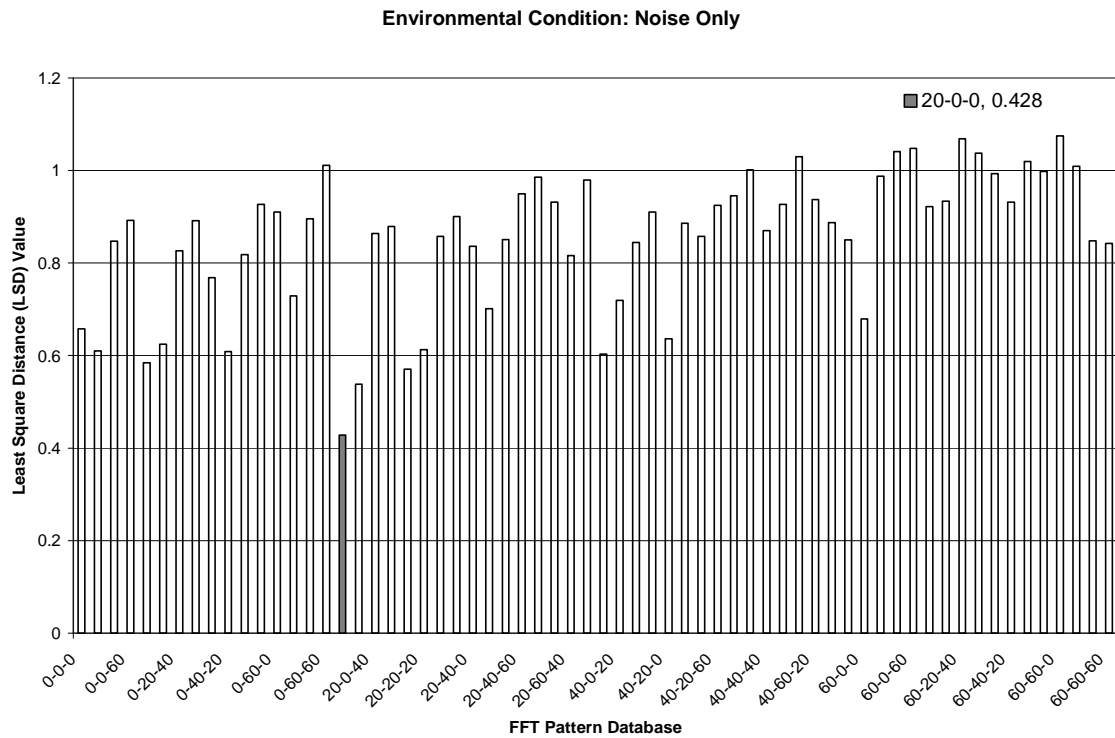
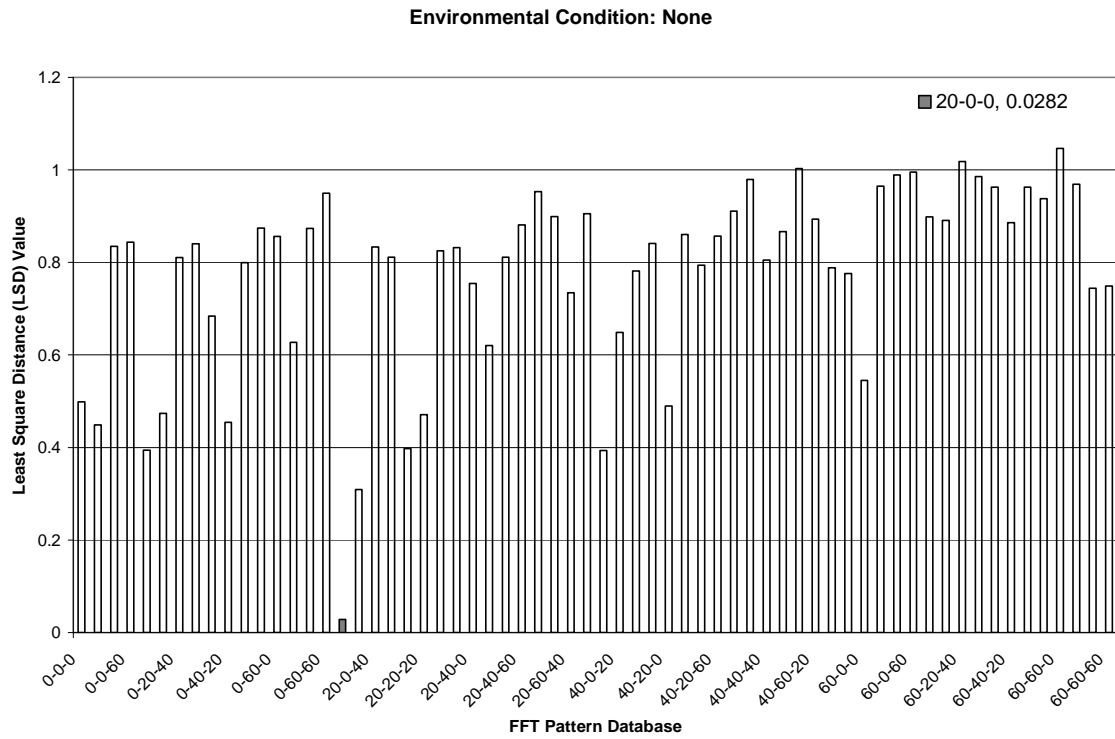
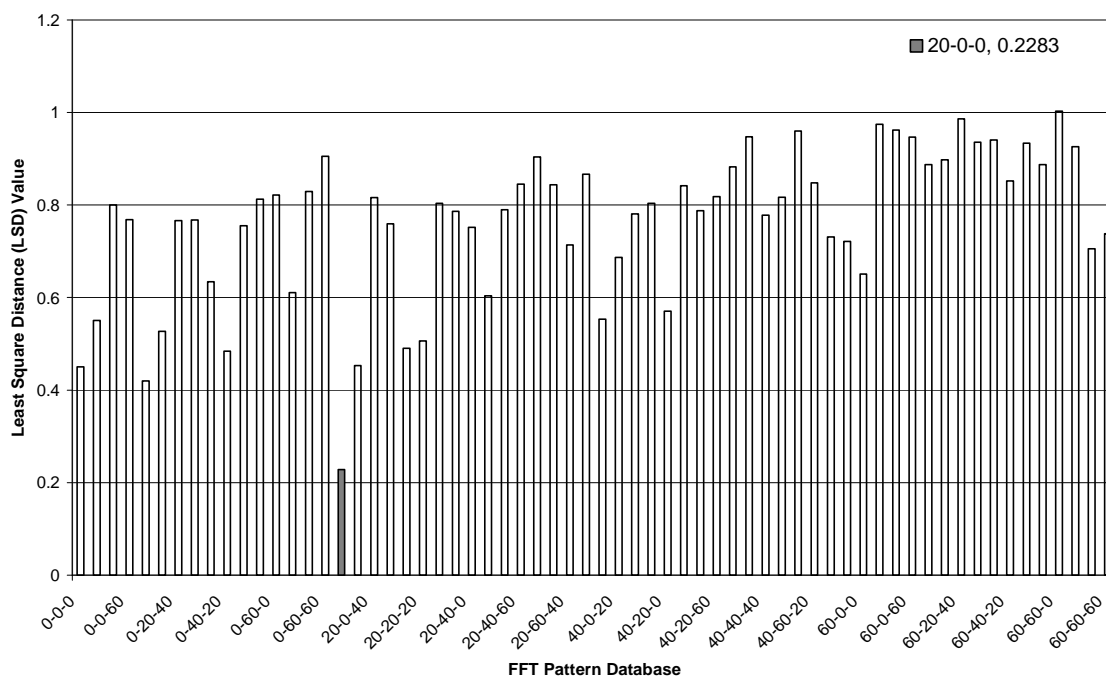


Figure B.5 Least Square Distance (LSD) Matching for Damage Case 19-0-0 (FFT Pattern Database)



Environmental Condition: Damping Only



Environmental Condition: Damping & Noise

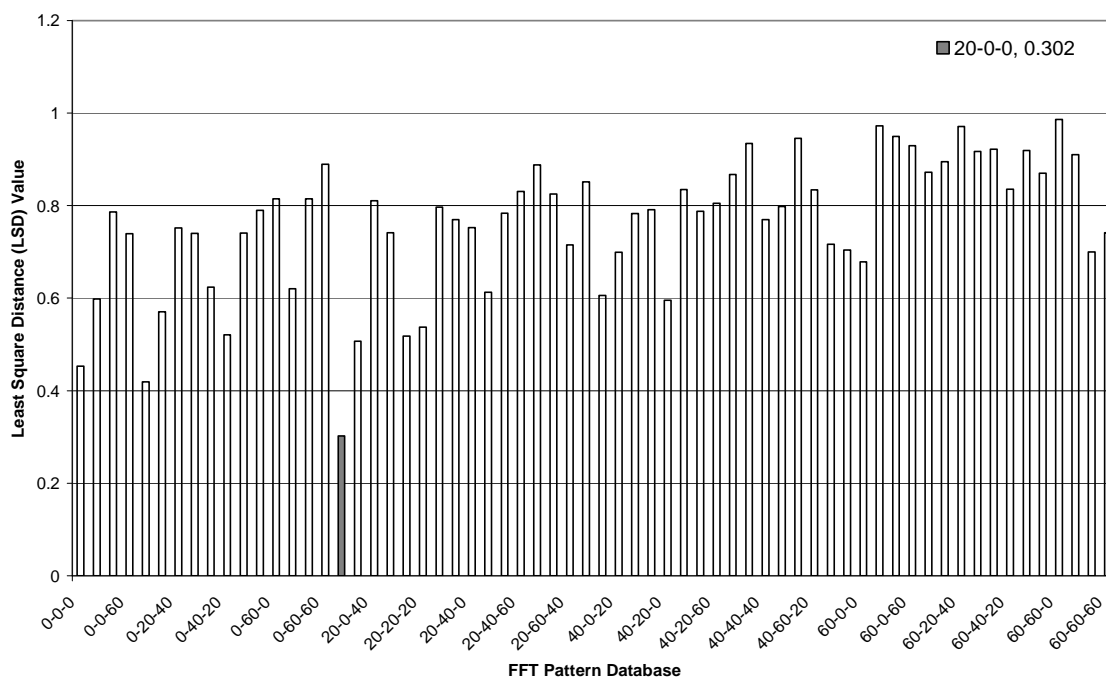
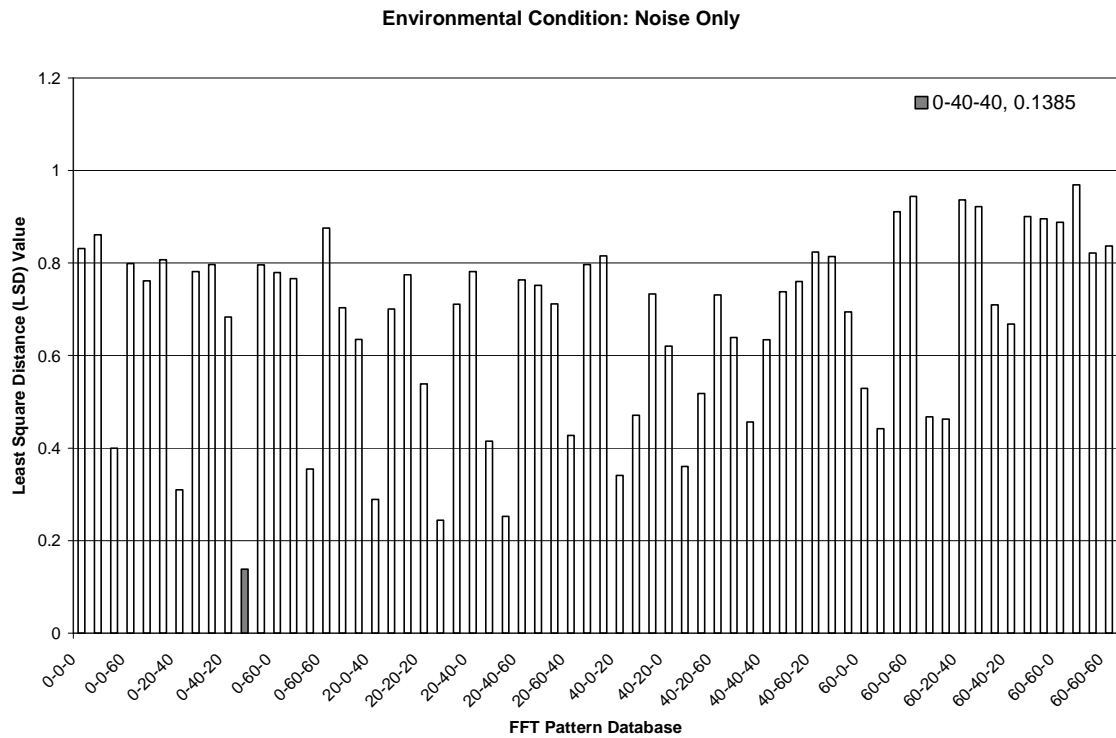
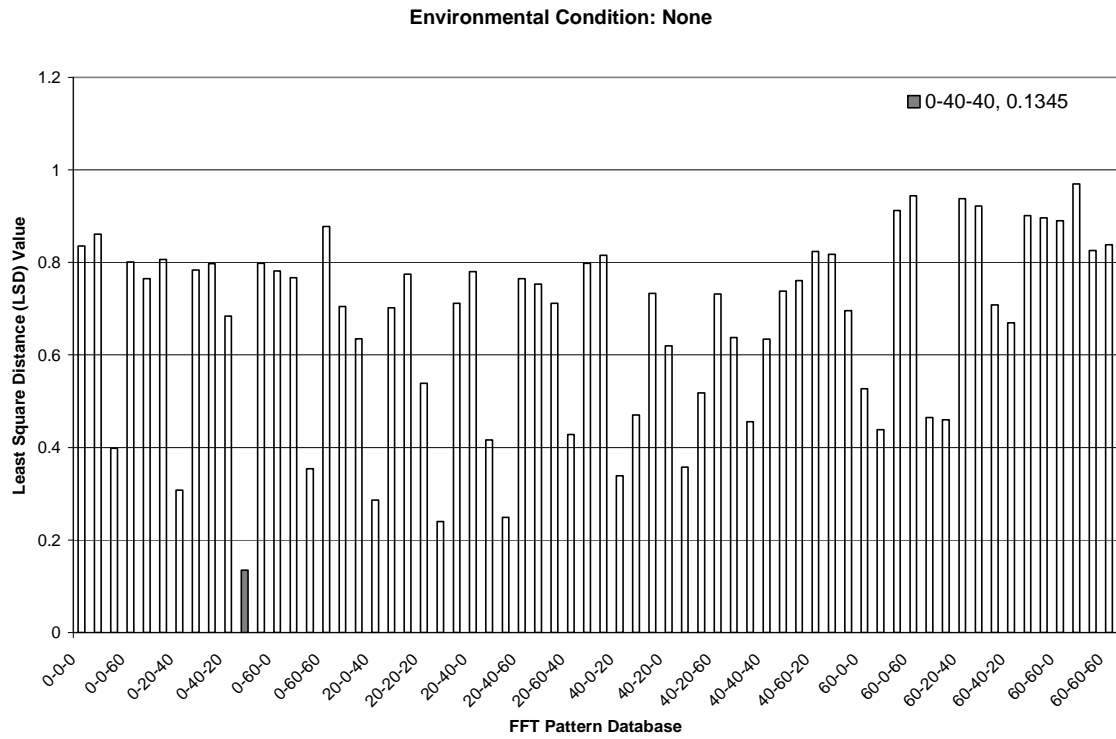
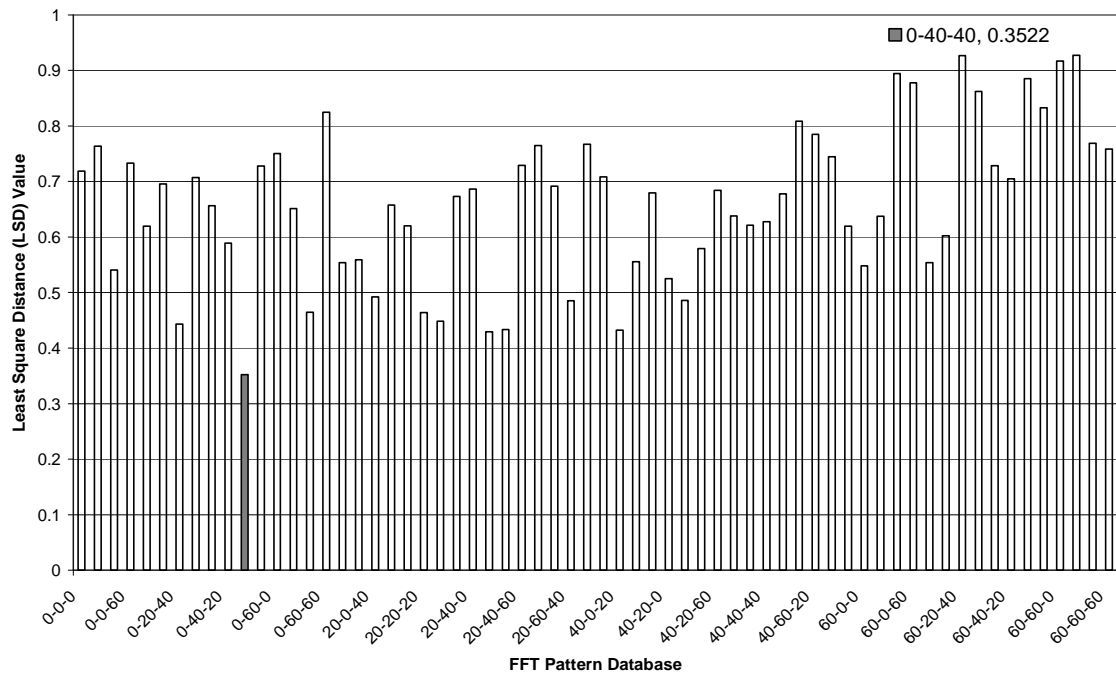


Figure B.6 Least Square Distance (LSD) Matching for Damage Case 0-38-38 (FFT Pattern Database)



Environmental Condition: Damping Only



Environmental Condition: Damping & Noise

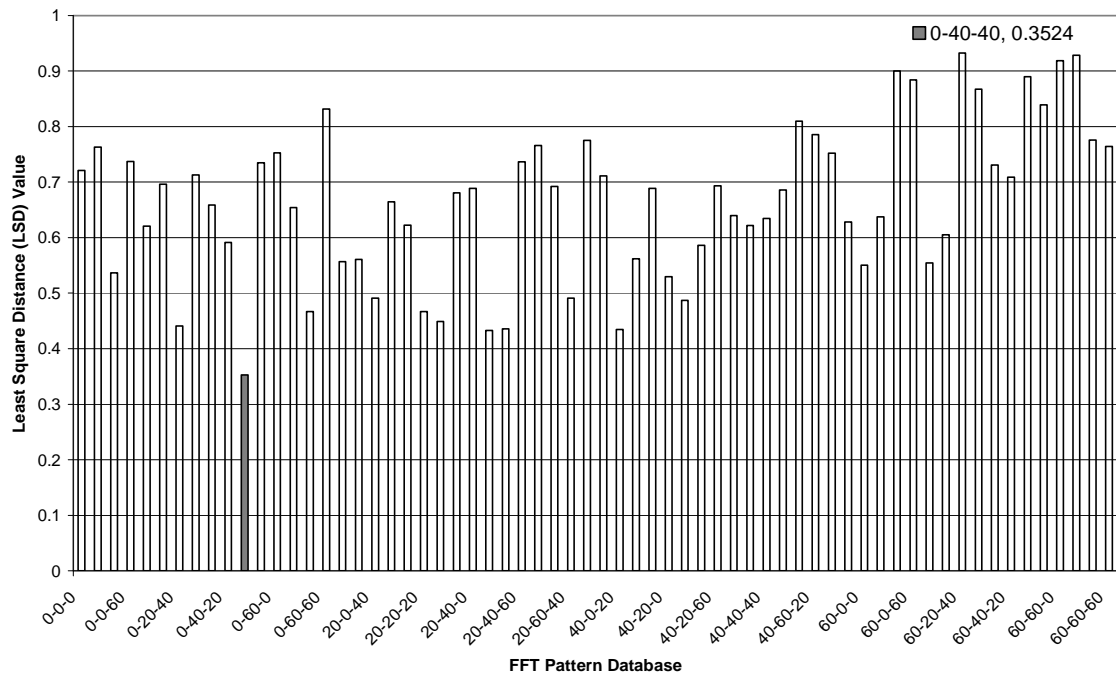
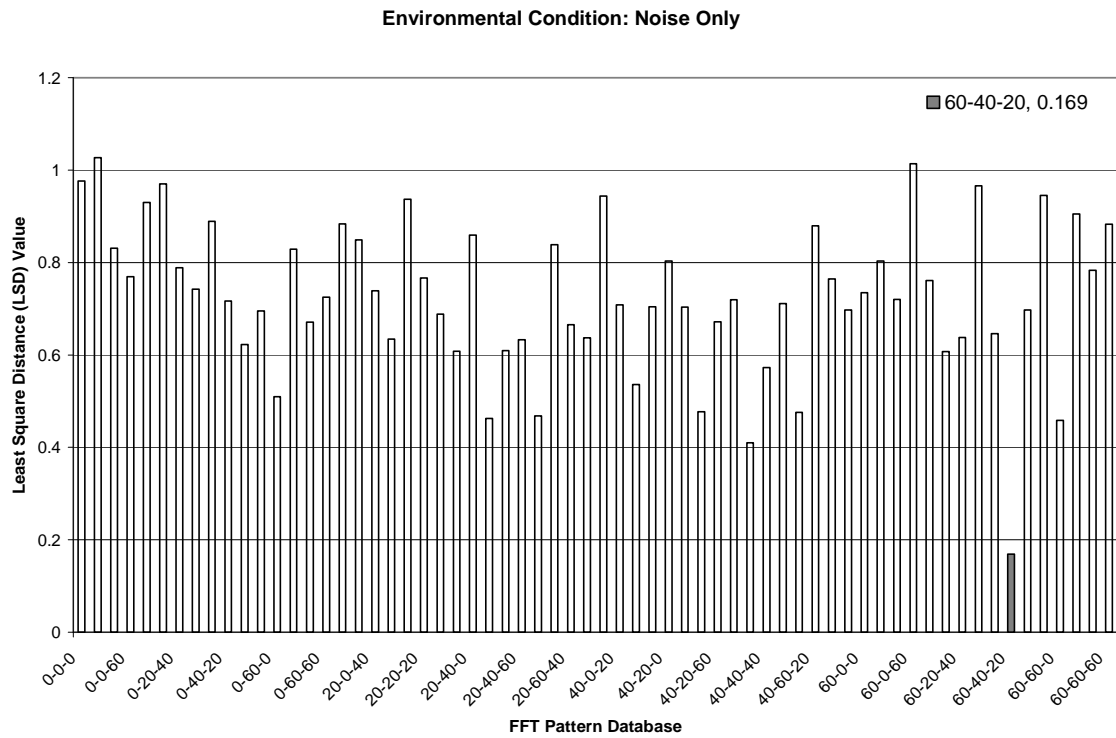
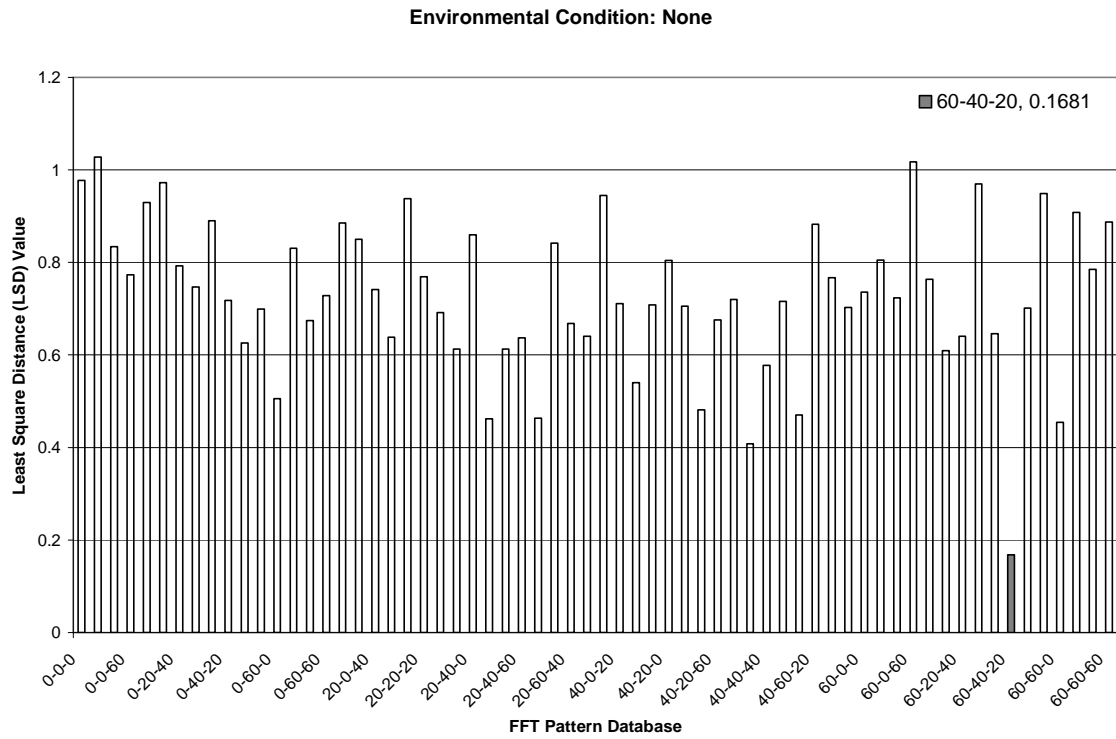
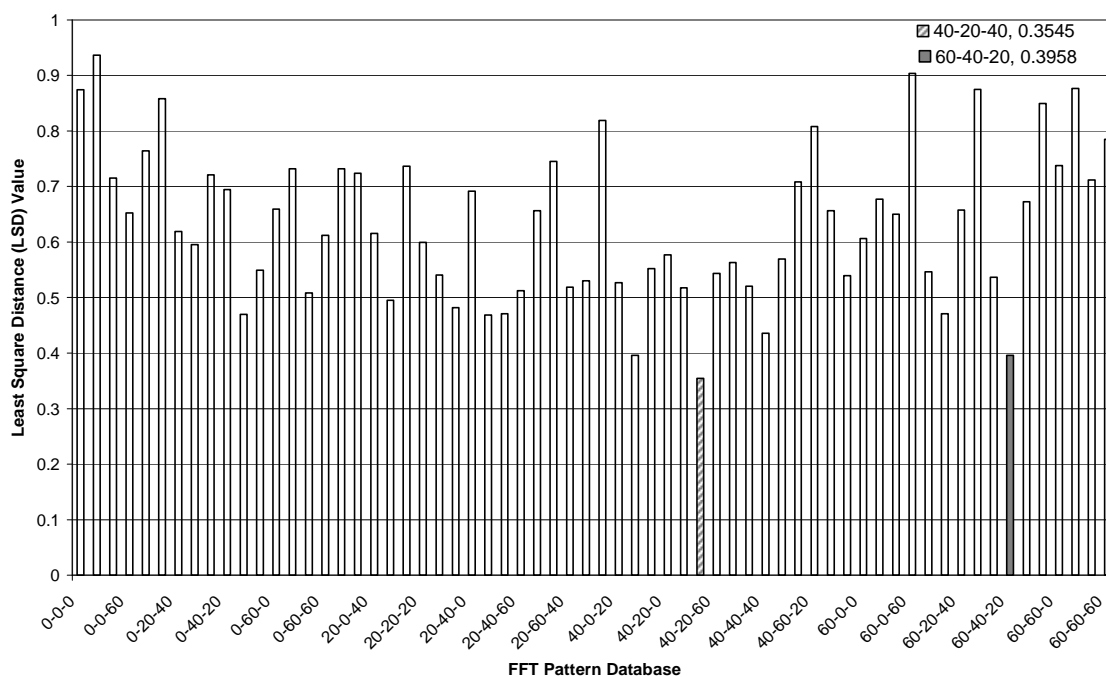


Figure B.7 Least Square Distance (LSD) Matching for Damage Case 58-38-19 (FFT Pattern Database)



Environmental Condition: Damping Only



Environmental Condition: Damping & Noise

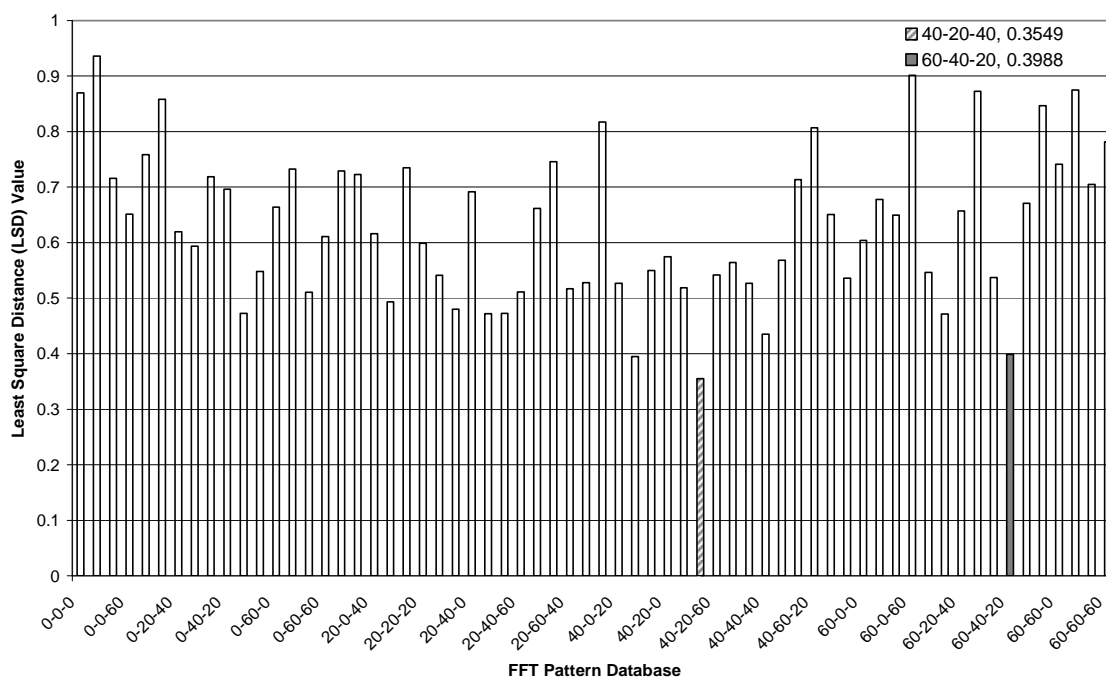
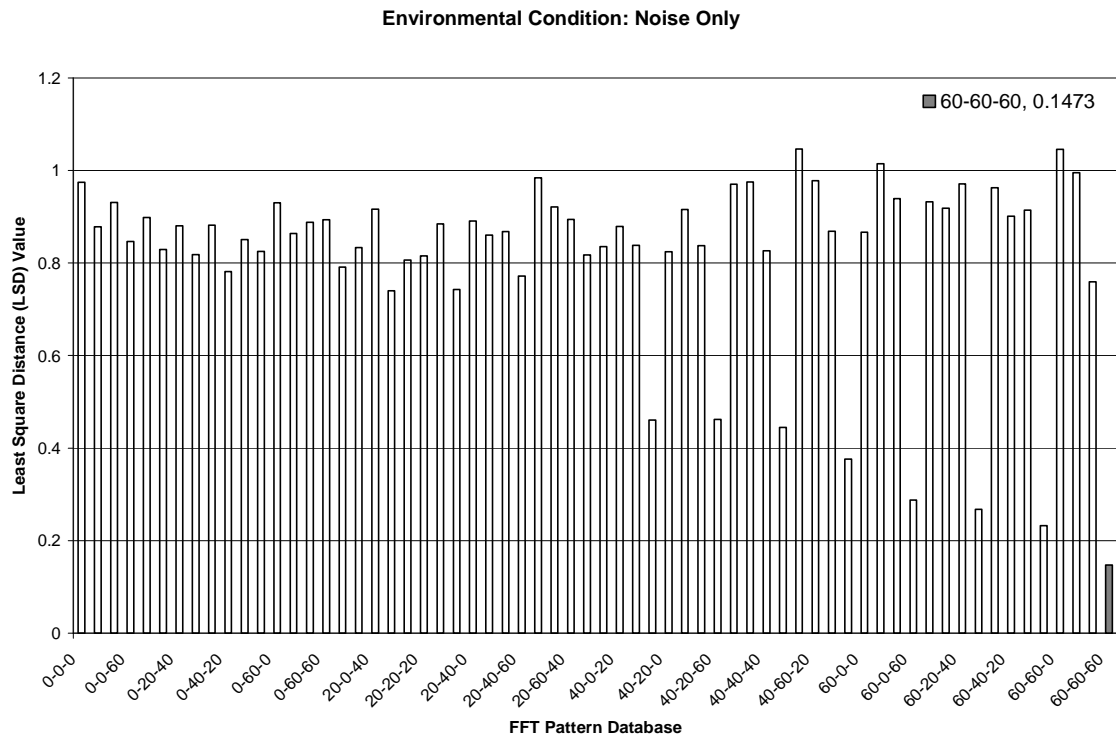
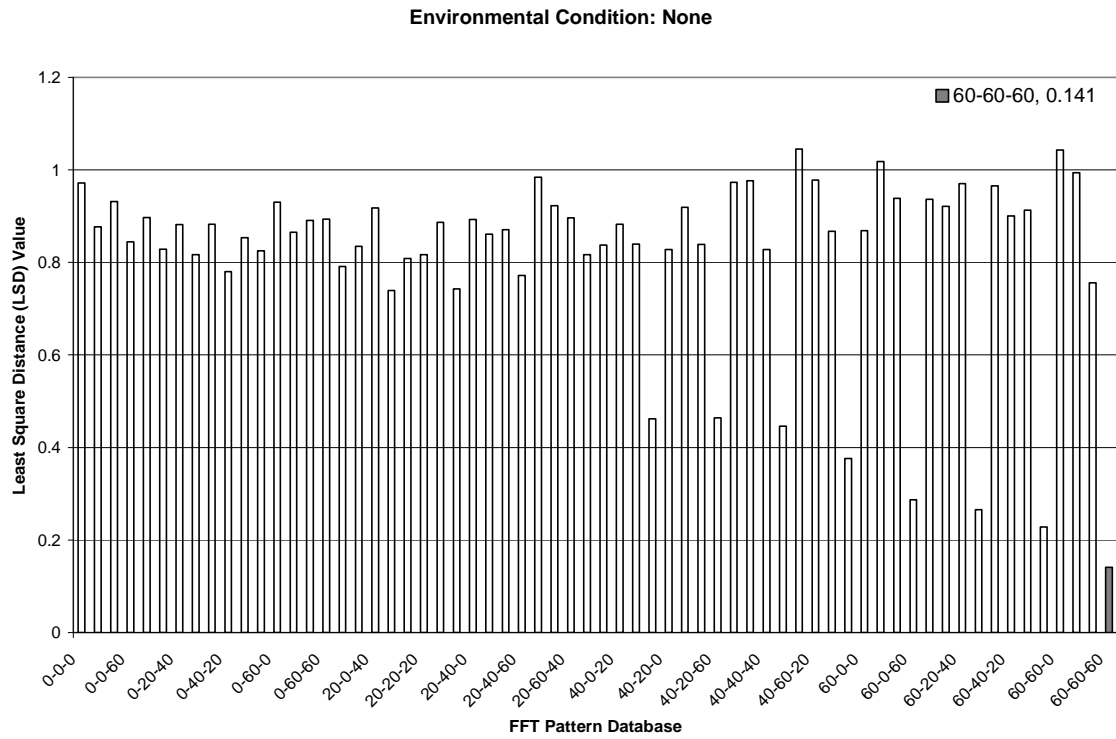
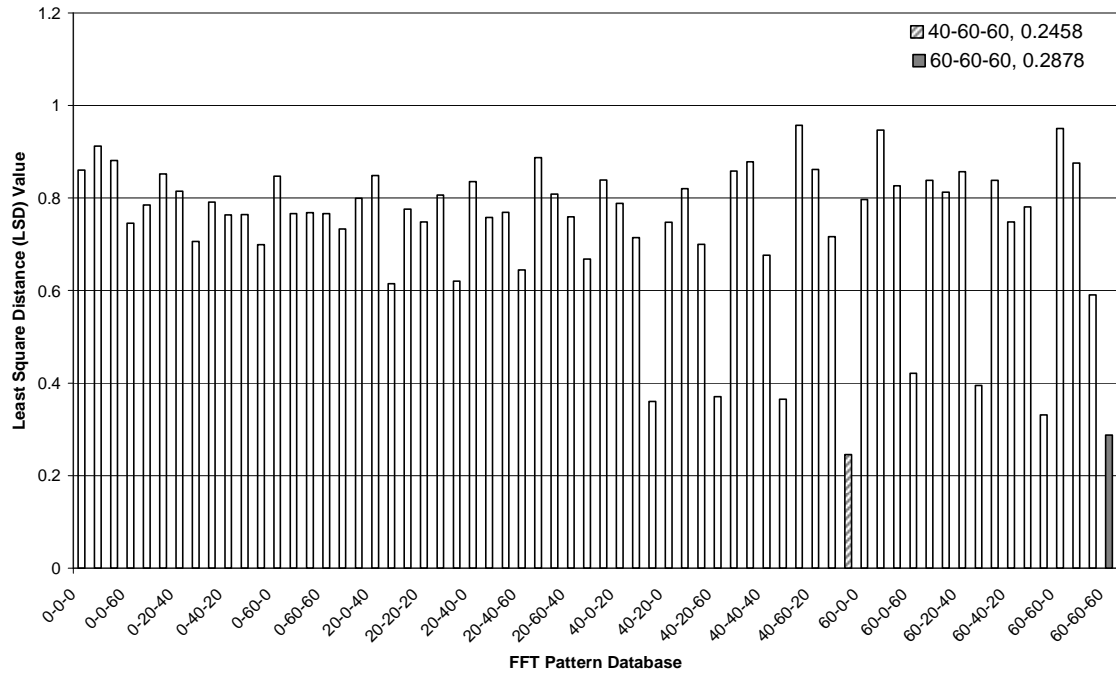


Figure B.8 Least Square Distance (LSD) Matching for Damage Case 58-58-58 (FFT Pattern Database)



Environmental Condition: Damping Only



Environmental Condition: Damping & Noise

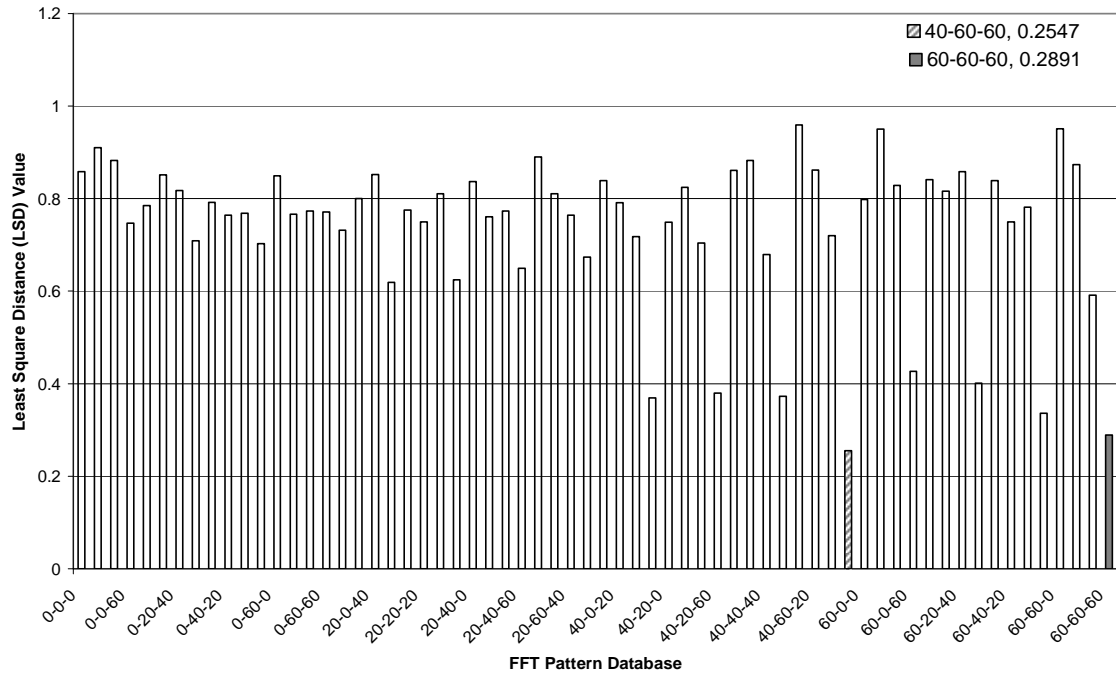
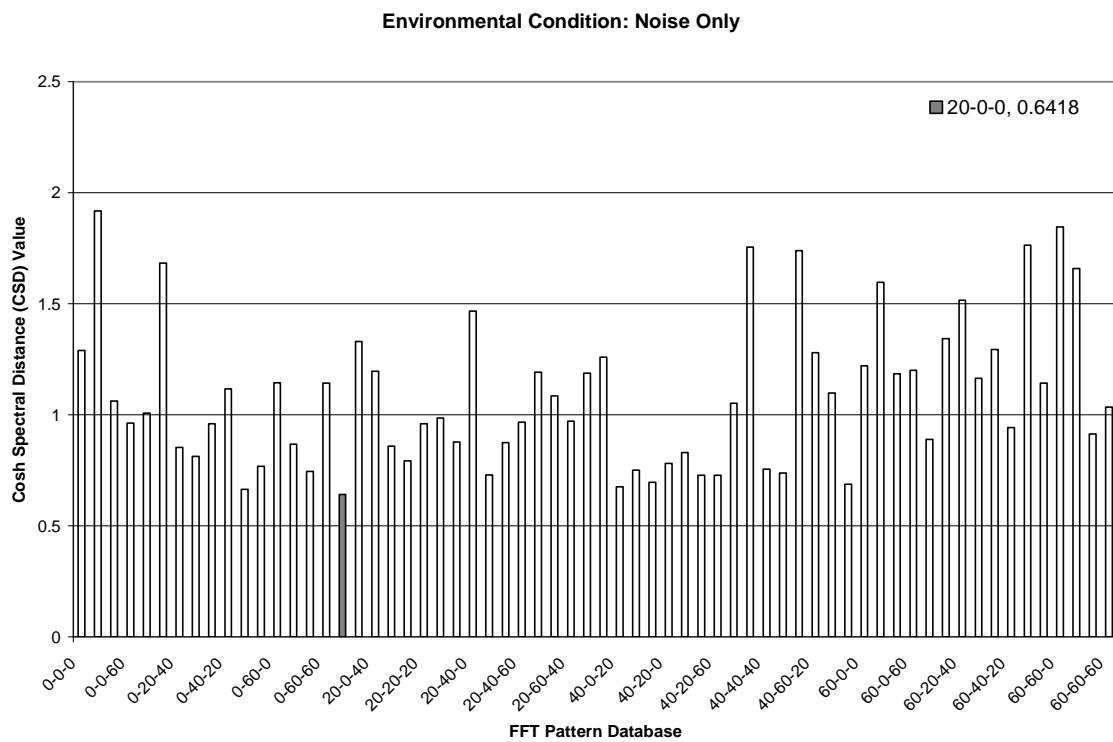
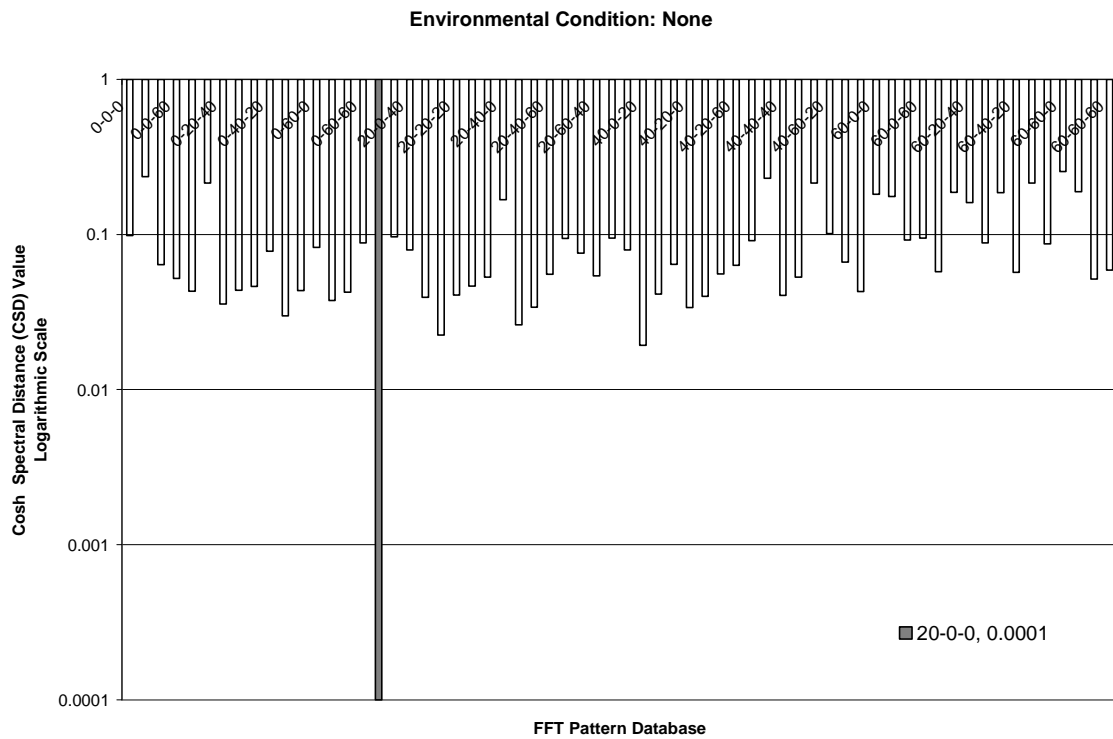
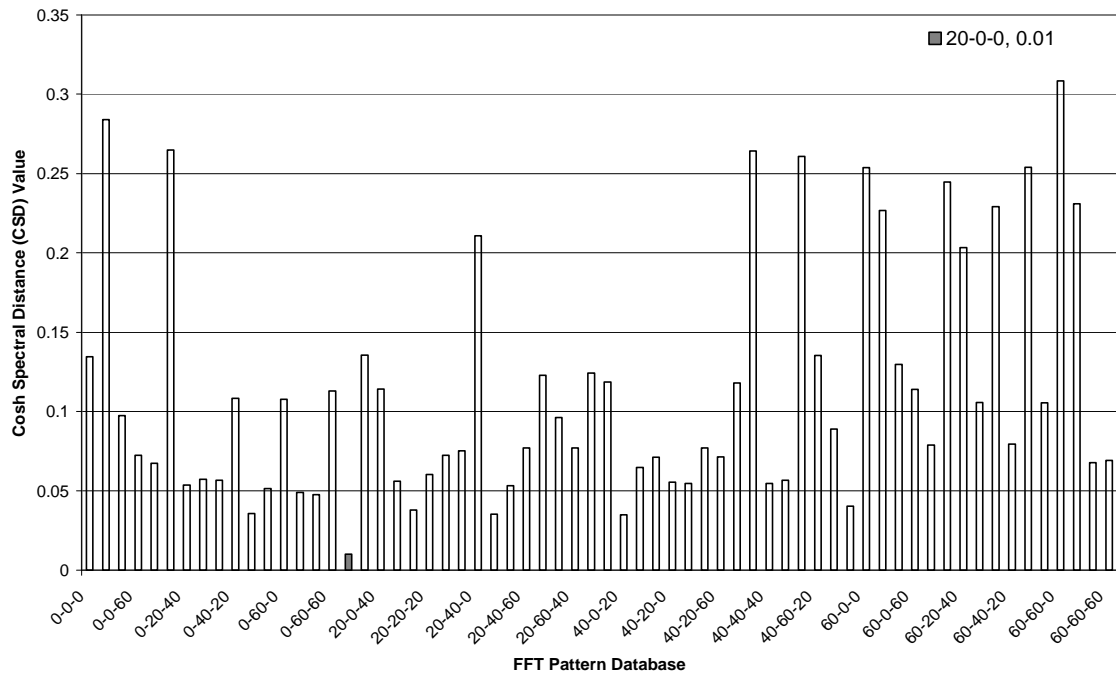


Figure B.9 Cosh Spectral Distance (CSD) Matching for Damage Case 19-0-0 (FFT Pattern Database)



Environmental Condition: Damping Only



Environmental Condition: Damping & Noise

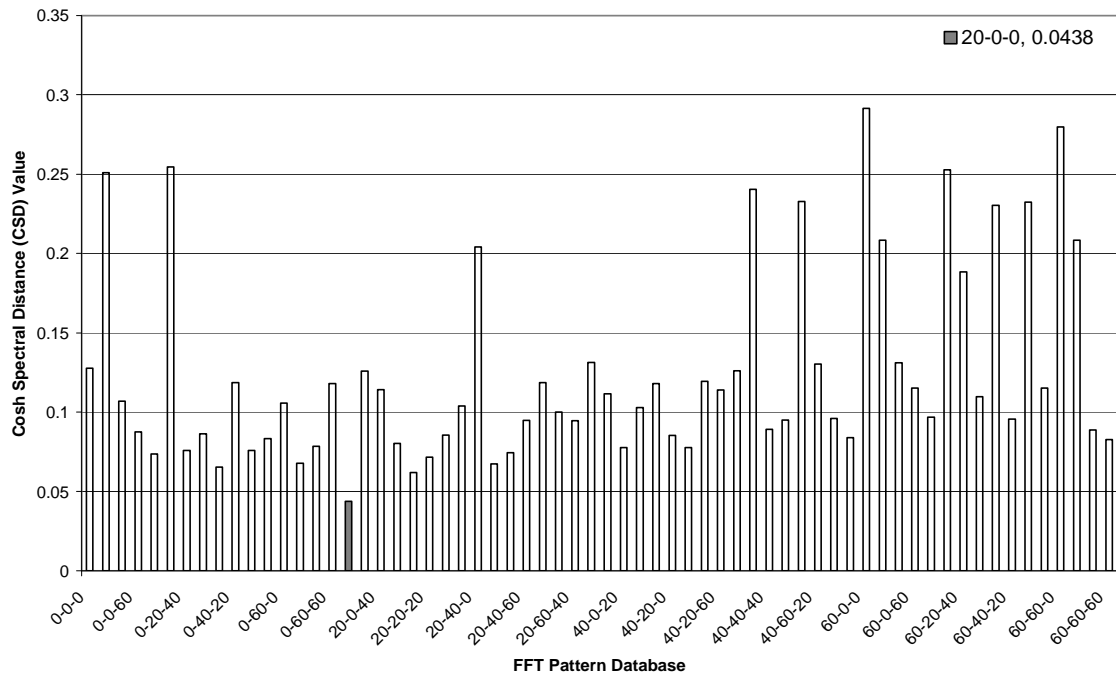
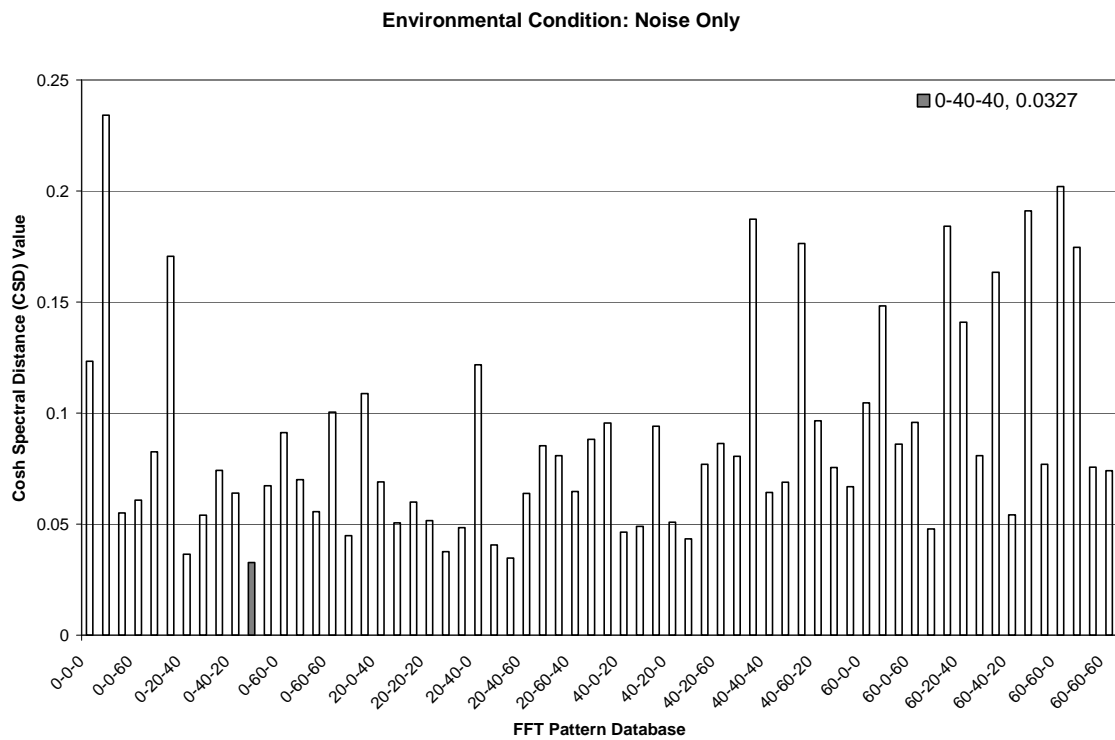
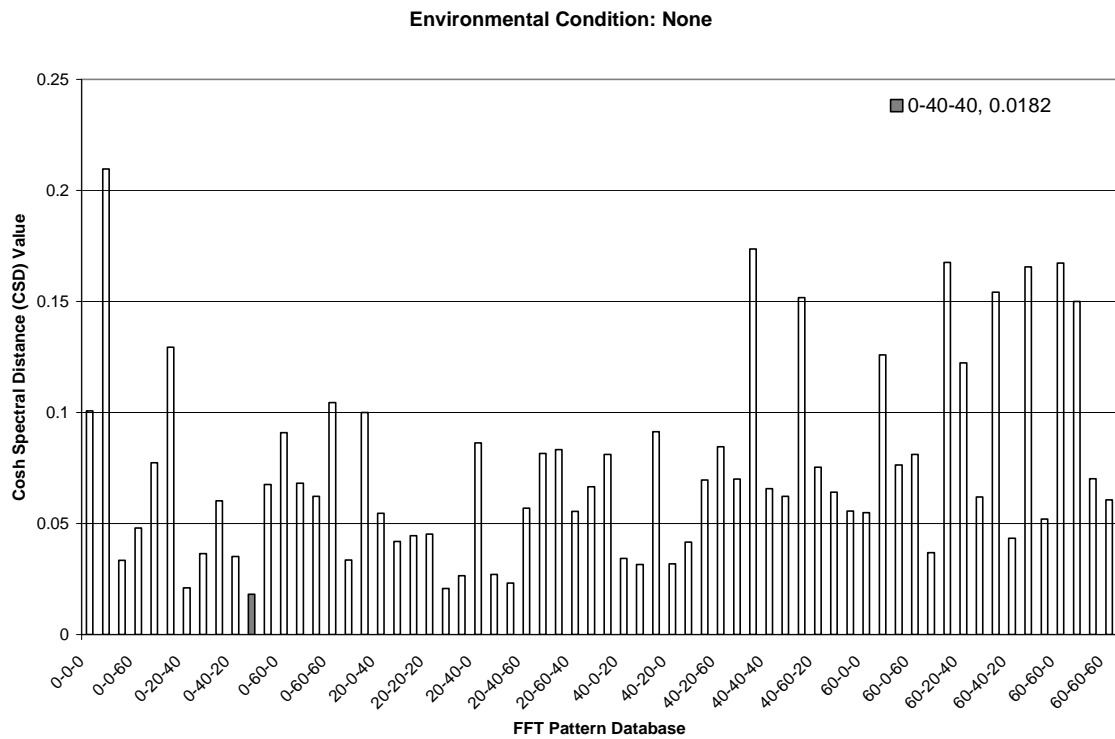
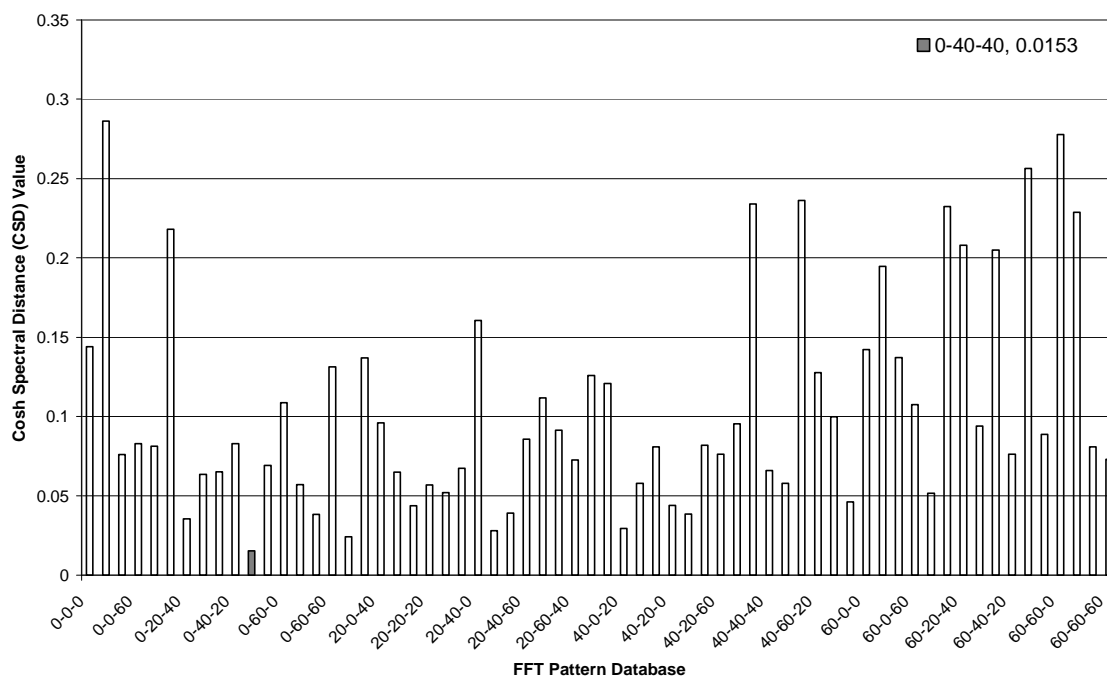


Figure B.10 Cosh Spectral Distance (CSD) Matching for Damage Case 0-38-38 (FFT Pattern Database)



Environmental Condition: Damping Only



Environmental Condition: Damping & Noise

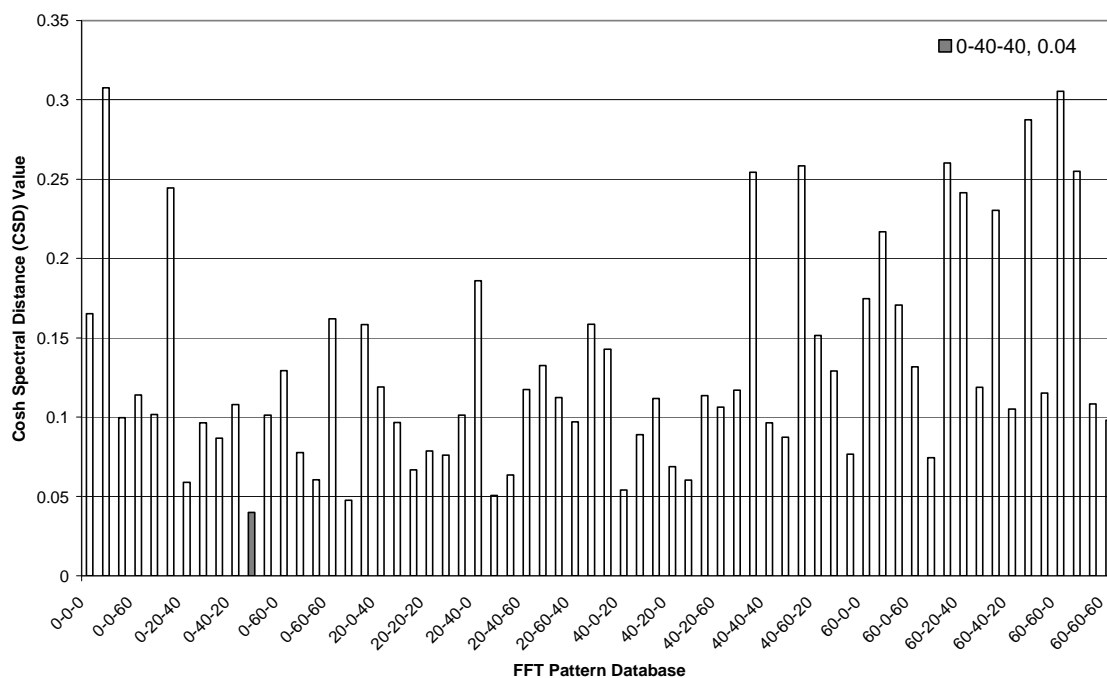
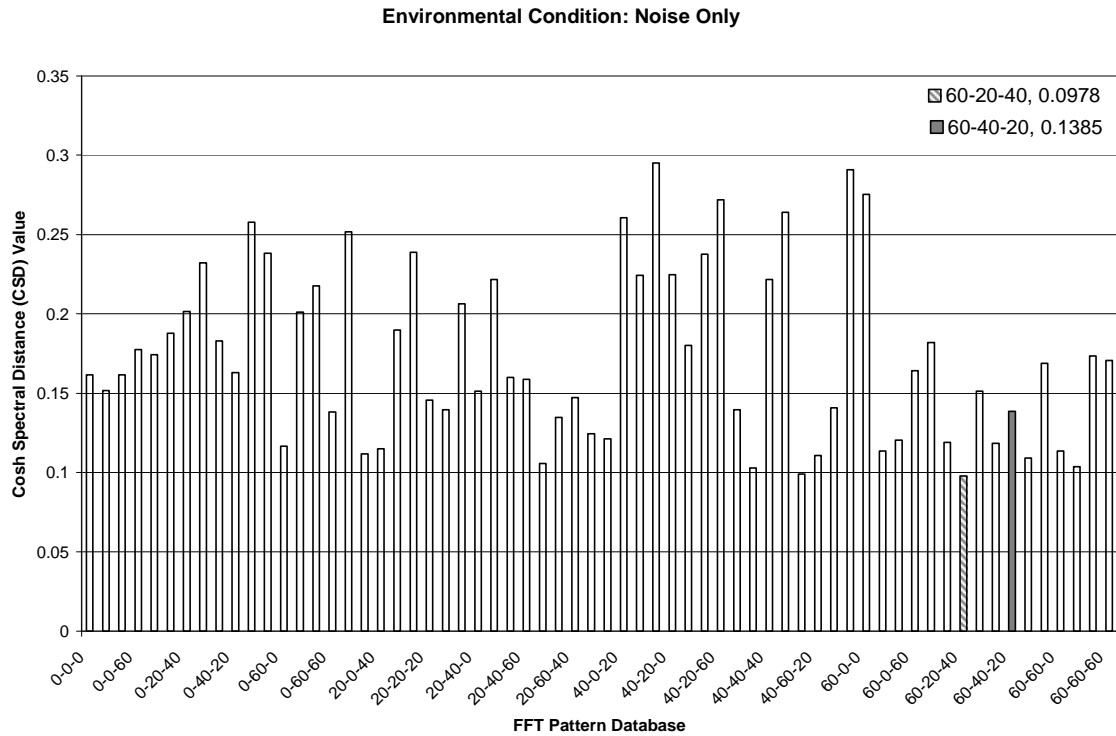
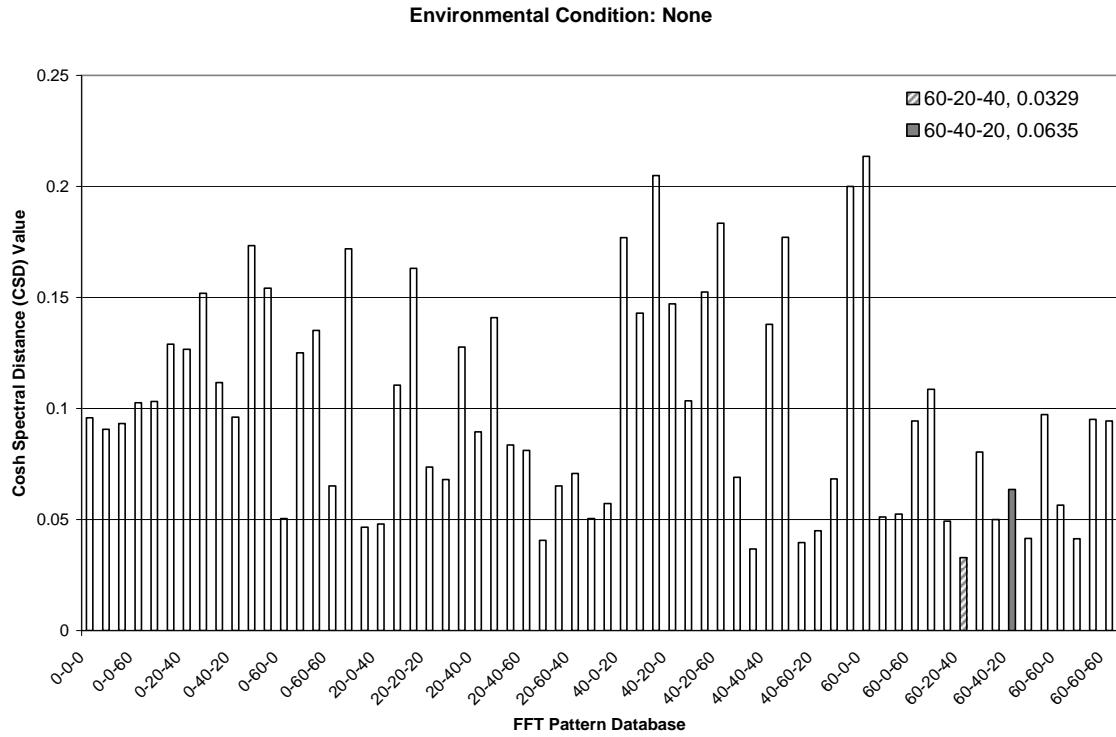
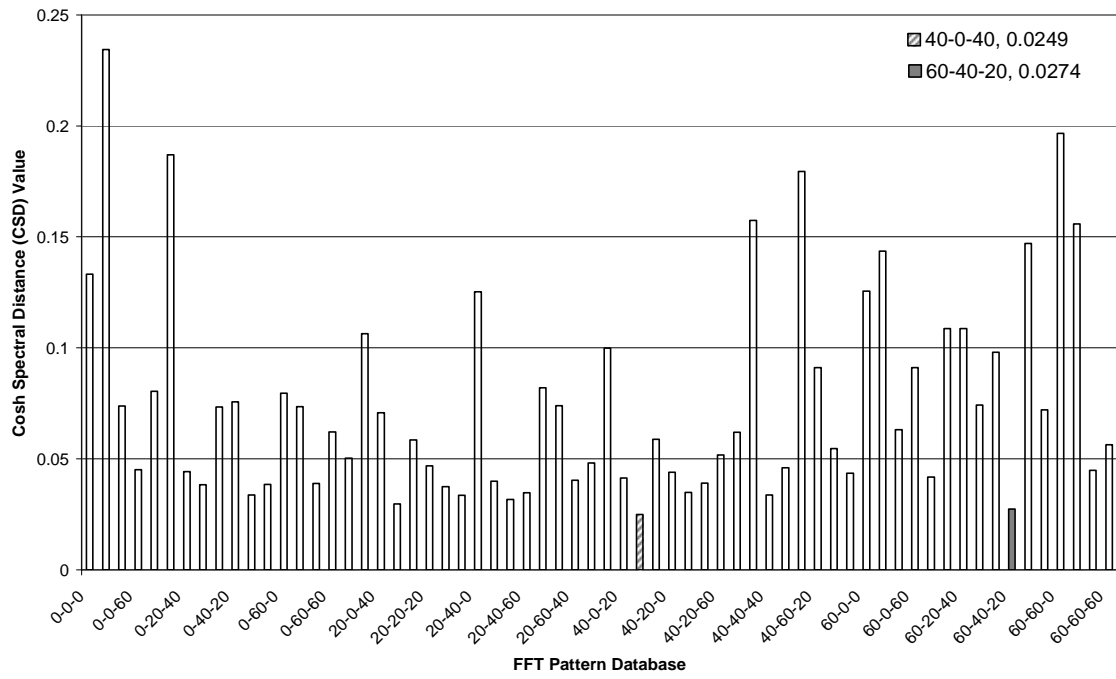


Figure B.11 Cosh Spectral Distance (CSD) Matching for Damage Case 58-38-19 (FFT Pattern Database)



Environmental Condition: Damping Only



Environmental Condition: Damping & Noise

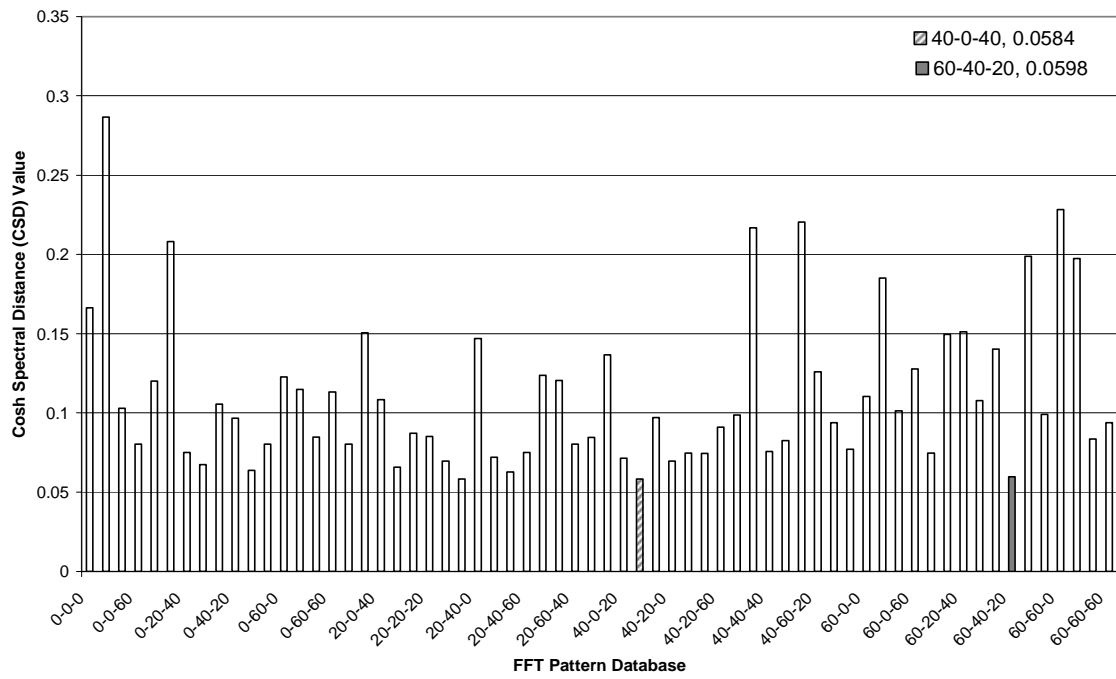
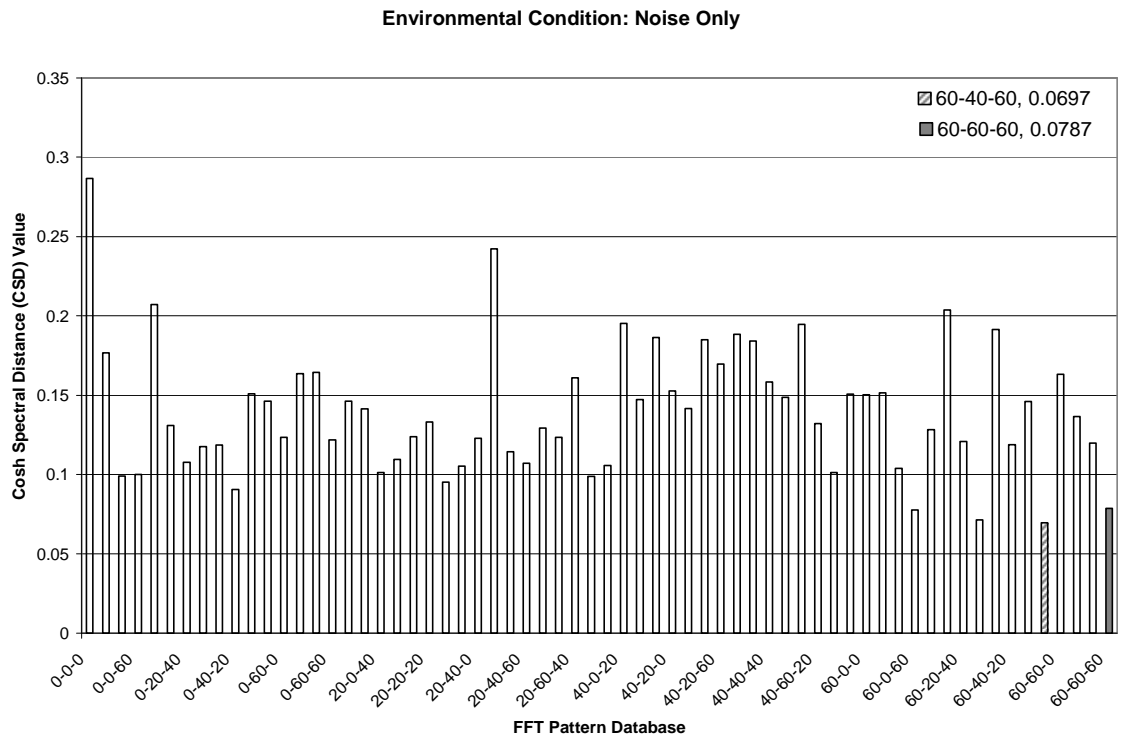
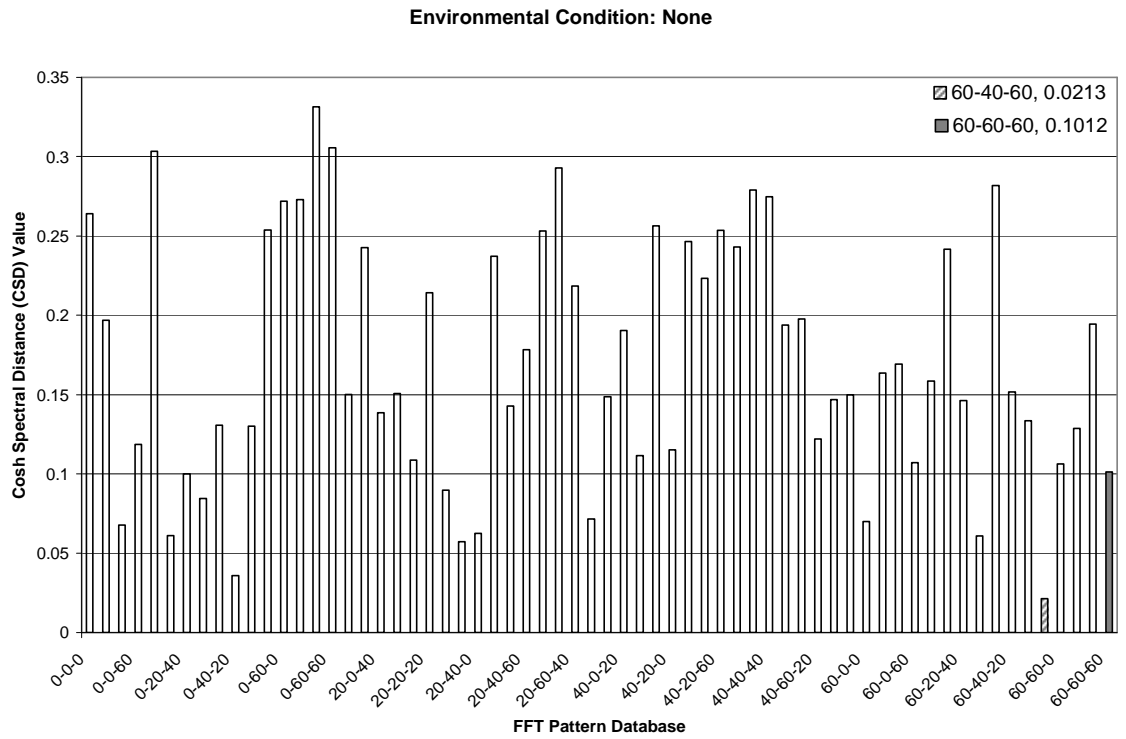
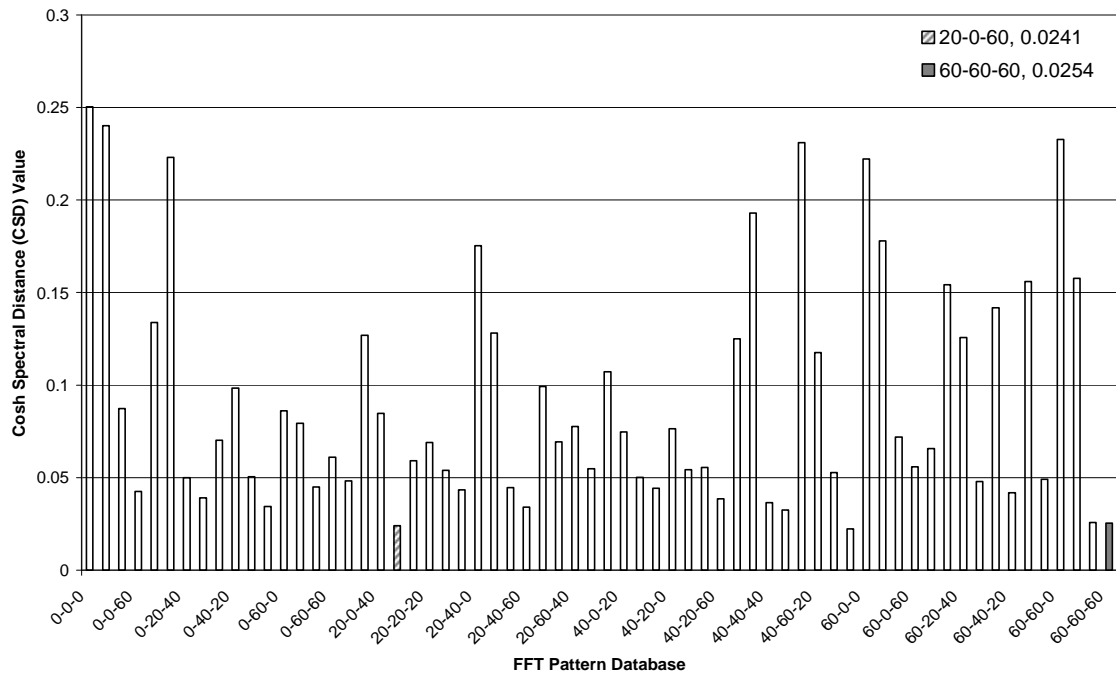


Figure B.12 Cosh Spectral Distance (CSD) Matching for Damage Case 58-58-58 (FFT Pattern Database)



Environmental Condition: Damping Only



Environmental Condition: Damping & Noise

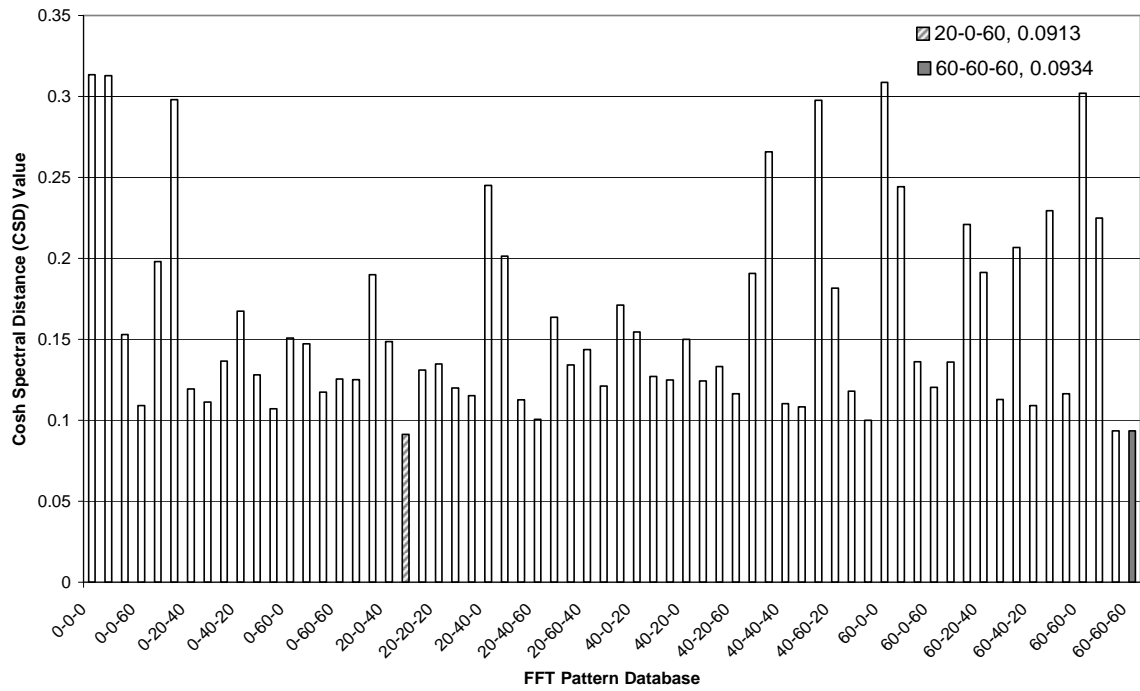
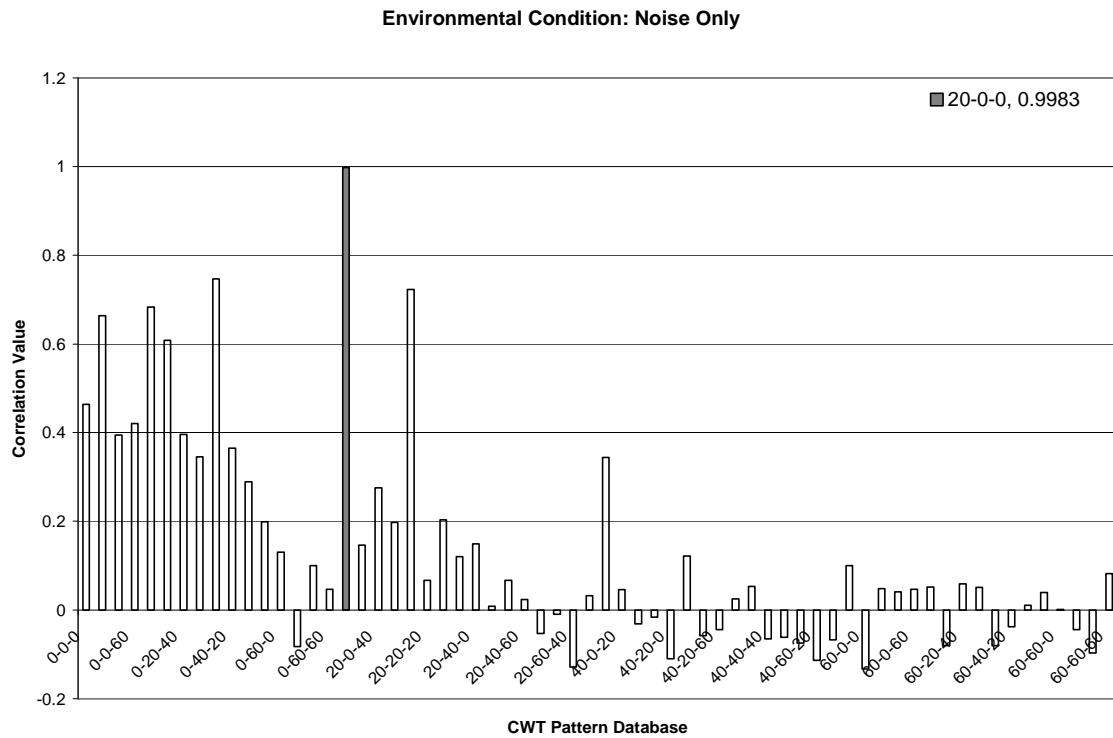
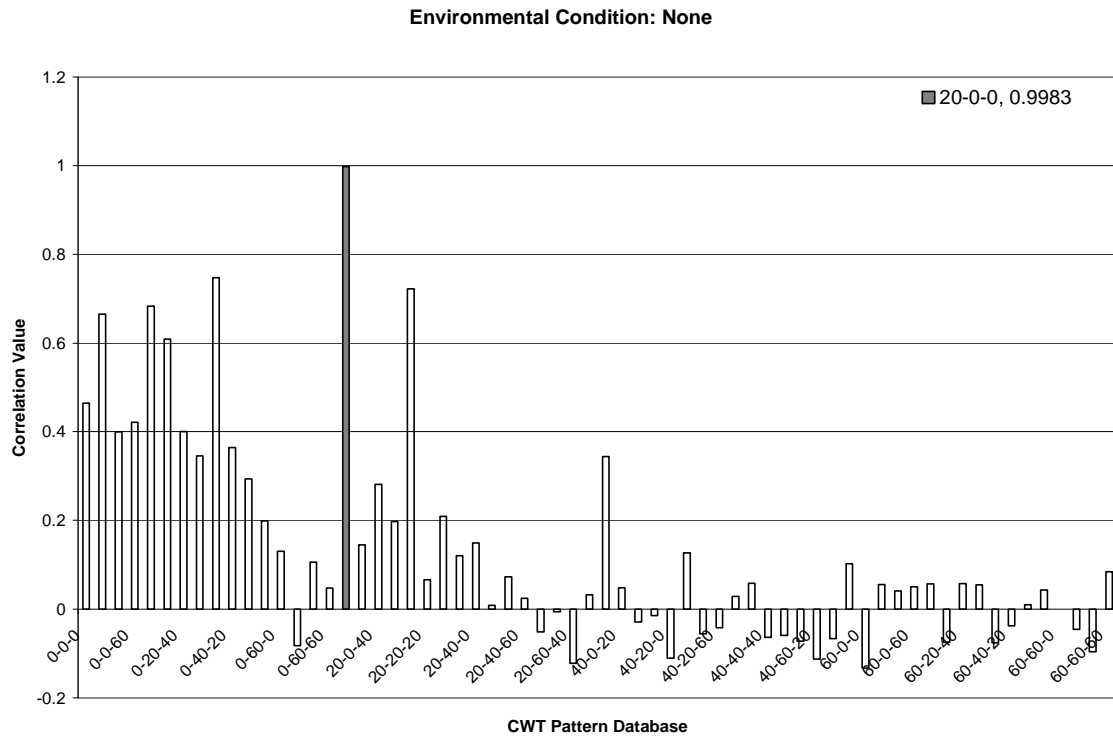
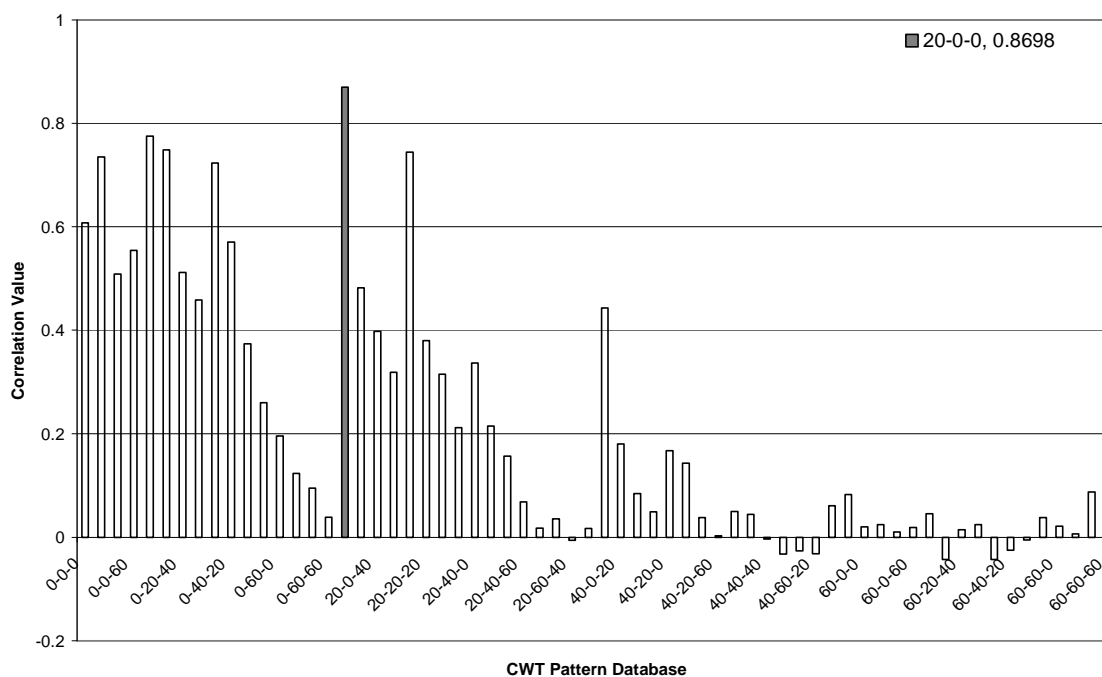


Figure B.13 Correlation Matching for Damage Case 19-0-0 (CWT Pattern Database)



Environmental Condition: Damping Only



Environmental Condition: Damping & Noise

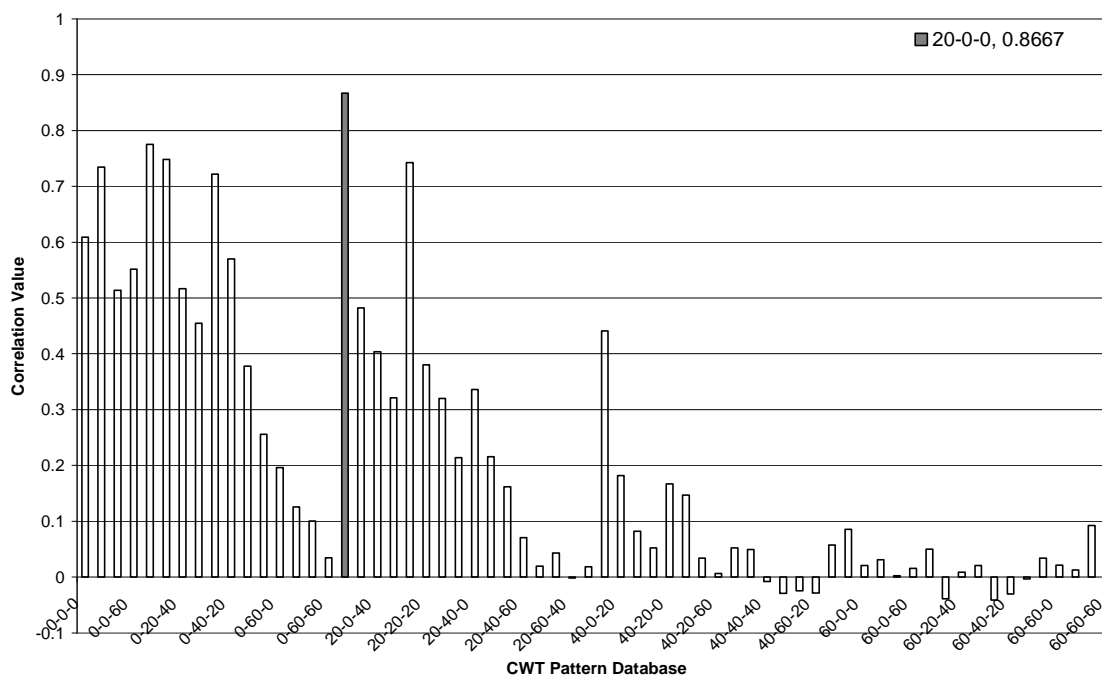
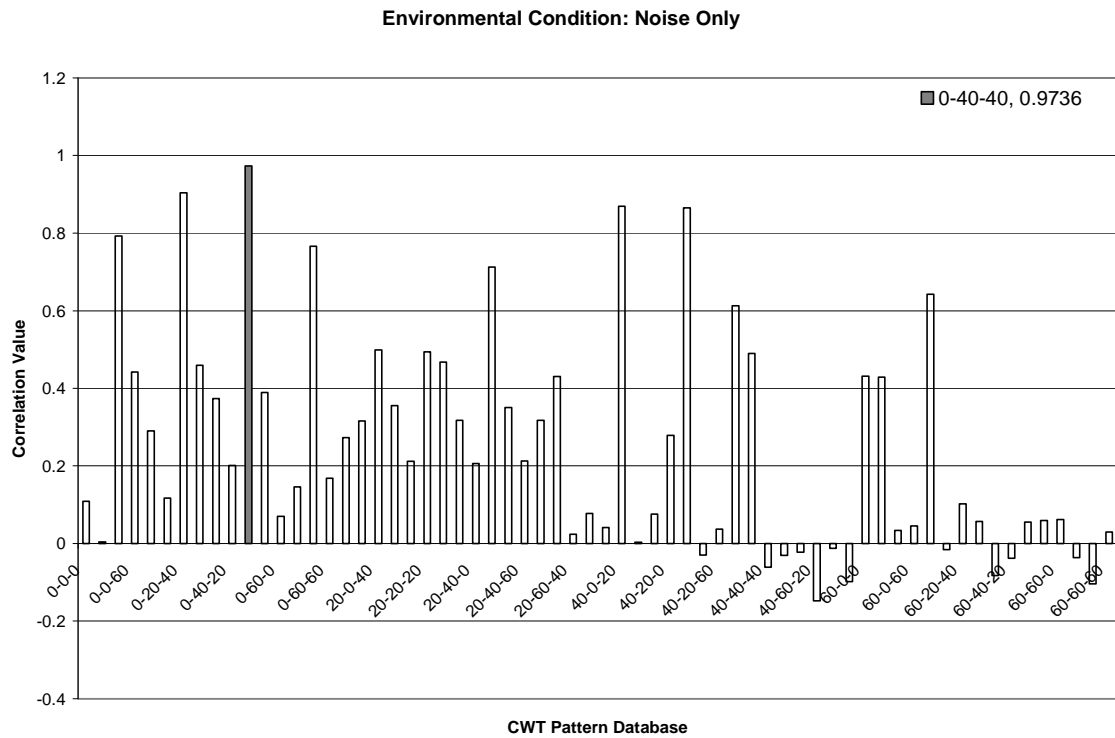
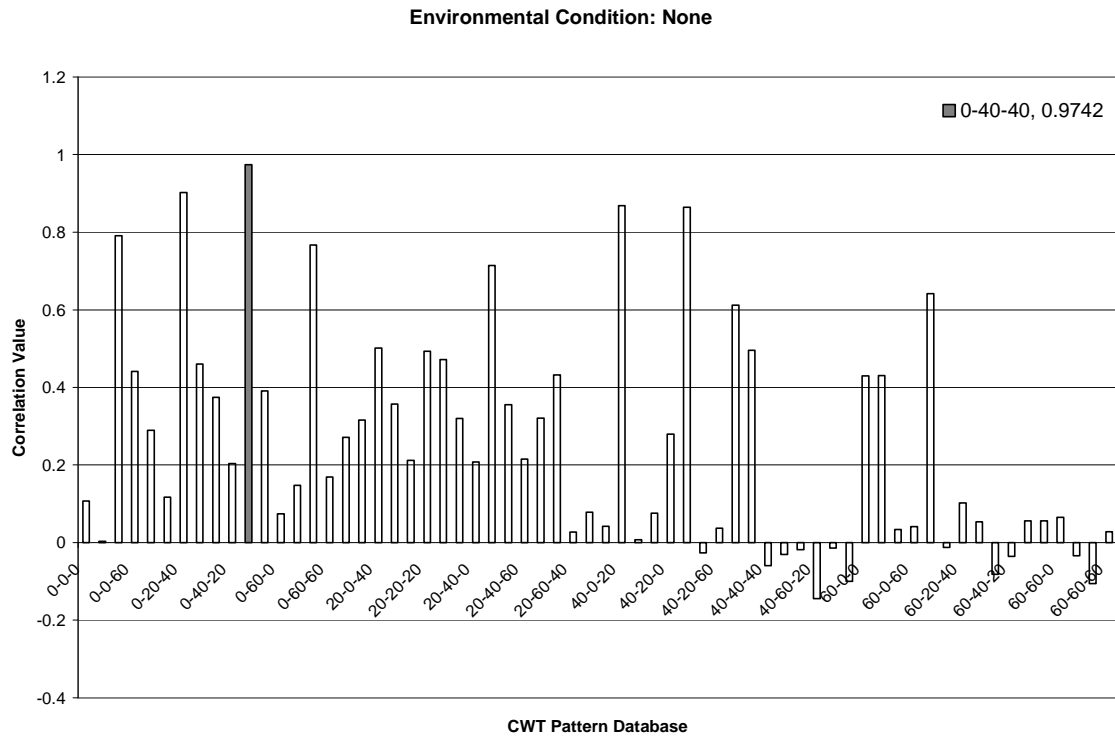
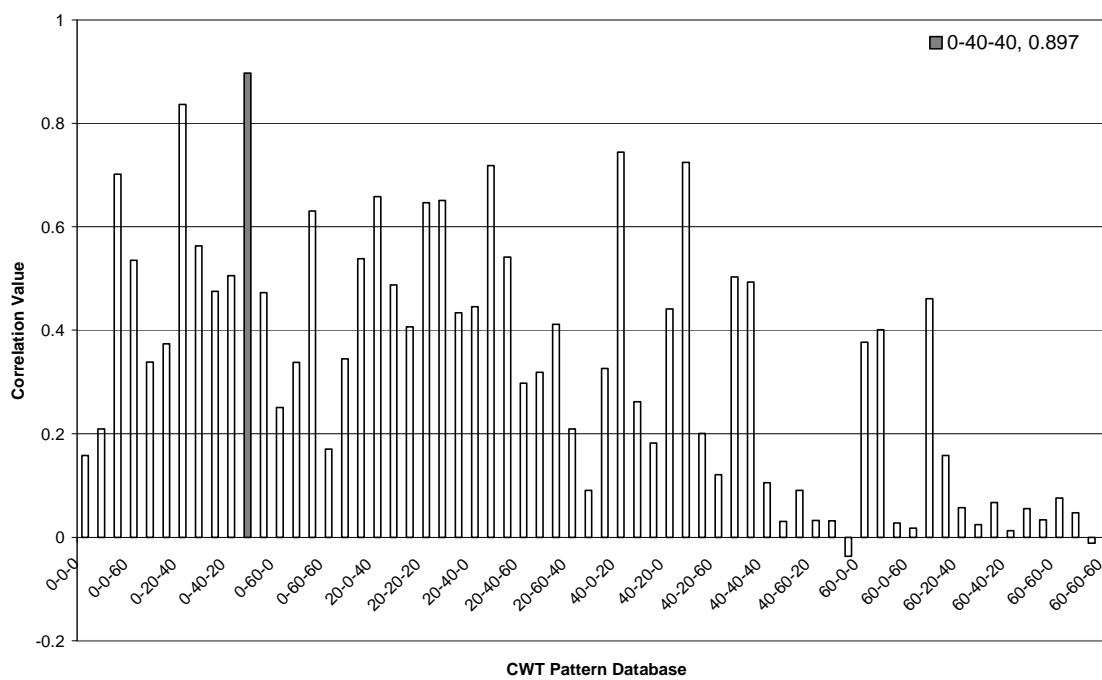


Figure B.14 Correlation Matching for Damage Case 0-38-38 (CWT Pattern Database)



Environmental Condition: Damping Only



Environmental Condition: Damping & Noise

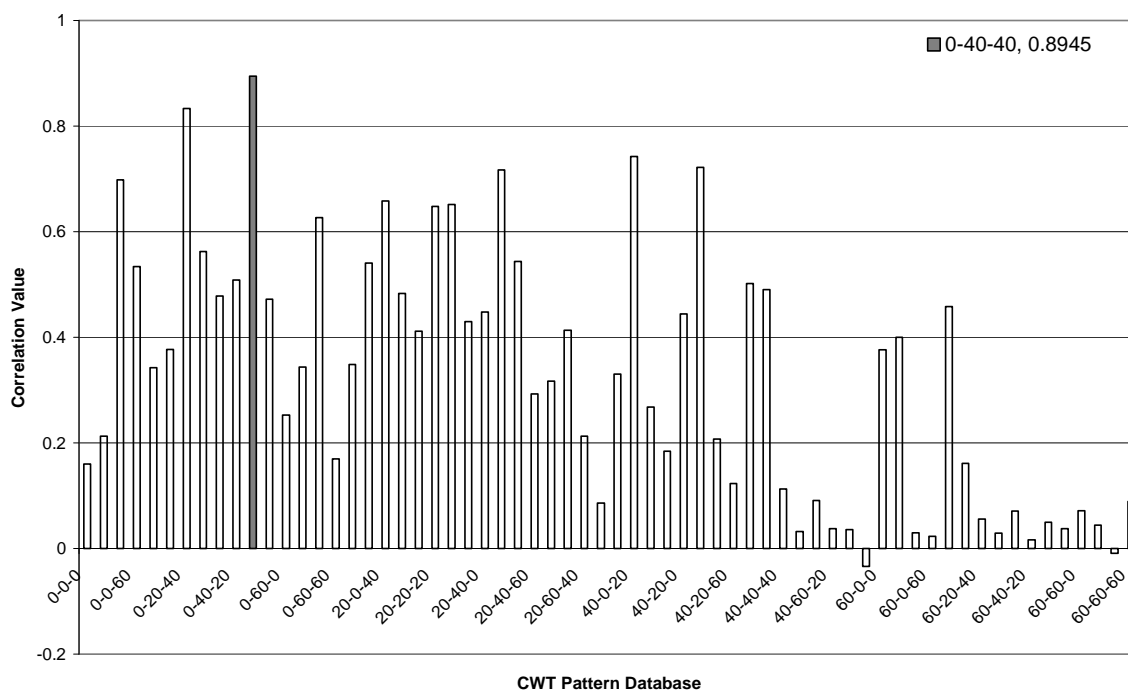
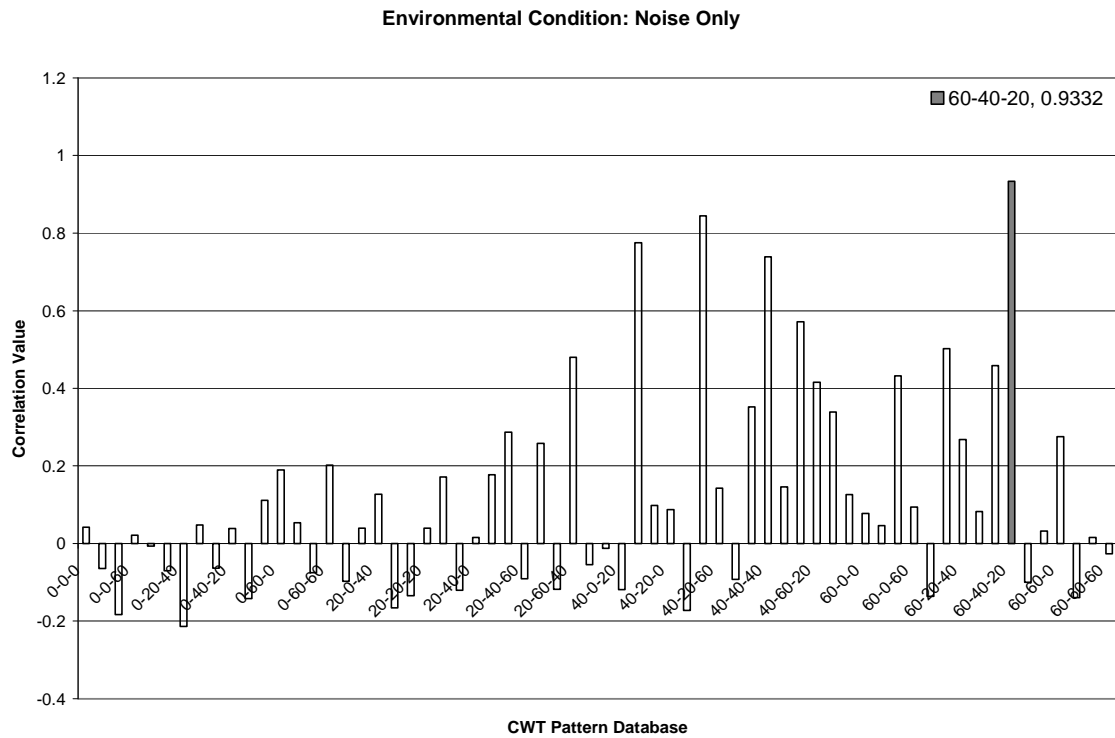
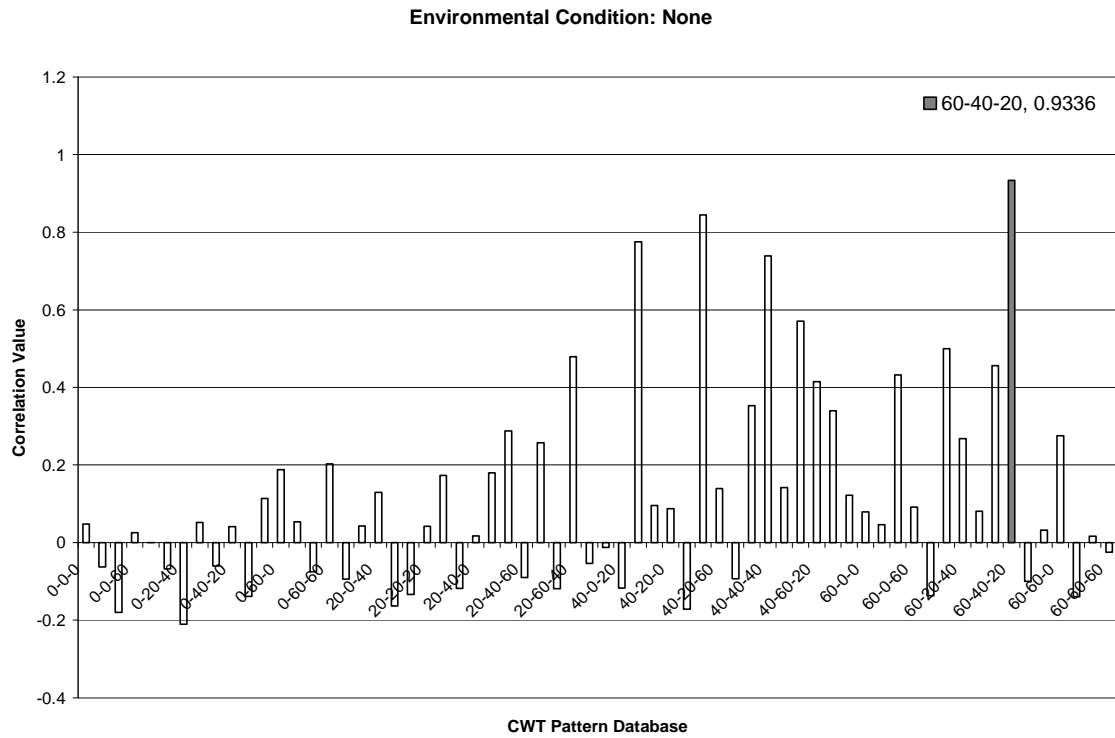
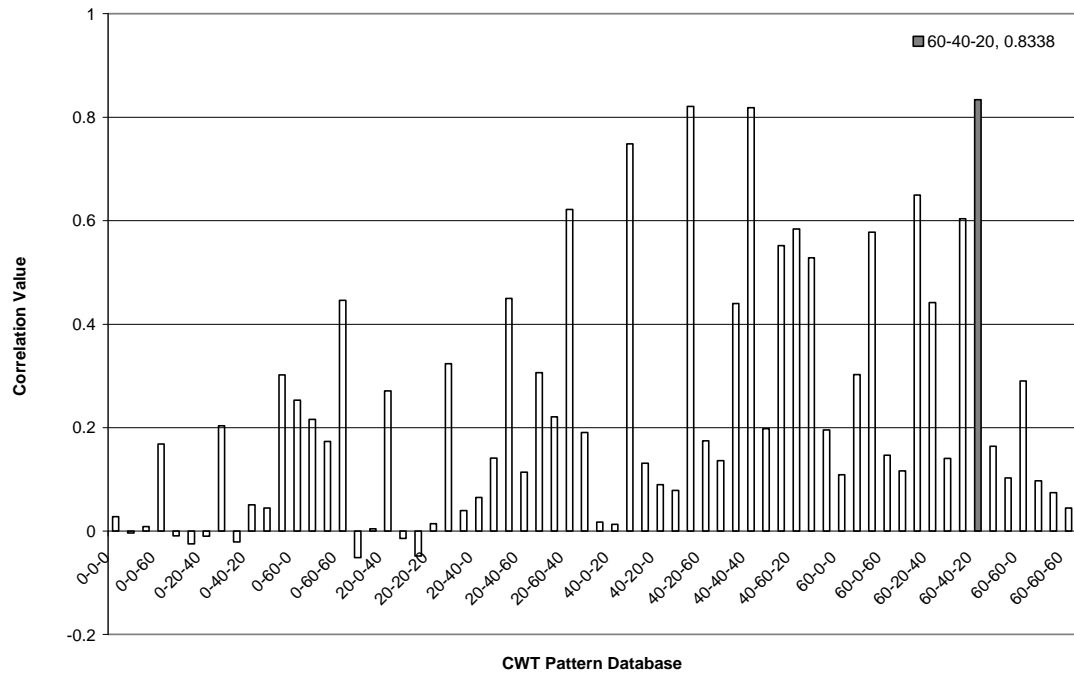


Figure B.15 Correlation Matching for Damage Case 58-38-19 (CWT Pattern Database)



Environmental Condition: Damping Only



Environmental Condition: Damping & Noise

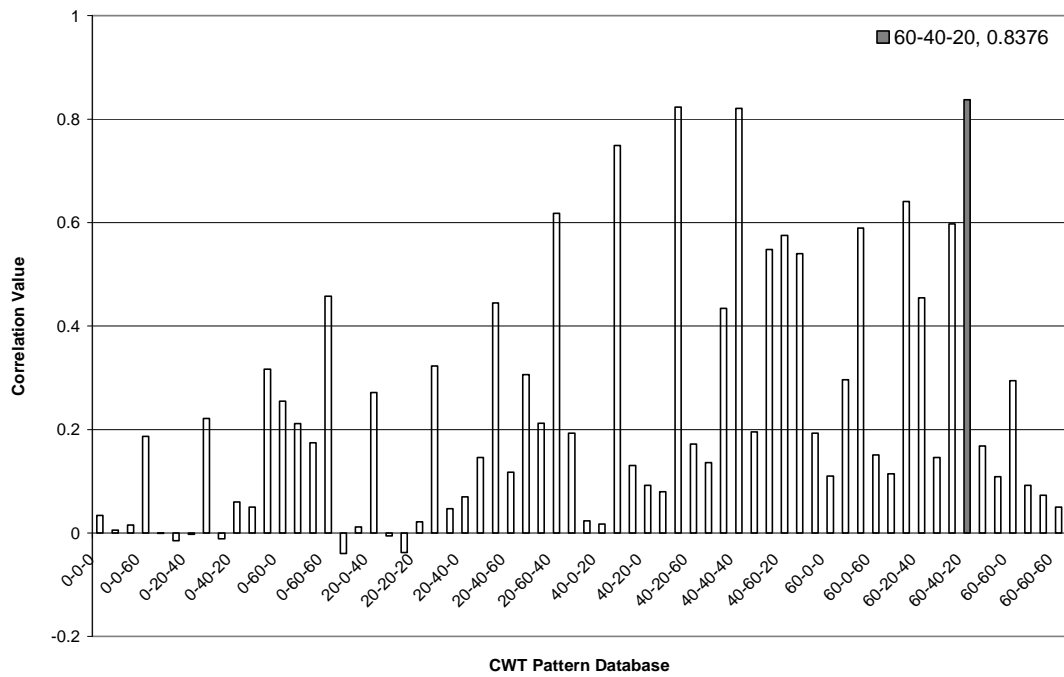
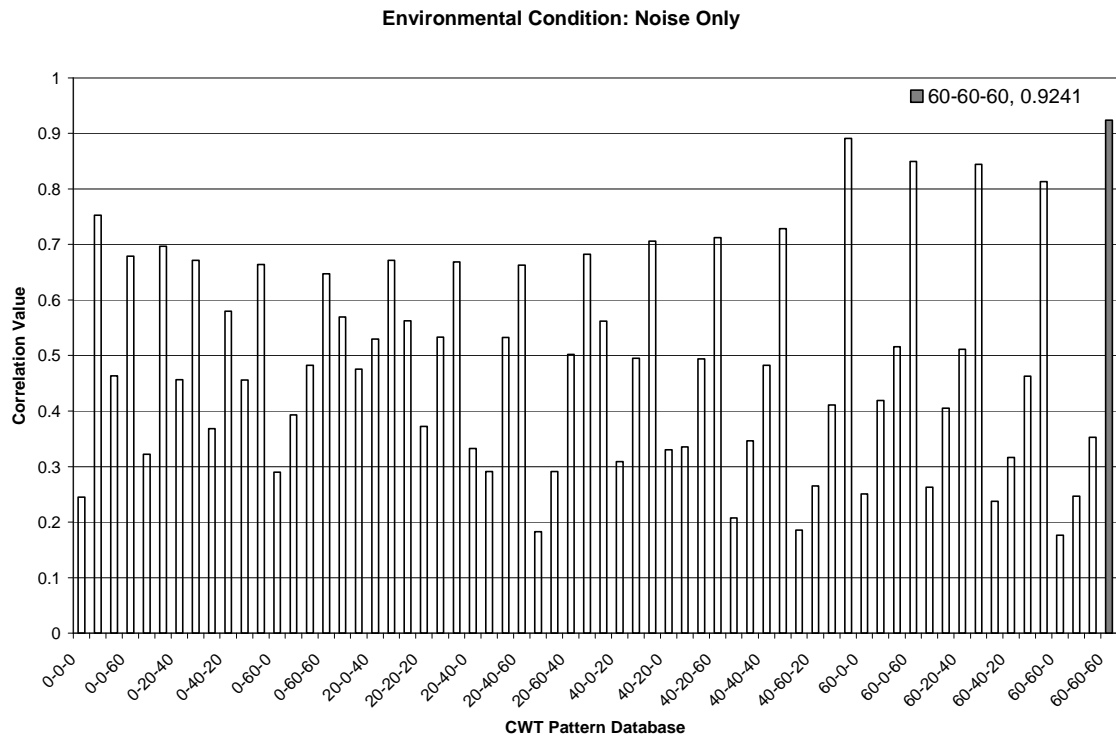
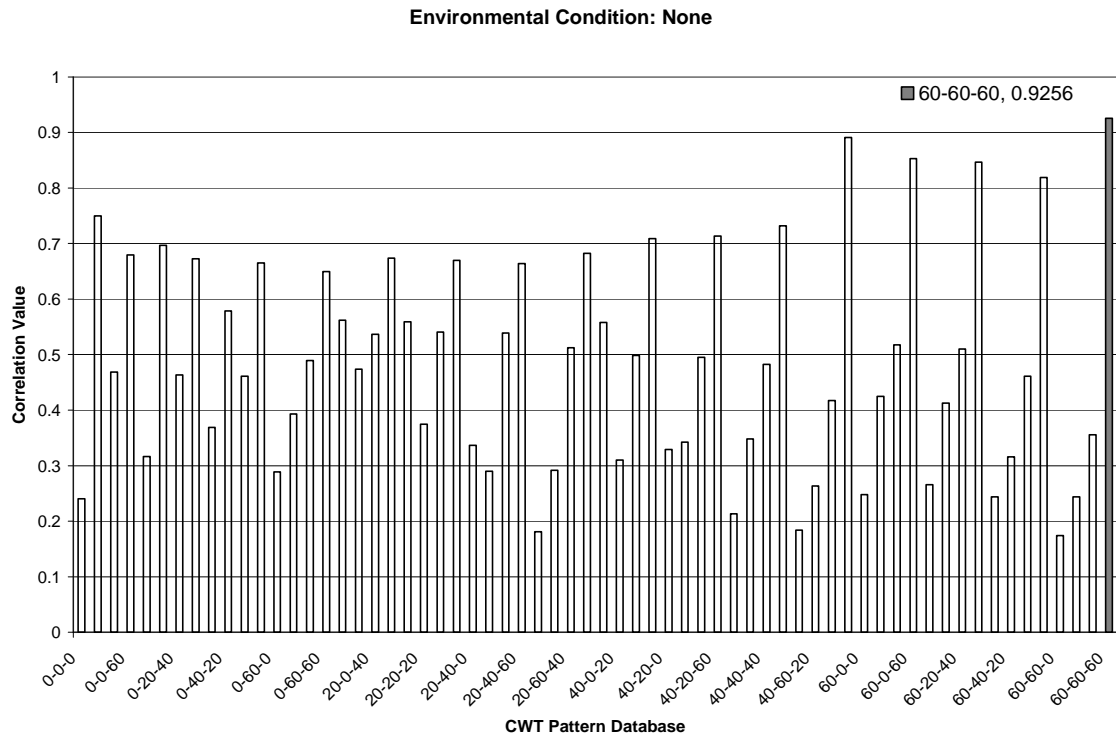
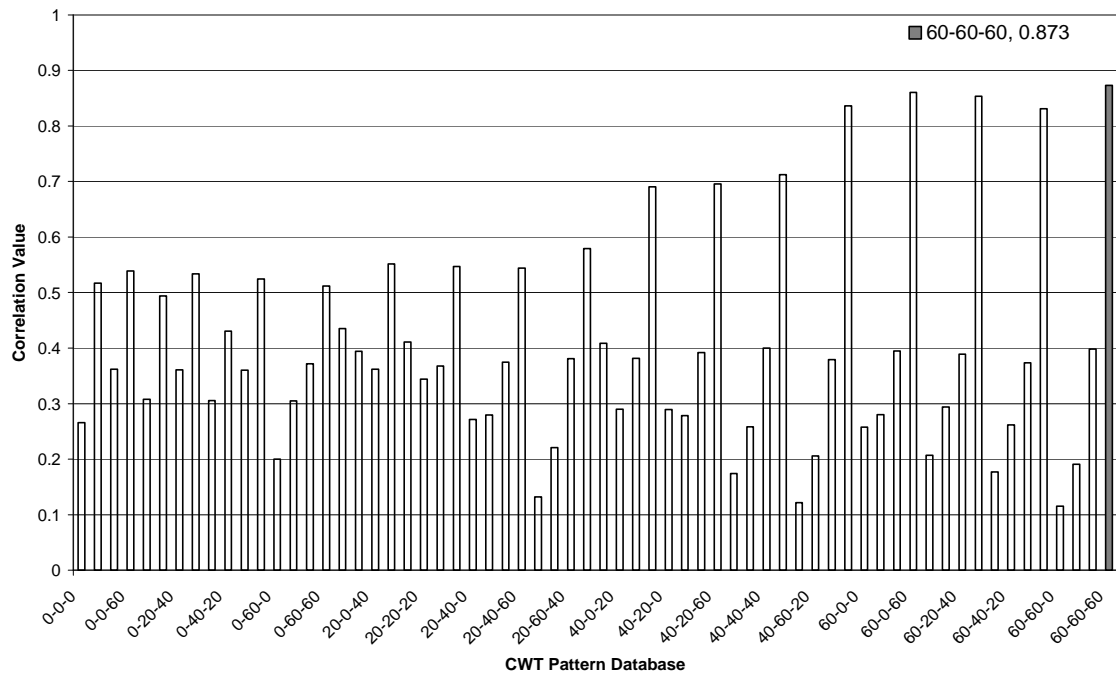


Figure B.16 Correlation Matching for Damage Case 58-58-58 (CWT Pattern Database)



Environmental Condition: Damping Only



Environmental Condition: Damping & Noise

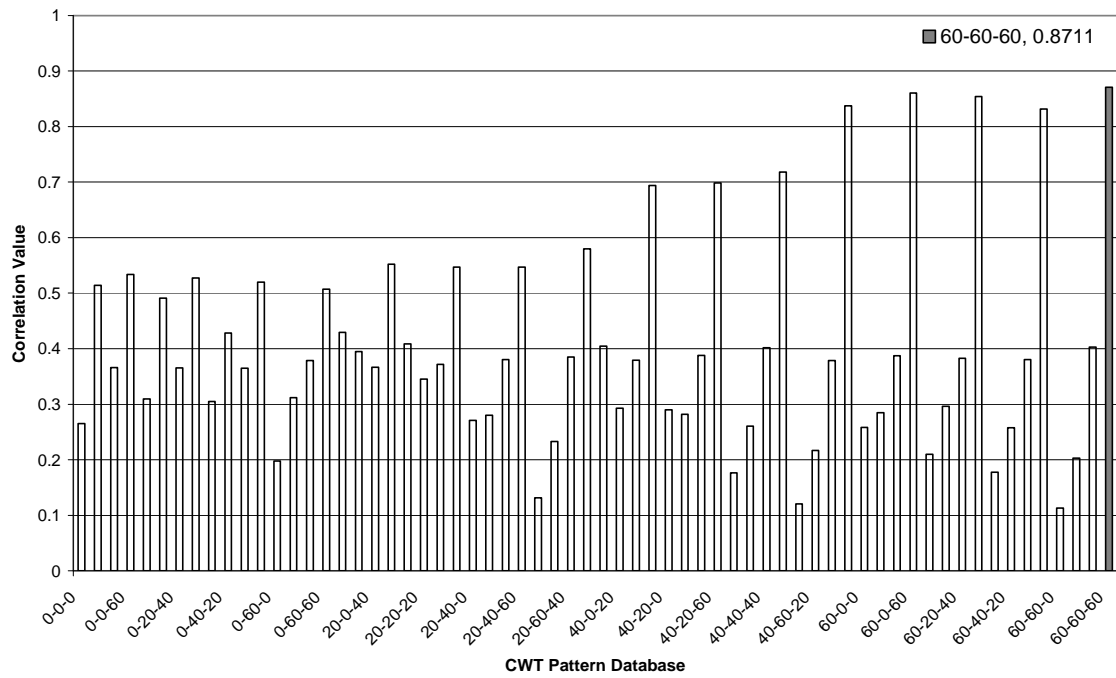
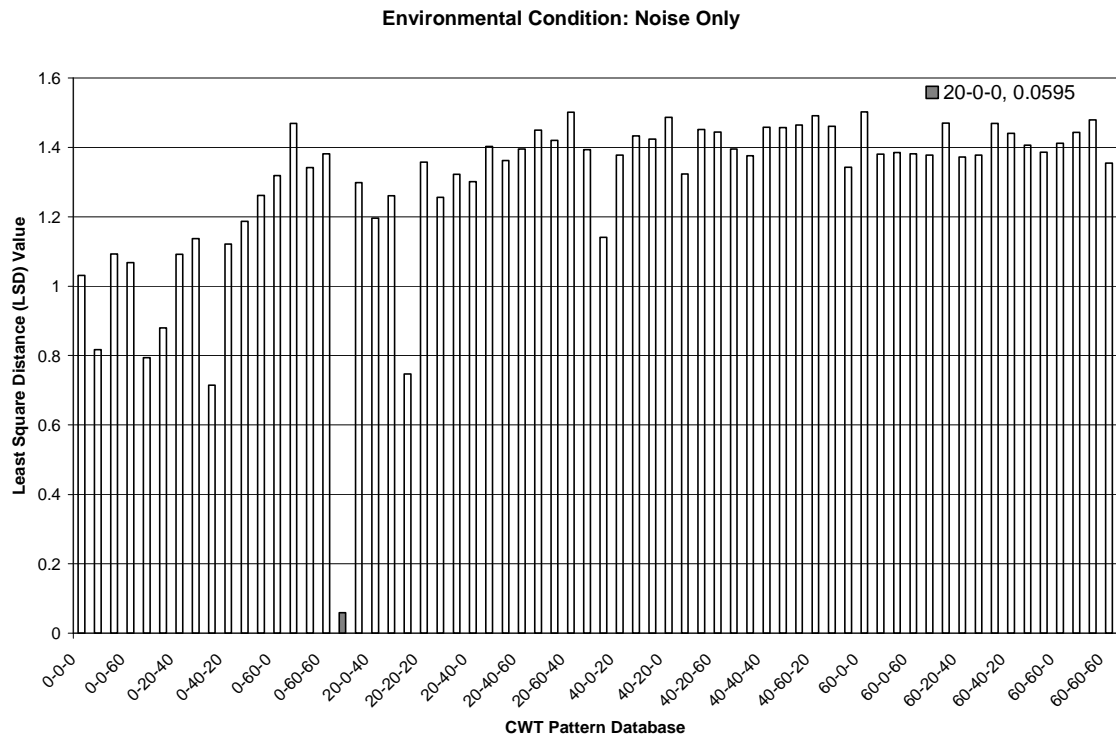
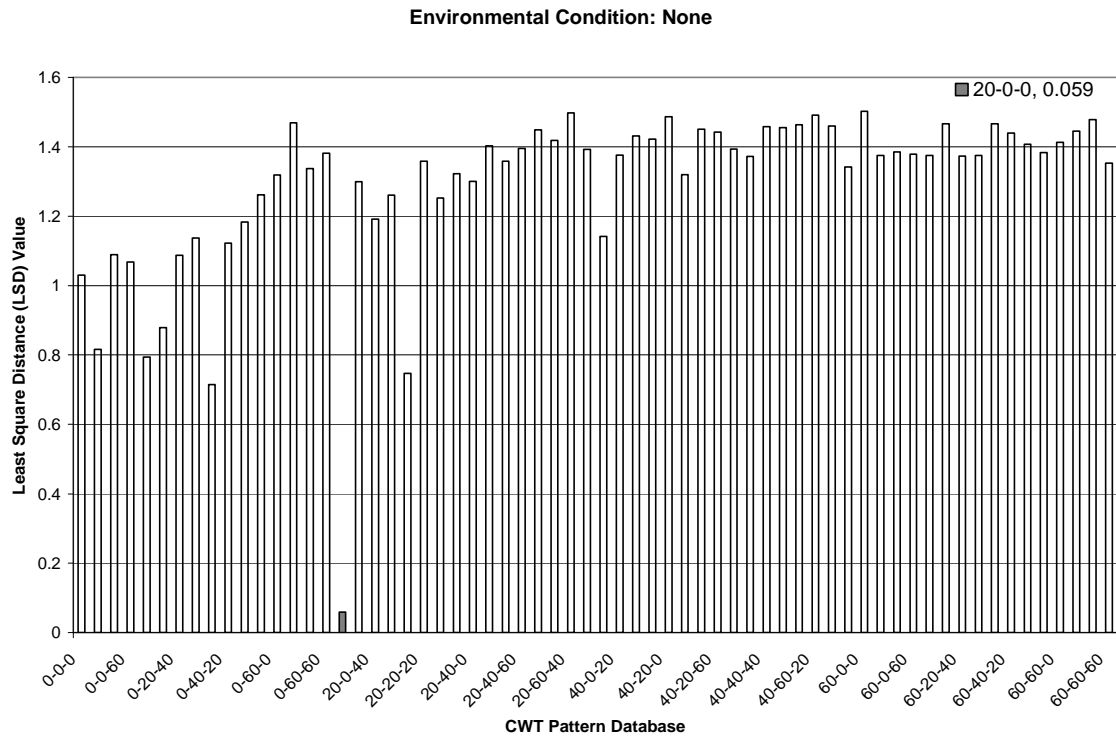
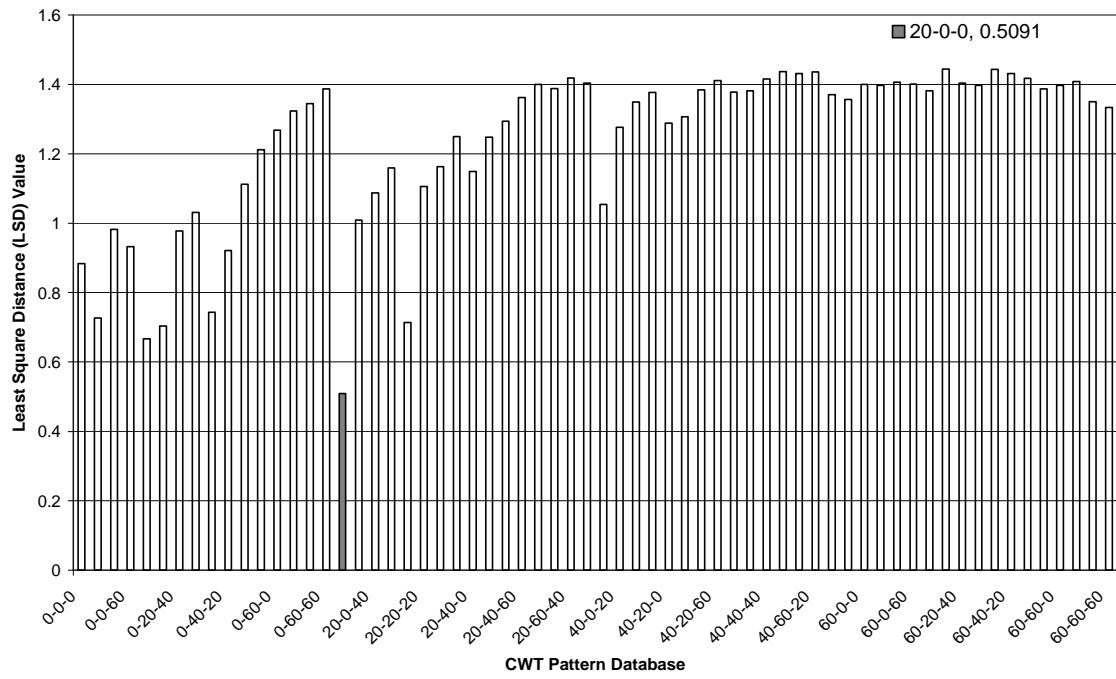


Figure B.17 Least Square Distance (LSD) Matching for Damage Case 19-0-0 (CWT Pattern Database)



Environmental Condition: Damping Only



Environmental Condition: Damping & Noise

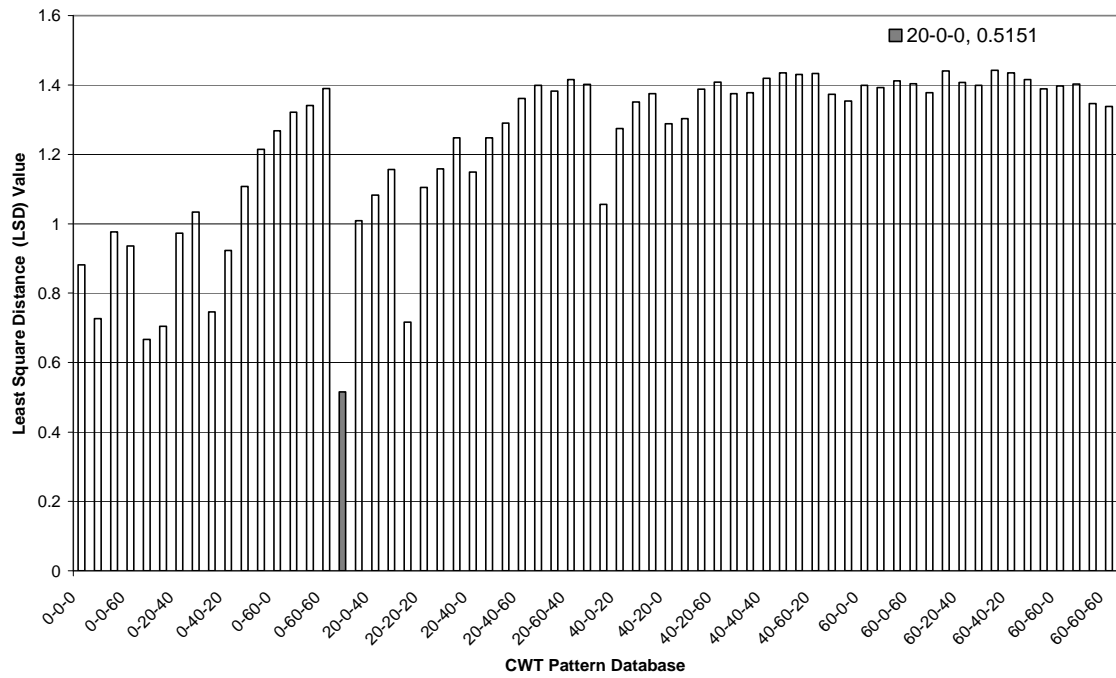
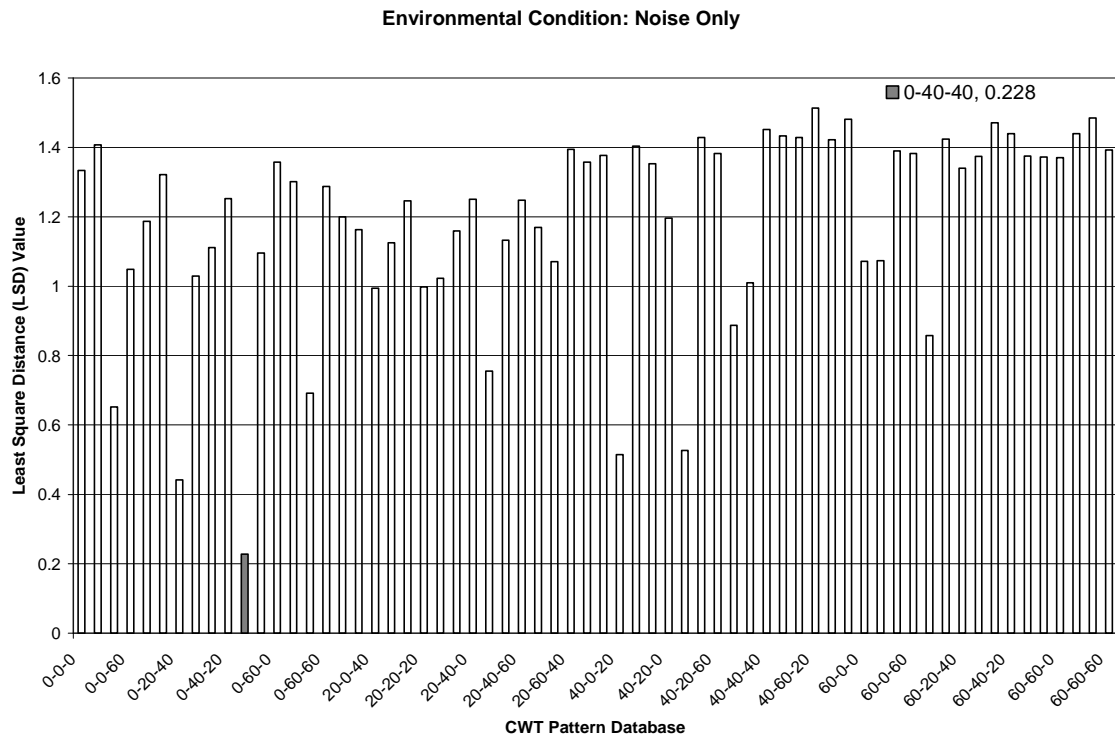
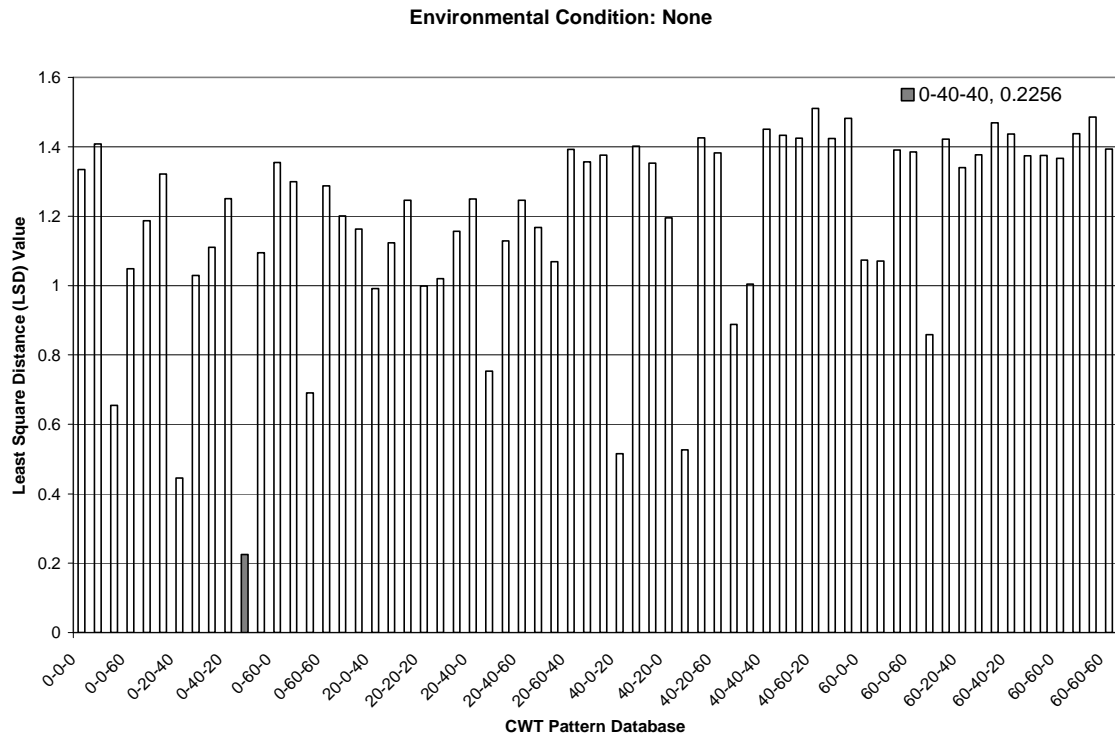
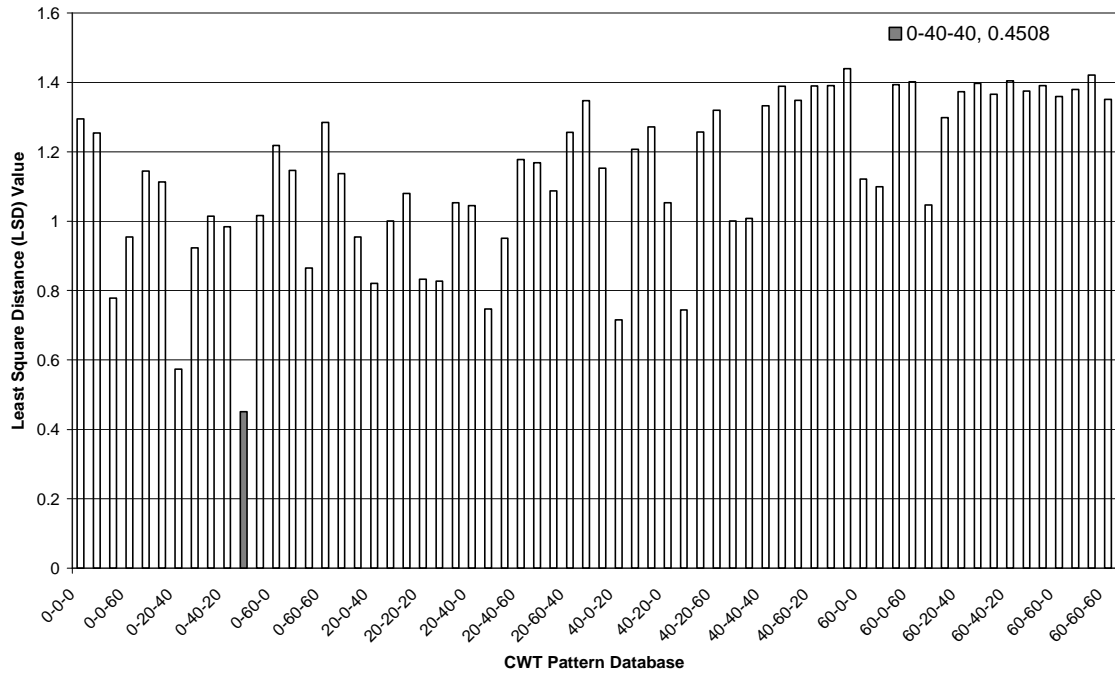


Figure B.18 Least Square Distance (LSD) Matching for Damage Case 0-38-38 (CWT Pattern Database)



Environmental Condition: Damping Only



Environmental Condition: Damping & Noise

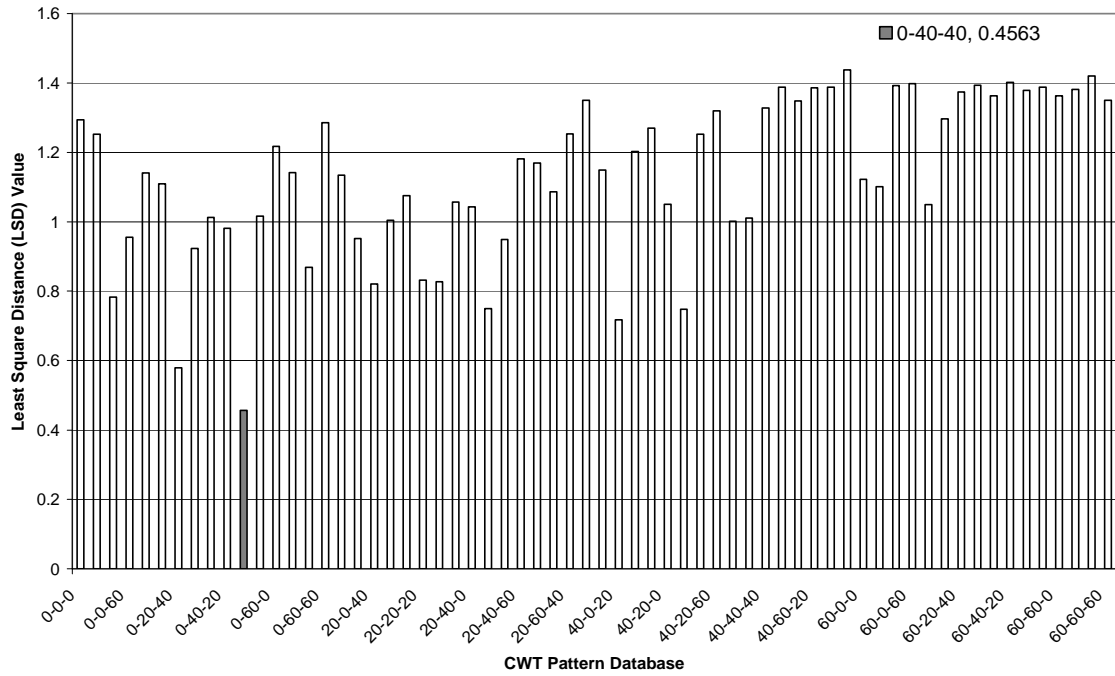
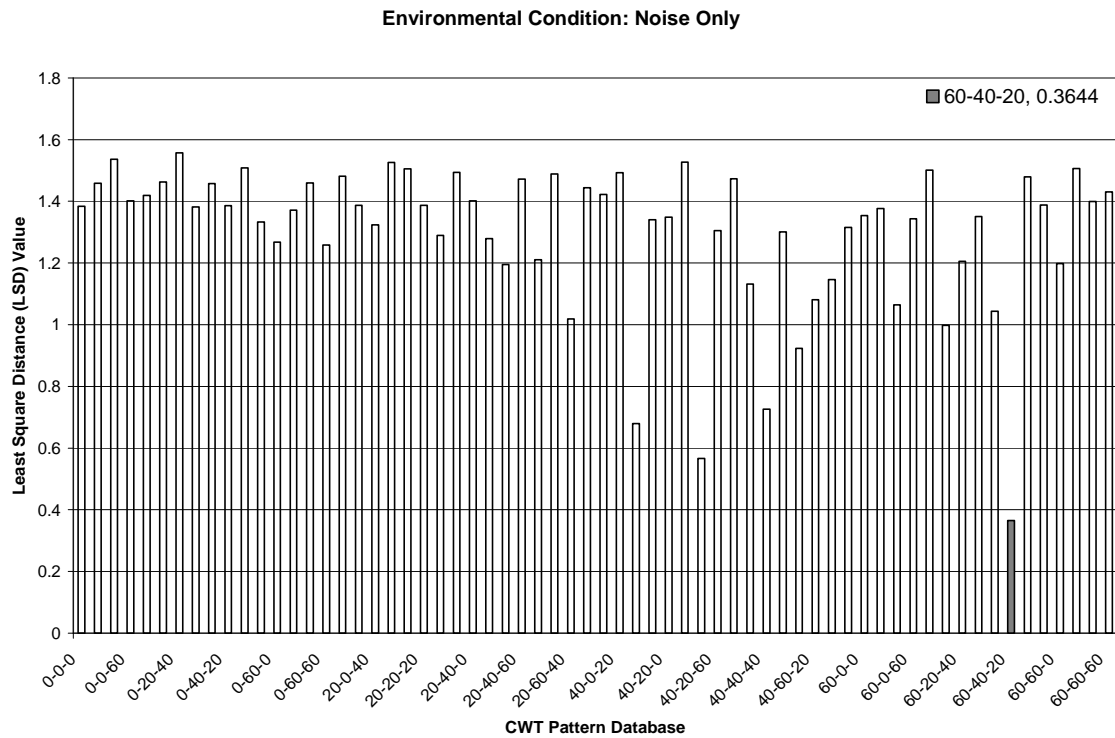
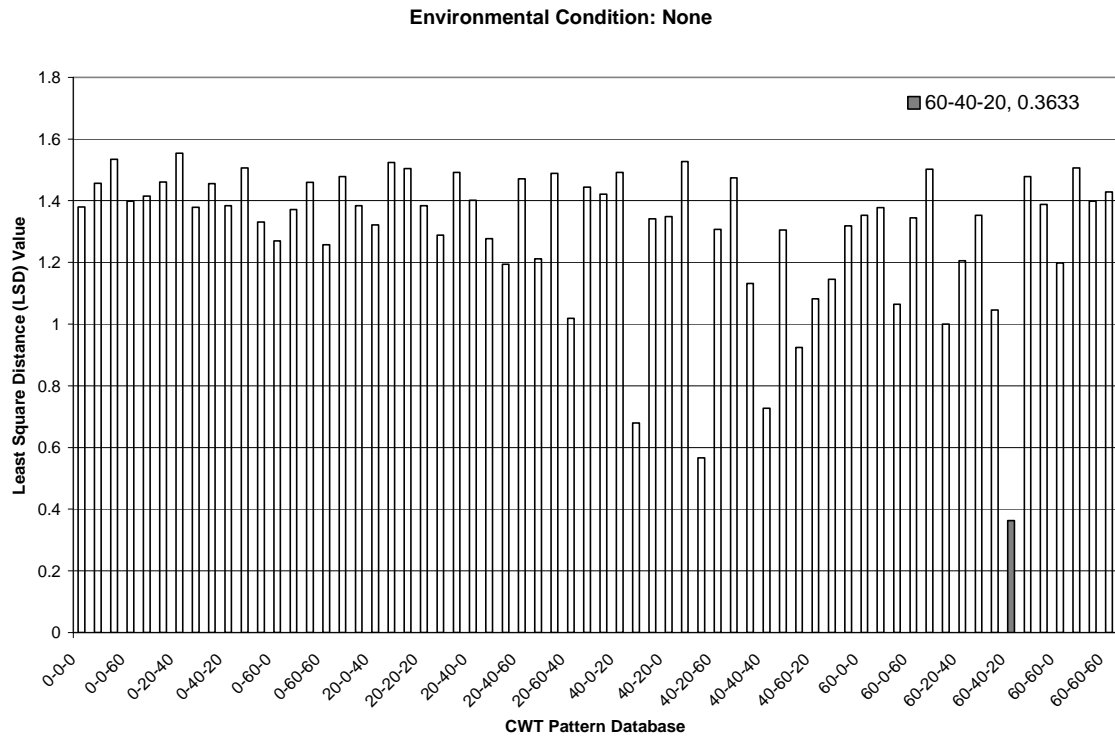
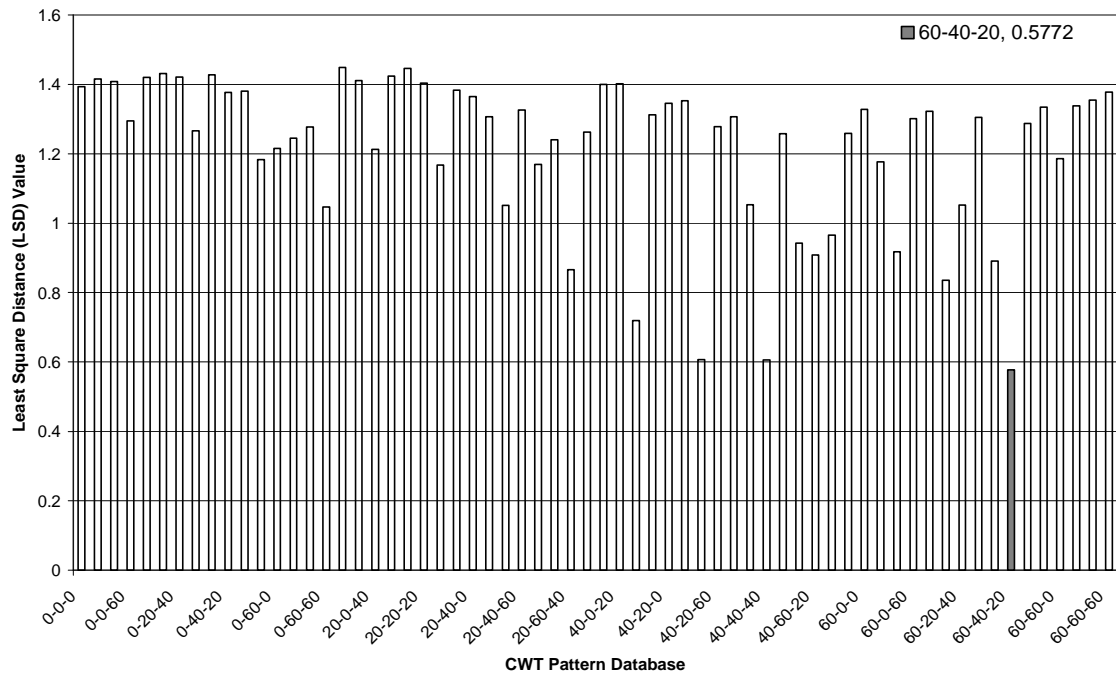


Figure B.19 Least Square Distance (LSD) Matching for Damage Case 58-38-19 (CWT Pattern Database)



Environmental Condition: Damping Only



Environmental Condition: Damping & Noise

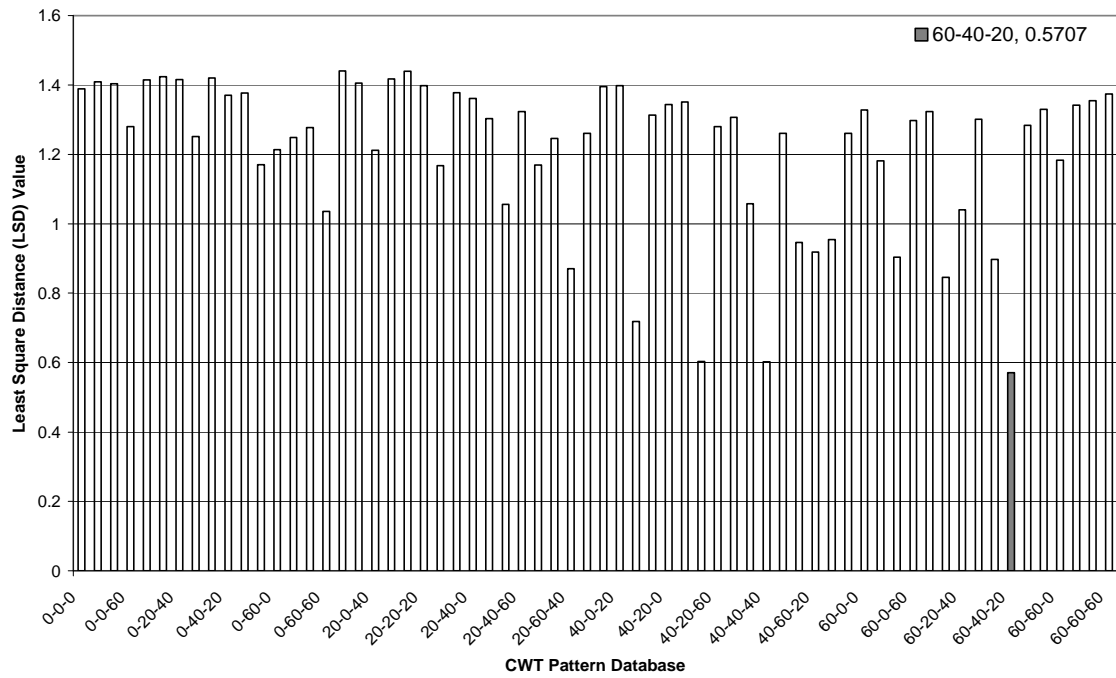
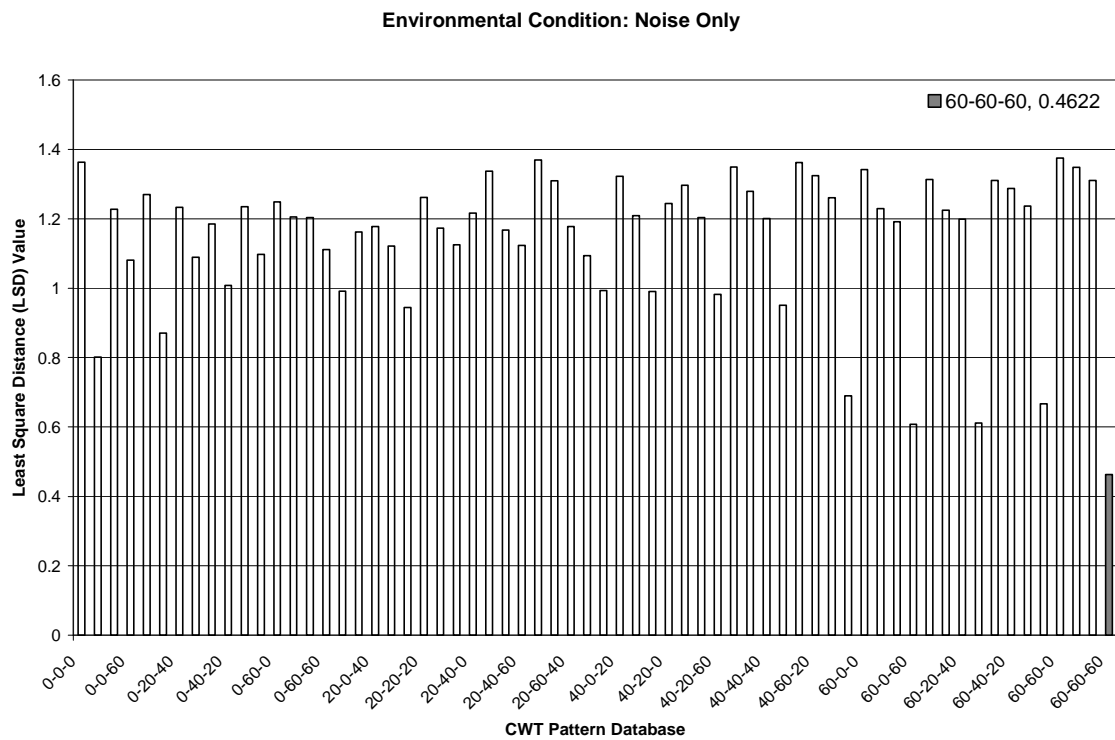
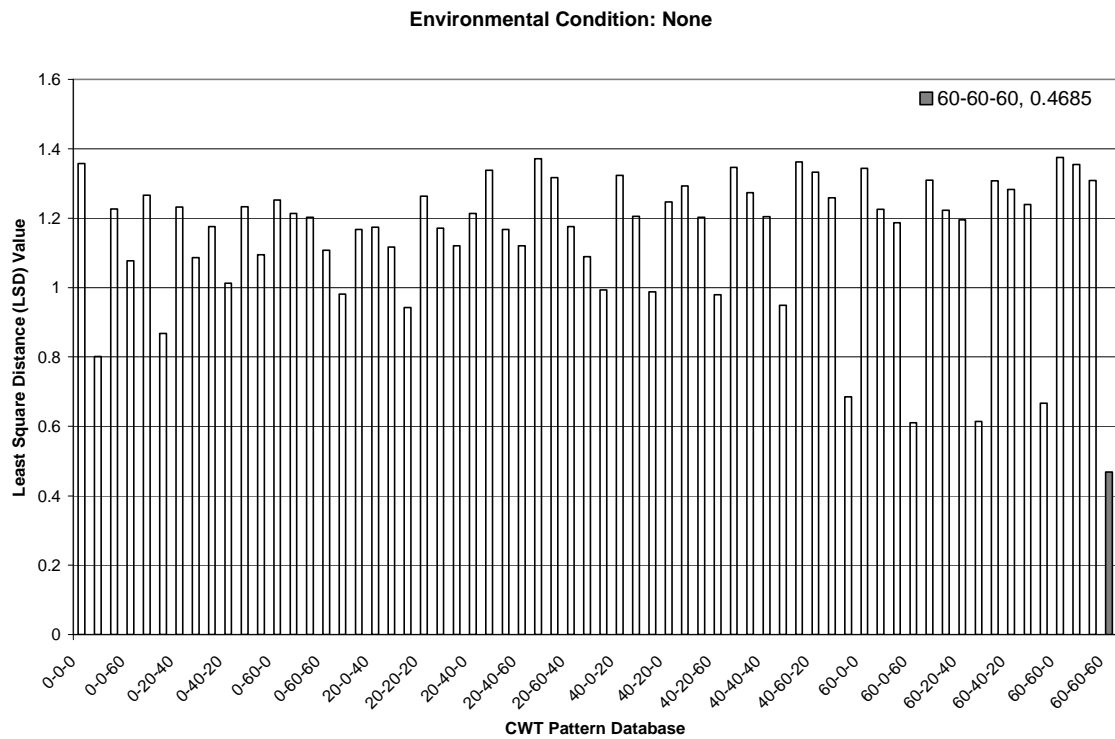
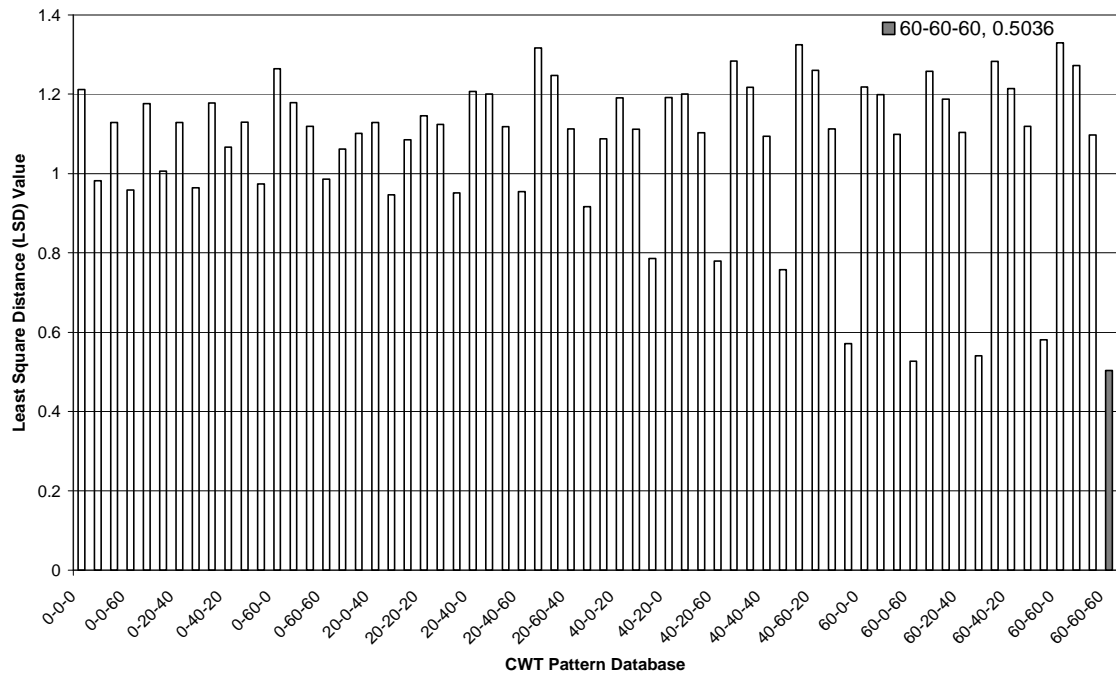


Figure B.20 Least Square Distance Matching for Damage Case 58-58-58 (CWT Pattern Database)



Environmental Condition: Damping Only



Environmental Condition: Damping & Noise

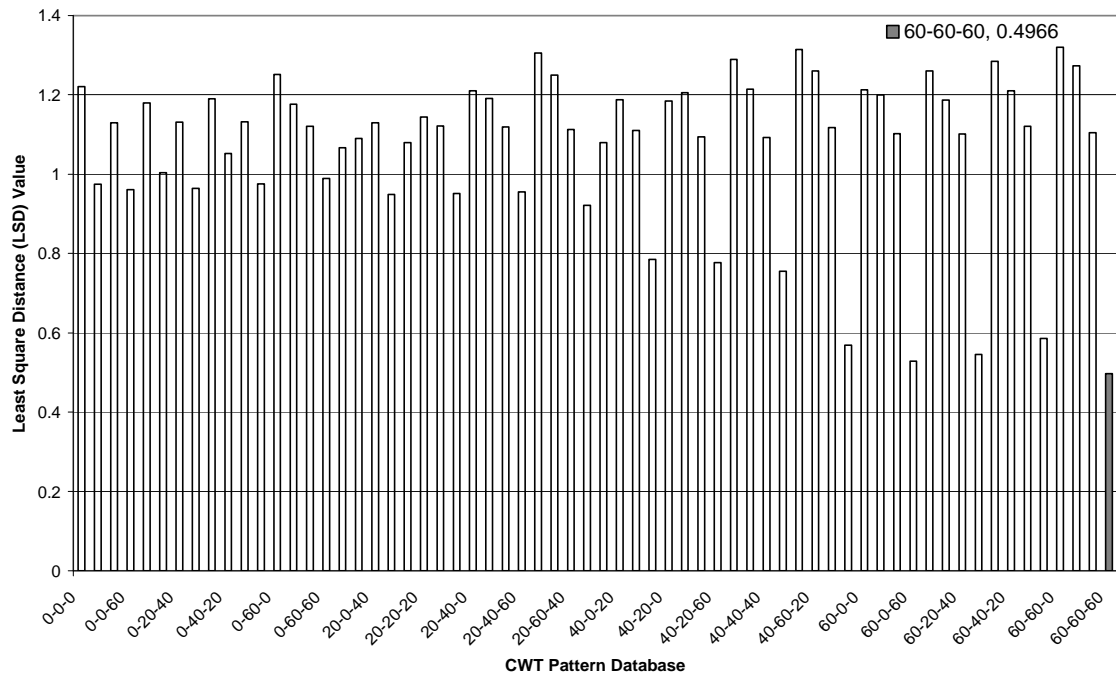
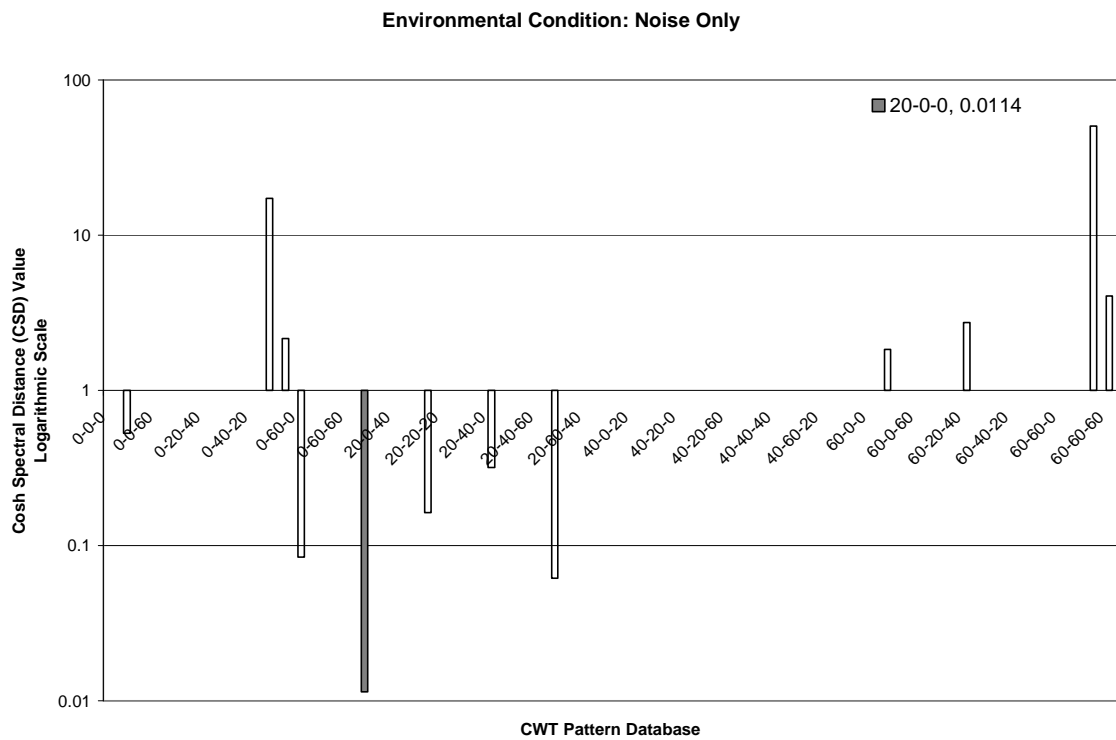
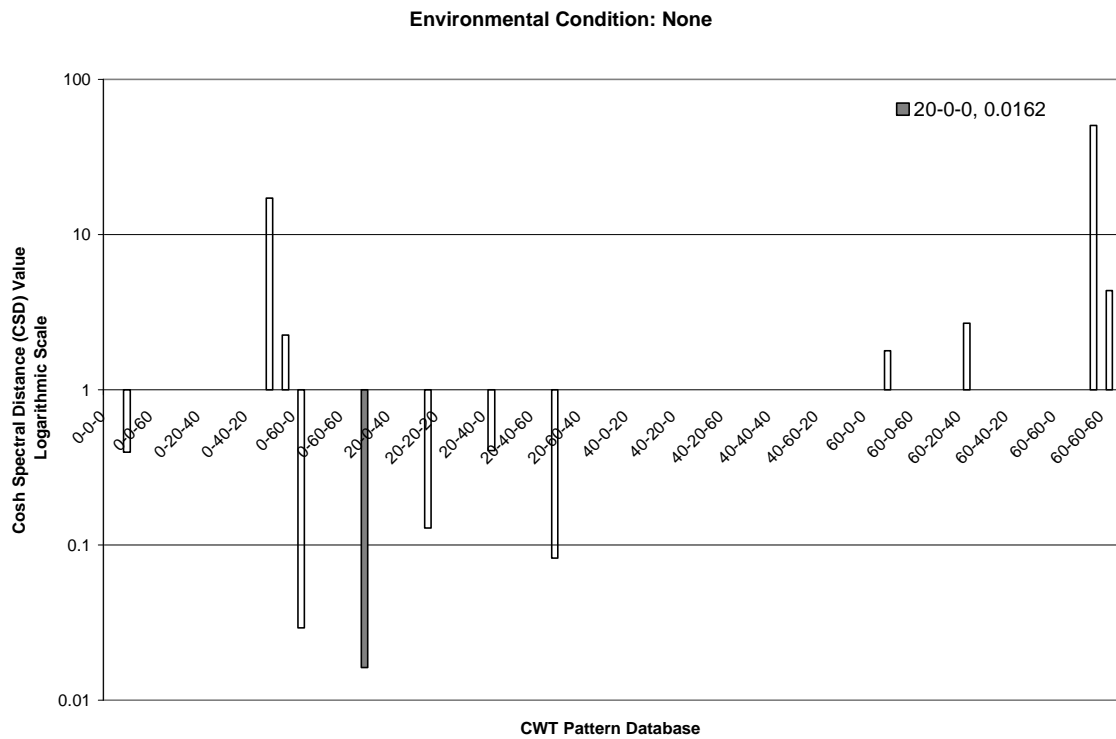
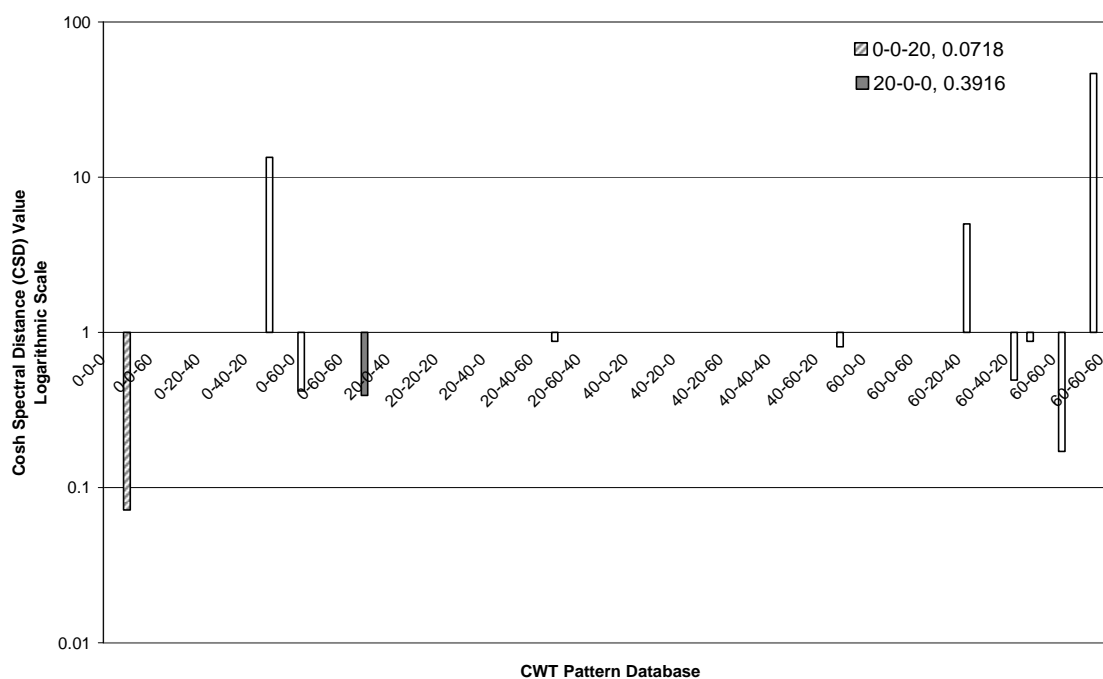


Figure B.21 Cosh Spectral Distance (CSD) Matching for Damage Case 19-0-0 (CWT Pattern Database)



Environmental Condition: Damping Only



Environmental Condition: Damping & Noise

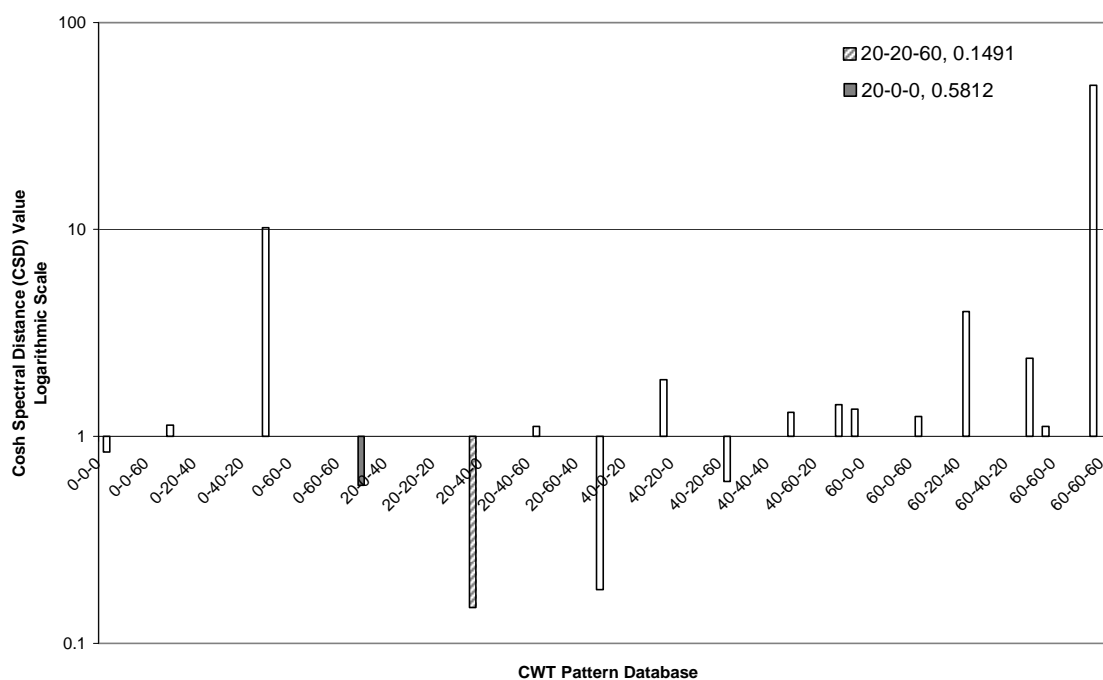
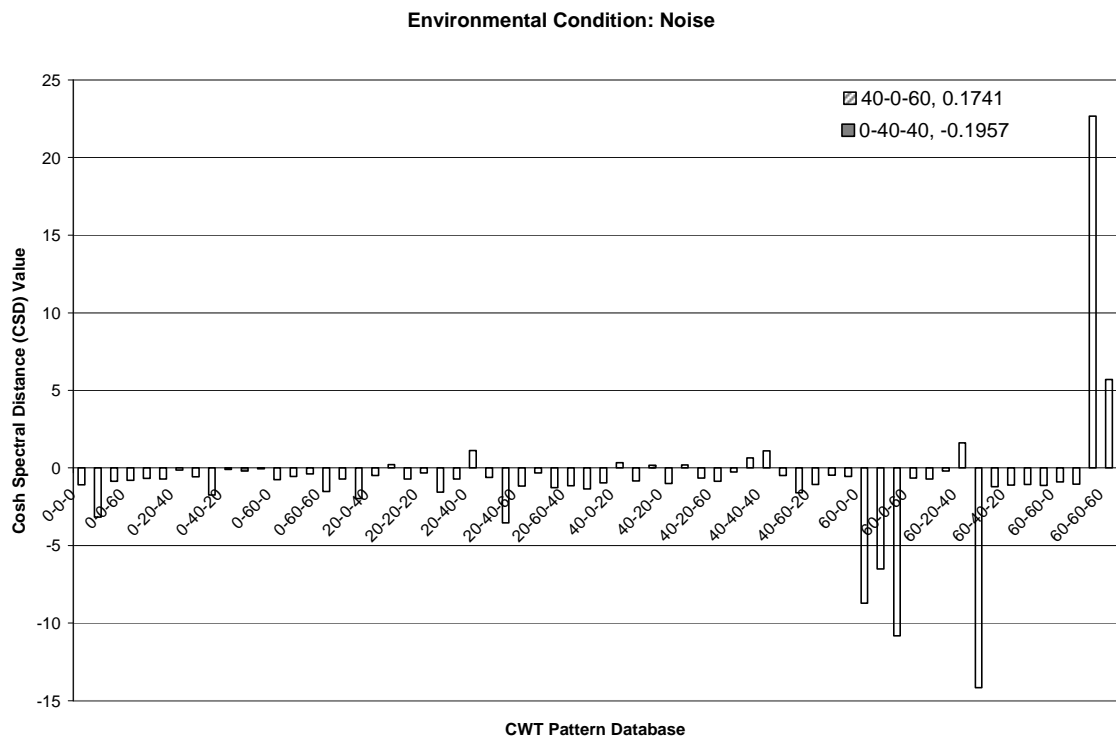
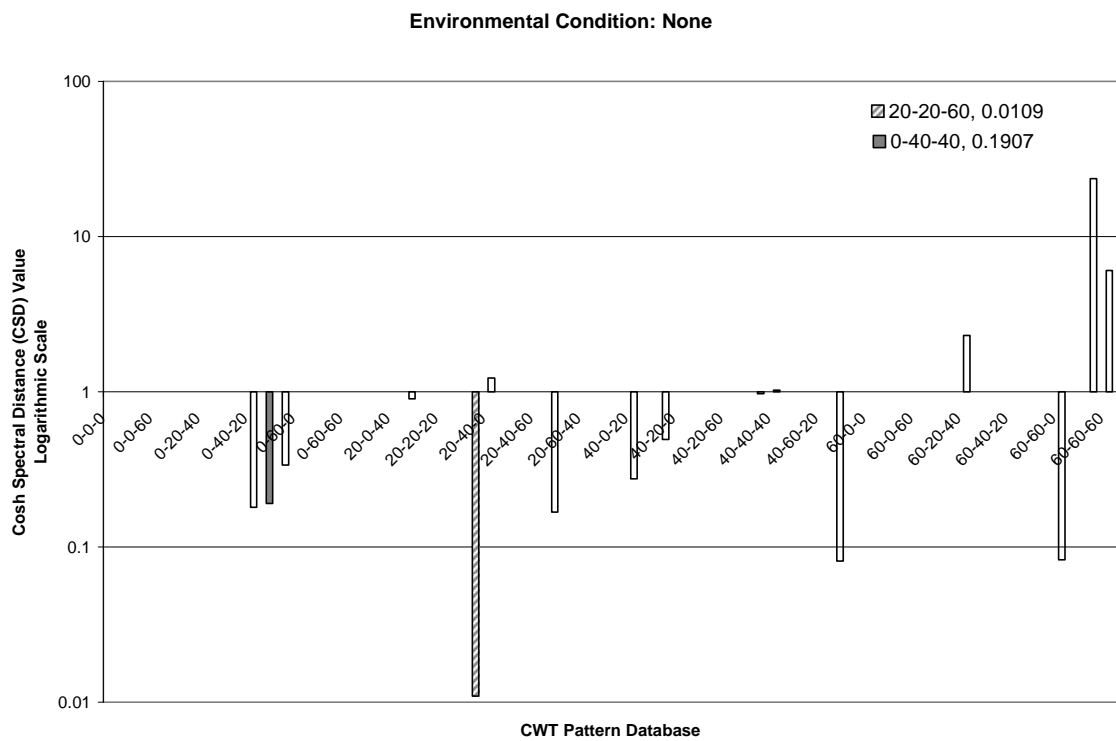
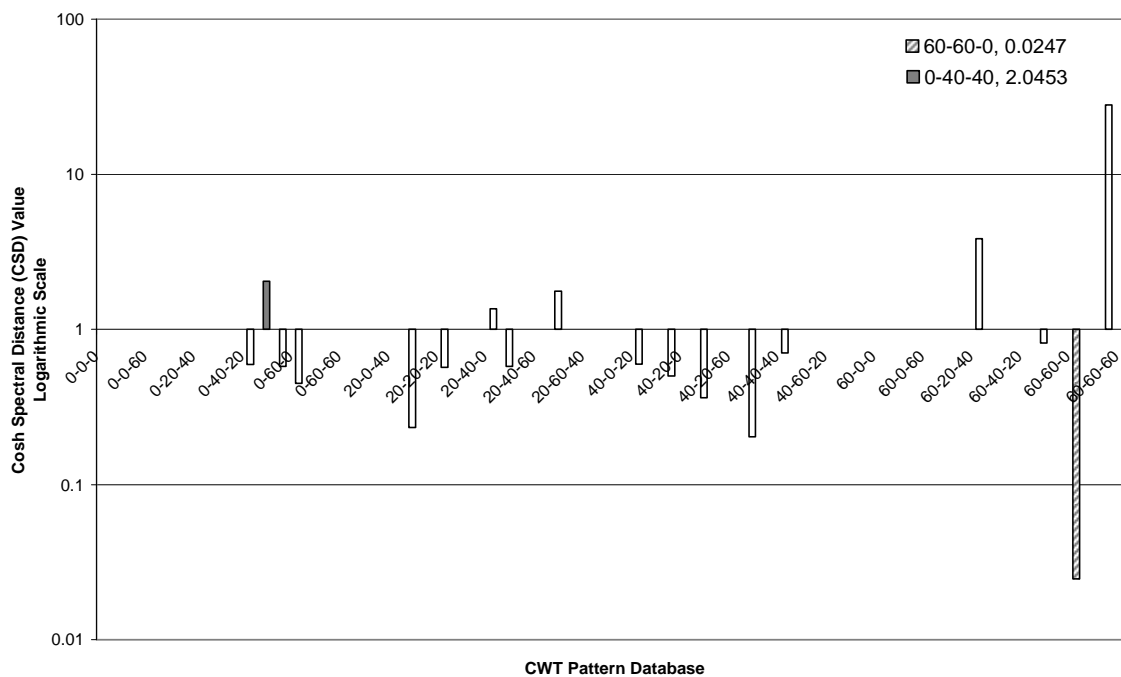


Figure B.22 Cosh Spectral Distance Matching for Damage Case 0-38-38 (CWT Pattern Database)



Environmental Condition: Damping Only



Environmental Condition: Damping & Noise

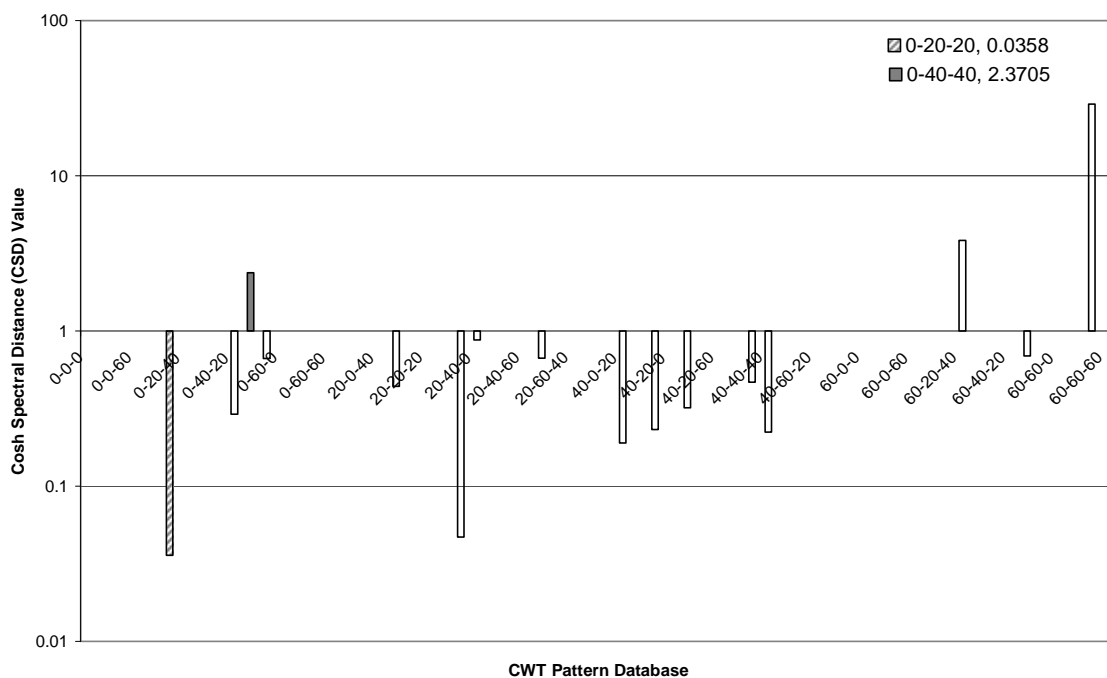
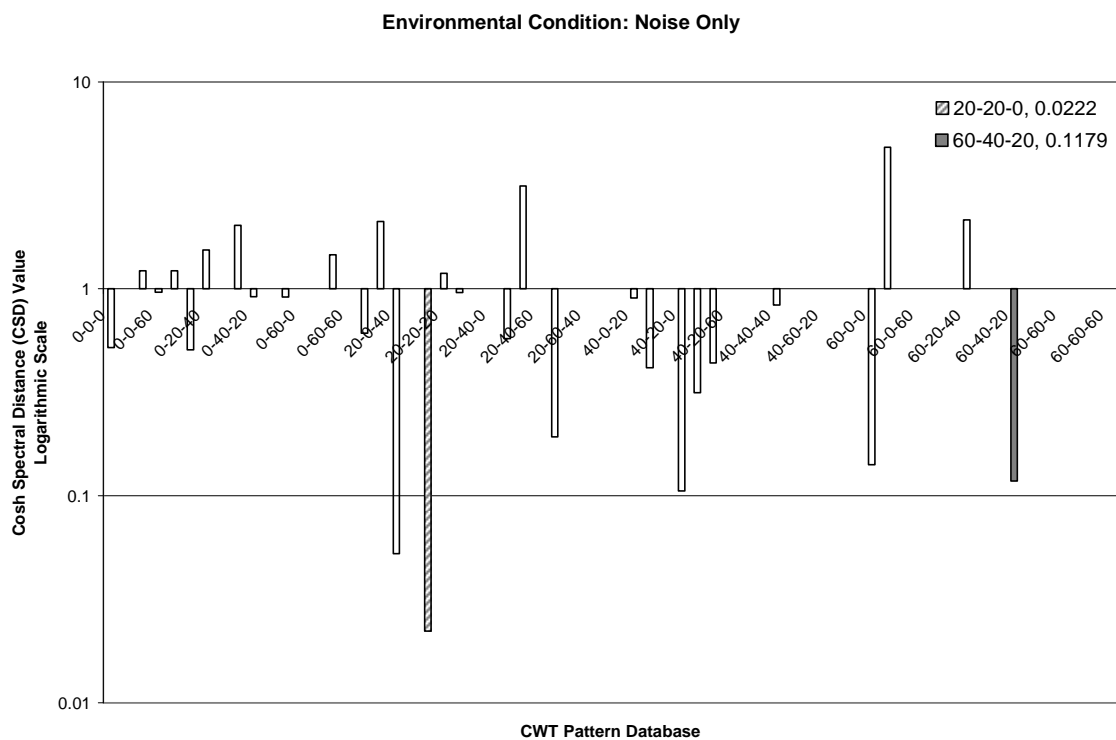
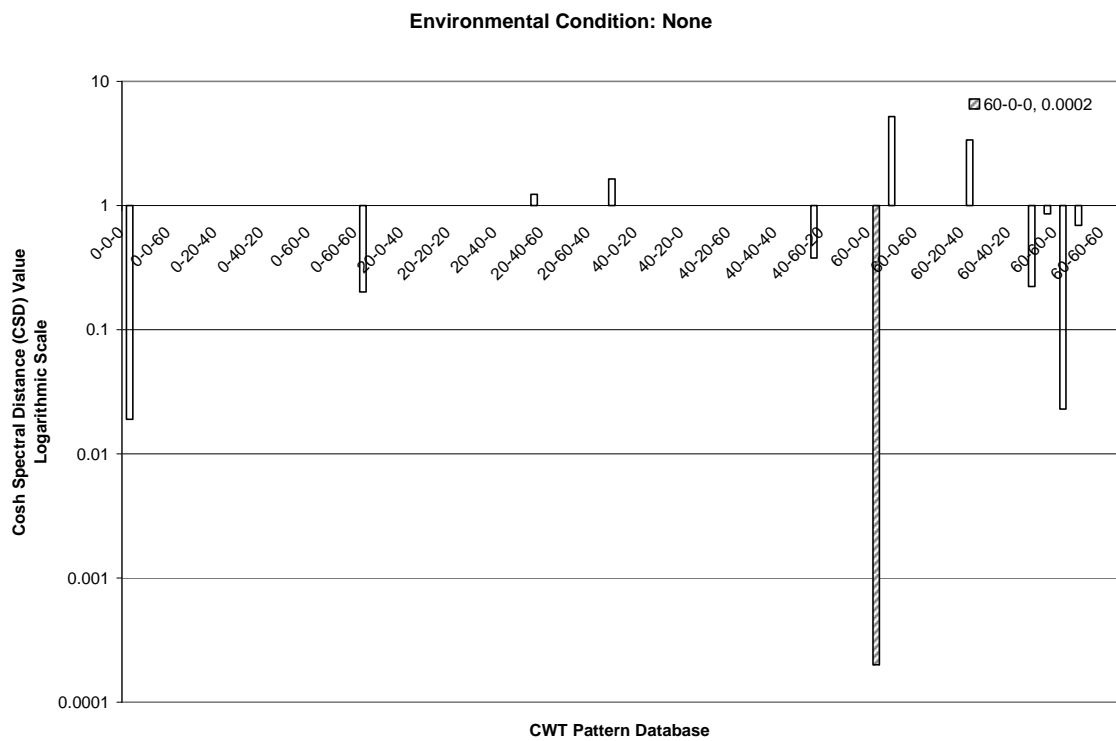


Figure B.23 Cosh Spectral Distance (CSD) Matching for Damage Case 58-38-19 (CWT Pattern Database)



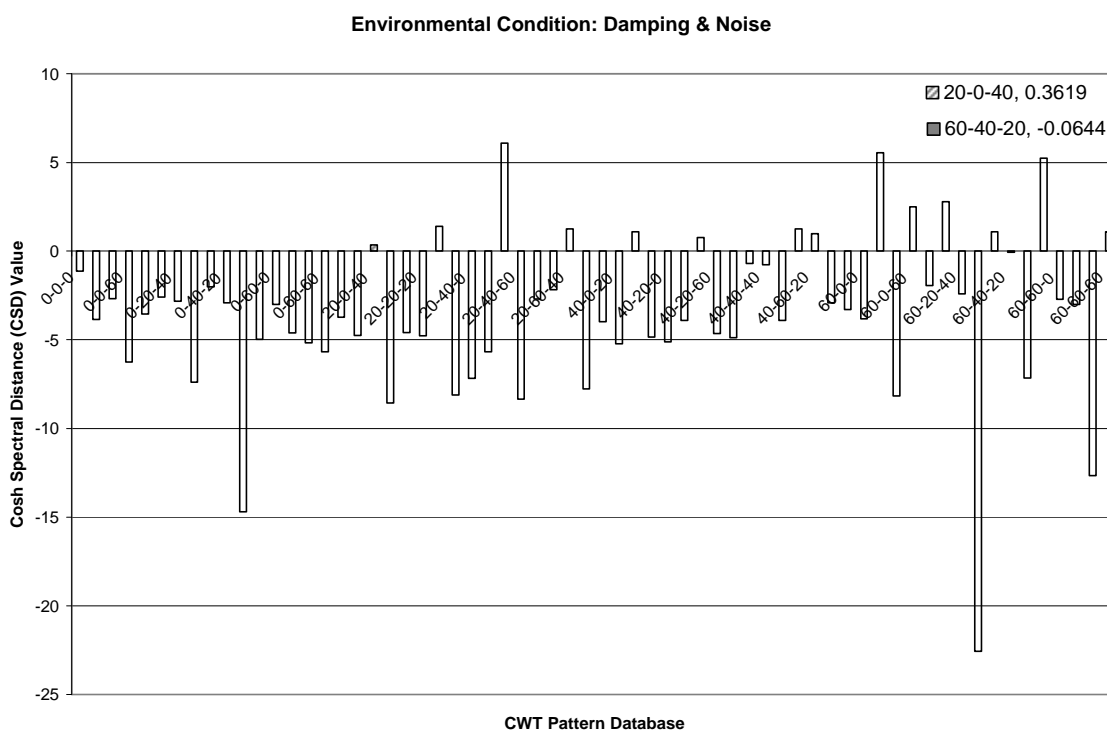
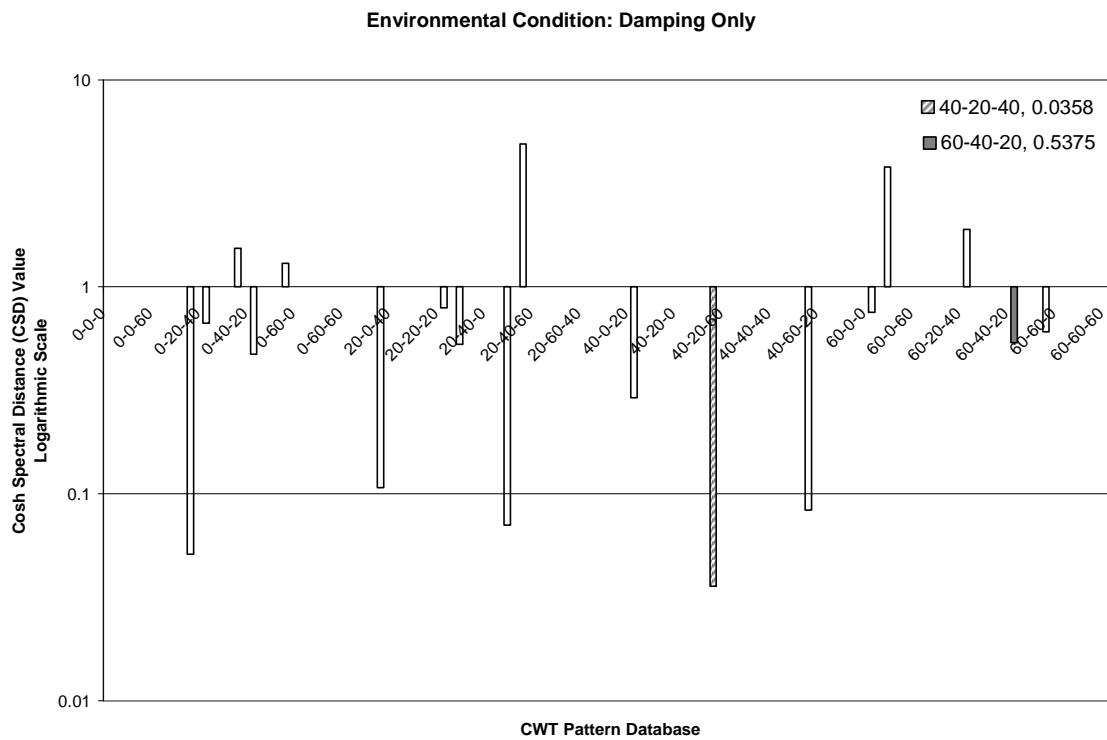
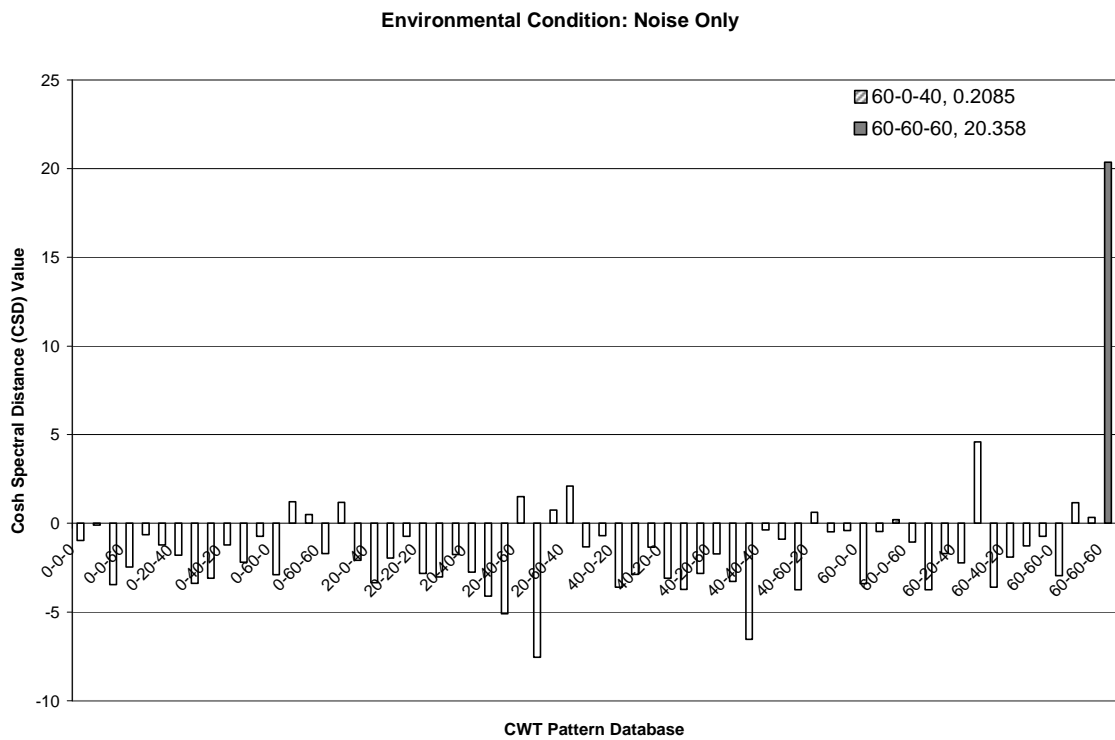
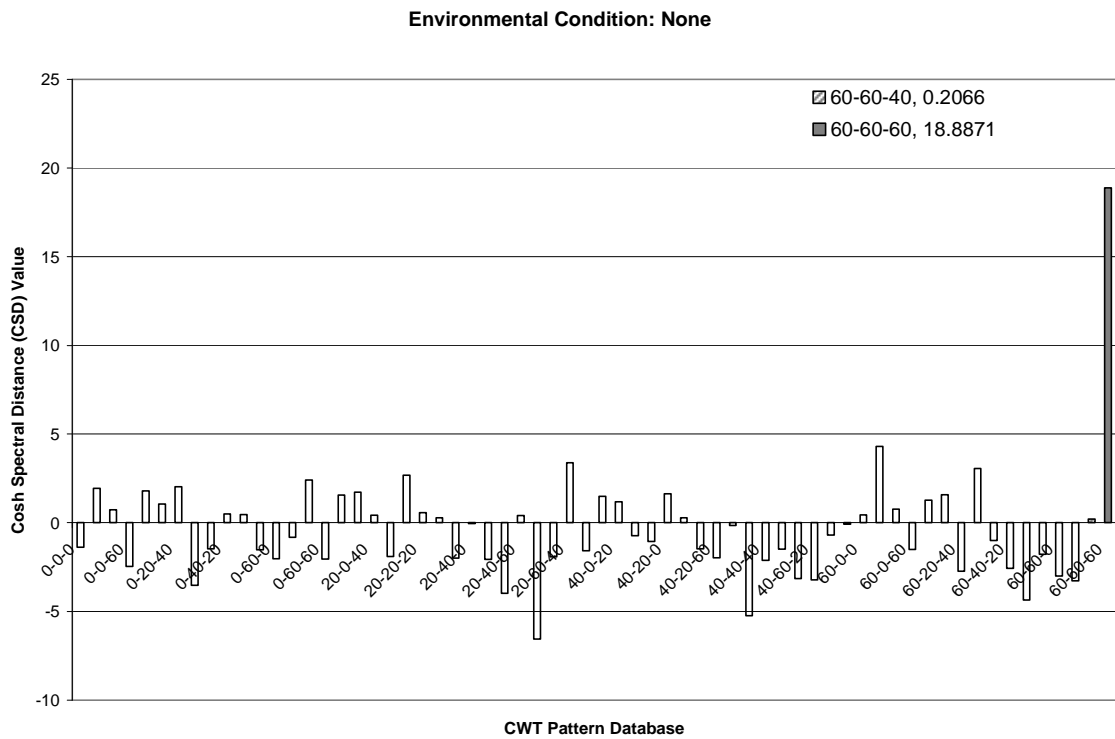
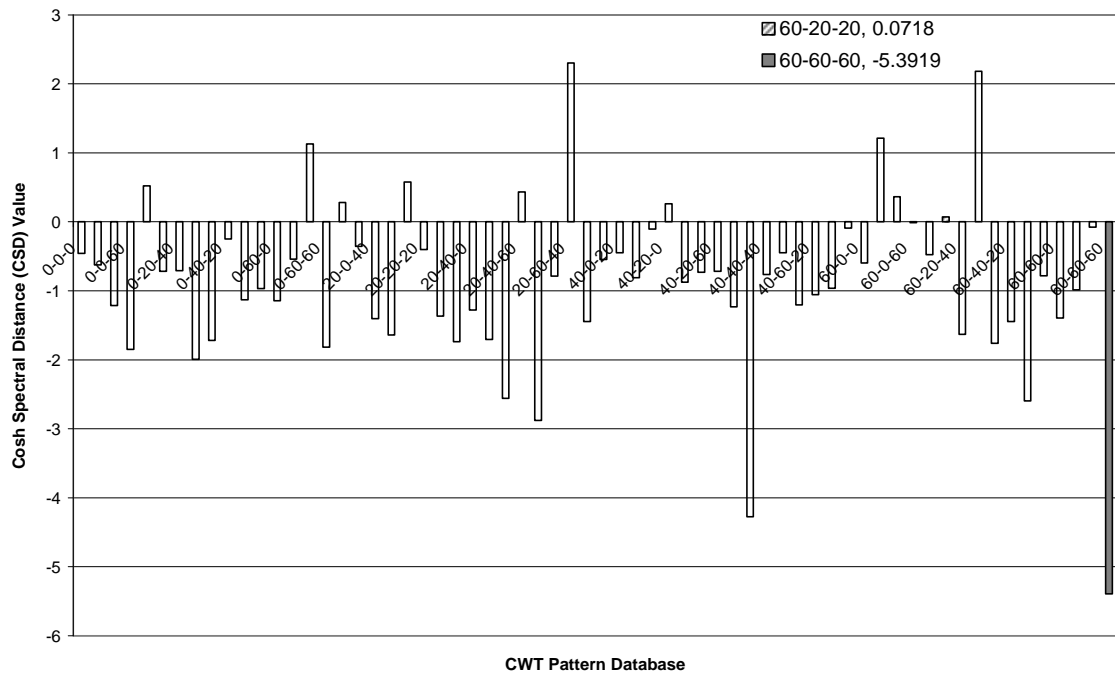


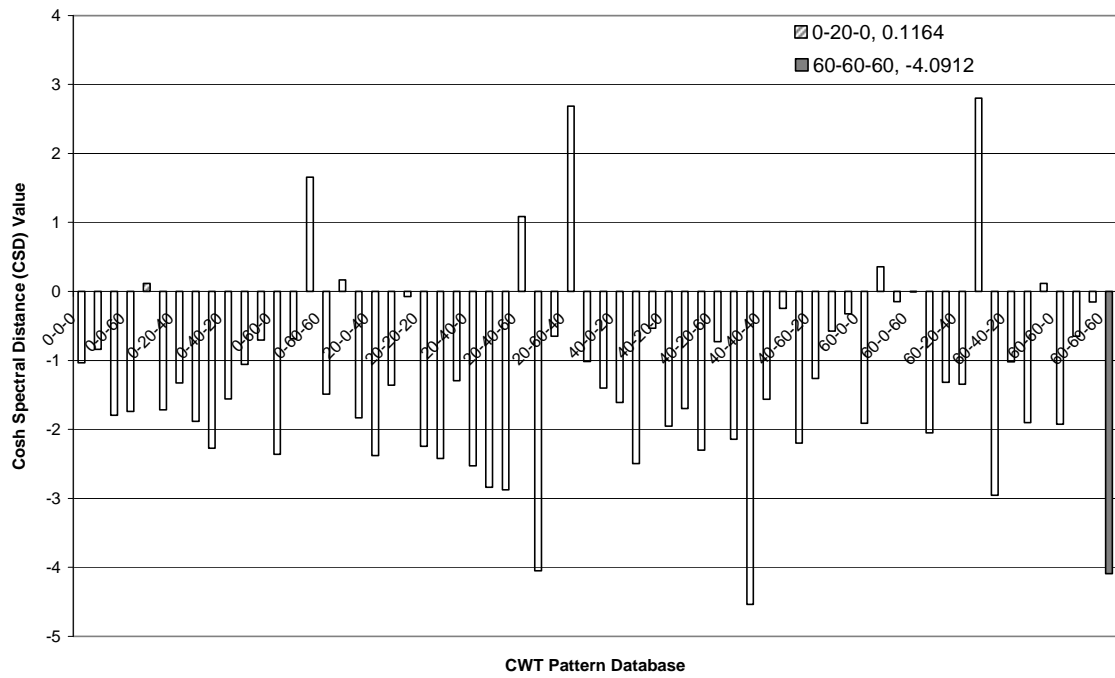
Figure B.24 Cosh Spectral Distance (CSD) Matching for Damage Case 58-58-58 (CWT Pattern Database)



Environmental Condition: Damping Only



Environmental Condition: Damping & Noise



Appendix C - Experimental Structure Properties

For the Column

$$b_c := 0.75 \quad h_c := \frac{1}{8} \quad E := 29000000 \quad L_c := 13$$

$$I_{c_single} := \frac{b_c \cdot h_c^3}{12}$$

$$I_{c_single} = 1.221 \times 10^{-4}$$

$$I_c := 5 \cdot I_{c_single}$$

$$I_c = 6.104 \times 10^{-4}$$

$$k := 2 \cdot \frac{12 \cdot E \cdot I_c}{L_c^3}$$

$$k = 193.357$$

$$K := \begin{pmatrix} k + k & -k & 0 \\ -k & k + k & -k \\ 0 & -k & k \end{pmatrix}$$

$$K = \begin{pmatrix} 386.713 & -193.357 & 0 \\ -193.357 & 386.713 & -193.357 \\ 0 & -193.357 & 193.357 \end{pmatrix}$$

$$\rho := 7.345 \cdot 10^{-4}$$

$$b_{floor} := 10 \quad h_{floor} := 1 \quad L_{floor} := 15$$

$$m := \rho \cdot b_{floor} \cdot h_{floor} \cdot L_{floor}$$

$$m = 0.11$$

$$\mathbf{M} := \begin{pmatrix} \mathbf{m} & 0 & 0 \\ 0 & \mathbf{m} & 0 \\ 0 & 0 & \mathbf{m} \end{pmatrix}$$

$$\mathbf{M} = \begin{pmatrix} 0.11 & 0 & 0 \\ 0 & 0.11 & 0 \\ 0 & 0 & 0.11 \end{pmatrix}$$

$$\left| \mathbf{K} - \omega^2 \cdot \mathbf{M} \right| \rightarrow 7228991.7677947941458 - 24714.555069021795643 \cdot \omega^2 + 11.735331608698918269 \cdot \omega^4 - 1.3373626116093750000 \cdot 10^{-3} \cdot \omega^6$$

$$7228991.7677947941458 - 24714.555069021795643 \cdot \omega^2 + 11.735331608698918269 \cdot \omega^4 - 1.3373626116093750000 \cdot 10^{-3} \cdot \omega^6 \text{ solve, } \omega \rightarrow \begin{pmatrix} -18.643994315562414336 \\ 18.643994315562414336 \\ -52.239311218905226278 \\ 52.239311218905226278 \\ -75.487991862235954239 \\ 75.487991862235954239 \end{pmatrix}$$

$$7228991.7677947941458 - 24714.555069021795643 \cdot \omega + 11.735331608698918269 \cdot \omega^2 - 1.3373626116093750000 \cdot 10^{-3} \cdot \omega^3 \text{ solve, } \omega \rightarrow \begin{pmatrix} 347.59852403872361858 \\ 2728.9456366256374381 \\ 5698.4369153930016505 \end{pmatrix}$$

$$\omega_1 := \sqrt{347.59852403872361858}$$

$$\omega_1 = 18.644$$

$$f_1 := \frac{\omega_1}{2 \cdot \pi}$$

$$f_1 = 2.967$$

$$T_1 := \frac{1}{f_1}$$

$$T_1 = 0.337$$

$$\omega_2 := \sqrt{2728.9456366256374381}$$

$$\omega_2 = 52.239$$

$$f_2 := \frac{\omega_2}{2 \cdot \pi}$$

$$f_2 = 8.314$$

$$T_2 := \frac{1}{f_2}$$

$$T_2 = 0.12$$

$$\omega_3 := \sqrt{5698.4369153930016505}$$

$$\omega_3 = 75.488$$

$$f_3 := \frac{\omega_3}{2 \cdot \pi}$$

$$f_3 = 12.014$$

$$T_3 := \frac{1}{f_3}$$

$$T_3 = 0.083$$

For the unit nodal rotation of the column

$$M_c := \frac{4 \cdot E \cdot I_c}{L_c}$$

$$M_c = 5.9 \times 10^3$$

For the floor

$$b_{\text{floor}} := 10 \quad h_{\text{floor}} := 1 \quad L_{\text{floor}} := 15$$

$$I_f := \frac{b_{\text{floor}} \cdot h_{\text{floor}}^3}{12}$$

$$I_f = 0.833$$

For the unit nodal rotation of the floor

$$M_f := \frac{4 \cdot E \cdot I_f}{L_{\text{floor}}}$$

$$M_f = 6.444 \times 10^6$$

$$n := \frac{M_f}{M_c}$$

$$n = 1.092 \times 10^3$$

Check the bucking

Both column ends fixed, lateral motion exists: $K=1$

$$E := 29000000 \quad k := 1$$

Theoretical bucking load

$$P_{cr} := \frac{\pi^2 \cdot E \cdot I_{c_single}}{(k \cdot L_c)^2}$$

$$P_{cr} = 242.63$$

$$P := 4 \cdot P_{cr}$$

$$P = 970.522$$

Design compression strength for flexural bucking

$$A_g := b_c \cdot h_c$$

$$A_g = 0.094$$

$$r := \sqrt{\frac{I_{c_single}}{A_g}}$$

$$r = 0.036$$

$$F_y := 36000$$

$$\lambda_c := \frac{k \cdot L_c}{r \cdot \pi} \cdot \sqrt{\frac{F_y}{E}}$$

$$\lambda_c = 3.73$$

$$\lambda > 1.5$$

$$F_{cr} := \frac{0.877}{\lambda_c^2} \cdot F_y$$

$$F_{cr} = 2.27 \times 10^3$$

$$P_n := A_g \cdot F_{cr}$$

$$P_n = 212.787$$

$$\phi := 0.85$$

$$P_{\text{total}} := 4 \cdot \phi \cdot P_n$$

$$P_{\text{total}} = 723.475$$

$$w_{\text{floor}} := 490 \cdot \frac{b_{\text{floor}}}{12} \cdot \frac{h_{\text{floor}}}{12} \cdot \frac{L_{\text{floor}}}{12}$$

$$w_{\text{floor}} = 42.535$$

$$w_{\text{column}} := 490 \cdot \frac{b_c}{12} \cdot \frac{h_c}{12} \cdot \frac{L_c}{12}$$

$$w_{\text{column}} = 0.319$$

$$W := 3 \cdot w_{\text{floor}} + 20 \cdot w_{\text{column}}$$

$$W = 133.984$$

$W < P$ that means under selfweight there is no buckling happened at each of the columns

$$P_{\text{column_compression}} := \frac{W}{4}$$

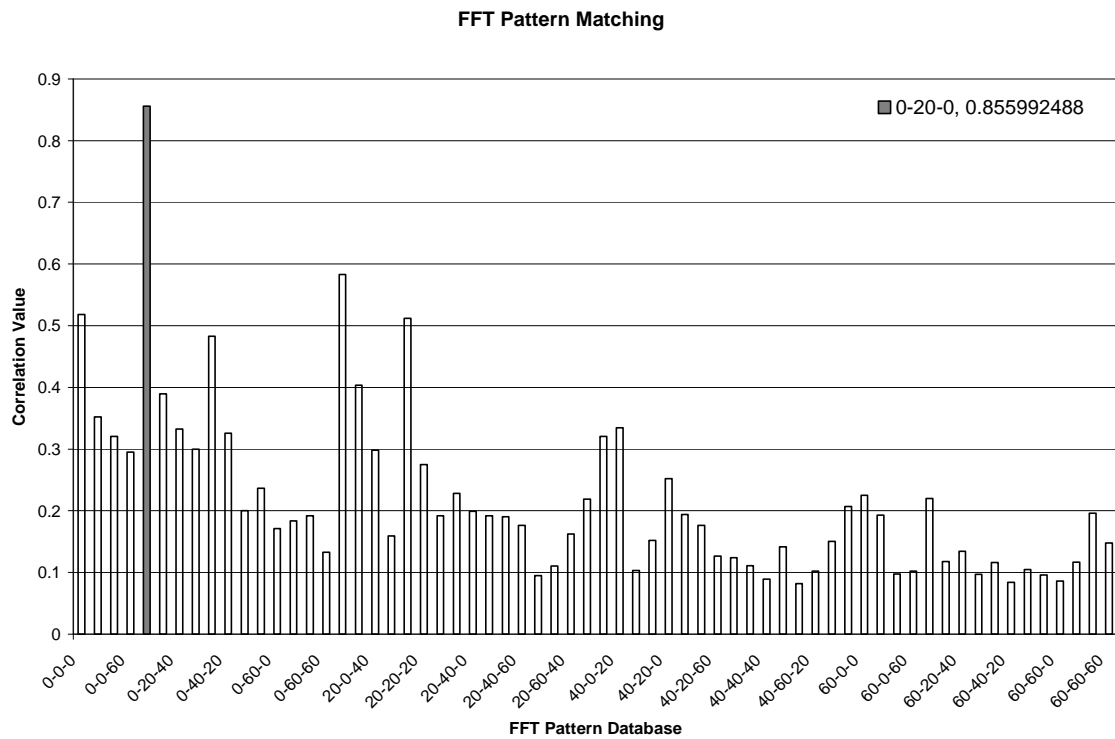
$$P_{\text{column_compression}} = 33.496$$

$$F := \frac{P_{\text{column_compression}}}{A_g}$$

$$F = 357.292$$

Appendix D - Matching Results in Experimental Study

Figure D.1 Correlation Matching for Damage Case 0-20-0, FFT & CWT Pattern Matching



CWT Pattern Matching

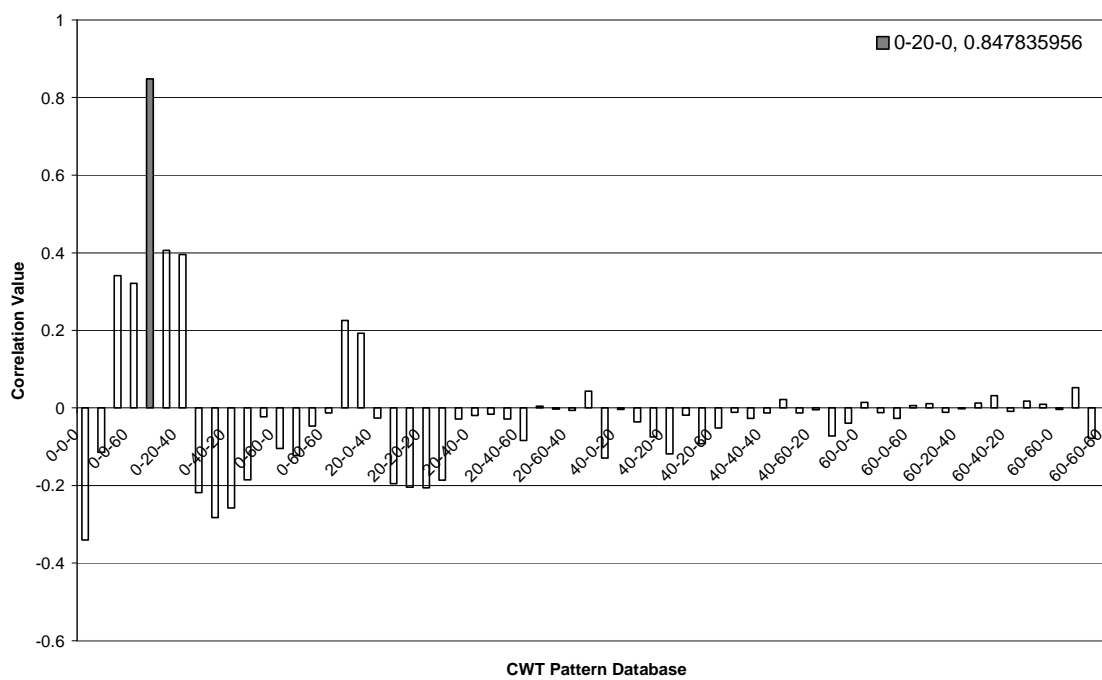


Figure D.2 Least Square Distance (LSD) Matching for Damage Case 0-20-0, FFT & CWT Pattern Matching

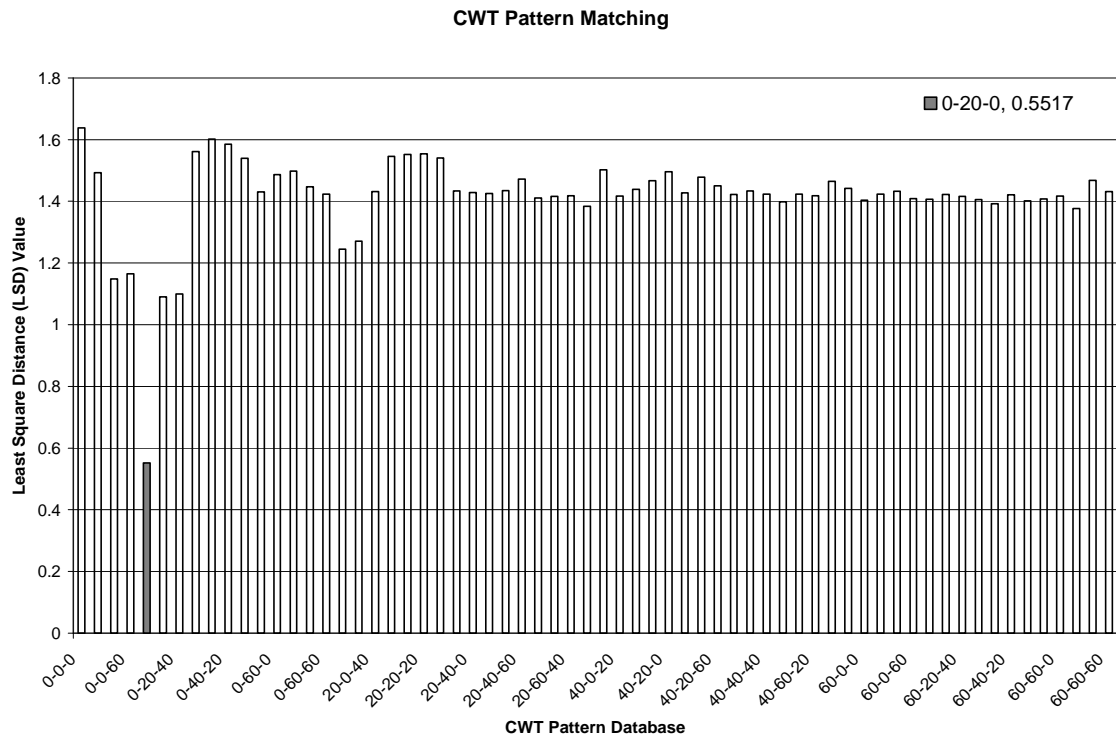
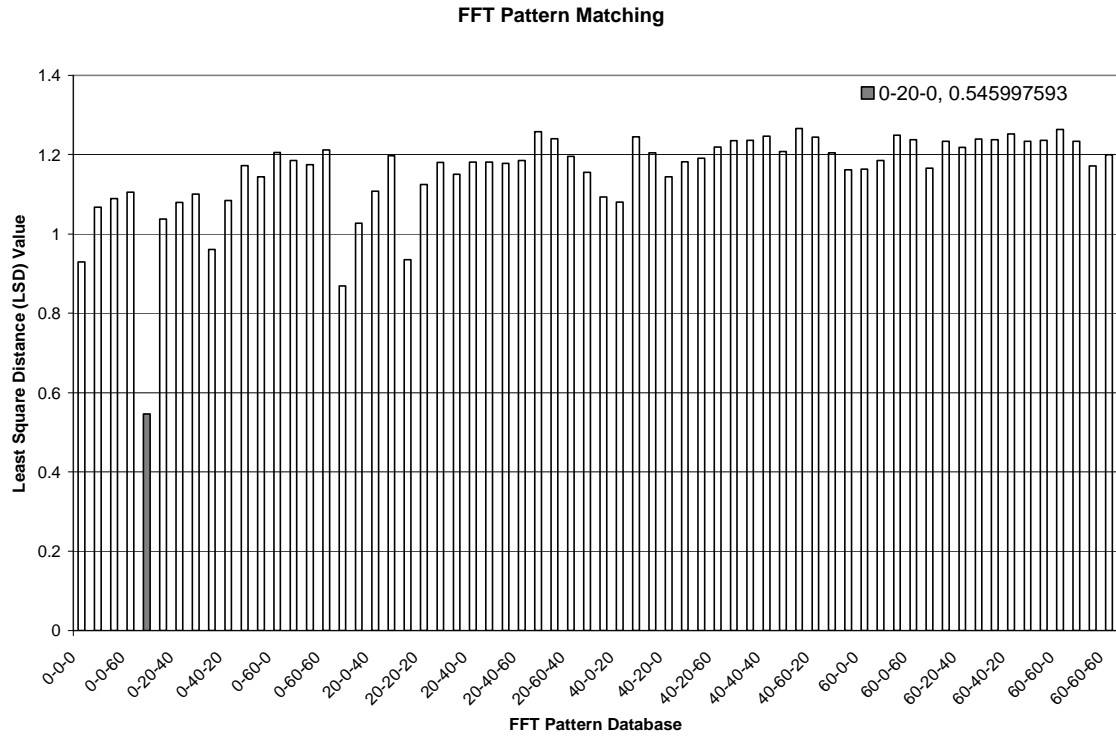


Figure D.3 Cosh Spectral Distance (CSD) Matching for Damage Case 0-20-0, FFT & CWT Pattern Matching

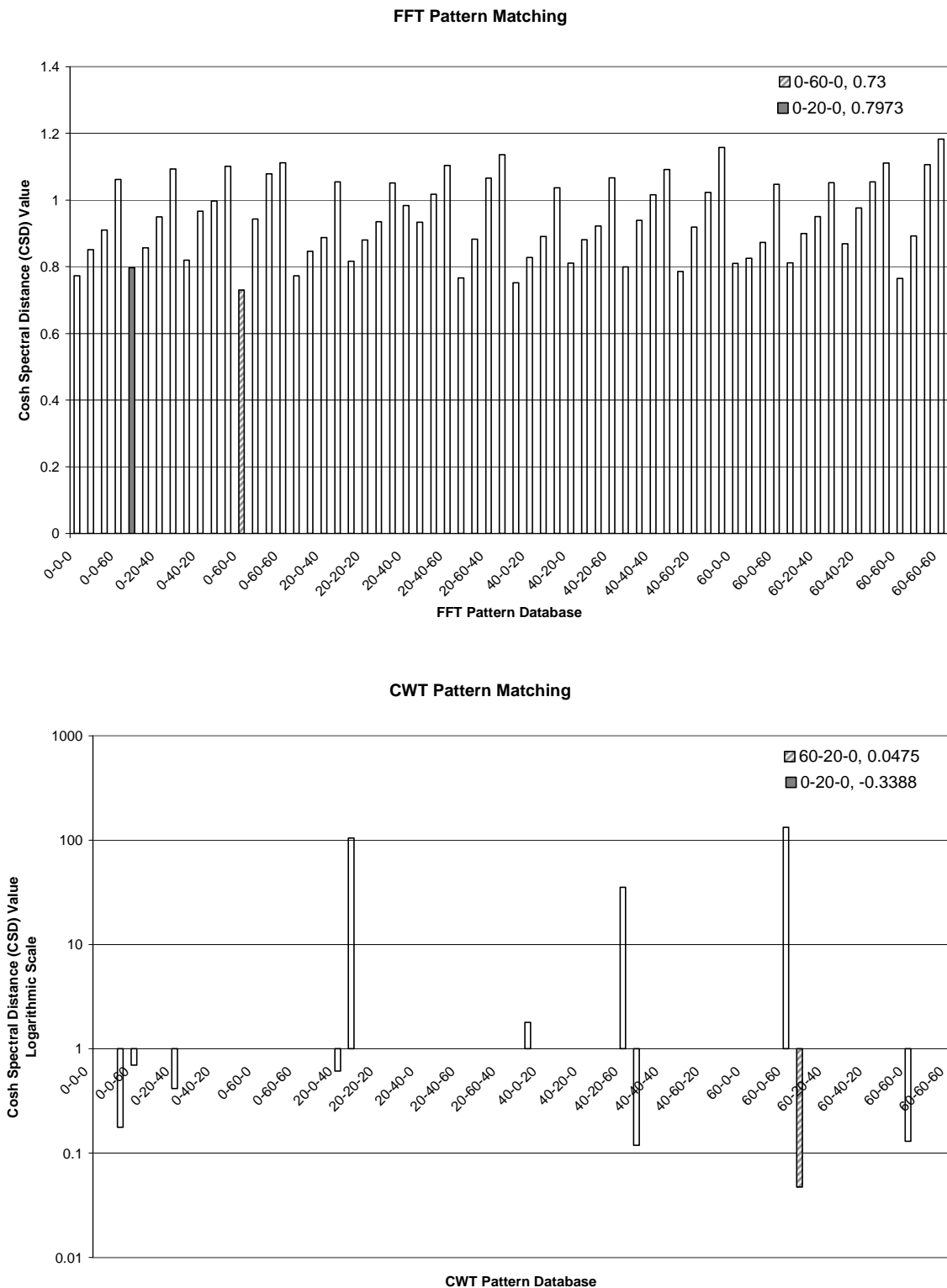


Figure D.4 Correlation Matching for Damage Case 20-0-0, FFT & CWT Pattern Matching

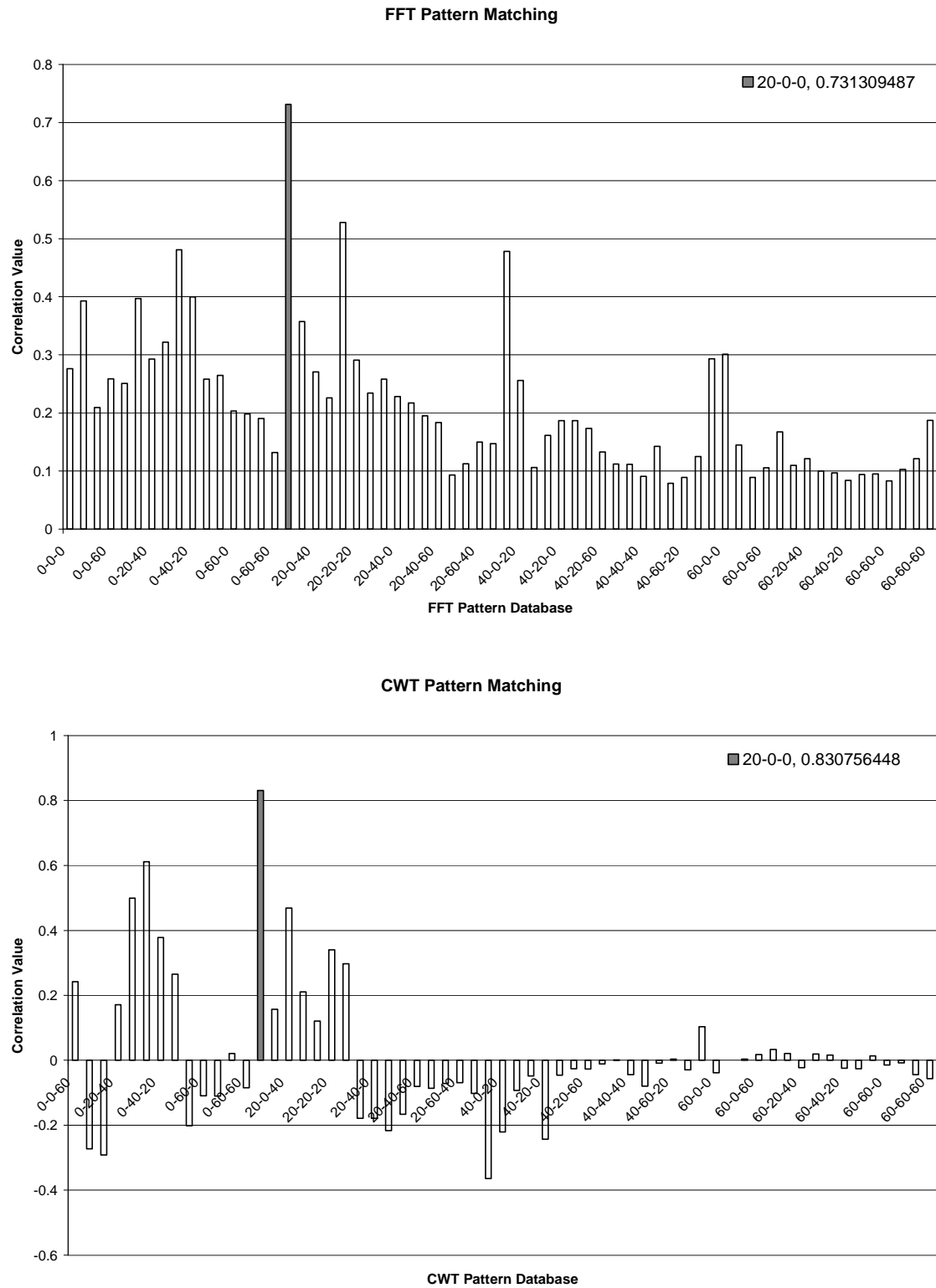


Figure D.5 Least Square Distance (LSD) Matching for Damage Case 20-0-0, FFT & CWT Pattern Matching

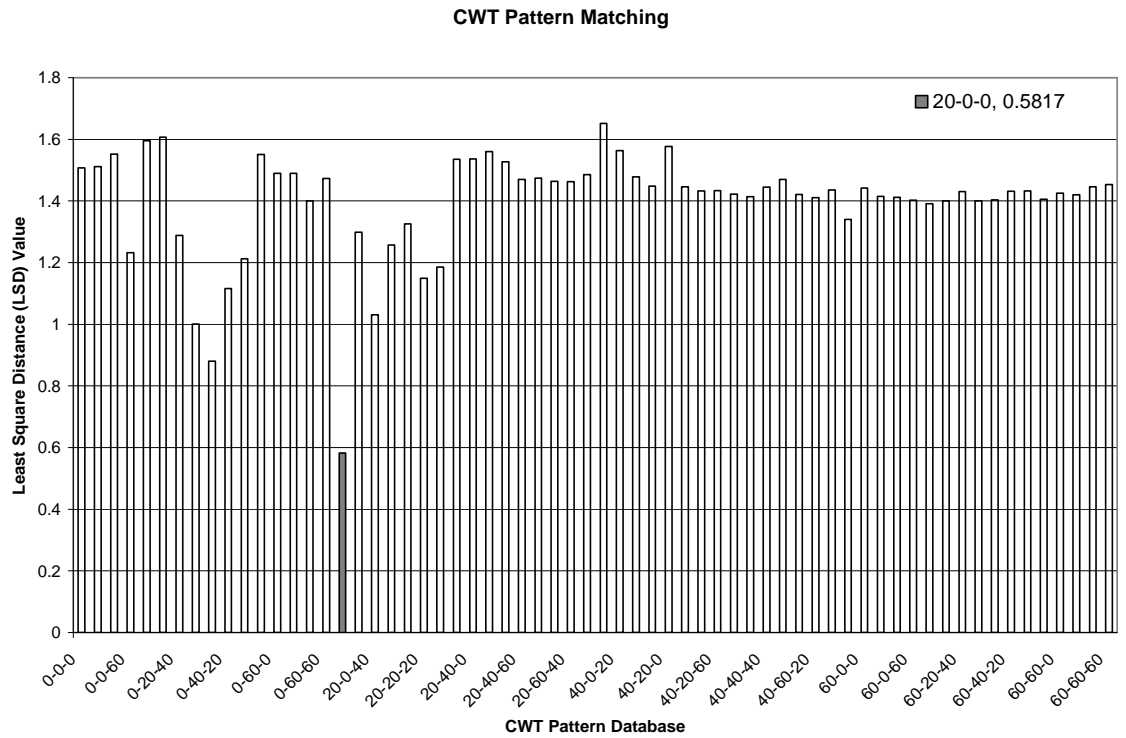
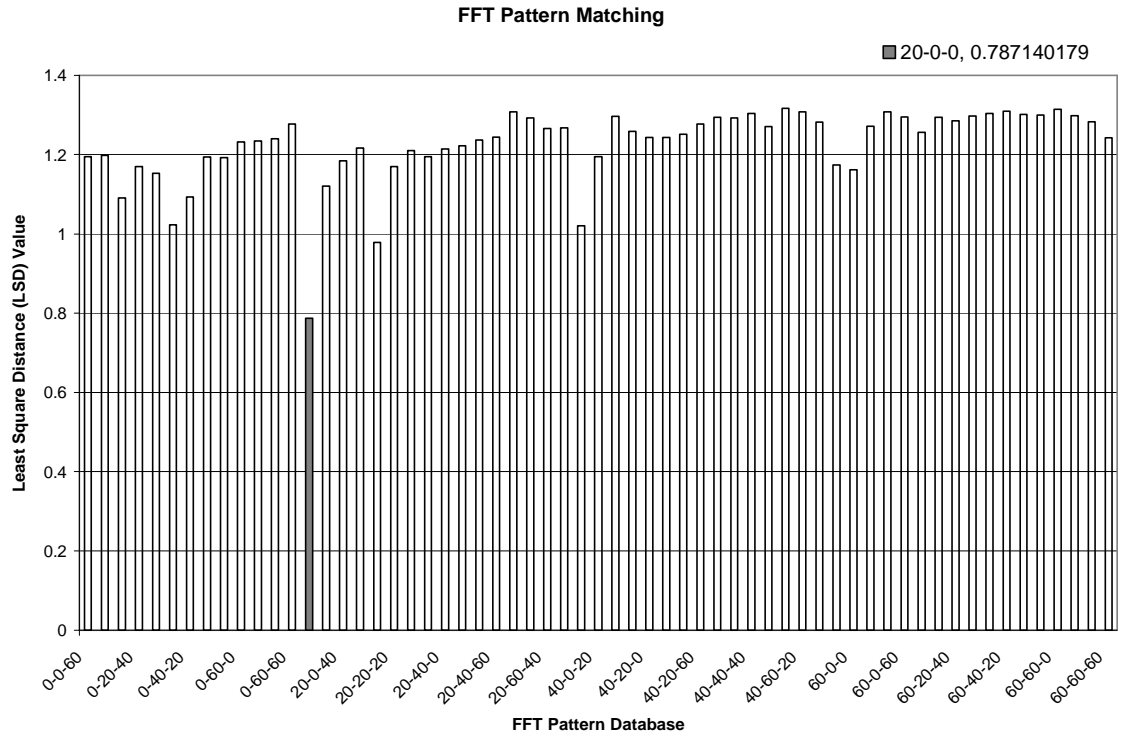


Figure D.6 Cosh Spectral Distance (CSD) Matching for Damage Case 20-0-0, FFT & CWT Pattern Matching

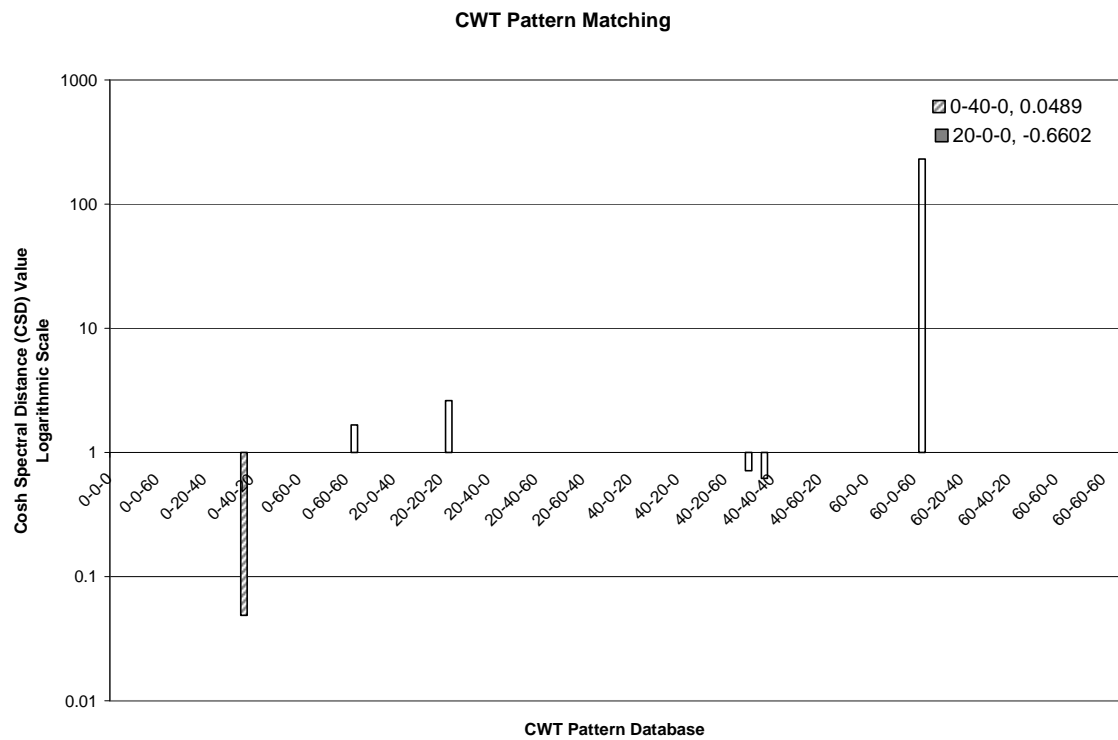
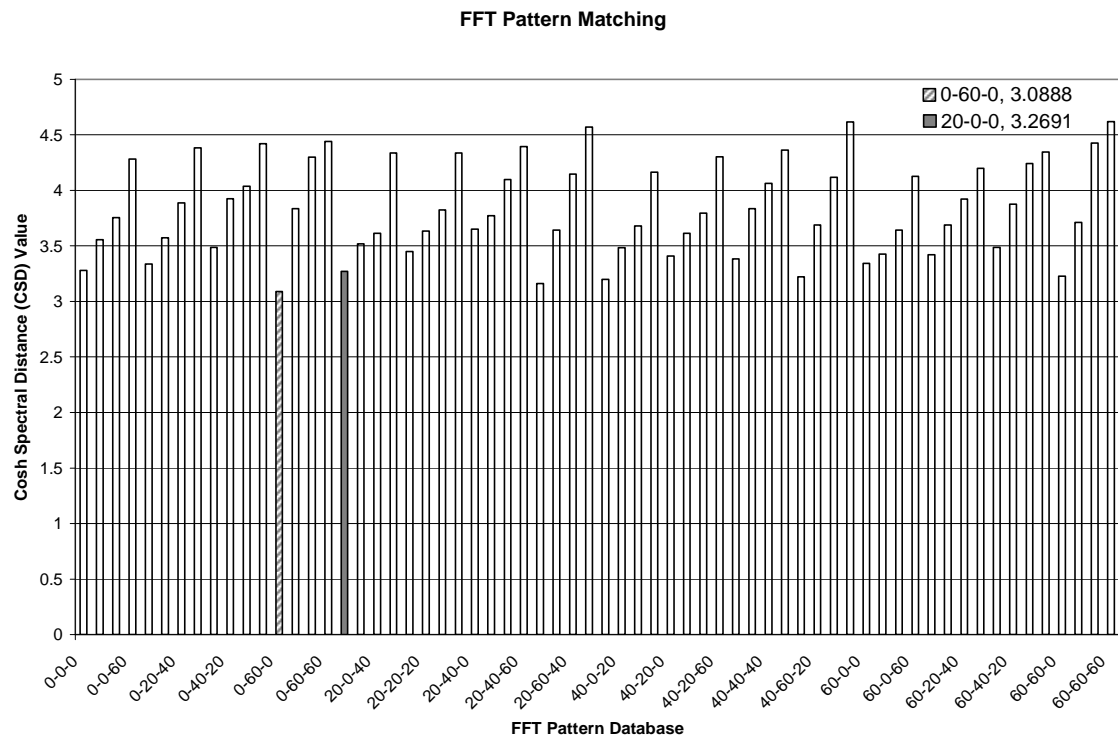


Figure D.7 Correlation Matching for Damage Case 0-20-20, FFT & CWT Pattern Matching

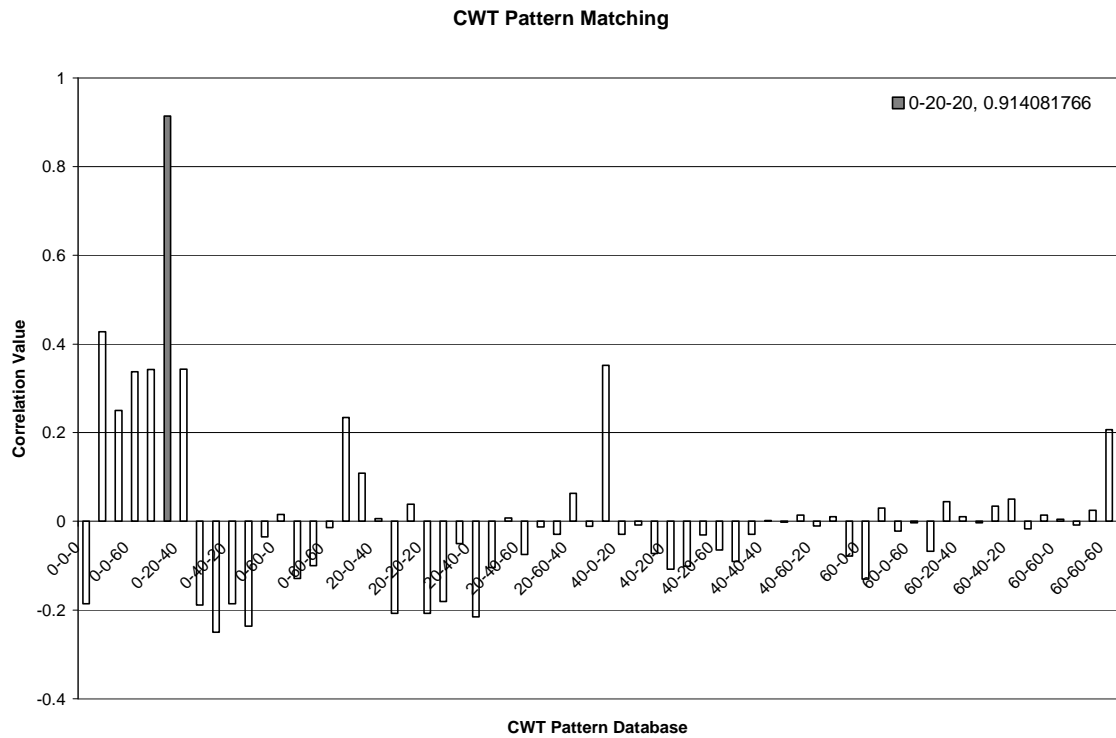
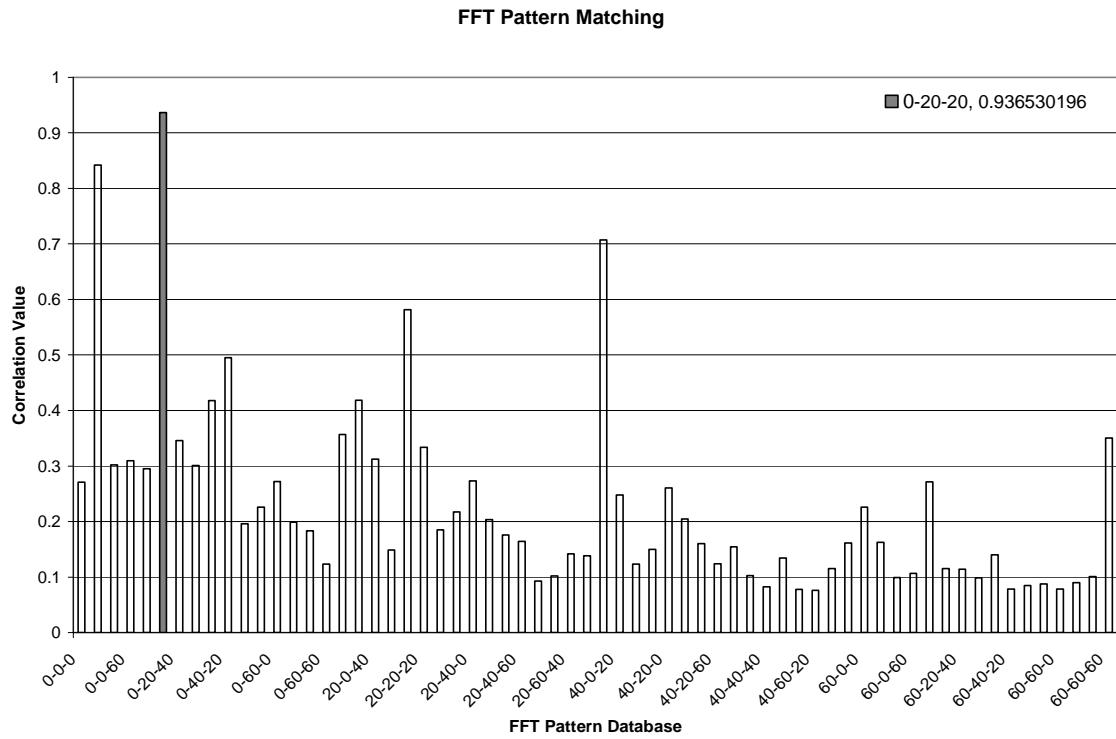


Figure D.8 Least Square Distance (LSD) Matching for Damage Case 0-20-20, FFT & CWT Matching

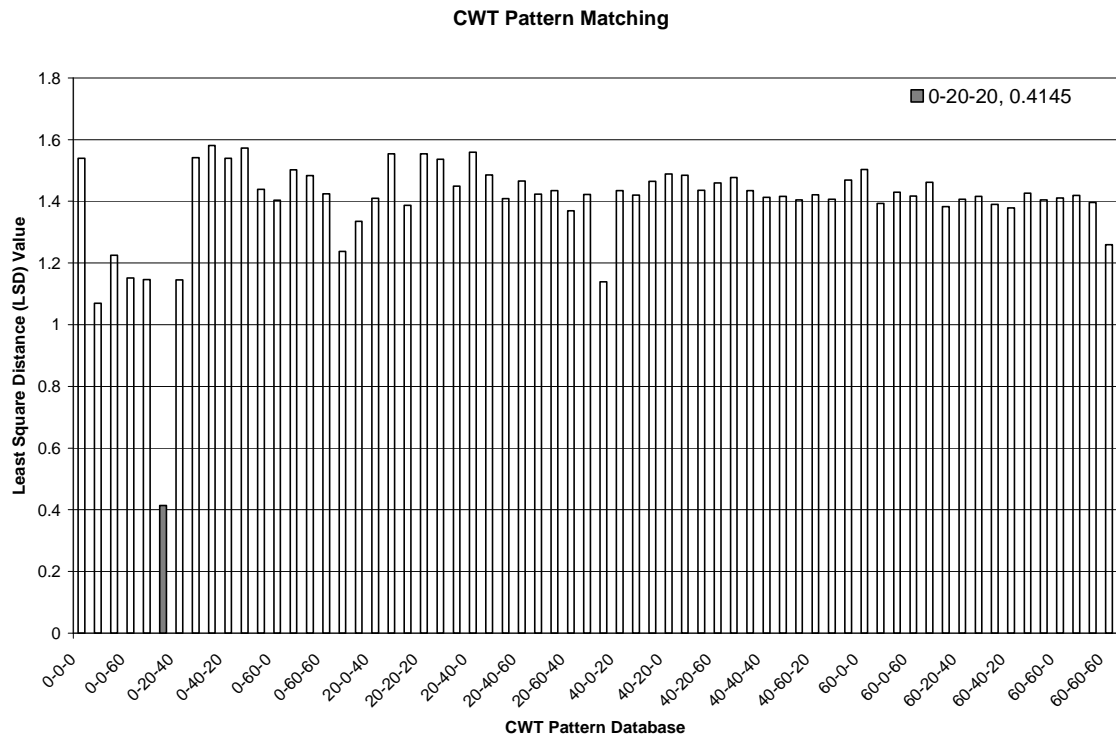
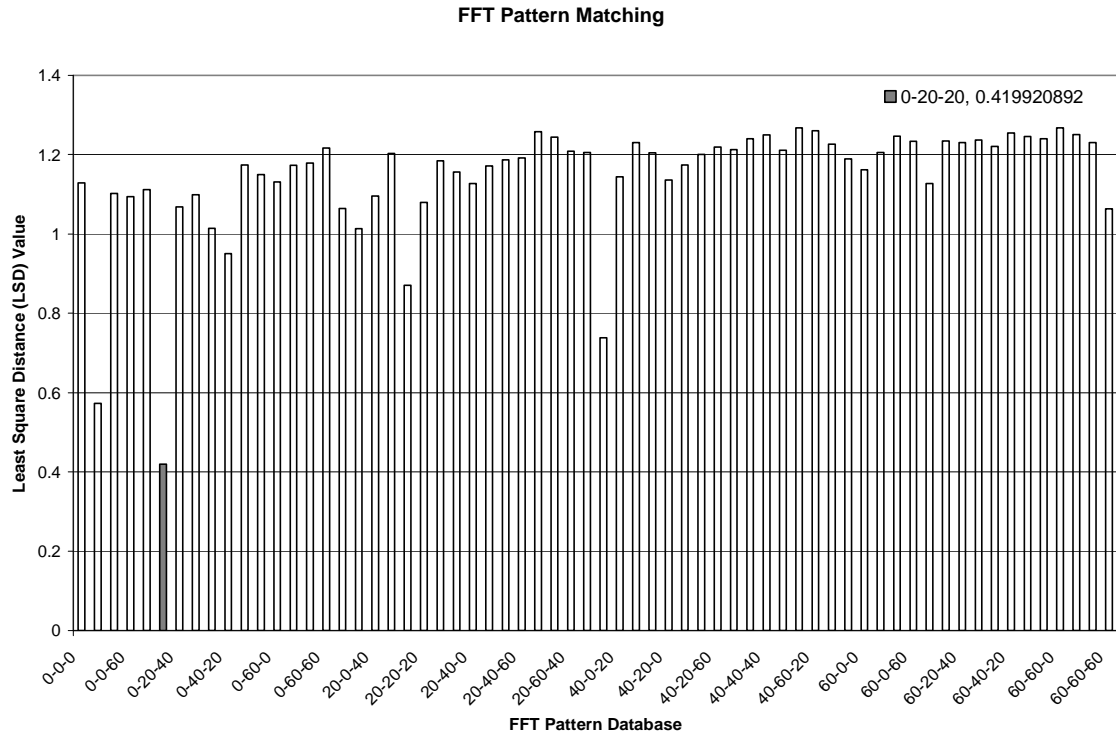


Figure D.9 Cosh Spectral Distance (CSD) Matching for Damage Case 0-20-20, FFT & CWT Pattern Matching

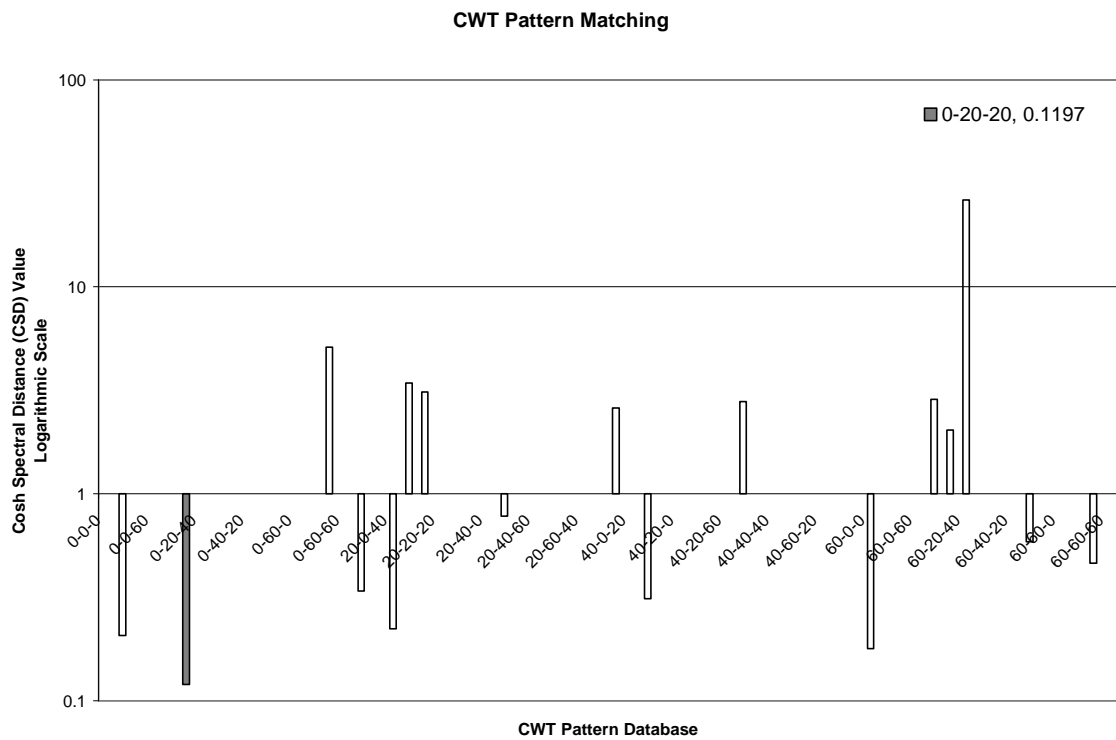
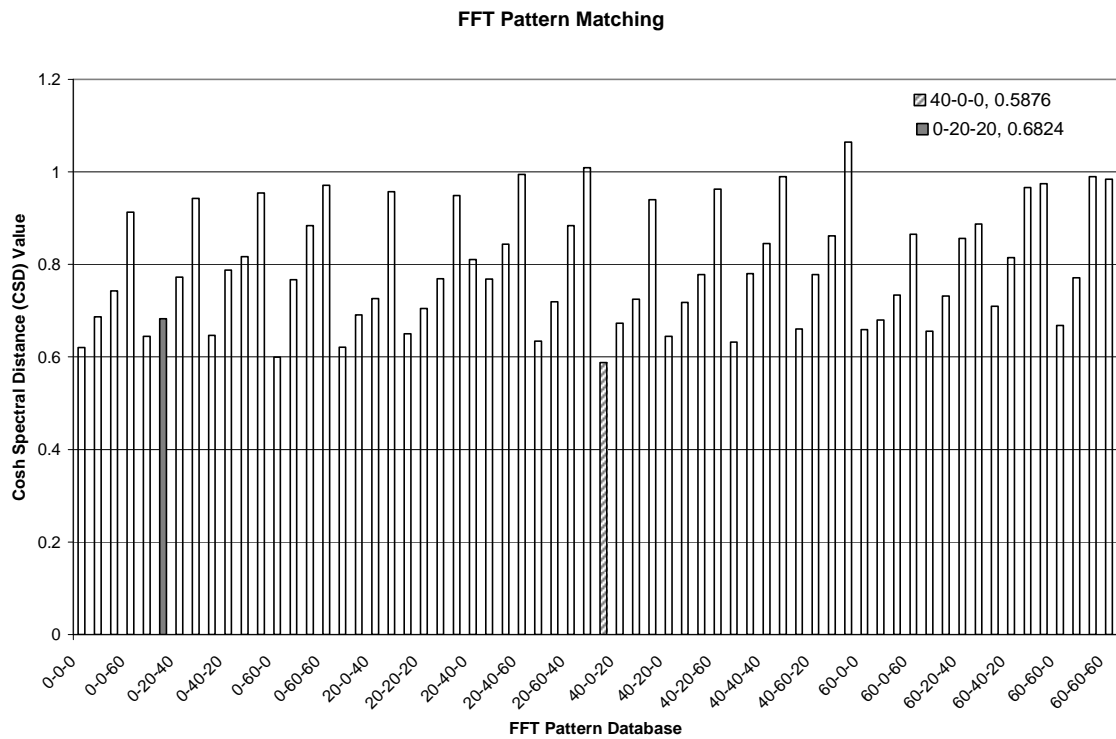


Figure D.10 Correlation Matching for Damage Case 20-0-20, FFT & CWT Pattern Matching

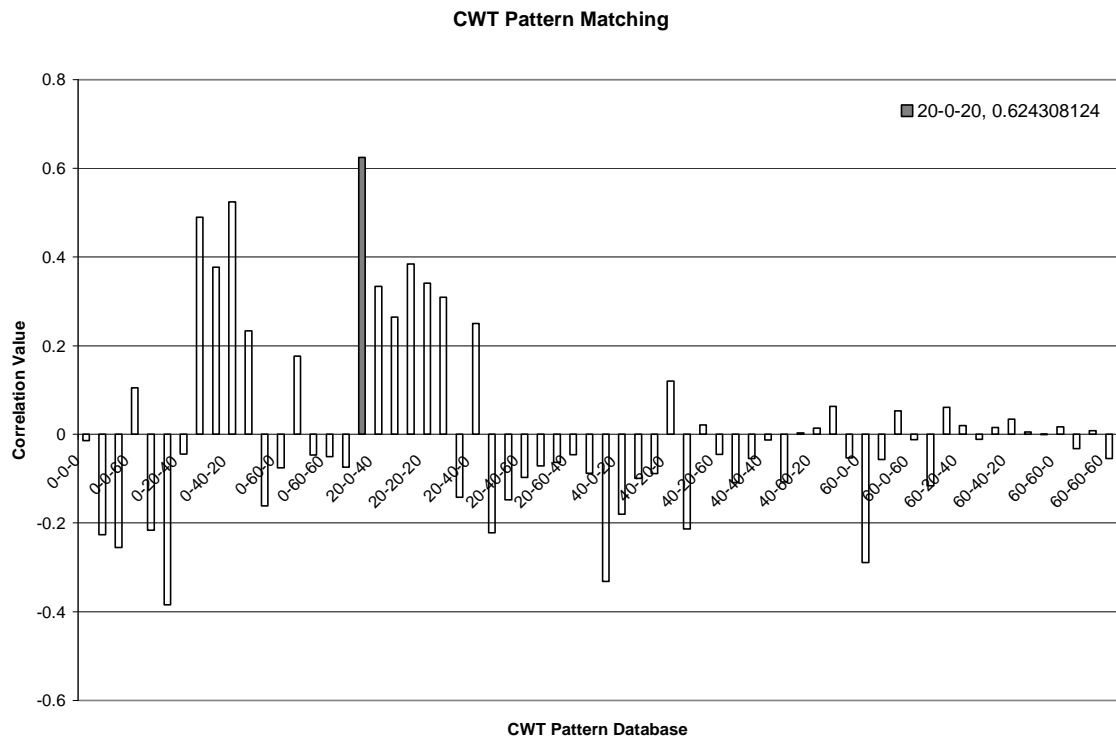
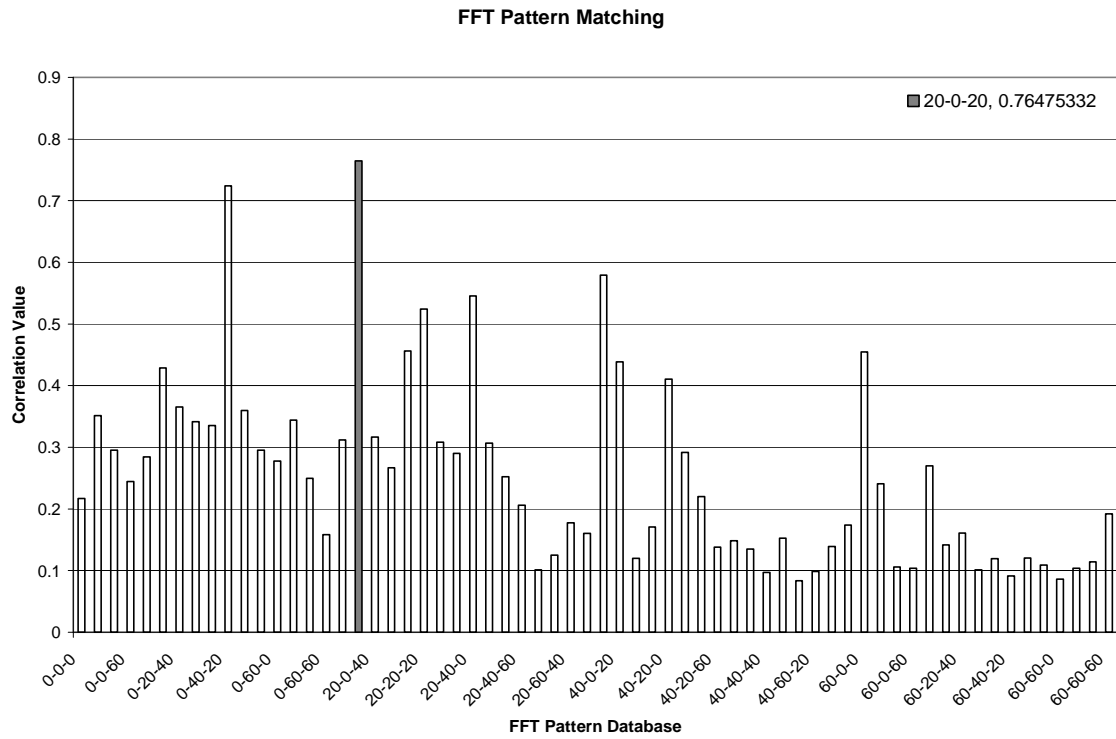


Figure D.11 Least Square Distance (LSD) Matching for Damage Case 20-0-20, FFT & CWT Pattern Matching

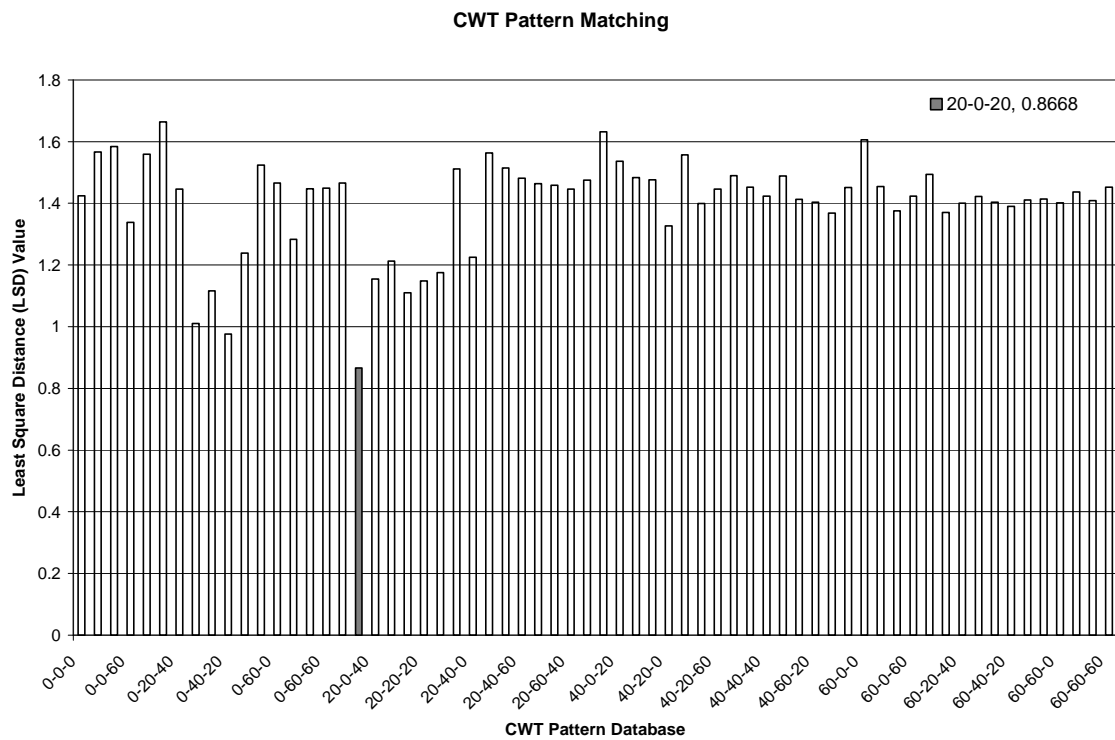
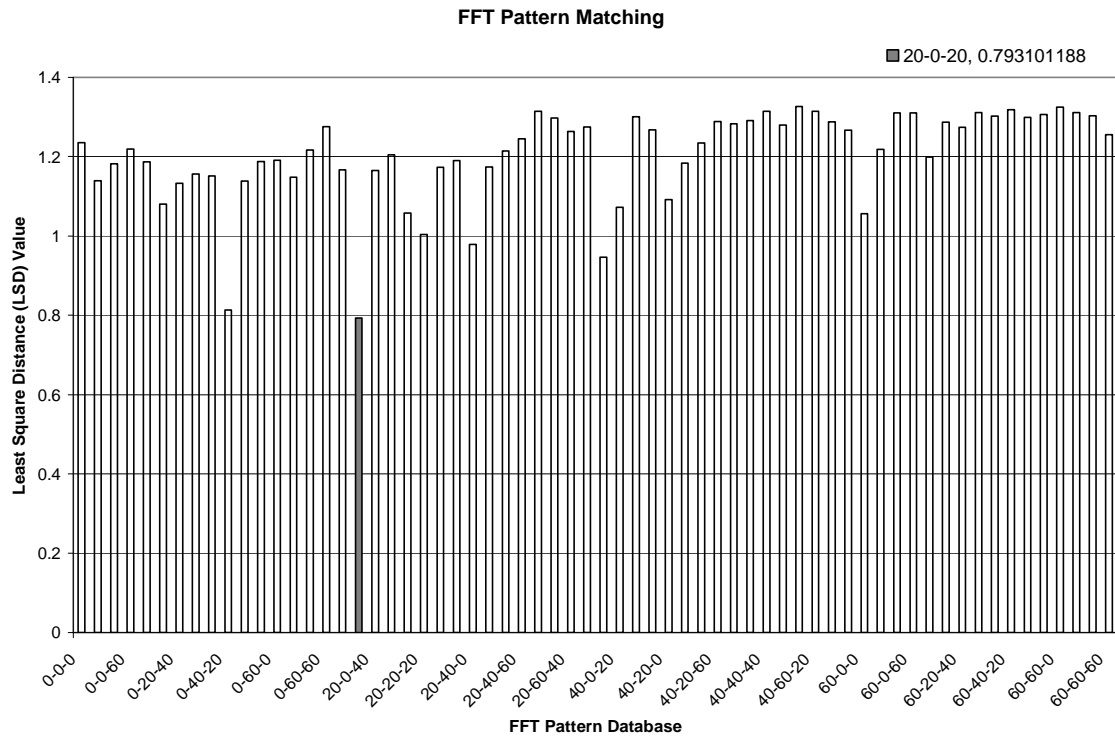


Figure D.12 Cosh Spectral Distance (CSD) Matching for Damage Case 20-0-20, FFT & CWT Pattern Matching

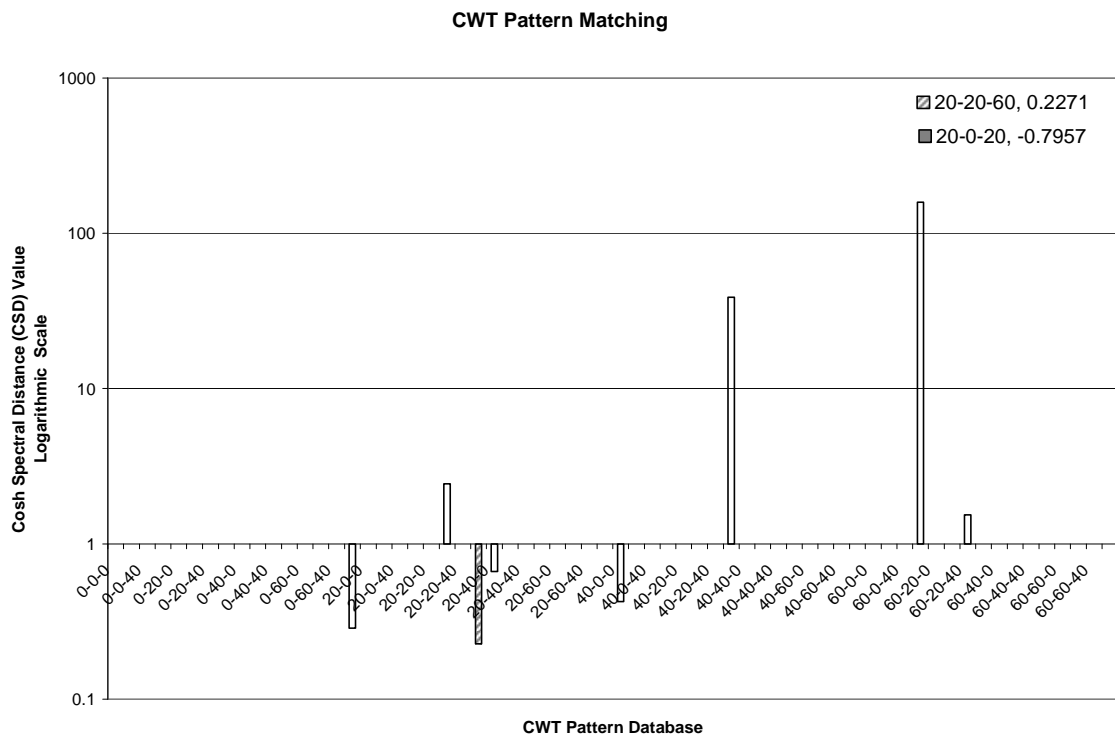
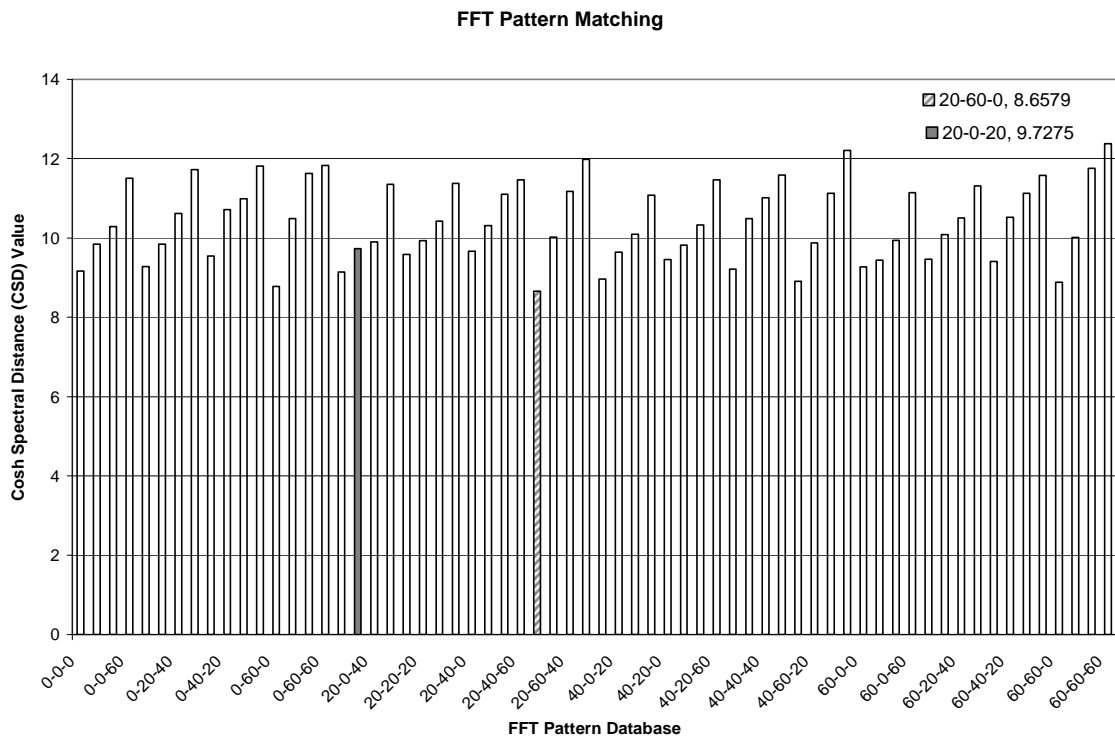


Figure D.13 Correlation Matching for Damage Case 20-20-0, FFT & CWT Pattern Matching

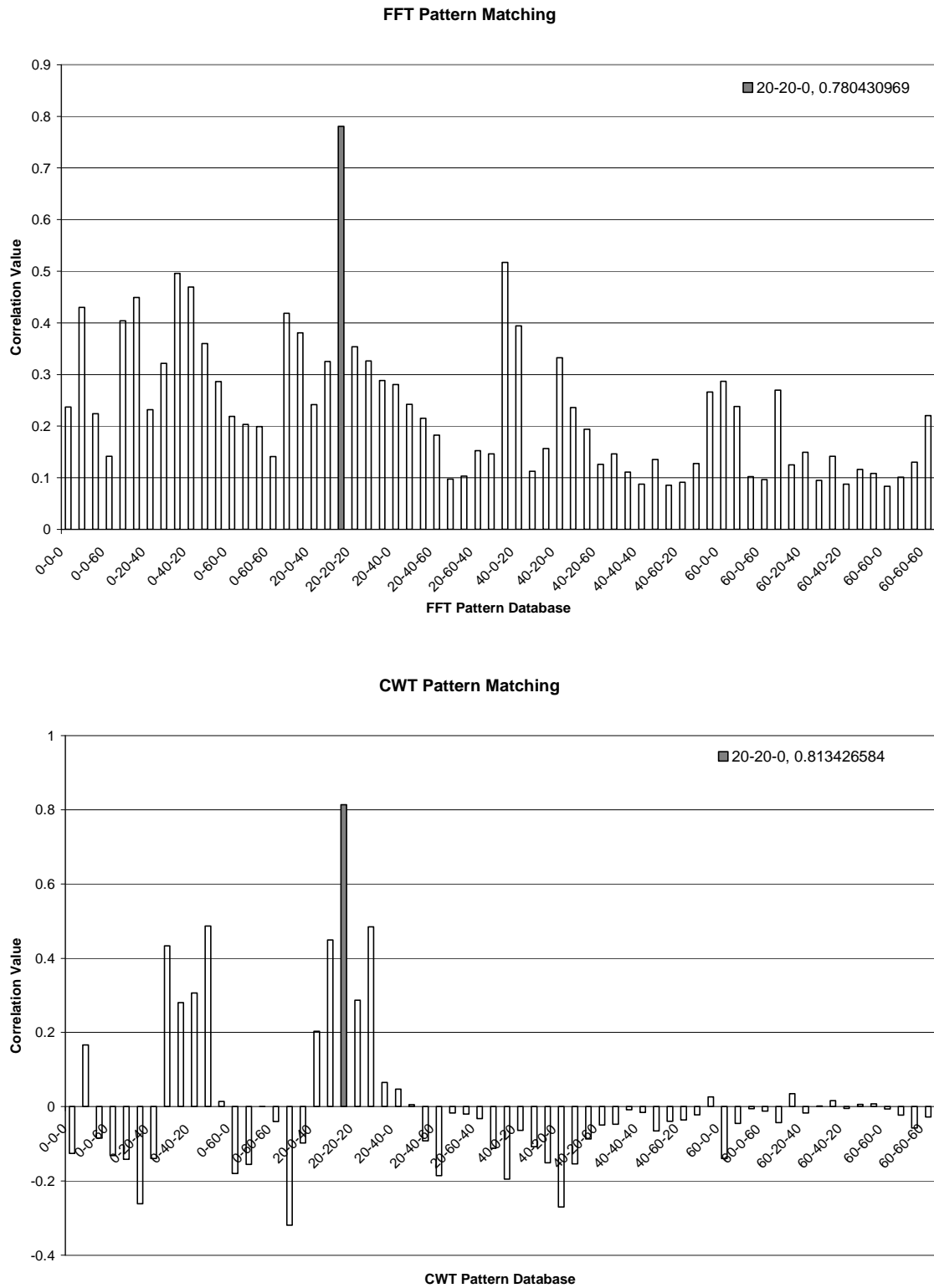


Figure D.14 Least Square Distance (LSD) Matching for Damage Case 20-20-0, FFT & CWT Pattern Matching

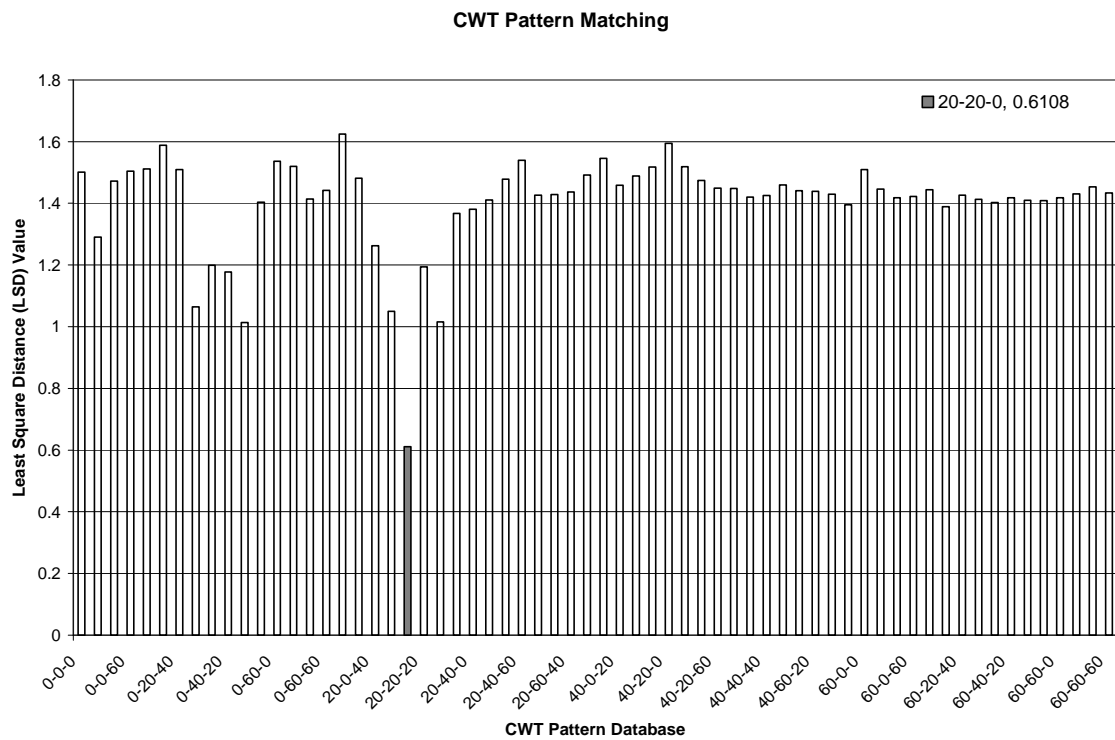
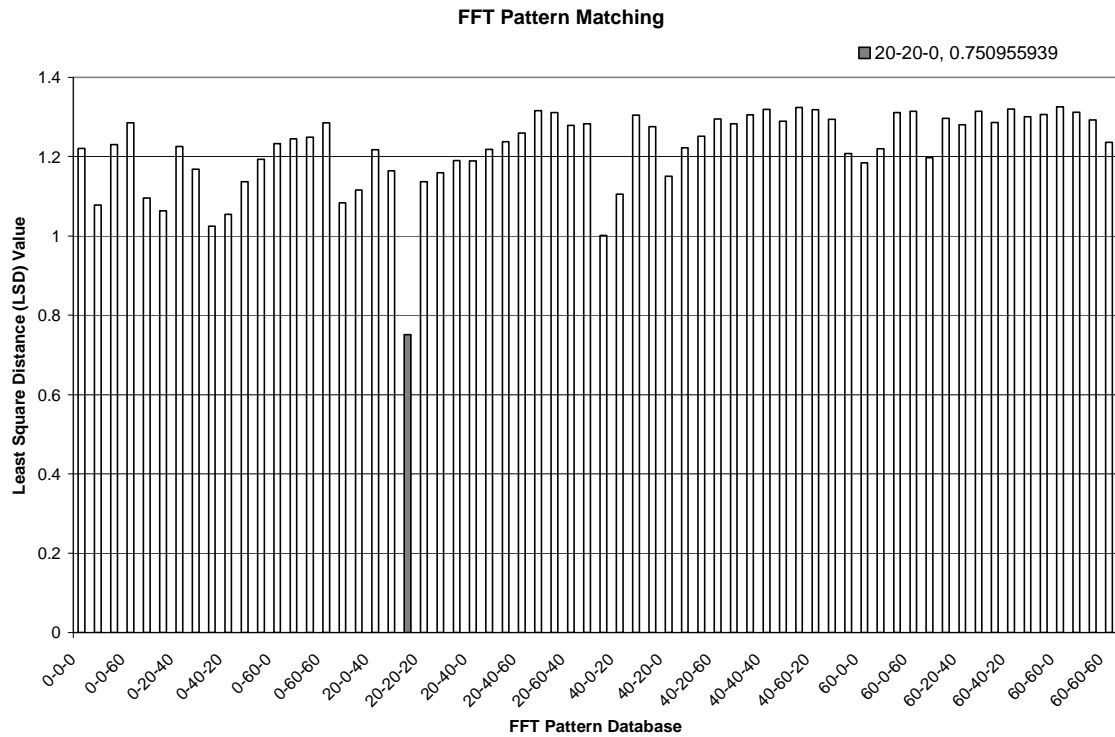


Figure D.15 Cosh Spectral Distance (CSD) Matching for Damage Case 20-20-0, FFT & CWT Pattern Matching

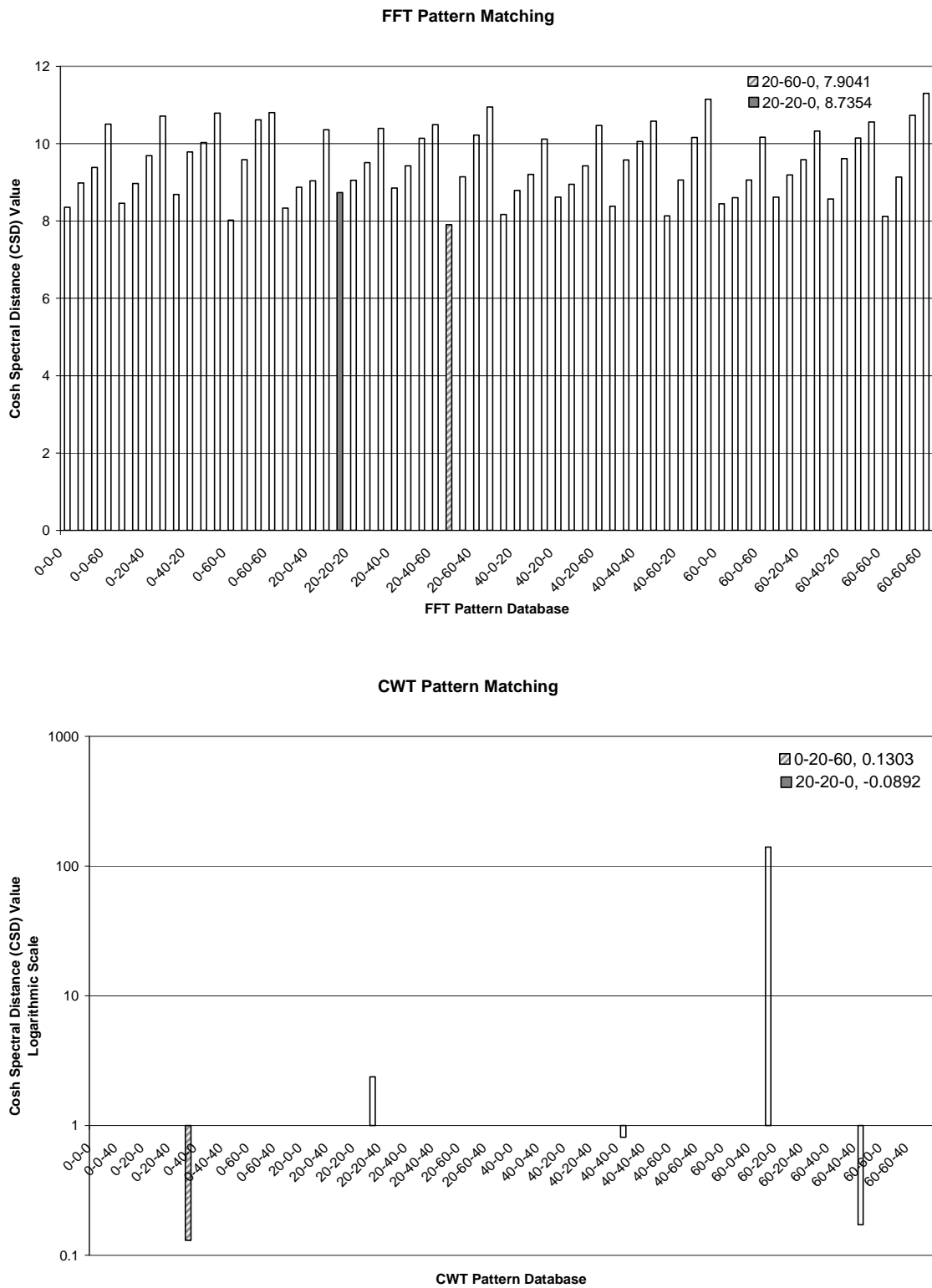


Figure D.16 Correlation Matching for Damage Case 0-20-40, FFT & CWT Pattern Matching

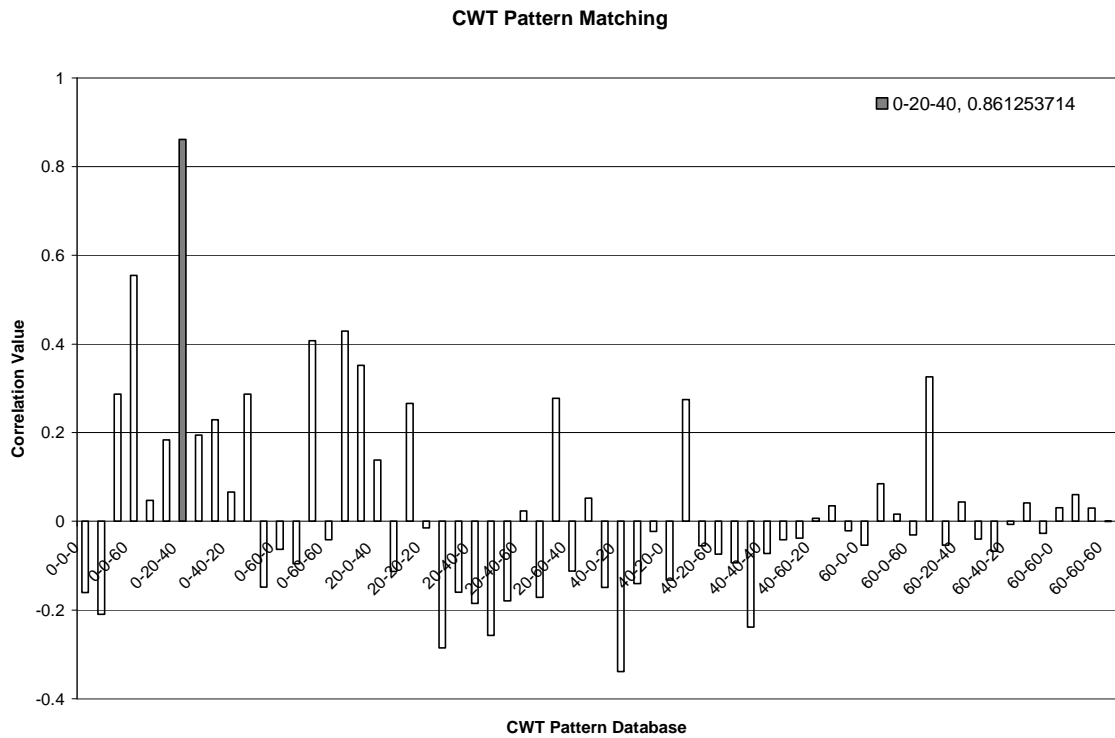
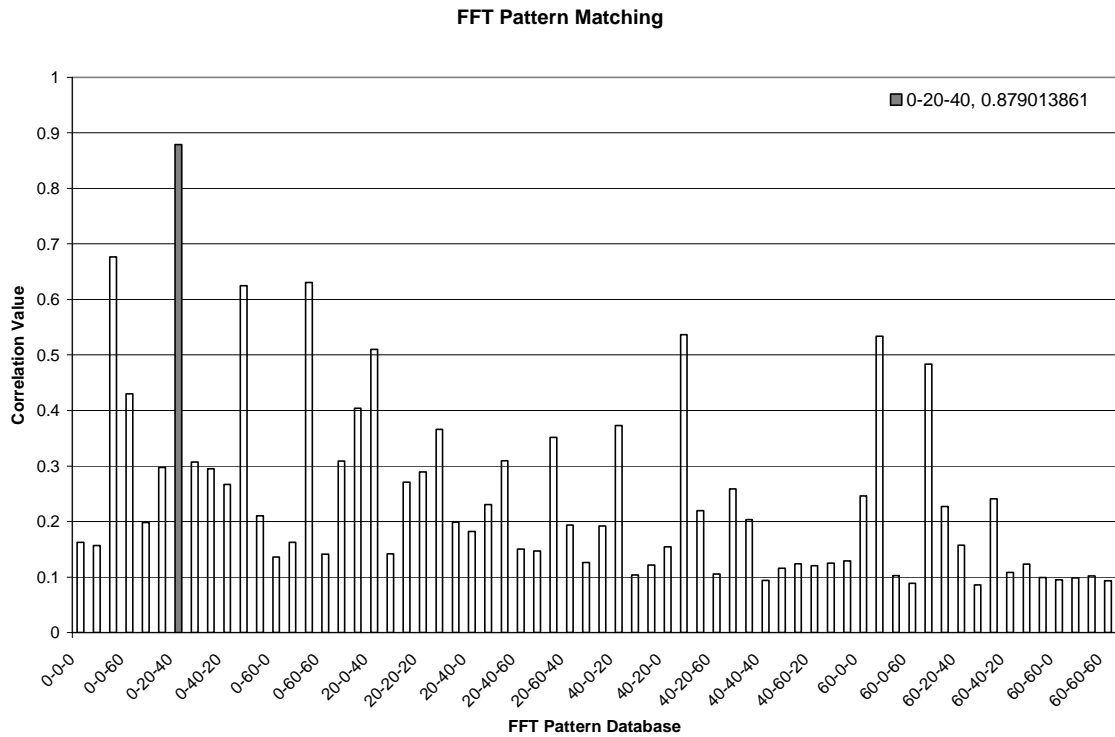


Figure D.17 Least Square Distance (LSD) Matching for Damage Case 0-20-40, FFT & CWT Pattern Matching

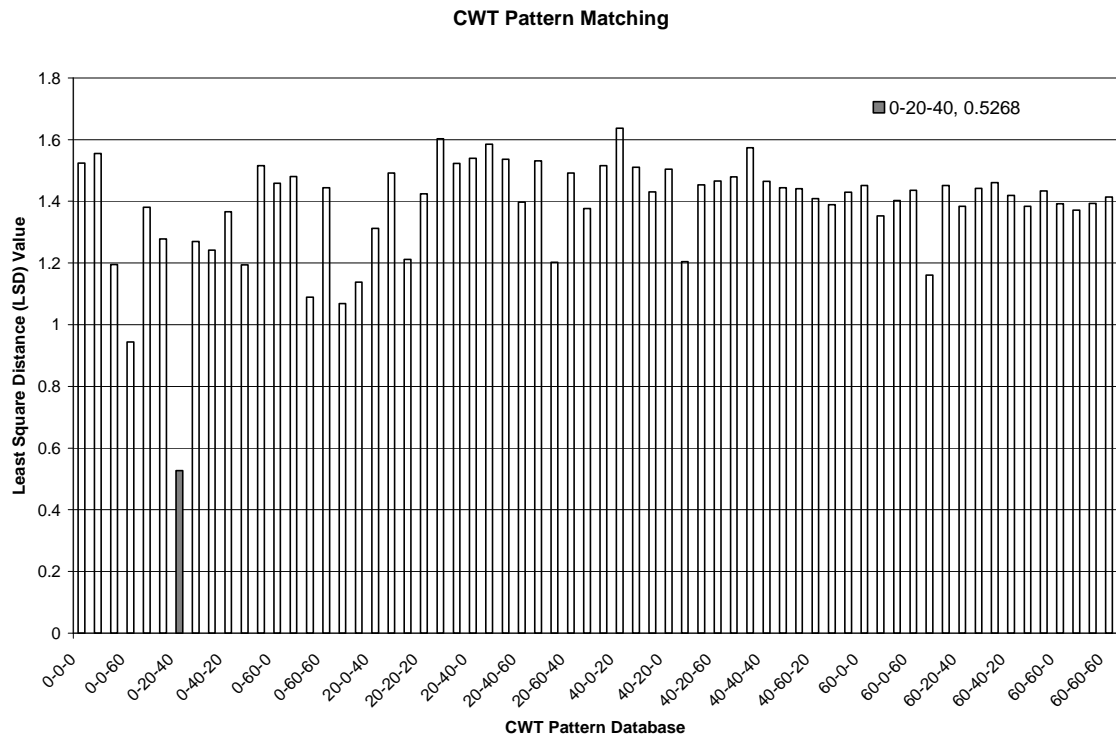
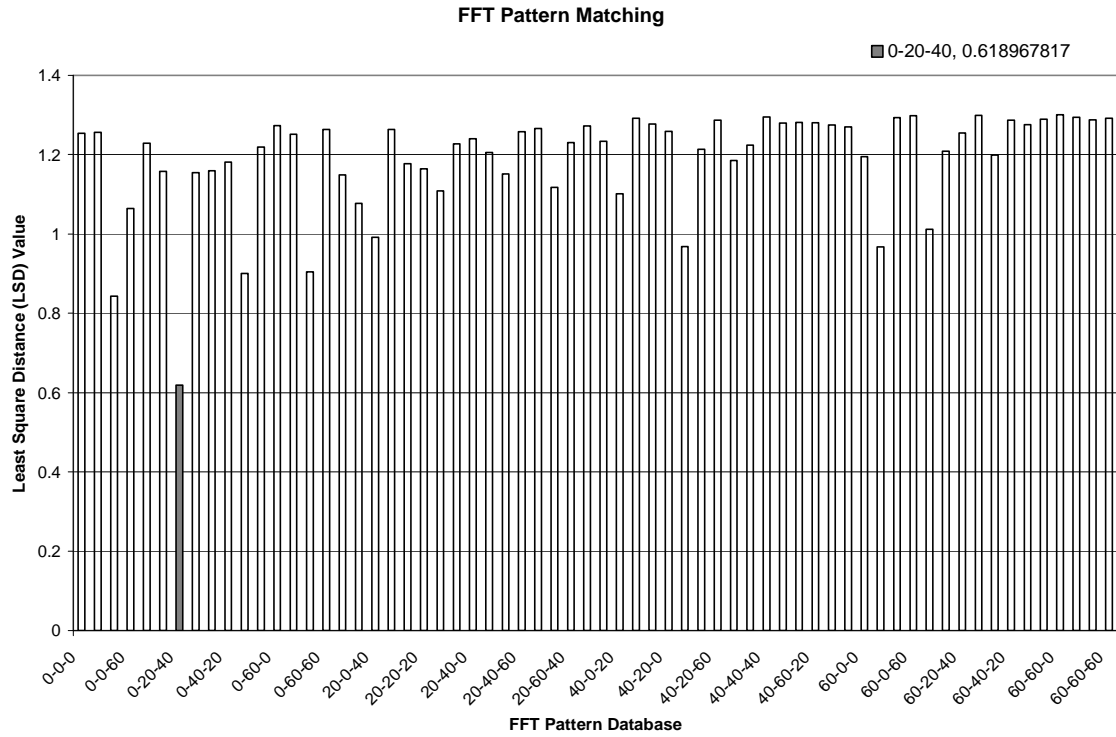


Figure D.18 Cosh Spectral Distance (CSD) Matching for Damage Case 0-20-40, FFT & CWT Pattern Matching

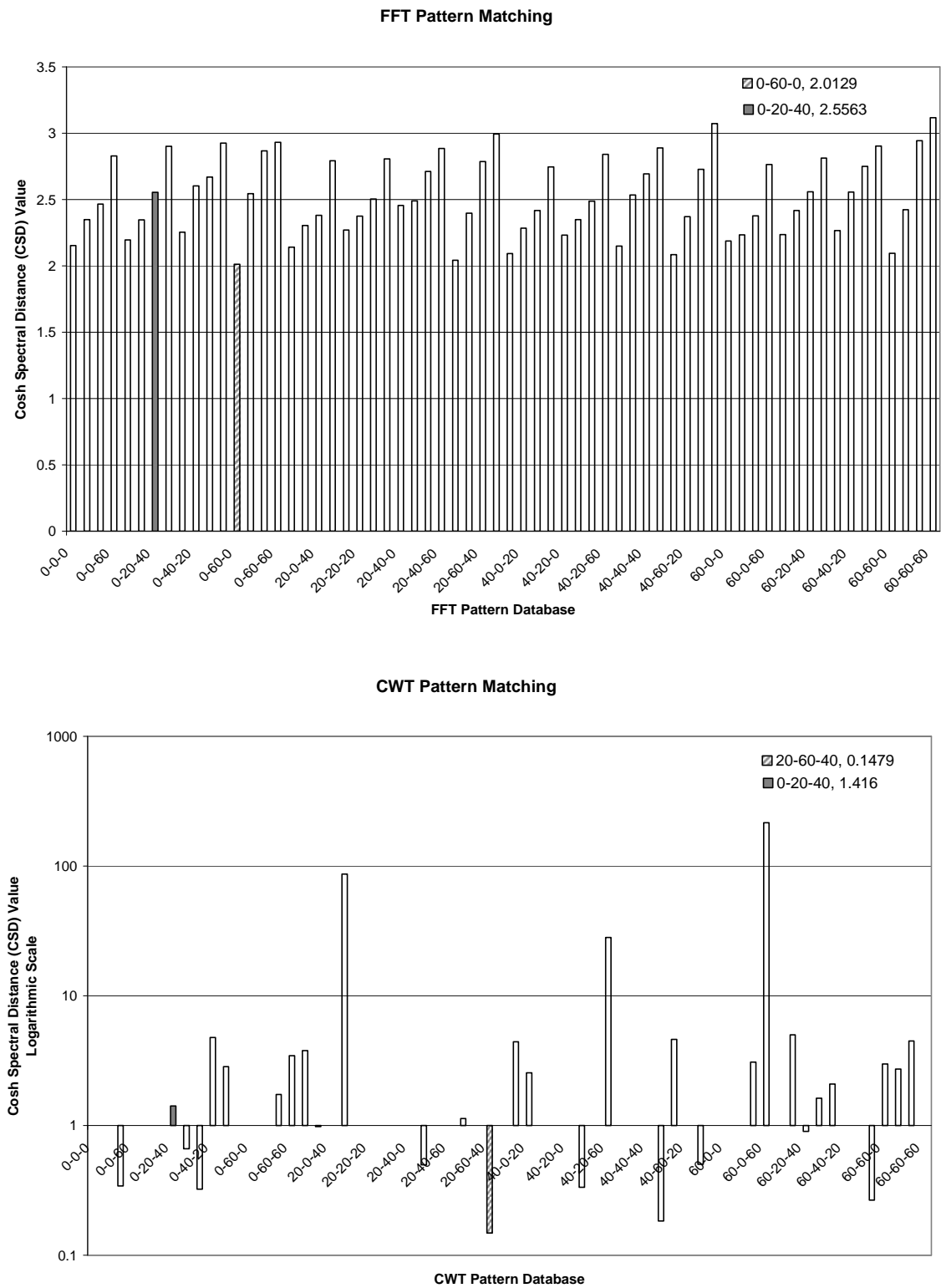


Figure D.19 Correlation Matching for Damage Case 20-20-20, FFT & CWT Pattern Matching

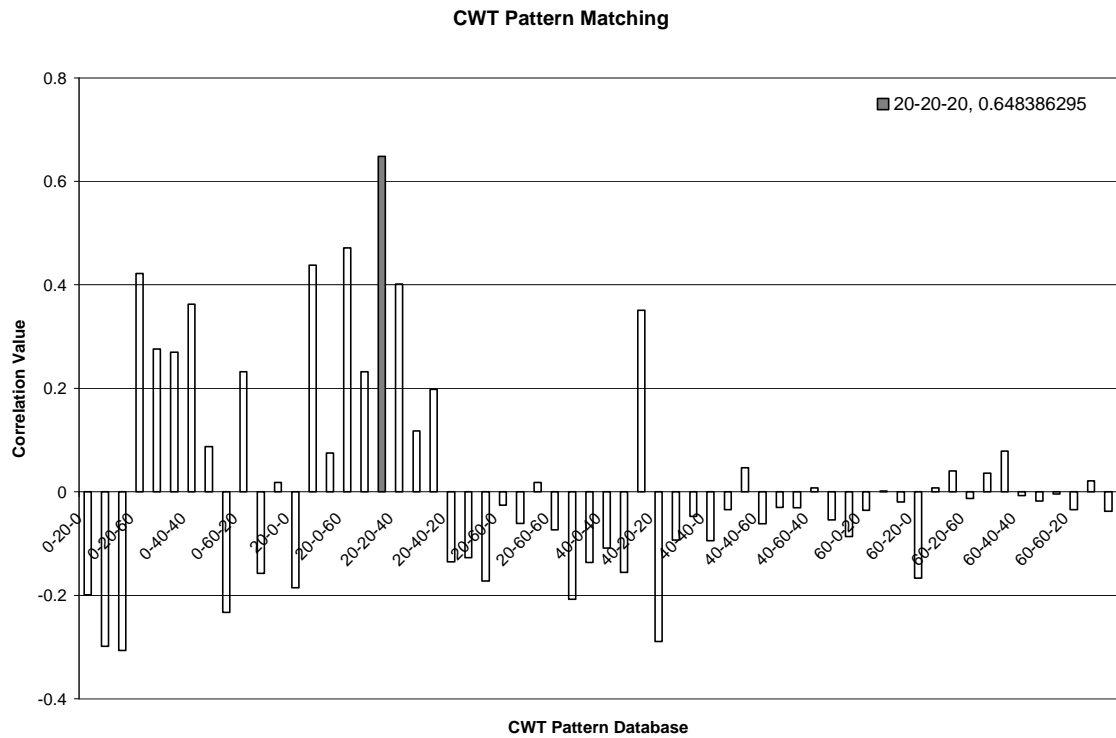
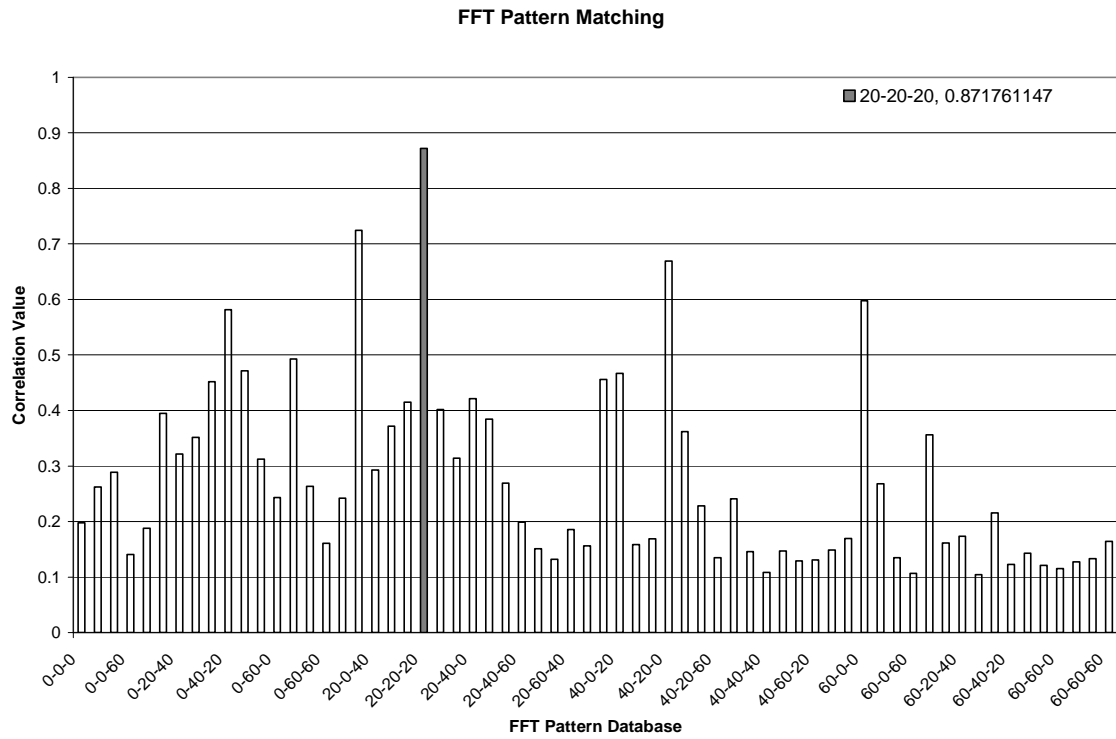


Figure D.20 Least Square Distance (LSD) Matching for Damage Case 20-20-20, FFT & CWT Pattern Matching

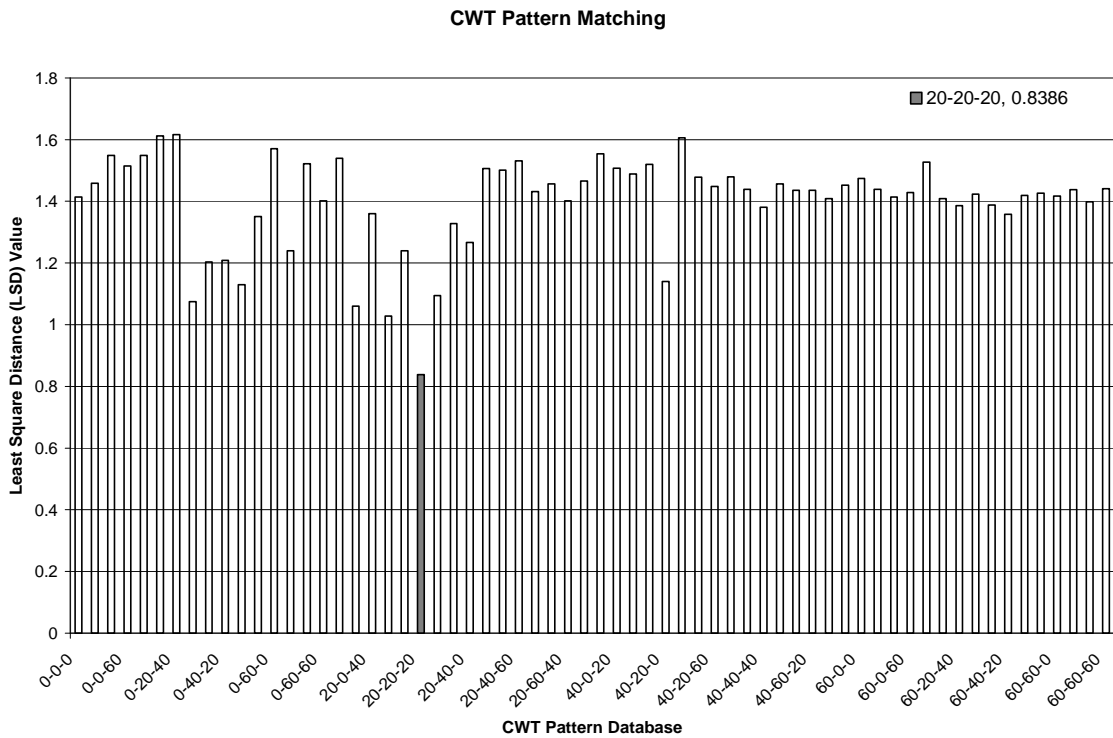
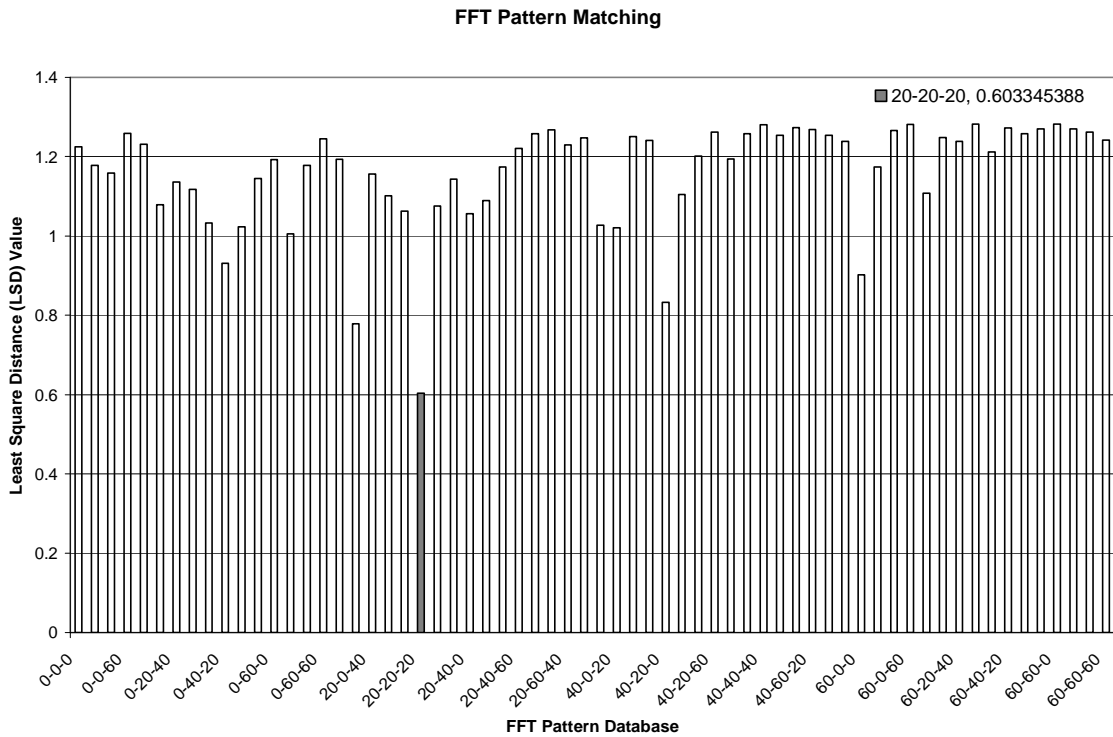


Figure D.21 Cosh Spectral Distance (CSD) Matching for Damage Case 20-20-20, FFT & CWT Pattern Matching

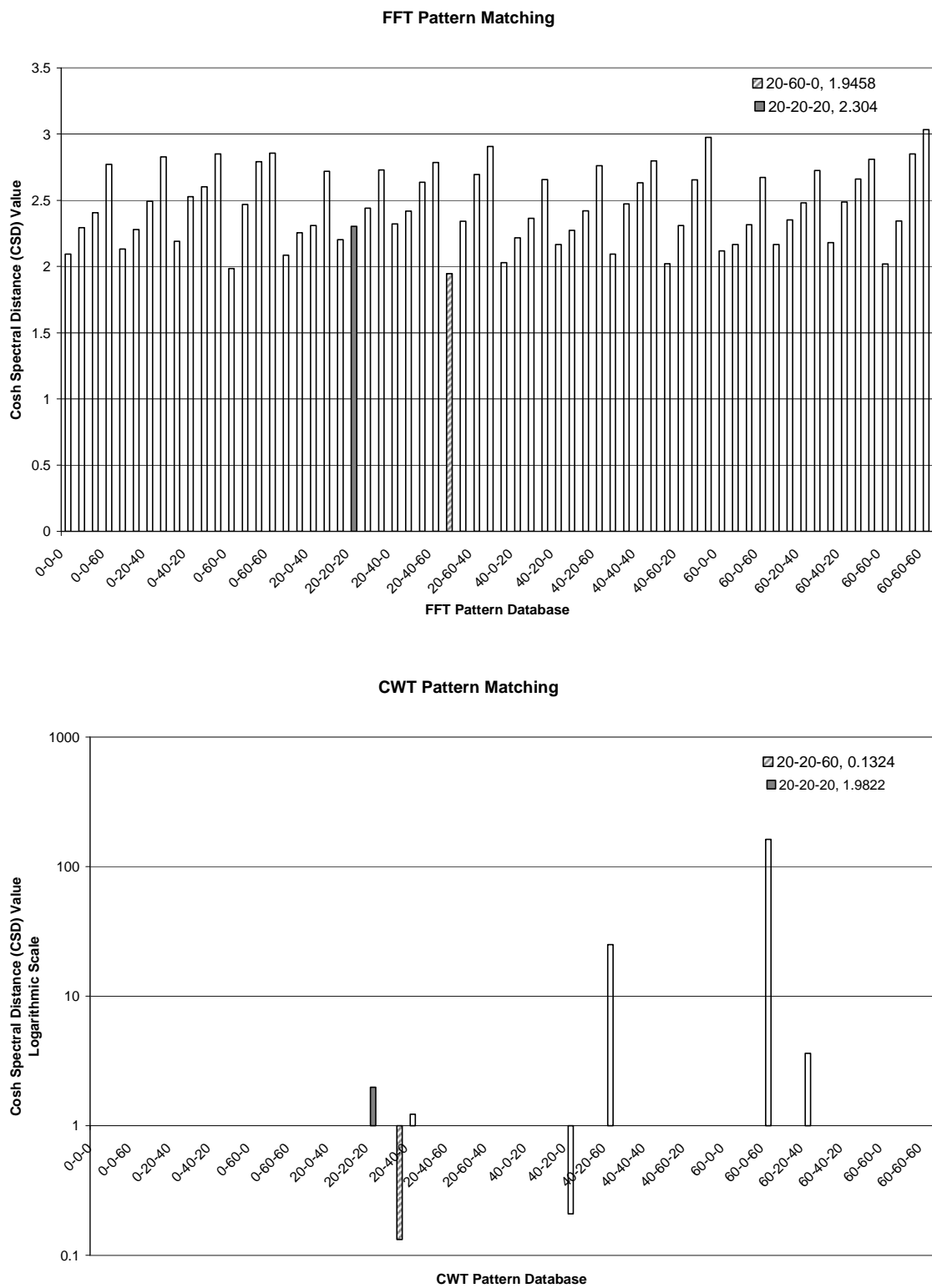


Figure D.22 Correlation Matching for Damage Case 20-20-40, FFT & CWT Pattern Matching

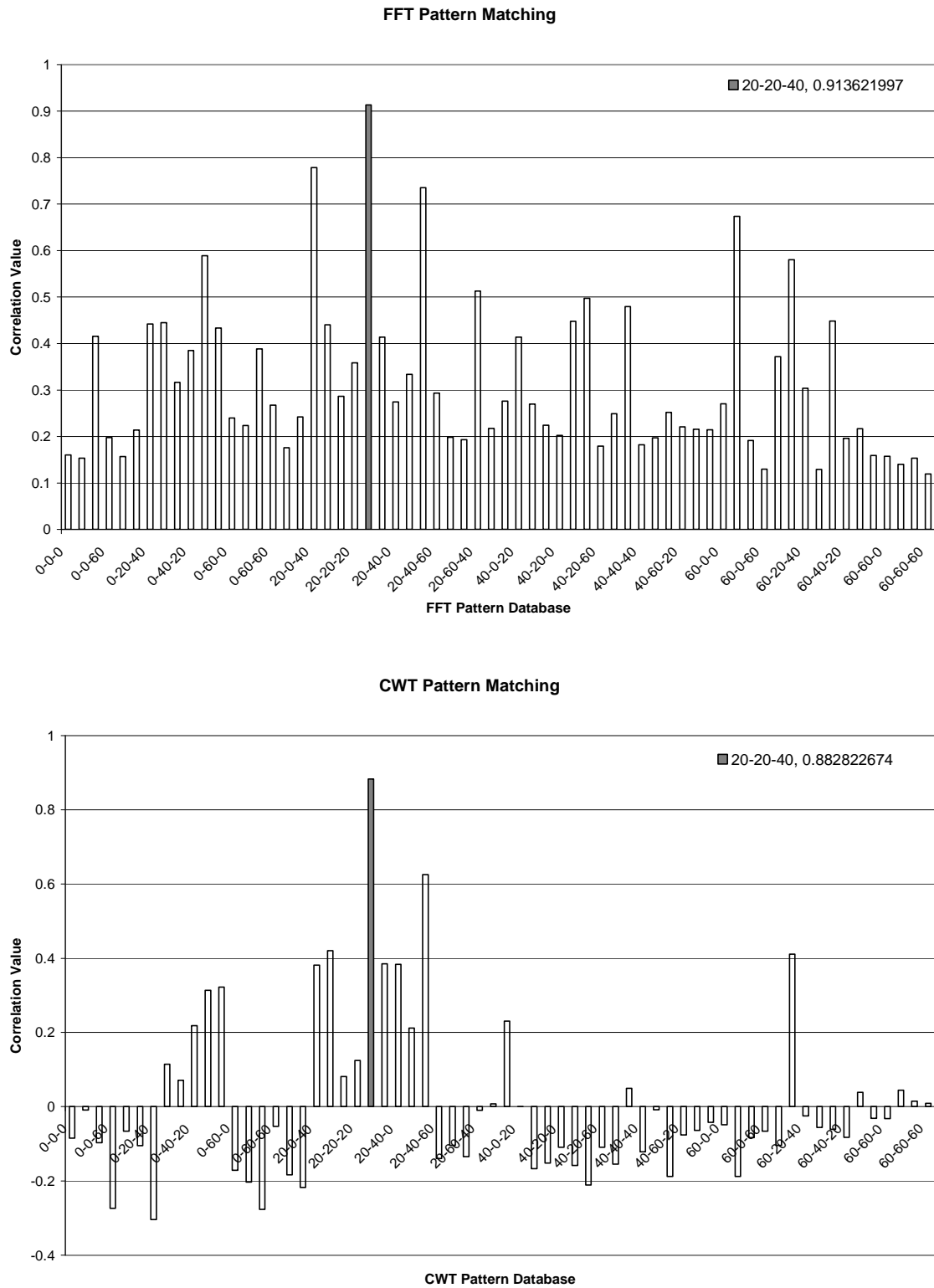


Figure D.23 Least Square Distance (LSD) Matching for Damage Case 20-20-40, FFT & CWT Pattern Matching

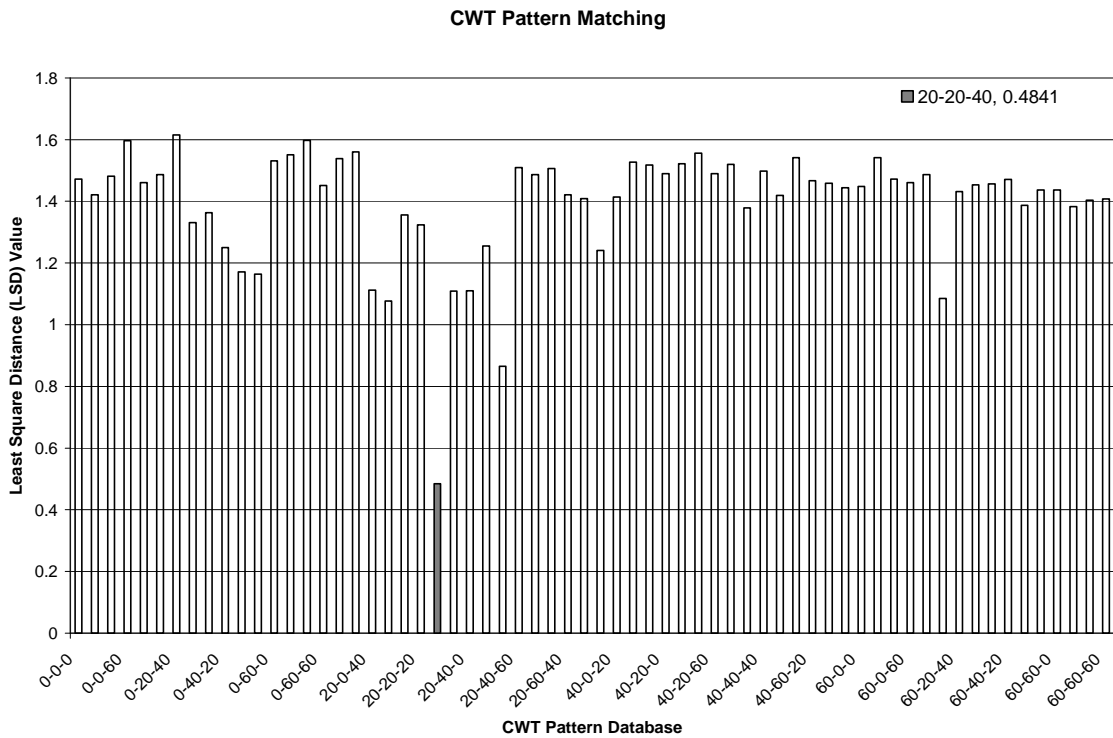
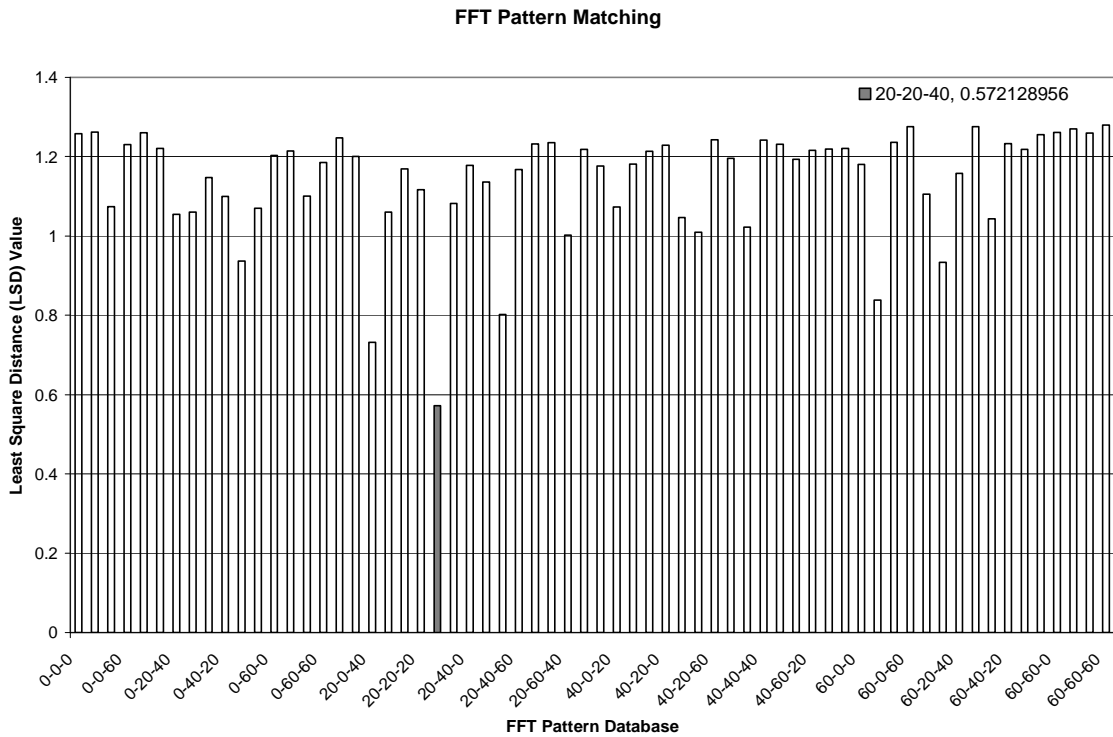


Figure D.24 Cosh Spectral Distance (CSD) Matching for Damage Case 20-20-40, FFT & CWT Pattern Matching

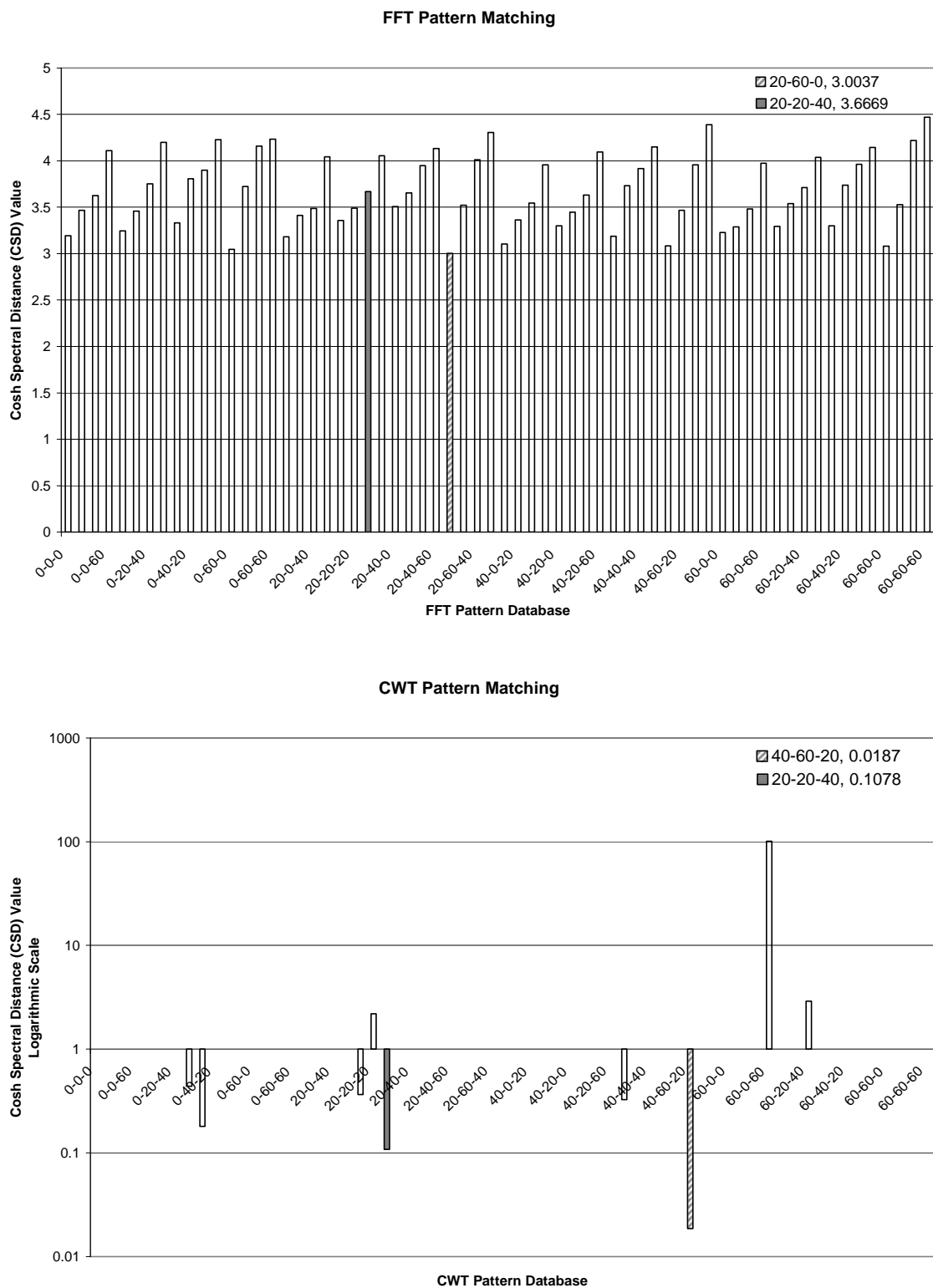


Figure D.25 Correlation Matching for Damage Case 40-60-20, FFT & CWT Pattern Matching

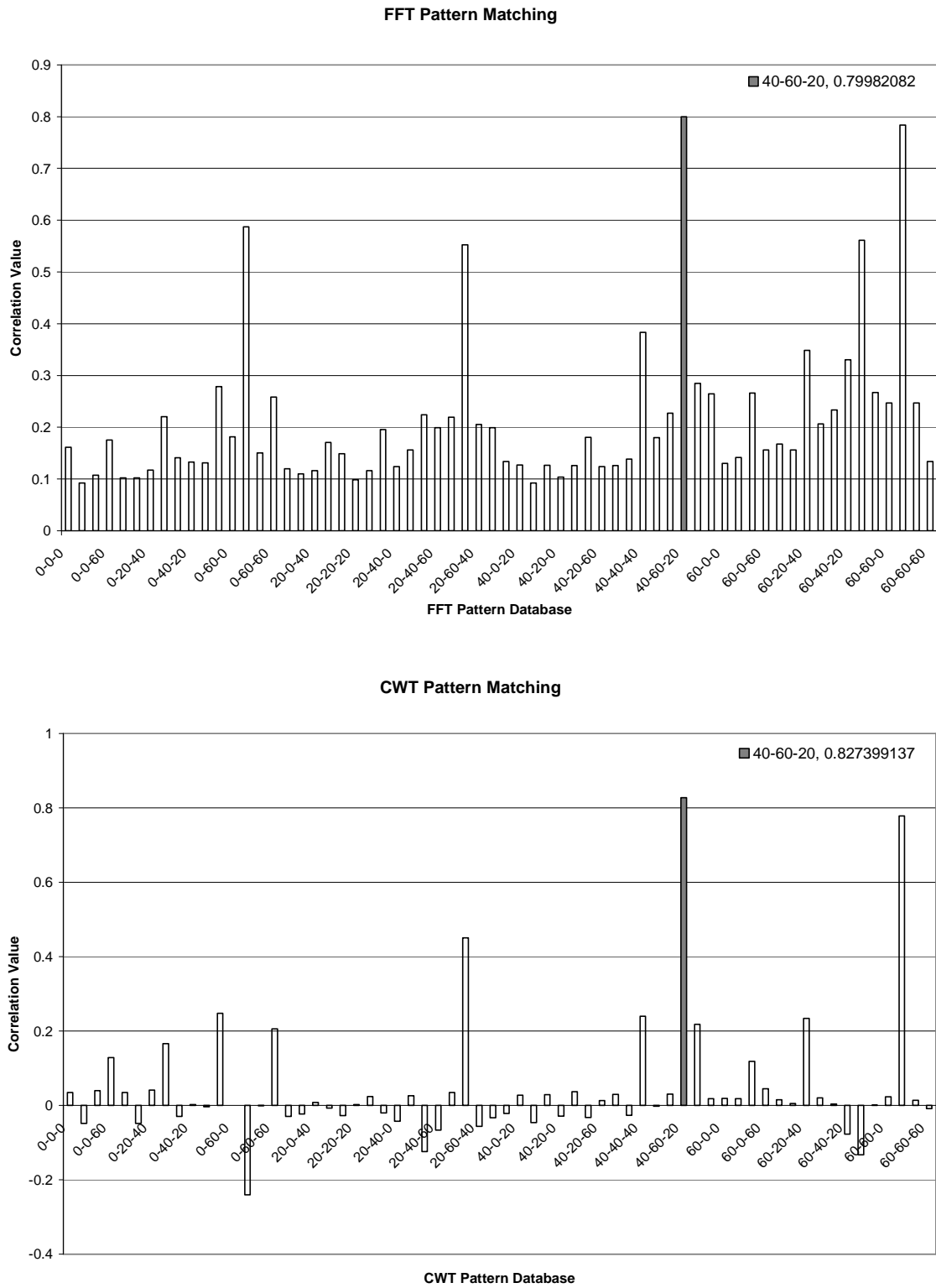


Figure D.26 Least Square Distance (LSD) Matching for Damage Case 40-60-20, FFT & CWT Pattern Matching

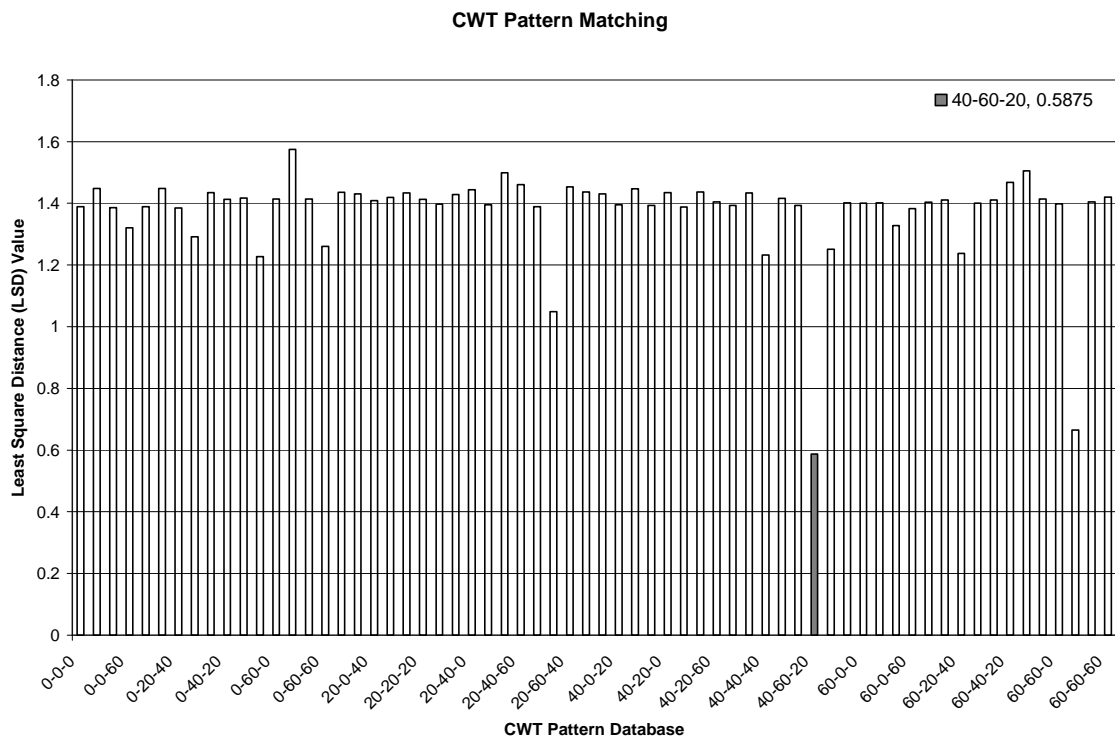
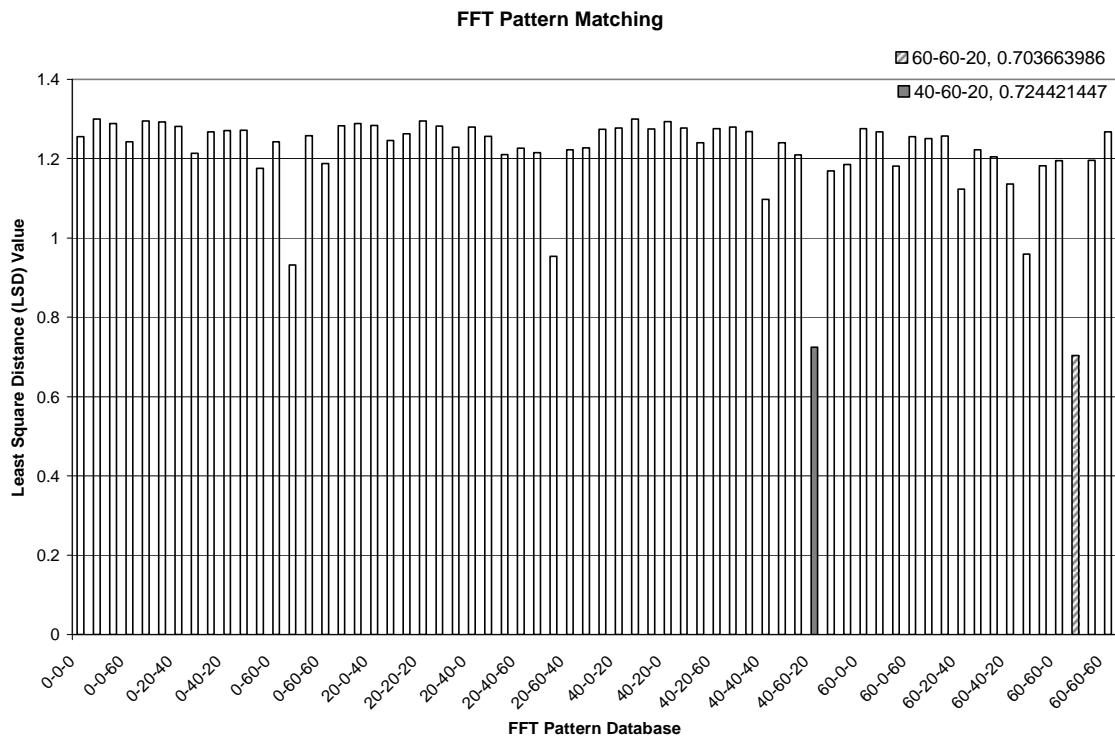
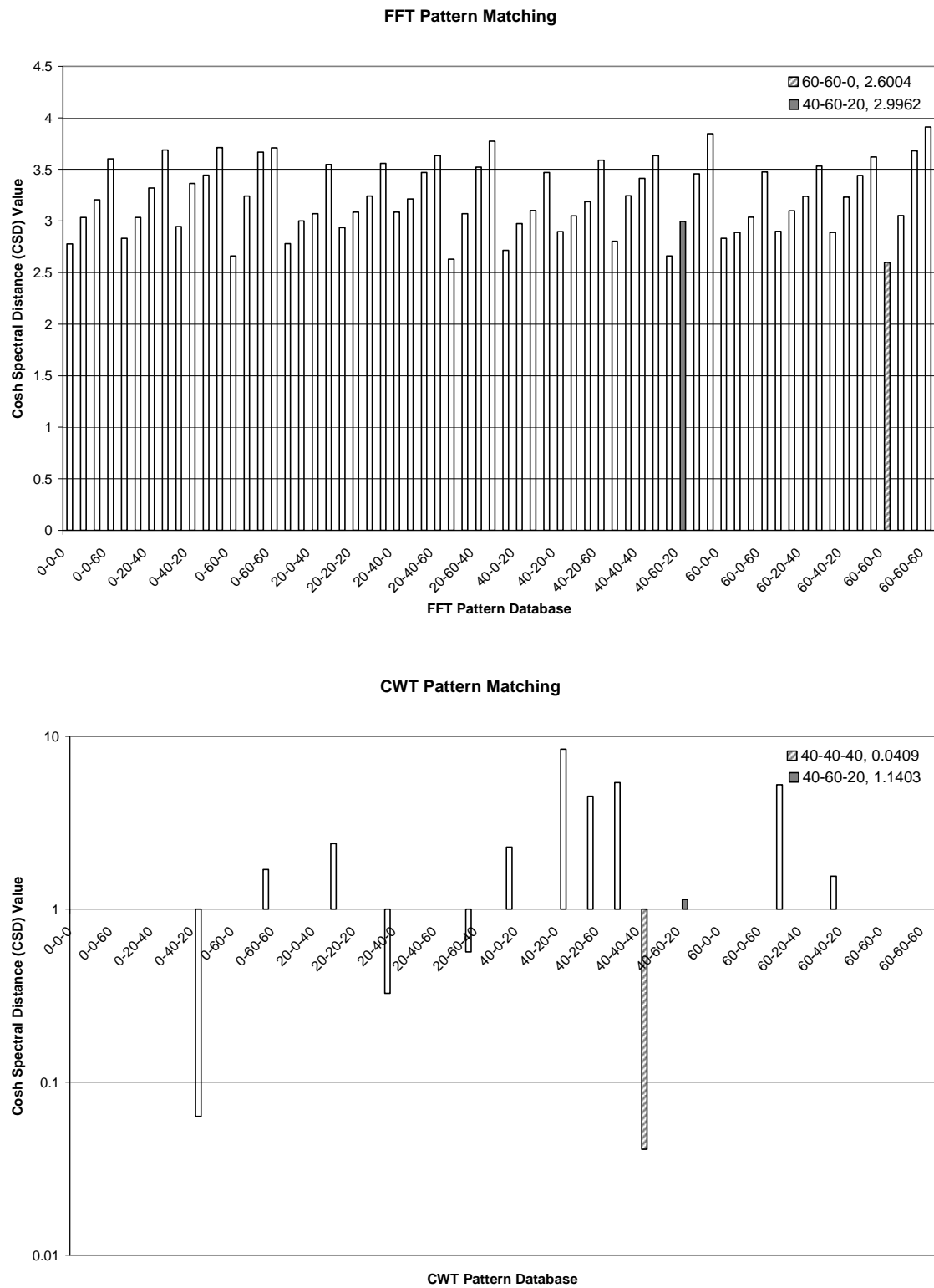


Figure D.27 Cosh Spectral Distance (CSD) Matching for Damage Case 40-60-20, FFT & CWT Pattern Matching



Appendix E - Wavelet Function Investigation

Table E.1 CWT Pattern-Matching Resolution Based on Different Wavelet Function

Mother Wavelet		Center Frequency (Hz)	Correlation Matching Resolution (%)		
			Damage Case 0-0-20	Damage Case 20-20-0	Damage Case 20-20-40
haar		0.9961	31.91	20.54	34.5
daubechies	db1	0.9961	31.91	20.54	34.5
	db2	0.6667	23.54	52.03	23.85
	db3	0.8	40.13	31.61	33.69
	db4	0.7143	36.94	43.5	28.02
	db5	0.6667	24.57	51.23	24
	db6	0.7273	41.35	40.12	29.14
	db7	0.6923	32.8	45.83	26.26
	db8	0.6667	25.43	50.29	24.16
	db9	0.7059	37.01	42.68	27.66
	db10	0.6842	30.92	46.69	25.48
symlets	sym2	0.6667	23.54	52.03	23.85
	sym3	0.8	40.13	31.61	33.69
	sym4	0.7143	36.78	43.56	28.13
	sym5	0.6667	24.42	50.83	24.34
	sym6	0.7273	41.09	40.21	29.63
	sym7	0.6923	32.67	46.06	26.87
	sym8	0.6667	25.22	50.12	24.56
coif	coif1	0.800	41.12	33.19	33.24
	coif2	0.7273	39.87	41.09	29.22
	coif3	0.7059	35.65	43.49	27.92
	coif4	0.6957	33.58	44.84	27.21

	coif5	0.6897	32.28	45.48	26.85
bior	bior1.1	0.9961	31.91	20.54	34.5
	bior1.3	0.8006	39.43	30.72	34.41
	bior1.5	0.7781	40.19	31.65	33.87
	bior2.2	1.0008	36.51	31.12	36.98
	bior2.4	0.8893	41.69	34.04	32.62
	bior2.6	0.9234	37.13	25.96	36.29
	bior2.8	0.8826	39.34	29.74	34.28
	bior3.3	1.0006	40.45	42.02	33.94
	bior3.5	1.0004	37.34	30.26	35.84
	bior3.7	0.9336	41.51	34.1	32.22
	bior3.9	0.9476	38.69	28.95	34.51
	bior4.4	0.7781	39.99	41.08	29.17
	bior5.5	0.6366	17.16	54.83	22.2
	bior6.8	0.7649	41.71	39.79	29.71
rbio	rbio1.1	0.9961	31.91	20.54	34.5
	rbio1.3	0.8006	42.81	36.9	31.8
	rbio1.5	0.6670	17.59	55.64	22.12
	rbio2.2	0.6005	43.33	39.64	30.13
	rbio2.4	0.5558	20.22	53.27	23.21
	rbio2.6	0.6156	35.98	43.25	28
	rbio2.8	0.5884	24.90	50.21	24.35
	rbio3.1	0.3338	13.44	59.43	21.32
	rbio3.3	0.4288	10.39	59.78	20.33
	rbio3.5	0.5456	42.12	39.24	29.98
	rbio3.7	0.5335	31.05	45.9	26.41
	rbio3.9	0.5264	23.35	50.53	23.88
	rbio4.4	0.6670	38.76	42.23	28.74
	rbio5.5	0.8185	39.71	30.48	34.28
	rbio6.8	0.6472	30.29	47.15	26.13

meyr		0.6902	34.28	45.79	26.12
dmey		0.6634	25.49	49.94	24.58
gaus	gaus1	0.2	19.74	55.60	22.85
	gaus2	0.3	31.84	47.18	26.40
	gaus3	0.4	42.28	35.49	31.87
	gaus4	0.5	36.03	24.45	37.08
	gaus5	0.5	43.63	37.83	30.41
	gaus6	0.6	35.96	24.1	37.02
	gaus7	0.6	41.75	34.35	31.81
	gaus8	0.6	30.08	45.13	26.29
mexh		0.25	38.81	29.97	35.03
morl		0.8125	38.78	28.65	34.2